



PHD

Nanomaterials for Membrane Protein Biology

Mason, Eleonore

Award date:
2023

Awarding institution:
University of Bath

[Link to publication](#)

Alternative formats

If you require this document in an alternative format, please contact:
openaccess@bath.ac.uk

Copyright of this thesis rests with the author. Access is subject to the above licence, if given. If no licence is specified above, original content in this thesis is licensed under the terms of the Creative Commons Attribution-NonCommercial 4.0 International (CC BY-NC-ND 4.0) Licence (<https://creativecommons.org/licenses/by-nc-nd/4.0/>). Any third-party copyright material present remains the property of its respective owner(s) and is licensed under its existing terms.

Take down policy

If you consider content within Bath's Research Portal to be in breach of UK law, please contact: openaccess@bath.ac.uk with the details. Your claim will be investigated and, where appropriate, the item will be removed from public view as soon as possible.

Nanomaterials for Membrane Protein Biology

submitted by

Eléonore Mason

for the degree of Doctor of Philosophy

of the

University of Bath

Department of Chemistry

September 2019

COPYRIGHT

Attention is drawn to the fact that copyright of this thesis rests with the author. A copy of this thesis has been supplied on condition that anyone who consults it is understood to recognise that its copyright rests with the author and that they must not copy it or use material from it except as permitted by law or with the consent of the author.

This thesis may be made available for consultation
within the University Library and may be photocopied
or lent to other libraries for the purposes of
consultation with effect from.....(date)

Signed on behalf of the Faculty of Science

*For my darlings,
you know who you are.*

Acknowledgements

To begin, I would like to express my deepest gratitude to all of those who helped and supported me throughout my PhD. You are too many to name, but you all have my gratitude.

Above all, I am immensely grateful to my supervisor Adam Squires for his guidance, support, and inspiration over the course of my research. I have greatly enjoyed our time working together, in particular all those beamtime trips, not just the ones pertaining to my research. I would also like to thank my other supervisor Nick Terrill for all his helpful advice and input throughout this research. Furthermore, I would like to thank both the EPSRC and Diamond Light Source for giving me the opportunity to do this research in an area I am passionate about. The past four years have been tough, but nonetheless memorable and I have learned a lot.

In addition, I am very much appreciative of the many collaborators and groups who have aided me to make this research possible. Firstly my fellow Squees, Ben Eves, Jacob Boswell, and Han Yin for making the Squires group such a fantastic and inspiring environment to work in. My Masters students, Ben Laurence and Wanli Liu, for their exemplary work. Also in particular, Aswin Doekhie for being willing to try and then succeeding in purifying a membrane protein from only a published protocol. To Chris Brasnett for all our insightful discussions, for pointing out the Topology summer school in Copenhagen where I met so many wonderful people, and for providing a membrane protein solution. It was lovely to chat Q_{II} phases with someone who understands. Finally, my thanks to Stephen Hall for providing the nanodisc solutions and James Dolan for making the hydrophobic silicon wafers.

I would also like to thank the many beamline scientists who have aided my research and helped me with multiple fruitful and not-so-fruitful experiments throughout my PhD. My gratitude also goes to Arwen Tyler for being a such magnificent beamtime buddy and brilliant collaborator. #comicSANSforever

Special thanks need to be given to my lovely friends. Jess, Charlotte, Jethro at the University of Reading who supported me at the start, and all of those at the University of Bath who welcomed me so warmly. Especially Antony Nearchou and the entire Sartbeava group, you are the best. The many fun discussions over copious cups of tea and lunch helped keep me sane. In that regards, my best friends Hannah Martin, Claire Todd, Gabriella Jardine, and my family have been invaluable. As have their proof-reading skills. Sam Childs, as well, my housemate during the last year who played the role of confidant, chauffeur, and long suffering colleague. Thanks for listening to my ranting.

Gabriella Jardine additionally deserves a special debt of gratitude for her help in providing motivation and encouragement in writing this thesis. I can honestly say that it would not be what it is without your support.

Abstract

The overall focus of this thesis is investigations into the preferential locations of biomolecules, including membrane proteins, in orientated self-assembled lipid nanostructured materials known as Q_{II} phases. The three Q_{II} phases, known as the Q_{II}^G , Q_{II}^D and Q_{II}^P , consist of 3 dimensional periodic self-assembled surfaces over which a lipid bilayer is draped. The lipid bilayer in each Q_{II} phase consists of regions of flat or high curvature into which it has been hypothesised that guest biomolecules will preferentially partition. Research efforts focus on orientated Q_{II} phase domains as more information can be extracted from characteristic Small Angle Scattering (SAS) experiments than from polydomain samples.

Different lipid mesophases including the Q_{II} phases, were prepared as orientated lipid films and an automated method of 2D Small Angle X-ray Scattering (SAXS) analysis for orientated samples was created. The addition of biomolecules to a Q_{II} phase was achieved by co-dissolving with the lipids in an organic solvent before formation of the orientated Q_{II} phase, or by addition to an already formed Q_{II} phase. Both methods are presented here and the incorporation of various biomolecules into a Q_{II}^D phase bilayer was monitored in two separate fashions, via SAXS and Raman Spectroscopy. Finally, the addition of biomolecules to orientated Q_{II} phases was undertaken and any preferential partitioning into flat or highly curved regions of the bilayer was investigated. It was found via Grazing Incidence Small Angle Neutron Scattering (GISANS) that monopalmitin and cholesterol in a monoolein Q_{II}^D phase, preferentially partition into the flatter regions of the bilayer.

At several instances during my research, variable humidity control was required. Lipid films require particular humidity to maintain specific phase behaviour and for the neutron experiments, the host lipid was contrast matched to a D_2O environment. To meet this requirement, two separate humidity control systems were designed and created: the first a low cost, portable, and chamber independent system, the second a fully automated system calibrated to a chamber at Diamond Light Source.

A separate study into the relaxed curvature of four lipids, monoolein, monolinolein, phytantriol, and phytantetrol using inverse micelles is also detailed. The relaxed curvature was obtained by calculating the parameters of the neutral surface, or the surface whose area does not change due to bending within a lipid monolayer.

Contents

Abbreviations	i
Lipid Phases	ii
Chemical Nomenclature	iii
Mathematical Nomenclature	iv
1 Introduction	1
1.1 Lyotropic Phase Behaviour	2
1.1.1 Phase Formation and Molecular Geometry	2
1.1.2 Phase Transitions and Curvature	3
1.1.3 Packing Frustration and Curvature Elasticity	5
1.1.4 Lipid Inverse Mesosstructures	6
1.1.5 Applications of Lipid Q_{II} Phases	8
1.1.6 Q_{II} Phase Forming Lipids	9
1.1.6.1 Monoolein	9
1.1.6.2 Phytantriol	11
1.2 Membrane Proteins	12
1.2.1 Membrane Protein Crystallisation	13
1.2.1.1 The <i>In Meso</i> Method	14
1.2.2 Curvature Driven Localisation in Q_{II} Phases	15
1.2.3 Model Membrane Proteins	17
1.2.3.1 Gramicidin	17
1.2.3.2 Outer Membrane Protein F	18
1.3 Research Aims	18
1.4 Domain Orientated Lipid Q_{II} Systems	19
1.4.1 Shear Alignment	19
1.4.2 Single Crystal Orientation	20
1.4.3 Surface Orientation	21
1.5 Thesis Overview	22
2 Techniques and Methods	24

2.1	Instrumentation and Characterisation	24
2.1.1	Small Angle X-ray Scattering	24
2.1.1.1	Real Space	25
2.1.1.2	Lattice Parameter	25
2.1.1.3	Reciprocal Space	26
2.1.1.4	The Diffraction Condition	27
2.1.1.5	Indexing Lipid Diffraction Patterns	29
2.1.1.6	GISAXS	30
2.1.2	SANS and GISANS	30
2.1.3	Raman	31
2.2	Materials	32
2.2.1	Lipids	32
2.2.2	Deuterated Lipids	32
2.2.3	Detergents	33
2.2.4	Nanodiscs	33
2.2.5	Membrane Proteins	33
2.2.6	Solvents	34
2.2.7	Other Chemicals	34
2.2.8	Capillaries	34
2.3	Methodology	34
2.3.1	Micelles	34
2.3.1.1	Solution SAXS	35
2.3.1.2	Modelling	36
2.3.2	GISAXS and GIWAXS Experiments	37
2.3.2.1	Spin Coating	37
2.3.2.2	Diamond I22	38
2.3.2.3	Diamond I07	38
2.3.2.4	GISANS Experiments	39
2.3.3	Thin Film Capillaries	40
2.3.4	Capillary Flow Through	40
2.3.4.1	SAXS	41
2.3.5	Raman	42
3	Lipid Domain Orientation	43
3.1	Prediction of Uniaxial Orientation	43
3.2	Experimental Details	45
3.2.1	Ratios of Cithrol/Glycerol	45
3.3	Updating the Peak Simulation	46
3.4	Indexing from a 2D Diffraction Pattern	47
3.5	New Uniaxial Q_{II} Phases	49

3.5.1	Q_{II}^P Phase	49
3.5.2	Micellar Cubic, Fd3m	51
3.6	Hexagonal Phases with Uniaxial Orientation	52
3.6.1	The Hexagonal Lattice	52
3.6.2	H_{II} Phase	53
3.6.2.1	Example	53
3.6.3	$P63/mmc$ Micellar Phase	55
3.7	Orientation in Capillaries	57
3.7.1	Experimental Details	57
3.7.2	Capillary Uniaxial Orientation	57
3.7.3	Addition of Water	60
3.8	Summary of Data Analysis	61
3.9	Conclusions	61
3.10	Future Work	62
3.10.1	Adaptation of Analysis	62
3.10.2	Addition of Aqueous Components	62
4	Additions to a Q_{II}^D Phase	63
4.1	SAXS and Raman	63
4.2	Prediction of Phase Behaviour	64
4.2.1	Nanodiscs	64
4.2.2	Detergents	65
4.3	SAXS Flow Through Experiments	65
4.3.1	SMA2000 Nanodiscs	66
4.3.1.1	SMALPS Nanodiscs	66
4.3.1.2	SMA2000 Polymer	67
4.3.1.3	Buffer Solution	69
4.3.1.4	Discussion	70
4.3.2	Detergent: LDAO	71
4.3.3	Protein: OmpF	72
4.3.3.1	Detergent: OG	73
4.3.3.2	Discussion	74
4.4	Raman	74
4.4.1	Raman of the Q_{II}^D phase	75
4.4.2	Styrene Maleic Acid Co-Polymer	76
4.4.3	Membrane Proteins	77
4.4.3.1	Gramicidin	77
4.4.3.2	OmpF	78
4.5	Aligned Lipid Phase Change	80
4.6	Conclusions	81

4.7	Future Work	82
4.7.1	Mechanism of Q_{II}^P Phase Transformation	82
4.7.2	Renaturing Membrane Proteins	82
4.7.3	Membrane Proteins with Orientated Phases	83
5	A Question of Curvature	84
5.1	Simultaneous GISAXS-GIWAXS	85
5.1.1	Obtaining a WAXS Signal	86
5.2	Gramicidin	87
5.2.1	The ratio of Gramicidin to Cithrol	87
5.2.2	Raman on a Thin Film	88
5.2.3	GISAXS-GIWAXS of Gramicidin	90
5.2.4	Gramicidin in the H_{II} Phase	91
5.2.5	Superstructure in the L_{α} Phase	92
5.3	Monoolein, Monopalmitin, Cholesterol	94
5.3.1	Orientated GISAXS	94
5.3.2	GIWAXS	95
5.4	GISANS	97
5.4.1	Prediction: Curved or Flat Regions	97
5.4.2	Methodology	98
5.4.3	Orientated GISANS of Monoolein	98
5.4.3.1	Successful Contrast Matching of d-Monoolein	99
5.4.3.2	Signal to Noise of GISANS	101
5.4.4	Monoolein, Monopalmitin, Cholesterol	101
5.4.4.1	Normalisation of the $\sqrt{3}$ to the $\sqrt{2}$ reflection	102
5.4.5	Dynamic Non-contrast Matching	103
5.4.6	Monopalmitin and Cholesterol sit in the Flatter Regions of the Q_{II}^D Phase	104
5.5	Conclusions	106
5.6	Future Work	106
5.6.1	GIWAXS	106
5.6.2	GISANS	107
5.6.2.1	Other Phases	107
5.6.2.2	Other Biomolecules	107
5.6.2.3	Addition of Aqueous Components	107
6	Humidity Control	109
6.1	Relative Humidity	110
6.2	First Prototype: Manual Humidity Control	110
6.3	The Raspberry Pi System	112
6.3.1	Hardware	114

6.3.1.1	Raspberry Pi and Arduino	114
6.3.1.2	Other components	116
6.3.2	Software	117
6.3.2.1	The GUI	117
6.3.2.2	Controlling the pumps	118
6.3.2.3	Control Loop	120
6.3.3	Examples of Use	121
6.3.3.1	Integration with a Raspberry Pi Camera	121
6.3.3.2	Acoustic Levitation at Diamond Light Source	123
6.3.3.3	GISANS at ISIS Neutron and Muon Source	124
6.4	Other Gases: Mass Flow Controllers	124
6.4.1	Chamber Design	125
6.4.2	Hardware Set-up	126
6.4.2.1	Initialising the Mass Flow Controllers	127
6.4.3	Flow Rate Control	128
6.4.4	Recording the Humidities	129
6.4.5	Calibration	130
6.4.5.1	Automatic Calibration	131
6.4.6	Humidity Control	132
6.4.6.1	Humidity Ramps	132
6.5	Conclusions	136
6.5.1	Raspberry Pi Control System	136
6.5.2	Mass Flow Control System	136
6.5.3	Future Improvements	136
6.5.3.1	Mass Flow Controllers	136
6.5.3.2	Control Box	137
6.5.3.3	Addition of More Sensors	138
6.5.4	Interchangeable Chambers	138

7 Micelles 139

7.1	Modelling the Q_{II} Phase	139
7.1.1	Molecular Dynamics	139
7.1.2	Continuum Models	140
7.1.3	The Neutral surface	141
7.2	From the Q_{II} Phase to a Micelle	141
7.3	SAXS Experiments	142
7.3.1	Creation of the Micelles	144
7.3.2	The Differences Between Salts	145
7.3.3	Modelling the Data	146
7.3.4	Micelle Size	148

7.4	Lipid Length of Monoolein	149
7.5	The Neutral Surface of a Micelle	151
7.5.1	The Neutral Surfaces of Monoolein, Phytantriol and Mono- linolien	153
7.5.1.1	Cross-sectional Area of the L_{α} Phase	153
7.5.1.2	Hydrophobic Volume from the Neutral Surface	153
7.6	Comparisons with the Literature for Monoolein and Monolinolein	155
7.6.1	Published Values for Monoolein	155
7.6.2	Comparisons	159
7.6.3	Monolinolein	159
7.7	Phytantriol and Phytantetrol Neutral Surfaces	160
7.8	Relaxed Curvature	162
7.9	Conclusions	163
7.10	Future Work	164
8	Summary	165
	Appendices	166
A	Phase behaviour of Cithrol	166
B	Uniaxial Orientation Azimuthal Angles	167
B.1	Q_{II}^P Phase	167
B.2	Micellar Fd3m Phase	174
B.3	H_{II} Phase	179
C	GISANS Peak Intensities	182
D	Micelle Sizes	184
D.1	Cithrol	184
D.2	Phytantriol	185
E	Python Code	186
	Bibliography	187
	List of Figures	188
	List of Tables	197
	List of Equations	199

Abbreviations

GISANS	Grazing Incidence Small Angle Neutron Scattering
GISAXS	Grazing Incidence Small Angle X-ray Scattering
GIWAXS	Grazing Incidence Wide Angle X-ray Scattering
GPIO	Graphical Purpose Input/Output
GUI	General User Interface
IPMS	Infinite Periodic Minimal Surface
PDB	Protein Data Bank
SANS	Small Angle Neutron Scattering
SAXS	Small Angle X-ray Scattering
SLD	Scattering Length Density
slm	standard litres per minute
WAXS	Wide Angle X-ray Scattering

Lipid Phases

Fd3m		Micellar Cubic Phase
H_{II}		2D Hexagonal Phase
L_α		Lamellar Phase
L_c		Crystalline Lamellar Phase
L_d		Liquid Disordered Phase
L_o		Liquid Ordered Phase
L₃		Sponge Phase
P63/mmc		3D Micellar Hexagonal Phase
9_{II}^D	Pn3m	Diamond Cubic Phase
9_{II}^G	Ia3d	Gyroid Cubic Phase
9_{II}^P	Im3m	Primitive Cubic Phase

Chemical Nomenclature

Brij-56	polyethylene glycol hexadecyl ether (C ₁₆ EO ₁₀)
DMPC	dimyristoyl-phosphatidylcholine
DOPA	dioleoyl-phosphatidic acid
DOPC	dioleoyl-phosphatidylcholine
DOPE	dioleoyl-phosphatidylethanolamine
DOPG	dioleoyl-phosphatidylglycerol
DOPS	dioleoyl-phosphatidylserine
E. coli	Escherichia coli
EDTA	ethylenediamine tetraacetic acid
LDAO	lauryldimethylamine oxide
OG	octyl β -glucopyranoside
OmpF	outer membrane protein F
SMALPS	styrene maleic acid co-polymer lipid particles

Mathematical Nomenclature

γ	Critical packing Parameter
λ	Wavelength
σ	Standard deviation
χ	Euler-Poincaré characteristic
σ	Ratio of the minimal surface in a unit cell to the quantity (unit cell volume) ^{2/3}
ρ_l	Density of lipid
ϕ_l	Lipid volume fraction
ρ_w	Density of water
δu	RH: Output change
A_V	Avogadro's constant
A_{cs}	Cross-sectional area per lipid molecule
C_w	Weight fraction of water
H	Mean curvature
K	Gaussian curvature
K_p	RH: Proportionality-gain
M_W	Molecular weight
a_{lam}	Lattice parameter of the L_α phase

d_{hkl}	The distance between lattice planes
d_{ns}	Distance to the neutral surface from the bilayer midplane
g_c	Bending modulus or curvature elastic energy
k_g	Gaussian modulus
n_{lipids}	Q_{II} number of lipids
$p_{H_2O}^o$	Partial pressure of water vapour in the air above a body of pure water at equilibrium
p_{H_2O}	Partial pressure of water vapour in a specific volume
r_w	Radius of the water core
v_d	RH: Desired value
v_l	Molecular volume of a lipid molecule
v_{ns}	Volume of a single molecule underneath the neutral surface
v_r	RH: Recorded value

Chapter 1

Introduction

The scope of this research is the investigation of the preferential partitioning of biomolecules in orientated curved lipid mesophases, with the target being membrane proteins. Lipids have rich polymorphic behaviour with regards to temperature and hydration. The main focus here in of this research are the Q_{II} phases. Q_{II} phases are 3 dimensional periodic mesophases with regions of flat and high curvature. It is hypothesised that biomolecules, including membrane proteins, will preferentially localise into these regions.

This introduction comprises of three sections: lipid phase behaviour, membrane proteins and their research intersection with the Q_{II} phases of lipids, and finally a brief discussion of previous methods of orientating lipid domains.

In more detail, lipid phase behaviour contains a consideration of the factors which go into lyotropic or hydration dependent mesophase formation. These factors include the roles of the geometric shape of amphiphilic molecules in phase formation, the effect of the curvature of the structures created on phase transitions, and energetic considerations in the formation of lipid mesophases. Afterwards an overview is given of the lipid mesophases discussed in this thesis, including the Q_{II} phases, and a discussion of some of the applications of the Q_{II} phases. Lastly the Q_{II} phase forming lipids used in this thesis are presented.

The section discussing membrane proteins briefly touches on general protein structure before moving onto membrane proteins. The crystallisation of membrane proteins using the lipid Q_{II} phase is discussed as is its link to the hypothesis of preferential location of membrane proteins within a Q_{II} lipid

bilayer. Subsequently the two model membrane proteins used in this thesis are presented.

The last section contains an overview of the three methods published to create orientated lipid Q_{II} phases. At the end of the introduction a short summary of the rest of the thesis is given.

1.1 Lyotropic Phase Behaviour

A subset of matter that exhibits behaviour between that of liquids and solids is called liquid crystals. Liquid crystals can be described in two ways, as either thermotropic or lyotropic where the self-assembly of structure is driven by temperature or solvent effects. Lyotropic liquid crystals are formed by amphiphilic molecules, consisting of a polar head group and a non-polar tail.

Amphiphilic molecules in aqueous environments will self-assemble to minimise the contact between hydrophobic regions and the bulk hydrophilic environment. The opposite is true in organic solvents, where self-assembly is driven to minimise the contact between the hydrophilic regions and the bulk hydrophobic media. This creates multitudes of phases whose topologies are based around layers, tubes, spheres or more complex mathematical minimal surfaces.^{???}

Lipids, classic biological amphiphilic molecules, which make up the main component of cell membranes,[?] self-assemble into different liquid crystalline structures or mesophases at different temperatures and hydration. Self-assembly can also be influenced by the incorporation of other molecules or pressure.[?] This polymorphism of lipids is of interest in many fields, only some of which will be discussed in this thesis.

1.1.1 Phase Formation and Molecular Geometry

Whilst temperature and water play a major role in determining the stability and formation of various mesophases, other factors determine the creation of certain structures. One such factor is the molecular geometry, which reflects their amphiphilic character. There are three types of shapes that amphiphiles form; type 0, type 1, and type 2, each shown in Figure 1.1. Type 0 molecules are considered cylindrical in shape, and tend to form flat bilayers in water. Type 1 molecules have a cone shape with large head groups and form phases with curvature towards the tail group. Type 2 molecules are wedge shaped molecules with small head group and form phases with curvature towards

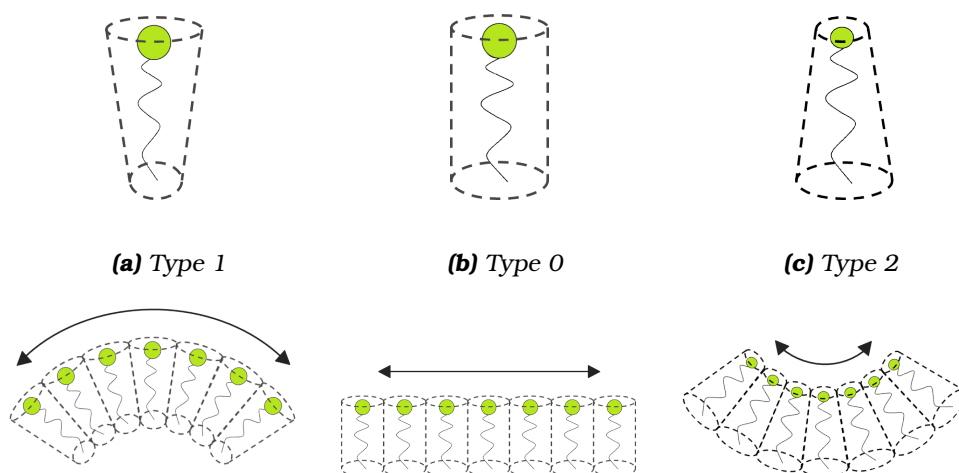


Figure 1.1: Schematic of types of shapes of lipid molecules. Type 1 **(a)** are cone like, type 0 **(b)** are cylindrical, and type 2 **(c)** are wedge like.

the head group.

The molecular geometry of a lipid can be qualitatively characterised by a shape factor or critical packing parameter γ .[?] The critical packing parameter can be calculated from Equation 1.1, using the molecular volume of a lipid molecule v_l , cross-sectional area per lipid molecule A_{cs} and the lipid length l .

$$\gamma = \frac{v_l}{a_0 l} \quad (1.1)$$

Type 1 molecules have a γ value <1 , type 0 close to 1 and type 2 molecules have a γ values >1 . Most amphiphiles form self-assemblies of 1, 2, or 3 dimensional structure. For type 1 molecules in water the quantitative relationship between γ and the shape of the aggregates has been explored[?] but it does not always describe the structures formed by type 2 molecules. The critical packing parameter is correlated to temperature, pressure, solvent composition, and concentration of amphiphiles.^{??} As all of these factors can change the head group area or extend the tail length of a molecule, any variation in them will therefore create a change in the phase structure.

1.1.2 Phase Transitions and Curvature

Phase transitions in lipids can occur due to changes in hydration[?] or humidity,^{??} temperature,^{?????} pressure,^{???} pH,[?] aqueous salt concentration,[?] addition of another surfactant or hydrophobic additive,^{???} or combinations thereof.^{??} Overall phase behaviour can be said to be governed by changes in the inter-facial curvature of the bilayer. A phase transition will occur where there is a driving force on the interface to curve away or towards

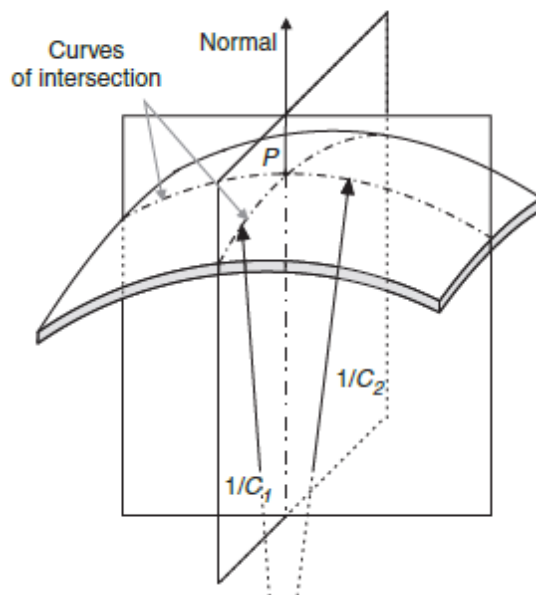


Figure 1.2: Principal curvatures C_1 and C_2 of a surface. Reproduced from Liu et al.[?]

the water.

The curvature of the surface of any monolayer can be described by two principal curvatures. At every point P there is a vector normal to the surface where two planes perpendicular to the surface cross. The two planes, shown in Figure 1.2, are orthogonal to each other with curves of intersection to the surface of maximum and minimum curvature. The curvatures are called principal curvatures and are the inverse of the radii of these two planes r_1 and r_2 .[?]

$$r_1 = \frac{1}{C_1} \quad \text{and} \quad r_2 = \frac{1}{C_2} \quad (1.2)$$

Half the sum of the two principal curvatures is the mean curvature H . The product of the two principal curvatures is the Gaussian curvature K .

$$H = \frac{C_1 + C_2}{2} \quad (1.3)$$

$$K = C_1 C_2 \quad (1.4)$$

Convention has led to net mean curvature towards the tail (type 1) as being labelled as positive, net zero mean curvature (type 0) as flat, and net mean curvature towards the water (type 2) as negative. Type 1 phases can also be known as normal phases, while type 2 phases can also be known as inverse phases.^{??} Mixtures of different types of molecules will affect the curvature and formation of different self-assembled structures. The phases discussed

in this thesis are those formed by type 2 lipids.

1.1.3 Packing Frustration and Curvature Elasticity

The phase behaviour, particularly of type 2 amphiphiles, cannot only be described by molecular geometry. Phases exist where the uniform curvature does not equal the uniform molecular packing arrangement. If molecules are forced to adopt a shape where the chain region is squashed or splayed, the surface curvature deviates from the ideal. This deviation is described by the curvature elastic energy and per unit area it can be defined by the Helfrich equation:[?]

$$g_c = 2k(H - H_o)^2 + k_G K \quad (1.5)$$

where the bending modulus g_c describes the energy cost per unit surface area of deformation, H_o is the mean curvature of the relaxed surface (also called the spontaneous or relaxed curvature), and the Gaussian modulus k_g is equal to the energy cost required to change the Gaussian curvature of the unit surface area. The curvature elastic energy is expected to increase in the geometrical shape in the following sequence:[?]

spheres < cylinders < saddle surface < flat surfaces

The relaxed curvature is determined by the distribution of lateral stresses across the surface or monolayer. The lateral stresses combine the attractive hydrophobic effect at the water interface and the packing frustration in the tail regions of the bilayer.[?] The packing frustration relates to the geometric packing of the hydrophobic chain due to phase constraints. For example, considering the packing of cylinders as in Figure 1.3 from type 2 molecules. Due to the geometrical packing, the hydrocarbon chain must stretch or compress to fill potential voids which would arise at the expense of frustration energy. The addition of hydrophobic molecules can relieve packing frustration by inserting into potential voids.^{? ? ?}

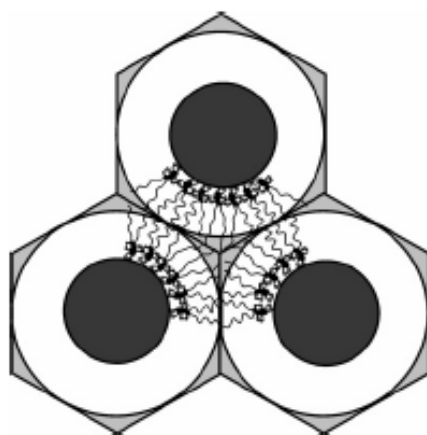


Figure 1.3: Schematic representation of packing frustration in type 2 lipids. The cross-sectional grey areas show potential voids from the cylindrical geometry which must be filled by the deformation of the hydrocarbon chains. Reproduced from Shearman et al.[?]

1.1.4 Lipid Inverse Mesophases

The most common inverse lipid mesophases are shown in Figure 1.4. These are the fluid isotropic, Figure 1.4a, or inverse micellar phase of spheres curved around the head groups. The lamellar phase L_α , Figure 1.4b, which consists of 1D stacks of fluid flat lipid bilayers separated by water. There is also the crystalline lamellar phase L_c where the molecules are ordered into a fixed position. Both the L_α and L_c phases are flat and have zero curvature, they are formed by type 2 lipids at low water concentrations and as such are noted here. The 2D hexagonal phase H_{II} , Figure 1.4c, which consists of close packed cylinders with an aqueous core are arranged in a 2D hexagonal lattice. These four phases are anisotropic under cross polarisers.

The bicontinuous cubic phases Q_{II} , Figure 1.4d-f, have curvature is between a flat L_α phase and the negatively curved H_{II} phase. Their topology can be described by the diamond,^{??} gyroid,[?] and primitive[?] Infinite Periodic Minimal Surface (IPMS) from which they get their name.^{???} The minimal surfaces can be interconverted via the Bonnet transformation,[?] a mathematical transformation which maps equivalent patches on each surface. These minimal surfaces have zero mean curvature and negative Gaussian curvature. The bilayer is considered draped over the minimal surface where at the center of the bilayer is the minimal surface. There are two water channels which are interpenetrating but do not connect. The Q_{II}^D phase has 4 way junctions which meet at a tetrahedral angle (109.5°), the Q_{II}^G phase has 3 way junctions which meet at 120°, and the Q_{II}^P phase has 6 way junctions which meet at 90°. The Q_{II} phases are transparent highly viscous isotropic gels which

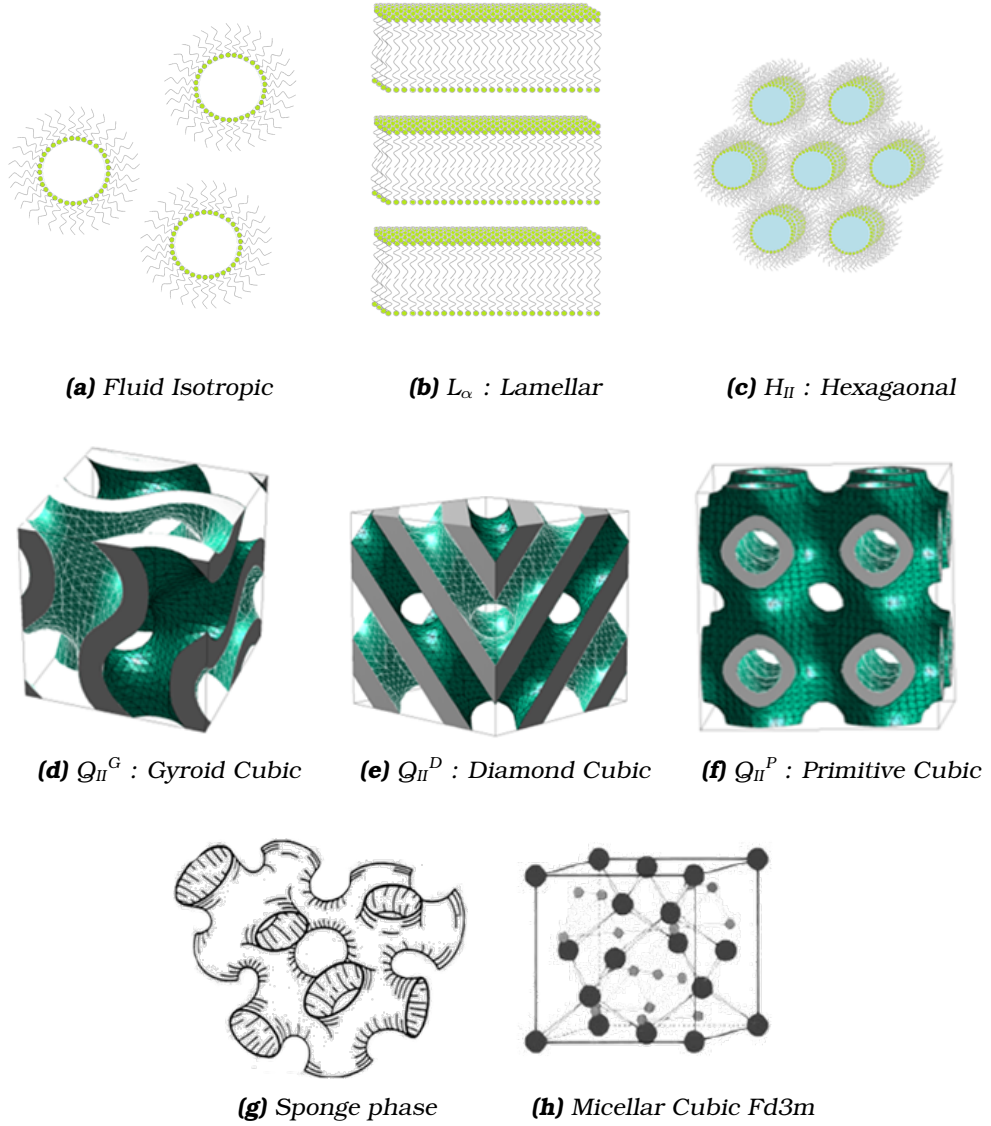


Figure 1.4: Lipid mesostructures, the green sphere represents the head group of the lipid and the wiggly line the tail. In the Q_{II} phases (d)-(f) the green surface represents the surface of the bilayer and grey area is inside. In (g) the bilayer midplane is represented and for (h) the black dots represent micelles. (g-h) are reproduced from Kulkarni et al.[?]

appear black under a cross polarising microscope.

The sponge phase L_3 , Figure 1.4g, is also considered a bicontinuous phase, however one which has been stretched and is more fluid.^{??} It has short-range order but is disordered at longer length scales. Lipids which form Q_{II} phases with water will often form L_3 phases in the presence of additives or spongegens which cause the relaxation of curvature.^{??} There is also a discrete micellar phase, Figure 1.4h, with cubic $Fd3m$ symmetry. This is where micelles form in an arrangement with a periodic lattice.^{??}

These mesophases are dynamically disordered at atomic distances but display long range periodicity. Typically lipid phase behaviour is characterised by Small Angle X-ray Scattering (SAXS). A comprehensive description of SAXS can be found in Techniques and Methods 2.1.1 (pg. 24).

1.1.5 Applications of Lipid Q_{II} Phases

The phases predominantly discussed in this thesis are the lipid Q_{II} phases. Q_{II} phases have been found in a variety of biological contexts, including within chloroplasts,[?] mitochondria,[?] and in the process of membrane fusion.^{??} Their infinite ordered nanostructures with large surface area per volume[?] and their porous character make the Q_{II} phases an attractive material in a variety of applications. They have the ability to encapsulate biomolecules of varying size making the Q_{II} phases useful in flavour delivery[?] and as drug delivery systems.[?] The drugs range from small molecules such as diazepam or vitamin E[?] to larger proteins such as hemoglobin[?] or insulin.^{??}

The Q_{II} phase is also a fairly responsive and easily tailored material. The tuneable size of the lattice parameter of a Q_{II} phase has been used for molecular separation via rates of diffusion.[?] The uniform sizes of the water channels have been used in the templating of metal nanostructures.^{???} By incorporating and immobilizing a lipid modified organo-catalyst into a host Q_{II} phase, the development of recyclable and sustainable scaffolds for catalysts has been possible.^{??} Different Q_{II} phases, with their different topologies and structural properties also exhibit slightly different properties which can be exploited. For example, with its straight water channels the Q_{II}^P phase has been shown to better accommodate linear additives such as siRNA.[?]

The Q_{II} phase's ability to incorporate membrane proteins has been capitalised on in a variety of research areas. The Q_{II} phases has been exploited as a membrane mimic for membrane protein crystallisation.^{???} They have been used to construct biosensors[?] with one such example where the Q_{II} phase

was used to create an electrochemical sensor for glucose by immobilising enzymes to an electrode surface.^{???} Higher efficiency catalysts to synthesis functionalised carbohydrates also have been created[?] by immobilising an enzyme in a lipid Q_{II} phase. Sustained release of a drug, glucose, has been achieved via a pH responsive channel protein.[?] It is the combination of membrane proteins and Q_{II} phases which is of interest in this thesis.

1.1.6 Q_{II} Phase Forming Lipids

There are two main Q_{II} phase forming lipids used within this thesis, monoolein and phytantriol. Both molecules are type 2 lipids with wedged shaped geometry and display similar phase behaviour.

1.1.6.1 Monoolein

The lipid 1-(cis-9-Octadecenoyl)-rac-glycerol, monoolein, forms a Q_{II}^D phase in excess water. Monoolein's structure is shown in Figure 1.5, it is comprised of a hydrophobic cis-alkene tail connected to a glycerol like hydrophilic head group by a acetic ester. Monoolein is the lipid most commonly used in membrane protein crystallisation^{??} and for other Q_{II} phase applications as it is non-toxic and readily available.[?]

The phase diagram for monoolein is shown in Figure 1.6. At low ($<20^{\circ}\text{C}$) temperatures monoolein exists in a L_c phase. Above 20°C monoolein forms the L_{α} , Q_{II}^G , and then the Q_{II}^D phase with increasing hydration. The excess water Q_{II}^D phase is at 40 % (w/w) at room temperature.[?]

In many previous studies where the phase behaviour of the lipid is of interest over the chemistry of that particular molecule, it is common to use a commercial less pure version of monoolein which exhibits the same phase behaviour.^{????} This is because monoolein's phase behaviour is dominant in multicomponent systems and low level impurities only exhibit small effects.[?] For an extreme example, a mixture of monoacylglycerols with a monoolein content of roughly 72 % had similar phase behaviour to monoolein.[?] Therefore for the majority of the experiments in this thesis utilising the Q_{II} phase of monoolein, a commercial monoolein called Cithrol ($<96\%$ purity) is used. Cithrol exhibits the same phase behaviour as monoolein with regards to hydration, though the temperature of the H_{II} phase transition is depressed to 55°C (Appendix A pg. 166). Consequently it was deemed as a suitable cheaper alternative for experiments requiring the Q_{II}^D phase in excess water.

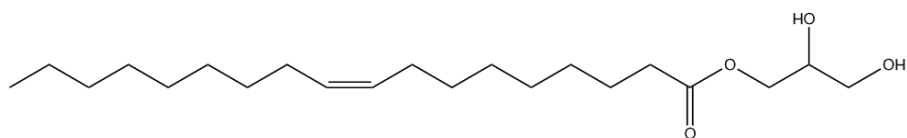


Figure 1.5: Chemical structure of monoolein

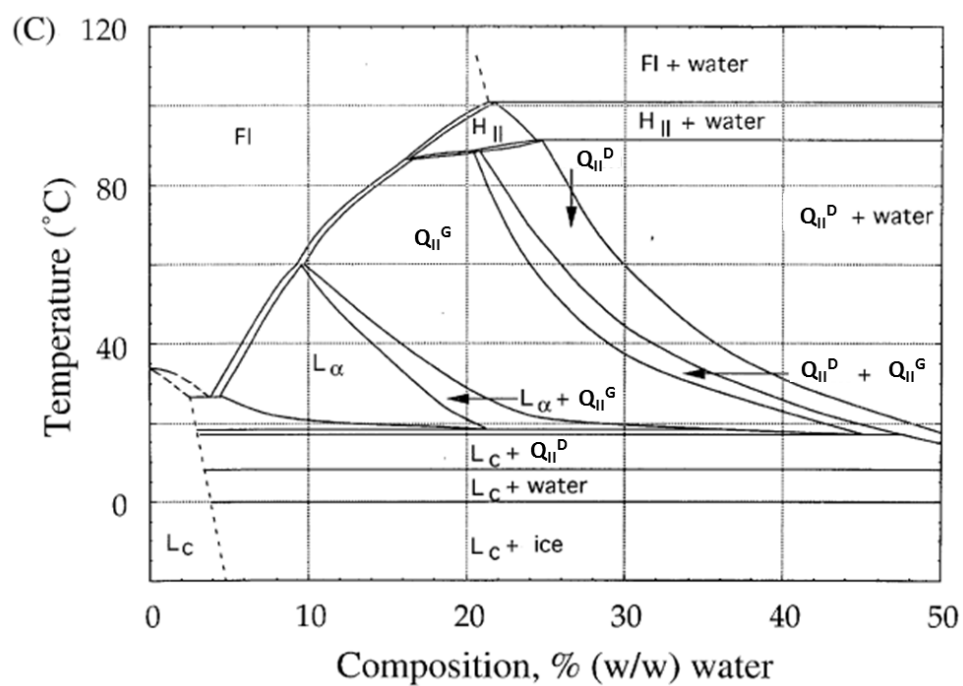
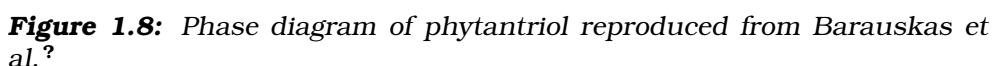
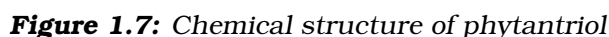


Figure 1.6: Phase diagram of monoolein, reproduced from Qiu et al.[?]



The lipid 3,7,11,15-tetramethyl-1,2,3-hexadecanetriol, phytantriol, also forms a $\text{Q}_{\text{II}}^{\text{D}}$ phase in excess water. Phytantriol's structure is shown in Figure 1.7, it is comprised of a hydrophobic branched alkane chain connected to a hydrophilic head group of three hydroxyl groups. Phytantriol is considered more chemically stable than monoolein due to the lack of ester bond which makes it less susceptible to acid hydrolysis.[?] Phytantriol's phase behaviour is more sensitive than monoolein to low level impurities[?] and by extension other additives. Its uses vary from cosmetics[?] to templating of metal nanomaterials.^{???}

The phase diagram for phytantriol is shown in Figure 1.8 and is very similar to that of monoolein. It forms the L_{α} , Q_{II}^G , and then the Q_{II}^D phase with increasing hydration though the excess water phase is at a lower water content than monoolein at 30 % (w/w) at 20°C.[?]

1.2 Membrane Proteins

Proteins are essential parts of organisms and participate in nearly all processes within a cell yet much is still unknown about them. As a comparison DNA and RNA, of which much about their structures is known, make up roughly 3 and 20 % of the dry weight of an *Escherichia coli* (*E. coli*) cell whereas proteins make up roughly half.[?] Proteins are large biological macromolecules made up of large polymer chains of 20 different amino acid building blocks. Proteins display primary, secondary, tertiary and sometimes quaternary structural features, shown in Figure 1.9. The sequence of amino acids determines a protein's primary structure, the secondary structure refers to how many α helices or β sheets are present, and the tertiary structure refers to the 3D spacial relations between different parts of the molecule. Should multiple proteins form a macromolecular complex, this is referred to as the quaternary structure.

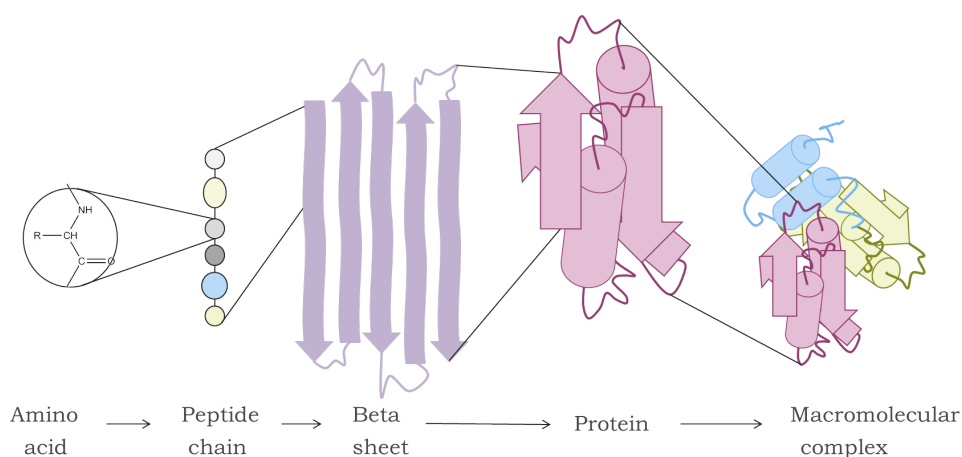


Figure 1.9: The levels of protein structure beginning with amino acids forming a peptide chain as a primary structure. The secondary structure is the stacking of peptide chains to form α helices or β sheets. Combinations of these form the tertiary structure of the protein. Multiple proteins together are macromolecular complexes with quaternary structure.

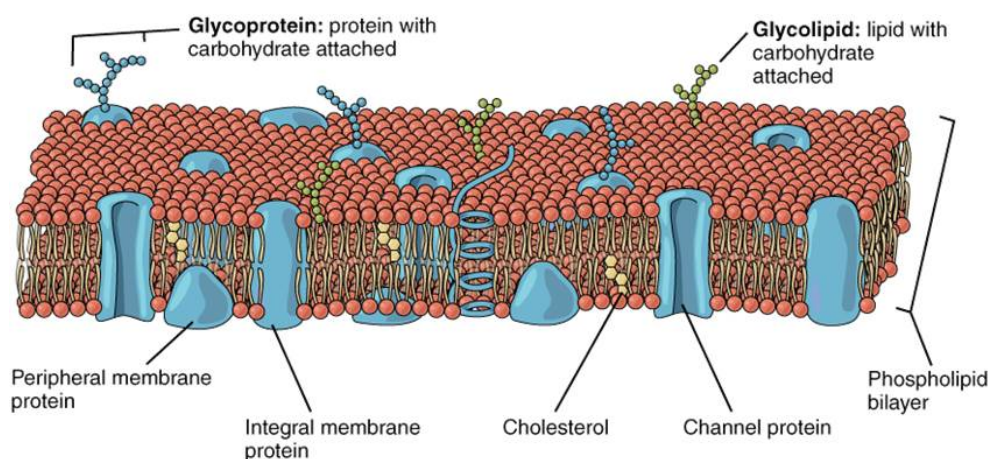


Figure 1.10: Cell membrane with component parts, reproduced from OpenStax.[?] Lipids are represented as brown ball head groups with yellow tail chains.

A subset of proteins which are discussed in this thesis, are membrane proteins. Membrane proteins are proteins which interact with the cell membrane, as shown in Figure 1.10. A quarter of the human genome is estimated to be responsible for the coding of membrane proteins and these macromolecules attract considerable research interest due to their ability to dictate a diverse range of biological activities. Membrane proteins can be categorised into three main types: transport, signal transduction, or catalyst proteins.[?] Transport proteins transport various molecules into and out of the cell, aiding in the regulation of intra/extracellular activities. Signal transduction receptor proteins involve the binding of ligand to induce signal cascade with regards to biological activity. Catalyst proteins catalyse biochemical reactions at the membrane surface, such as ATPase.[?]

Membrane proteins are often identified as drug targets, they currently comprise of 60 % of all drug targets.[?] For example in Alzheimer's treatment, the scavenger receptors on cell surfaces are recognised as one of the drug targets.^{??} In order to retrieve important parameters in designing an effective drug, for example the pharmacophore, acquiring the crystal structure and therefore the molecular and spacial structure is highly desired.[?]

1.2.1 Membrane Protein Crystallisation

To know the structure of a molecule is to know many of its properties. Not only does the structure detail a molecule's atomic bonds and their spatial arrangements but it also defines a molecule's chemical nature, function, and biological activity. As a group, membrane proteins can be notoriously

hard to crystallise[?] as there are many bottlenecks within the process. These happen in expressing the protein in sufficient quantities, in purifying and then solubilising the protein, and in producing structural grade crystals.[?] Any crystallographers dream is a medium sized, perfect habit, single crystal which produces intense well-resolved diffraction patterns.[?] This is particularly true of protein crystallographers who also have to deal with large molecular size, inherent flexibility and conformational inhomogeneity,[?] as well as the predilection for salt crystals to form from precipitants. Multiple crystals are often also required as the x-ray beam damages the protein.[?]

For membrane proteins, their insolubility in aqueous solutions due to their inherent amphiphilic or sometimes purely hydrophobic nature creates a large barrier in traditional crystallisation methods. Organic solvents denature the protein[?] and aqueous solvents won't solubilise the protein. Therefore there are two main methods to crystallise membrane proteins; the *in surfo* and the *in meso* method.

The *in surfo* method[?] uses surfactants to produce mixed micelles containing the target protein and any residual lipid within an appropriate buffer solution. These mixtures are then used to produce crystals via vapour diffusion, counter diffusion, microdialysis, or batch methods. The *in meso* method,^{??} also known as lipid Q_{II}^D phase crystallisation, uses the Q_{II}^D phase of a lipid to act as a reservoir for a target protein and to help facilitate the nucleation and growth of a crystal. The crystals produced are generally lower in solvent content and of better diffraction quality than the *in surfo* method.[?]

1.2.1.1 The *In Meso* Method

The exact mechanism for *in meso* crystallisation is still under debate. The popular hypothesis, shown in Figure 1.11, proposes that upon mixing the purified detergent solubilised membrane protein with the lipid, the protein reconstitutes within the lipid bilayer.[?] Both electron absorption and fluorescence measurements have shown that the protein remains in a native-like and active conformation when reconstituted in the Q_{II} phase.[?] Due to the Q_{II} phase's 3D continuity, the protein is free to move within the bilayer. This means upon the addition of a precipitant which causes the Q_{II} phase to change, leads to phase separation and causes locally high concentrations of protein. These local high concentrations may then form crystal aggregates which may then become diffraction worthy crystals. The transport of the reconstituted protein from the Q_{II} phase to the protein crystal aggregates happen via a conduit made from a local L_{α} phase.^{????}

Usually the incorporation of membrane proteins into the Q_{II} phase is achieved by mixing the aqueous solution with monoolein, the typically used lipid, in a 60:40 ratio via two coupled syringes.[?] Which according to the phase diagram of monoolein[?] should produce a Q_{II}^D phase. However additives such as the protein's solubilising detergent,^{???} precipitation salts,^{???} and sponge-gens (additives which promote the formation of the L_3 phase)^{??} or their combinations can all effect the phase formed and as such the crystallisation process. Though the most successful method so far,[?] the process is one of trial and error for crystallisation conditions and the *in meso* method has yet to be optimised. Often the protein gets stuck in a smaller aggregate than in a diffraction worthy crystal.

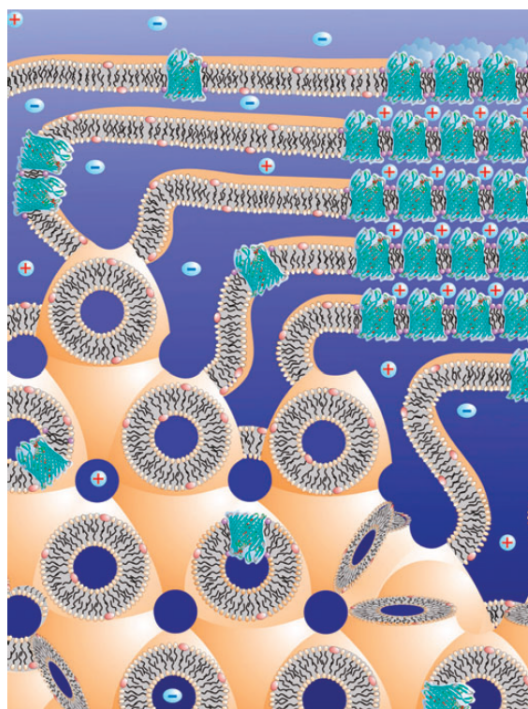


Figure 1.11: Cartoon representation of the proposed mechanism for *in meso* crystallisation reproduced from.[?] The protein is first reconstituted in the Q_{II} phase. Once a precipitant is added, the equilibrium is shifted away from stability and a phase separation occurs. The protein molecules diffuse from the Q_{II} phase to lock into the crystal lattice by way of a L_{α} portal. The Q_{II}^P phase is shown for ease of viewing.

1.2.2 Curvature Driven Localisation in Q_{II} Phases

As previously mentioned, the lipid Q_{II} phases are used as an encapsulation matrix for membrane proteins in a variety of applications. This is in part because their amphiphilic nature makes them particularly suitable to reconstitute the membrane proteins in their active and native-like conformation.

Whilst the effect of many incorporated membrane proteins and peptides on the structure of the Q_{II} phase has been investigated^{???} the exact location within the curvature of the Q_{II} phase's lipid bilayer is still unknown.

At the bilayer midplane the Q_{II} phase has zero mean curvature, yet the Gaussian curvature constantly varies from zero at the flat points to the most negative at the saddle points. Lateral diffusion of proteins within the lipid bilayer has been demonstrated[?] which suggests that membrane proteins could preferentially move to an optimal region of the bilayer with specific curvature to maintain their active conformation or reduce hydrophobic mismatch.[?] It has been hypothesised that to minimise the elastic energy of deformation, some membrane proteins in the Q_{II}^D phase will concentrate in the flatter regions of the bilayer.[?] This hypothesis of proteins preferentially locating in flatter regions of the bilayer has been linked to the beginnings of the mechanism for *in meso* crystallisation with regards to the eventual formation of the L_α conduit stacks.^{?????} Other membrane proteins, such as TAP of HIV, have been reported to produce negative Gaussian curvature channels within biological membranes,[?] where the type of Q_{II} phase formed and lattice parameter are dependent on peptide sequence. This implies that different proteins and peptides will preferentially locate in different locations within a Q_{II} phase bilayer which may have implications on *in meso* crystallisation.

It has also been hypothesised that other biomolecules, such as other lipids, will segregate within the Q_{II} phase bilayer.[?] Whilst modelling studies indicate that phase separation within the Q_{II} phase occurs, there has yet to be any confirmed preferential location of either membrane proteins or other guest biomolecules using experimental methods. A few studies have been attempted^{??} however no preferential location was confirmed. The lack of knowledge therefore leaves the evolution of the location and diffusion of biomolecules in *in meso* crystallisation, drug delivery, or any other Q_{II} phase applications currently unknown.

It is this question of curvature driven localisation of guest biomolecules within the Q_{II} phase in which the research within this thesis focuses. As such, two membrane proteins were used in this investigation as model membrane proteins.

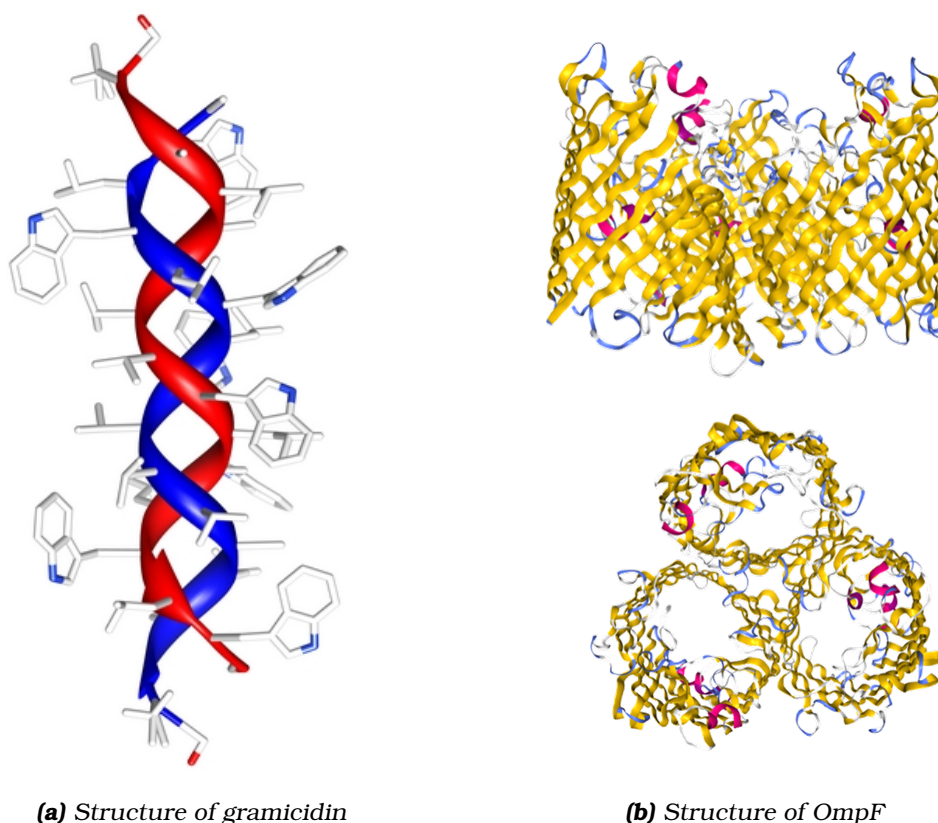


Figure 1.12: The structure of gramicidin dimer reproduced from Hoefer et al.² and the ompF trimer reproduced from Efremov et al.² with a from the bilayer view (top) and into the channel (bottom).

1.2.3 Model Membrane Proteins

The two membrane proteins used as model membrane proteins in this thesis are gramicidin and outer membrane protein F (OmpF). Both membrane proteins are considered particularly stable for membrane proteins and can be handled at room temperature.

1.2.3.1 Gramicidin

Gramicidin is a linear hydrophobic pentadecapeptide produced by *Bacillus brevis*.² An antibiotic, gramicidin forms a pore in membranes stopping them from forming the life sustaining transmembrane gradients.² Gramicidin has previously been crystallised using the *in meso* method.²² The structure of gramicidin is shown in Figure 1.16a and comprises of a double stranded intertwined β helix.

Gramicidin is an attractive model peptide for a few reasons. One, it is very stable and easy to handle.²² Two, it can be purchased from commercial

sources at high purity, devoid of any detergents or membrane lipids for a relatively low price. As a hydrophobic peptide it can be dissolved in organic solvents along with lipids^{??} and its effect on the Q_{II} structure of monoolein has previously been investigated.[?]

1.2.3.2 Outer Membrane Protein F

OmpF is a major component of the outer membrane of gram negative bacteria. Gram negative bacteria have two lipid membranes which are separated by a layer of peptidoglycan. The outer membrane acts as a protective sieve for the bacteria of which the majority, between 60 % to 90 %, of the membrane surface is made up of porins,[?] of which ompF is a particularly abundant one. In typical growth conditions of the bacteria *Escherichia coli*, ompF constitutes about 7 % of the total protein mass of the bacteria.[?]

OmpF's stability and it's abundance without the need for over-expression make it a particularly desirable protein for *in meso* crystallisation studies[?] and this research. It was the first membrane protein to be crystallised with crystals diffracting to high resolution.^{??} The OmpF monomer, which usually exists as a trimer, is a β -barrel protein formed by 16 antiparallel transmembrane β strands.

1.3 Research Aims

The purpose of the research discussed in this thesis is to obtain orientated lipid samples containing guest biomolecules, including membrane proteins, as orientated materials yield more information than polydomain samples.^{???} This could address questions of curvature driven localisation, be of use in *in meso* crystallisation, or investigations into mechanisms of Q_{II} phase electrochemical sensors.

Towards this goal I have developed different ways to prepare orientated lipid phases and analyse 2D SAXS data. During my research it was determined that humidity control was required and two separate humidity control systems were created. The alignment methods used begin with lipids dissolved in organic solvents, yet membrane proteins (with few exceptions), denature in organic solvents.[?] As such during my research, I have also investigated the incorporation of biomolecules into an already formed bulk Q_{II} phases and aligned Q_{II} phases using both SAXS and Raman. The research culminated in the incorporation of biomolecules into orientated lipid films and the confirmation of their preferred location within a Q_{II}^D phase using Grazing Incidence

Small Angle Neutron Scattering (GISANS).

In addition, in a separate study I have used solution scattering on inverse lipid micelles to determine the location and relaxed curvature of the area neutral surface of lipid monolayers.

1.4 Domain Orientated Lipid Q_{II} Systems

Single crystal or orientated materials can behave differently or have different properties when compared to their polydomain analogues.[?] For example, single domain bicontinuous structures feature interesting electronic properties such as a negative refractive index and have been predicted to display enhanced mechanical and transport properties.^{??} Within lipids internal domain boundaries in bulk samples have been shown to affect phase transition kinetics.^{??} Diffusion of molecules and membrane protein crystallisation are also affected by internal interfaces.[?]

There have been three different published ways to achieve orientation of lipid domains: shear alignment during the L_3 to Q_{II}^D phase transition, single crystal formation via dilution of the L_3 to the Q_{II}^D phase, and surface alignment of thin films. The research within this thesis is built on the surface alignment of thin films, in part because it limits the size of the lipid sample which in turn limits the required membrane protein concentration. The ease of the method and lack of time constraints, were also a determining factor.

1.4.1 Shear Alignment

An aligned Q_{II}^D film has been achieved by controlled dilution under shear from a precursor L_3 phase, created using the lipid monoolein and spongegen 1,4 butanediol^{??} shown in Figure 1.13. The L_3 phase is introduced into a capillary with an air gap between it and the water. The sample is subjected to oscillatory shear where both the water and L_3 phase leave a residual coating which transforms into an orientated Q_{II}^D phase with the gradual hydration. Uniaxial orientations of [1,1,0] or [1,0,0] were reproducibly achieved, dependent on the flow direction.

The mechanism of orientation is suggested to be simultaneous hydration and shear. The Q_{II}^D phase does not produce orientation under shear, possibly because it is very stiff with a typical shear moduli in the order of hundreds of kilopascals.[?] The L_3 phase, although with much lower viscosity, also does not produce orientation under shear. Instead both shear and hydration of

the L_3 phase are required.

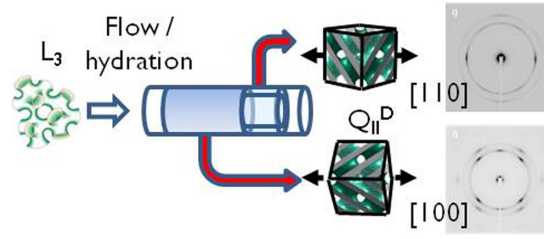


Figure 1.13: Shear orientation schematic, including the 2D SAXS patterns produced, reproduced from Squires et al.[?]

1.4.2 Single Crystal Orientation

Building on the shear alignment method, it was found that single crystals of Q_{II}^D phase can be created by the slow dilution of a L_3 phase precursor,^{???} shown in Figure 1.14. This method involved creating a capillary filled with L_3 phase from a monoolein 1,4 butanediol water mixture. One end of the capillary was then left in water for at least a week. This produced sections of the capillary which were orientated. However the quality of the single crystal regions was not consistent and the direction of orientation with regards to the capillary axis was not always the same.

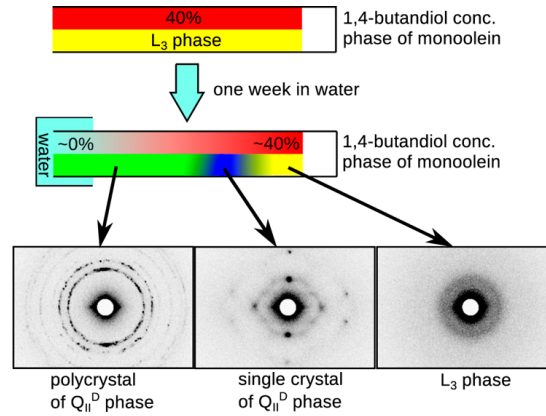


Figure 1.14: Single crystal orientation schematic, including the 2D SAXS patterns produced, reproduced from Oka et al.[?] The top red bar represents the concentration of 1,4-butandiol in the sample while the bottom bar of the capillary represents the phase present.

Single crystals of the Q_{II}^G phase have also separately been reported at phase boundaries between the micellar and Q_{II}^G phases.[?] It is thought that the mechanism for creating the single crystal regions of the Q_{II}^D phase is similar in that it occurs at the interface between the L_3 and the Q_{II}^D phase, from a highly fluid phase to the Q_{II} phase.

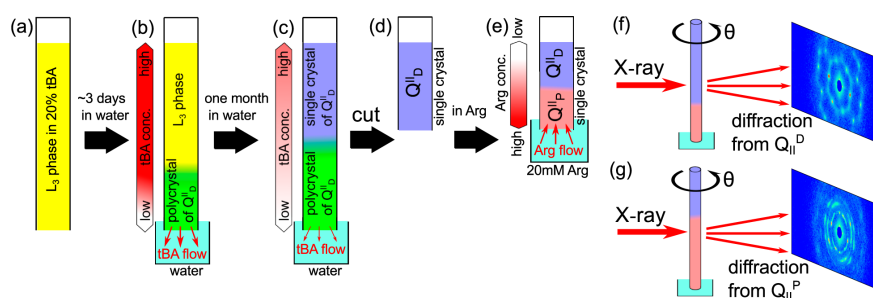


Figure 1.15: Single crystal transformation from the Q_{II}^D phase to the Q_{II}^P phase using L-arginine (Arg), reproduced from Oka et al.[?] The L_3 phase was created from t-butyl alcohol (tBA) which was diluted out before the capillary cut at the end of the single crystal region. The capillary was then placed in Arg solution to induce a phase change to the Q_{II}^P phase.

The creation of single crystal regions of the Q_{II} phase have been used to create regions of single crystal Q_{II}^G phase[?] and single crystal Q_{II}^P phase[?] from solutions of polyethylene glycol 4000 (PEG-4K) and L-arginine respectively. These phase transitions have been used to analyse the potential transformation pathways which occur.^{??} A schematic showing the method of the phase change from the single crystal region of Q_{II}^D phase to the Q_{II}^P phase is presented in Figure 1.15. Essentially once a single crystal region of Q_{II}^D phase is formed, it is placed in an additive solution and a phase change occurs. The influence that the additives have on the bilayer is unknown, they either induce curvature changes via insertion or cause osmotic stress on the water channels which induces the phase change.

1.4.3 Surface Orientation

The last method discussed is the surface alignment via spin coating onto a substrate from a lipid dissolved in an organic solvent.^{????} This produces thin films of uniaxial orientation, which must be characterised via Grazing Incidence Small Angle X-ray Scattering (GISAXS) rather than SAXS. Introducing glycerol into the solution to be spin coated stops the films from dehydrating and can produce Q_{II} phases at low humidity.[?] The thickness of the films is dependent on the spin coating speed, with a 1000 rpm producing film thicknesses of 1440 ± 10 nm.[?]

The most thermodynamically favourable orientation for the Q_{II}^G phase and Q_{II}^D phases are $[1,1,0]$ and $[1,1,1]$ respectively^{????} perpendicular to the substrate. These orientations represent a minimization of interfacial energy for the two phases. The thin films are stable for multiple cycles of dehydration and hydration via the change in humidity and will preferentially adopt these orientations.^{??}

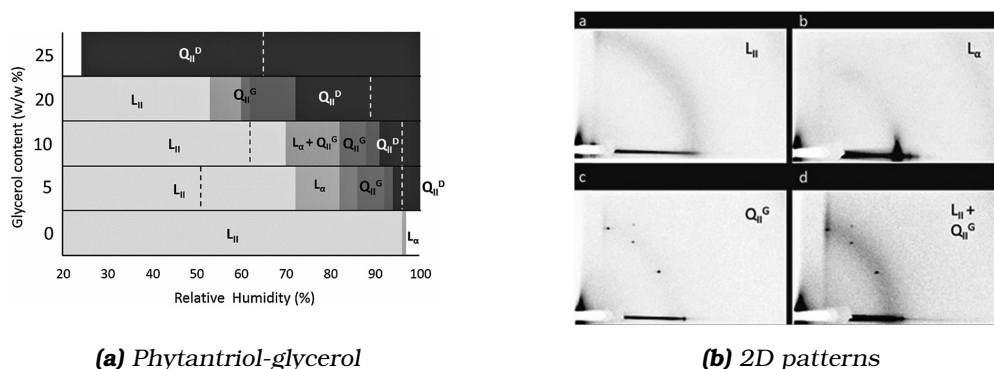


Figure 1.16: (a) The identity of phases present of the phytantriol-glycerol system with respect to humidity, reproduced from Richardson et al.⁷ The white dotted line represents the upper limit measured and black dotted line is the lower limit measured. (b) GISAXS images of phytantriol/glycerol films showing different phases, reproduced from Richardson et al.⁷

1.5 Thesis Overview

The thesis is structured as follows. The first three results chapters are linked with an overarching aim of finding the preferred location of biomolecules within the Q_{II} phase. The next two chapters can stand alone though the humidity control is utilised in some experiments in Chapter 5.

Chapter 2 describes an overview of the techniques used in this research as well as the different methods adopted in this thesis.

Chapter 3 describes the creation and analysis of other lipid uniaxially orientated phases including simulations of the uniaxial orientation. A new analysis of lipid 2D diffraction patterns is presented. The stability of the orientated films under water is verified via the observation of orientation of capillary coatings created through a different mechanism of orientation.

Chapter 4 describes the confirmation of the insertion of biomolecules into the Q_{II}^D phase bilayer of monoolein. The transformation to an orientated Q_{II}^P phase of an orientated Q_{II}^D film is induced via the the insertion of a detergent into the bilayer with no loss of orientation.

Chapter 5 consists of two investigations into the preferred location of biomolecules within a Q_{II} phase. The use of simultaneous GISAXS-Grazing Incidence Wide Angle X-ray Scattering (GIWAXS) proved inconclusive. However the use of GISANS with contrast matching of the host Q_{II}^D phase resulted in the confirmation that the molecules monopalmitin and cholesterol preferentially partition into the flatter regions of the Q_{II}^D phase bilayer.

Chapter 6 describes the design and creation of two separate humidity control systems to reliably change and maintain humidity. Both have been used in experiments at national facilities. The first is a low cost, portable, and chamber independent system powered and controlled from a Raspberry Pi. The second is a fully automated system calibrated to a chamber using mass flow controllers at Diamond Light Source, UK. Humidity control can be used to keep spin-coated lipid films in specific phases with regards to hydration.

Chapter 7 consists of a separate solution SAXS study of four lipid inverse micelles. The location of the area neutral surface and the volume underneath is then calculated. The validity of this method is then discussed and compared to previous values.

Chapter 2

Techniques and Methods

2.1 Instrumentation and Characterisation

2.1.1 Small Angle X-ray Scattering

Small Angle X-ray Scattering (SAXS) is the most common technique used to analyse lipid phases[?] as it probes the periodicity of a substance on the nanometre scale. It is the process where X-rays collide with a sample and the atoms provide interference ranging from constructive to destructive dependent on their arrangement. The arrangement or order of the molecules within is described by its repeating lattice units.[?]

For discrete monodomain samples or single crystals the long range order extends in all directions with repetitions and symmetry relationships. The distance between these repeating units is known as the lattice parameters, and the repeating unit "unit cell" is represented by a parallelepiped. Summing up all symmetry elements available there are 230 different possible arrangements for these repeating units.[?] Though these can be simplified into 7 different unit cell parallelepipeds or crystal systems: triclinic, monoclinic, orthorhombic, tetragonal, rhombohedral, hexagonal and cubic.

For the sake of completeness, it should also be noted that the unit cell can be described by its lattice points as either primitive (P) with lattice points at each corner; body centred (I) with lattice points at each corner and one in the middle; and face centred (F) with lattice points at each corner and one on each face as well. For lipids the Q_{II}^D has a space group of Pn3m, Q_{II}^G of Ia3d, Q_{II}^P of Im3m, the micellar cubic of Fd3m and the hexagonal phase is a P lattice.[?]

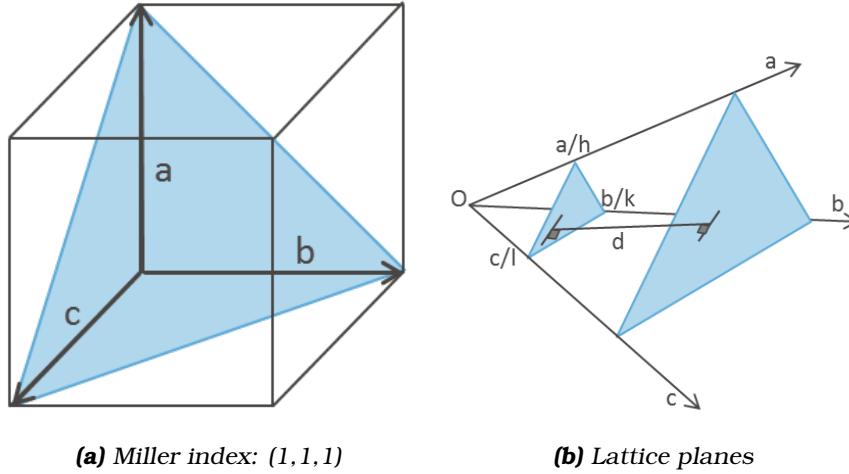


Figure 2.1: (a) Graphical representation of a parallelepiped with side lengths a , b , c and a lattice plane $(1,1,1)$. (b) Graphical representation of the relationship between parallel diffraction planes with a distance d apart.

2.1.1.1 Real Space

A unit cell is described by three noncoplanar vectors \vec{a}_1 , \vec{a}_2 , and \vec{a}_3 with inter-axial angles α , β , and γ where the magnitude of the vectors corresponding to the lattice parameters a , b , and c . Lattice planes can be described as passing through three noncolinear lattice points, usually not in the same unit cell and as such bisecting the unit cell at different points.^{??} The first plane is defined at a lattice point of origin O and the next intercepts the unit cell at $\frac{a}{h}$, $\frac{b}{k}$, $\frac{c}{l}$. In this way the Miller index can be defined as a set of parallel planes with distance d from which diffraction could occur dependent on the fulfilment of the Bragg condition.[?] A set of Miller indices is written as (h,k,l) where the reciprocals of the intercept fractions are multiplied by a common factor to give the lowest integers.[?] A graphical representation of this is shown in Figure 2.1.

2.1.1.2 Lattice Parameter

The lattice parameters of a unit cell can be found from the inter planar distance.[?] The vector normal of a lattice plane can be written as:

$$d_{hkl} = |h\vec{a}_1 + k\vec{a}_2 + l\vec{a}_3| \quad (2.1)$$

Consider the case shown in Figure 2.1b with two triangular planes. At the center of the plane there is a point equidistant to each vertex. This point is a distance d_{hkl} from the origin where a series of right angled triangles can be drawn to each intercept of the unit cell. These are drawn in Figure 2.2 with

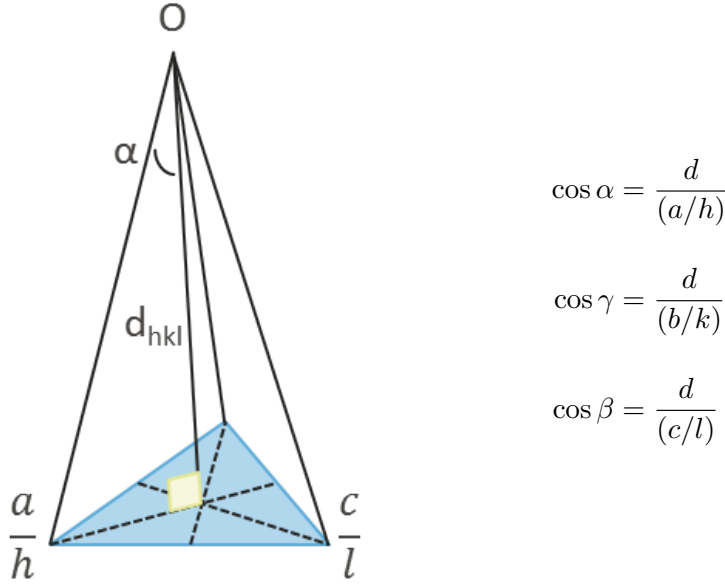


Figure 2.2: Graphical representation of the vector normal of a lattice plane. The corresponding trigonometric \cos relationship for each plane vertex is listed on the right.

the corresponding \cos relationships listed on the right. For an orthogonal axis Equation 2.2 is true which gives Equation 2.3.

$$\cos^2 \alpha + \cos^2 \beta + \cos^2 \gamma = 1 \quad (2.2)$$

$$\left(\frac{d_{hkl}}{(a/h)} \right)^2 + \left(\frac{d_{hkl}}{(b/k)} \right)^2 + \left(\frac{d_{hkl}}{(c/l)} \right)^2 = 1 \quad (2.3)$$

2.1.1.3 Reciprocal Space

The reciprocal lattice is geometric abstraction which is used to explain the geometry of X-ray and electron diffraction patterns.[?] Like real space it has lattice points, basis vectors and lattice planes. The basis vectors of the reciprocal space are the reciprocal of the basis vectors of real space. Therefore a unit cell can be sketched out using the vectors \vec{b}_1 , \vec{b}_2 , and \vec{b}_3 with interaxial angles α' , β' , and γ' with Miller indices of (h', k', l') . Mathematically real space and reciprocal space are related by Equation 2.4.

$$(h\vec{a}_1 + k\vec{a}_2 + l\vec{a}_3) \cdot (h'\vec{b}_1 + k'\vec{b}_2 + l'\vec{b}_3) = \text{integer} \quad (2.4)$$

Using vector algebra the real space lattice vectors can be used to find the reciprocal lattice vectors, where the volume of the unit cell is $\vec{a}_1 \cdot (\vec{a}_2 \times \vec{a}_3)$.

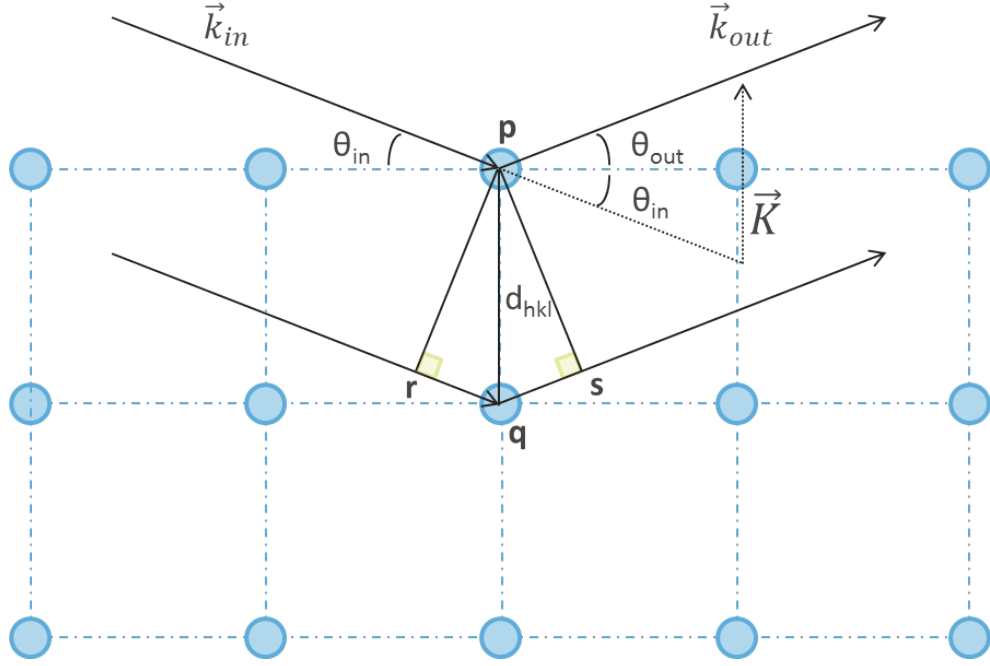


Figure 2.3: X-ray scattering from two different lattice planes. The distance between planes is d_{hkl} . The second ray travels further by $\vec{r}\vec{q} + \vec{q}\vec{s}$ or $2d_{hkl} \sin \theta$. As $\theta_{in} = \theta_{out}$ the change in wave vector \vec{k} is 2θ with a momentum change of $\Delta \vec{k}$.

This means that \vec{b}_1 is perpendicular to the plane consisting of \vec{a}_2 and \vec{a}_3 or is the cross-product of \vec{a}_2 and \vec{a}_3 . Similarly \vec{b}_2 is the cross-product of \vec{a}_3 and \vec{a}_1 and \vec{b}_3 is the cross-product of \vec{a}_1 and \vec{a}_2 .

$$\vec{b}_1 = 2\pi \frac{\vec{a}_2 \times \vec{a}_3}{\vec{a}_1 \cdot (\vec{a}_2 \times \vec{a}_3)} \quad (2.5a)$$

$$\vec{b}_2 = 2\pi \frac{\vec{a}_3 \times \vec{a}_1}{\vec{a}_1 \cdot (\vec{a}_2 \times \vec{a}_3)} \quad (2.5b)$$

$$\vec{b}_3 = 2\pi \frac{\vec{a}_1 \times \vec{a}_2}{\vec{a}_1 \cdot (\vec{a}_2 \times \vec{a}_3)} \quad (2.5c)$$

The distance between lattice planes or the vector normal can then be written as:

$$d_{hkl} = \frac{2\pi}{|h'\vec{b}_1 + k'\vec{b}_2 + l'\vec{b}_3|} \quad (2.6)$$

2.1.1.4 The Diffraction Condition

The reciprocal space is related to real space via the diffraction experiment. The condition for diffraction or scattering, the Bragg condition where constructive interference occurs is where the change in the X-ray wave vector is a reciprocal lattice vector. At the Bragg condition known as Bragg's law?

(Equation 2.8) the incoming wave vector \vec{k}_{in} is scattered by an angle θ_{out} . The second plane with the distance between lattice planes d_{hkl} scatters a second incoming wave vector at the same angle, shown graphically in Figure 2.3. The second ray travels a longer distance $\vec{r}\vec{q} + \vec{q}\vec{s}$ than the first. Constructive interference occurs when the path length distance is an integer multiple n of the wavelength λ .

$$\vec{r}\vec{q} + \vec{q}\vec{s} = d_{hkl} \sin \theta + d_{hkl} \sin \theta = 2d_{hkl} \sin \theta \quad (2.7)$$

$$2d_{hkl} \sin \theta = n\lambda \quad (2.8)$$

The change in the wave vector is related to the change in direction or the scattering angle 2θ and the momentum transfer $\Delta\vec{k} = \vec{k}_{out} - \vec{k}_{in}$. Considering the trigonometry of the wave vector gives Equation 2.9a or Equation 2.9b.

$$\sin \theta = \frac{|\Delta\vec{k}/2|}{|\vec{k}_{in}|} \quad (2.9a) \quad |\Delta\vec{k}| = 2|\vec{k}_{in}| \sin \theta \quad (2.9b)$$

where the magnitude of the wave vector is $k = 2\pi/\lambda$

$$|\Delta\vec{k}| = \frac{4\pi \sin \theta}{\lambda} \quad (2.10)$$

Combining Equation 2.10 with the Bragg equation, Equation 2.8, shows the reciprocal relationship between the change in wave vectors \vec{k} and the inter-planar spacing distance between lattice planes.

$$\frac{\sin \theta}{\lambda} = \frac{|\Delta\vec{k}|}{4\pi} \quad (2.11a) \quad \frac{\sin \theta}{\lambda} = \frac{n}{2d_{hkl}} \quad (2.11b)$$

$$|\Delta\vec{k}| = \frac{2\pi}{d_{hkl}} n \quad (2.12)$$

Therefore the change in the wave vector is the same as a reciprocal space lattice plane vector or a Fourier transform of the real space lattice vector.

$$\Delta\vec{k} = n(h'\vec{b}_1 + k'\vec{b}_2 + l'\vec{b}_3) \quad (2.13)$$

2.1.1.5 Indexing Lipid Diffraction Patterns

In a diffraction pattern peaks of intensity correspond to constructive interference. Typically for lipid samples with many micro-domains this produces something akin to a powder diffraction pattern with characteristic 2D rings. Integrating over the rings gives a 1D diffraction pattern with peaks of a certain position or d-spacing which can then be used to index the pattern and calculate a lattice parameter. Due to the integrated nature of the 1D pattern every (h,k,l) index is unnecessary. Rather the general [hkl] values which are permitted due to symmetry elements give characteristic peak positions for each phase that are used for characterisation.

For example, for the lipid Q_{II}^D phase where d_1 , d_2 , d_3 corresponds to first, second, third peak respectively and the first three [hkl] reflections ($h^2 + k^2 + l^2$) are 2, 3, 4. The lattice parameter a can then be calculated from the peak positions as follows:

$$a = \frac{d_{hkl}}{\sqrt{(h^2 + k^2 + l^2)}} = \frac{d_1}{\sqrt{2}} = \frac{d_2}{\sqrt{3}} = \frac{d_3}{\sqrt{4}}$$

Reflections: First Second Third

A table of the other phases and their characteristic SAXS reflections is given Table 2.1. For the H_{II} phase of lipids c is considered continuous and as such is not considered in lattice parameter calculations ($l = 0$).

Phase	[hkl]						
L_α	1,	4,	9,	16,	25,	36,	49
Q_{II}^G	6,	8,	14,	16,	20,	22,	24
Q_{II}^D	2,	3,	4,	6,	8,	9,	12
Q_{II}^P	2,	4,	6,	8,	10,	12,	14
H_{II}	1,	3,	4,	7,	9,	12,	13
Fd3m	3,	8,	11,	12,	16,	19,	24

Table 2.1: Characteristic [hkl] for the first 7 peaks of a lipid phase.

For lipids with domain orientation the 2D pattern has defined peaks of intensity however it can still be indexed the same by integrating to get a 1D pattern. An example of this has been shown in Figure 2.4.

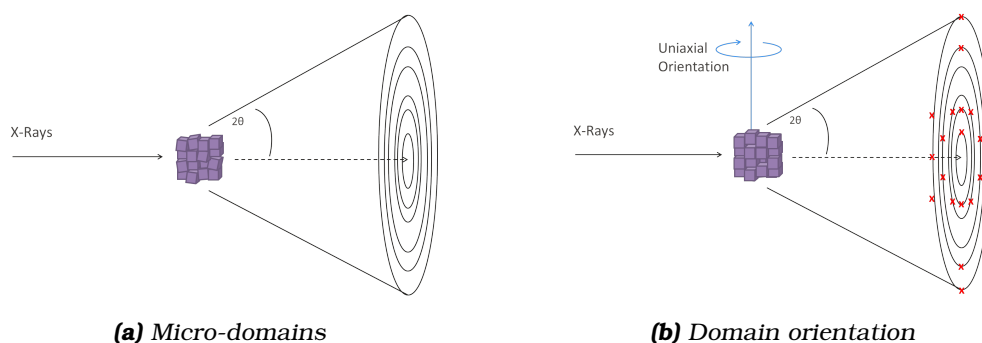


Figure 2.4: Simplified schematic of corresponding 2D diffraction patterns from lipid micro-domains and domain orientation

2.1.1.6 GISAXS

Grazing Incidence Small Angle X-ray Scattering (GISAXS), instead of transmitting the beam through the sample the beam's angle of incidence to the sample is below the critical angle of reflection.[?] This allows for a sampling of a large surface area of a surface. GISAXS is used to investigate the nanostructures of orientations of lipid thin films about an axis perpendicular to the substrate.^{??}

2.1.2 SANS and GISANS

Small Angle Neutron Scattering (SANS) and Grazing Incidence Small Angle Neutron Scattering (GISANS) have similar methods and basic analysis to SAXS and GISAXS. The main difference is that instead of x-rays, the incident beam is made up of neutrons which are scattered by atomic nuclei. Biological neutron scattering experiments take advantage of the difference in contrast for deuterium and hydrogen. Each molecule present in the sample has a different scattering length density and as such it is possible to eliminate different components from the diffraction signal by matching their scattering length densities to the aqueous solvent. The matching is done by using a mixture of deuterated molecule and hydrogenated molecule to give an average scattering length density which matches the solvent.[?] A useful metaphor for contrast matching is considering a pink panther in a grey room which can clearly be seen. However a pink panther in a pink room leaves only the red nose visible.

One particular advantage of GISANS to SANS is the reduction of the signal-to-noise ratio allowing for extremely small amounts of sample to be used. It combines the methodology of SANS with the techniques of GISAXS.[?]

2.1.3 Raman

Raman scattering provides similar information to infrared (IR) absorption in the energies of molecular normal modes of vibration though the two methods differ in mechanism and selection rules. Raman, unlike IR, is an optical technique which is insensitive to water therefore making it a useful technique in studying biological samples in solution and thereby preserving the biological activity. More specifically for proteins, the water bending vibration mode in which for IR obscures a prominent protein backbone (Amide I) stretching band has low intensity in Raman spectra.[?] Raman analysis is based on the detection of chemical group frequencies which are sensitive to spacial structure. A distortion of electron density in the vicinity of a vibrating nuclei, or change in polarizability will generate a Raman band for a specific localised molecular vibration.

As large polypeptides, proteins have complex sets of overlapping bands in their vibrational spectra. The Raman scattering of aromatic amino acids and the polypeptide backbone known as amide vibrational modes, is however particularity strong and will give rise to dominant sets of peaks.[?] This is in part due to the fact that localised vibrations of electron-rich groups such as these will produce more intense Raman bands than electron-poor groups. The most characteristic bands are listed in Table 2.2.

	Vibrational mode	wave number / cm^{-1}
Amide A	N-H stretching	3500
Amide B	N-H stretching	3100
Amide I	C=O stretching	1600 – 1690
Amide II	C-N stretching/ N-H stretching	1480 – 1580
Amide III	C-N stretching/ N-H stretching	1230 – 1300
Amide IV	O-C-N bending	625 – 770
Amide V	out of plane N-H bending	640 – 800
Amide VI	out of plane C=O bending	540 – 600
Amide VII	skeletal mode	200
Trp	Tryptophan doublet	1360 / 1340
Tyr	Tyrosine doublet	860 / 833

Table 2.2: Characteristic peptide backbone vibrational modes.[?]

For lipids the most characteristic features in a Raman spectra are related to the long non-polar acyl chains, listed in Table 2.3, as the difference in the functional head group of a lipid can drastically change. Other factors affecting the Raman spectra between different lipids are saturation of the tail, geometrical isomerism, and polymorphic form solubility.[?]

	Vibrational mode	wave number / cm^{-1}
acyl chain	C-C stretching	1200 - 1050
acyl chain	CH_2 & CH_3 twisting	1250 - 1300
acyl chain	CH_2 & CH_3 scissoring	1400 - 1500
acyl chain	C-H stretching	2800 - 3100

Table 2.3: Characteristic lipid vibrational modes.[?]

2.2 Materials

Unless otherwise stated all water was MilliQ water and the compounds were used as purchased.

2.2.1 Lipids

Pure monoolein, 1-(cis-9-Octadecenoyl)-rac-glycerol, (< 99 %), monolinolein, 1-([cis,cis]-9,12-octadecadienoyl)-rac-glycerol, (< 97 %), monopalmitin 1-monoheptadecanoyl-rac-glycerol, and cholesterol were purchased from Sigma Aldrich, UK.

Cithrol, a commercially available type of monoolein of < 96 % purity, was a gift from Croda Chemicals (Tunbridge Wells, Kent, UK).

Phytantriol, 3,7,11,15-tetramethyl-1,2,3-hexadecanetriol ($\text{C}_{20}\text{H}_{42}\text{O}_3$) was purchased from Adina Cosmetics Ingredients UK of >98.3 % purity.

Dioleoyl-phosphatidylethanolamine (DOPE), dioleoyl-phosphatidylcholine (DOPC) and oleic acid were supplied by collaborators at Imperial College London.

2.2.2 Deuterated Lipids

The deuterated lipids, monoolein and phytantriol, were purchased from Dr Tamim Darwish, ANSTO Australia.

2.2.3 Detergents

Octyl β -glucopyranoside (OG), was purchased from Sigma Aldrich, UK.

Lauryldimethylamine oxide (LDAO), was provided by Chris Brasnett (University of Bristol) as a solution of 0.1 % LDAO in 20mM tris buffer.

Polyethylene glycol hexadecyl ether (C₁₆EO₁₀) (Brij-56), was purchased from Sigma Aldrich UK.

2.2.4 Nanodiscs

Nanodiscs were provided by Stephen Hall at the University of Birmingham. The nanodiscs were 603 μ M styrene maleic acid co-polymer lipid particles (SMALPS) (SMA2000) with the phospholipid dimyristoyl-phosphatidylcholine (DMPC) in a buffer of 50 mM sodium phosphate (Na₂HPO₄) pH 8.0 and 0.2 M sodium chloride. Extra buffer solution was also provided.

2.2.5 Membrane Proteins

Gramicidin was from *Bacillus Anaurinolyticus* (*Bacillus Brevis*) and was a mixture of gramicidins A, B, C and D was purchased from Sigma Aldrich, UK.

Outer membrane protein F (OmpF), was grown and purified in house with the help of Aswin Doekhie (University of Bath) following the protocol published by Efremov.[?] In short OmpF was purified from the waste membrane fraction of *E. coli*. The outer membrane fraction was collected from the clarified cell lysate via centrifugation. The outer membrane pellet was resuspended in a protein buffer of 20 mM Tris pH 8.0, 1 mM EDTA (ethylenediamine tetraacetic acid). After successive purifications of the outer membrane pellet with Triton-X and centrifugation, OmpF was solubilised using 3 (w/v) % β -octyl glucoside.

The purity of the ompF was checked using SDS-PAGE (SDS-Polyacrylamide Gel Electrophoresis) and the concentration gained from UV Vis absorption spectra at 280 nm. The extinction coefficient is 54 210 cm⁻¹ mol⁻¹ with a molecular weight of 37 kDa.

For higher concentration of OmpF, the solutions were concentrated with 10 kDa molecular weight cut-off concentrators. The filters were first washed with water then protein buffer by centrifugation. The protein solution was then concentrated using 4000 rpm and the concentrations of both the filtered waste buffer and the concentrated protein were found by UV-vis.

2.2.6 Solvents

Research grade hexadecane and ethanol were purchased from Sigma Aldrich, UK.

2.2.7 Other Chemicals

The salts sodium chloride, potassium chloride, and potassium iodide all came from Sigma Aldrich, UK and were dissolved (w/w) in MilliQ water to make appropriate solutions.

Glycerol and d-glycerol were purchased from Sigma Aldrich, UK.

2.2.8 Capillaries

Thin walled SAXS capillaries of 1.5 mm diameter of thickness 10 μm were purchased from Capillaries Suppliers Ltd. (Reading, UK) made in borosilicate and quartz.

For screw cap SAXS capillaries these were then glued into metal (steel or brass) capillary holders using Lockite glue. For Raman experiments quartz capillaries were needed and the metal capillary holders had a second hole at right angles to the first for the laser to pass through.

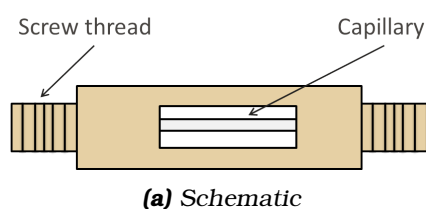


Figure 2.5: Metal capillary holders

2.3 Methodology

2.3.1 Micelles

Lipid stock solutions were created by dissolving the lipid in hexadecane to a concentration of 6 mg mL^{-1} . All lipids dissolved in hexadecane with gentle warming and vortexing. Further dilutions to 3 mg mL^{-1} and 2 mg mL^{-1} were then created to form 3 concentrations from the 6 mg mL^{-1} stock solution. The

aqueous component was added in excess at a ratio of 9:1 organic to aqueous. A full list of the compositions of lipid type and aqueous can be found in Table 2.4.

Lipid	Aqueous	Concentration mg mL ⁻¹	Temperature °C
Cithrol	Water	6, 3, 2	20, 30, 37
	3 % KCl	6, 3, 2	20, 30, 37
	5 % KCl	2	20, 30, 37
Phytantriol	Water	6, 3, 2	20, 30, 37
	3 % KCl	6, 3, 2	20, 30, 37
	5 % KCl	3, 2	20, 30, 37
	10 % KCl	3, 2	20, 30, 37
Monolinolein	Water	6	20
Tetrol	Water	6	20

Table 2.4: Full list of micelles formed

Once left to settle, two layers are formed in the solution: a clear top hexadecane layer and a smaller white cloudy layer formed at the bottom of the glass vial which was assumed to be excess water and lipid. This was confirmed by the creation of a 50/50 hexadecane solution to water sample which had a larger cloudy bottom layer. The hexadecane layer was examined by solution scattering SAXS. If the mixture is agitated a single cloudy emulsion forms which over time will settle back into the two layers.

2.3.1.1 Solution SAXS

SAXS measurements were taken at bending magnet beam line B21, the solution scattering SAXS beam line at Diamond Light Source, UK. The detector was placed at 3.9 m from the sample to give a useful q-range of 0.008 - 0.4 Å⁻¹ and the wavelength was 0.99 Å or 12.4 keV.

At the end of each experimental run, SAXS data were integrated using beam line software and the background subtracted using a running background. The integration procedure ensured that only SAXS data from the peak of interest were abstracted and subjected to further analysis. Data were inspected for radiation damage and aggregation by inspection of Guinier plots in ScÅtter.

The samples were placed in 96 well plates and the BIOSAXS robot injected

the sample into an in-line vacuum quartz capillary (diameter 1.6 mm). The capillary was washed with ethanol then water and dried after each sample or background run. Each sample and background was X-rayed for 10 frames of 3 seconds each.

The background consisted of the organic solution for the micelles, hexadecane. To ensure a correct background, as hexadecane is hygroscopic, a dummy sample was created by vortexing hexadecane with water in a 9:1 ratio and left to settle for at least 30 minutes. This was then pipetted into the 96 well plate for each sample.

2.3.1.2 Modelling

The raw data was background subtracted in ScÅtter, a program created by Rob Rambo for B21 and the data was modelled in SasView software (<http://www.sasview.org/>). Two models were considered for modelling the micelles, the sphere model and the core shell model.

The Sphere Model:

$$I(q) = \frac{scale}{V} \left(\frac{3V(\Delta\rho) \sin(qr) - qr \cos(qr)}{(qr)^3} \right) + background \quad (2.15)$$

The model provides $I(q)$ form factor for monodisperse spherical particle with a uniform scattering density. The particle volume normalises the form factor. *Scale* is the volume fraction, V the volume of the scatterer, and r is the radius of the sphere.

The Core Shell Model:

$$P(q) = \frac{scale}{V_s} \left(3V_c(\rho_c - \rho_s) \frac{\sin(qr_c) - qr_c \cos(qr_c)}{(qr_c)^3} + 3V_s(\rho_s - \rho_{solv}) \frac{\sin(qr_s) - qr_s \cos(qr_s)}{(qr_s)^3} \right)^2 + background \quad (2.16)$$

The model provides $P(q)$ form factor for a spherical particle of a core shell structure. The particle volume normalises the form factor. *Scale* is the scale factor, V_s is the volume of the shell, V_c is the volume of the core, r_s is the radius of the shell, and r_c is the radius of the core. All core values are notated by $_c$, shell values by $_s$ and the solvent by $_{solv}$. The goodness of fit of the model can be seen by low χ^2 values and small residuals.

2.3.2 GISAXS and GIWAXS Experiments

2.3.2.1 Spin Coating

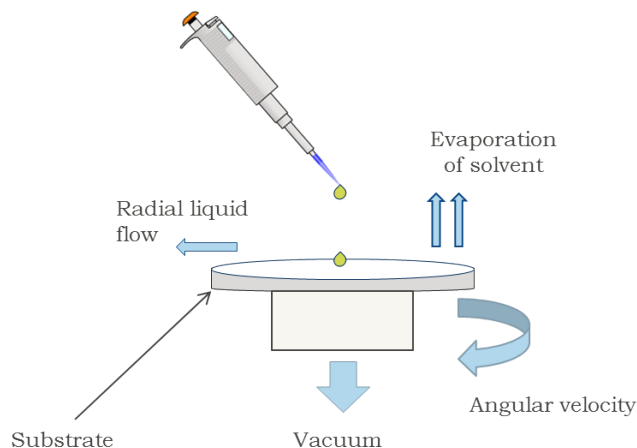


Figure 2.6: Schematic of spin-coating

Spin coating a stable lipid thin film was successful using hydrophobic silicon wafers, plain silicon wafers, and glass slides as substrates. The hydrophobic silicon wafers were created by James Dolan at the University of Cambridge. The protocol was based on that described by Richardson et al.^{??} In brief, a lipid and glycerol were dissolved separately in (w/w) ethanol. For ease, Cithrol and phytantriol are heated to 50 °C and 70 °C respectively before being dissolved in ethanol. These solutions were then mixed in appropriate (v/v) ratios for the desired phase. An example of phases for Cithrol at 30 % RH is presented in Table 2.5. A more comprehensive description of lipid thin film phase behaviour of monoolein and phytantriol with regards to glycerol content and humidity has been published by Richardson et al.[?]

% (v/v) Cithrol	% (v/v) glycerol	Phase
100	0	L_{α}
95	5	L_{α}
90	10	Q_{II}^G
85	15	Q_{II}^G
80	20	Q_{II}^G
75	25	Q_{II}^D
70	30	Q_{II}^D

Table 2.5: Lipid phases of Cithrol at different glycerol concentrations at 30% RH.

For more complex mixtures the phase is dependent on the additives. Either the additive is dissolved in (w/w) ethanol and mixed with the lipid and glycerol solutions (v/v) or the additive is dissolved in ethanol along with the lipid. The (v/v) ratio to glycerol to lipid is usually set past the excess water point so that the difference in lattice parameter or phase of the film is due to the additive.

The lipid/glycerol solution is spin coated onto an a 2 cm x 2 cm substrate. A schematic of spin-coating is provided in Figure 2.6. A three spin-cycle method was used for all spin-coating procedures; a sample deposition cycle, a drying cycle and finally an ethanol wash of the edges with final drying. The drying and ethanol wash cycles were not varied and consisted of 1500 rpm and 6000 rpm for a minute each respectively. The deposition cycle was either 500 rpm for a thicker film or 1000 rpm for a thinner film for 20 s.

2.3.2.2 Diamond I22

Multiple simultaneous GISAXS/WAXS experiments took place on the I22 beamline at Diamond Light Source, UK. Data processing was performed using the DAWN software package^{??} and a set of pipelines developed at Diamond Light Source.

The first iteration of the humidity control used a beam wavelength of 0.99 Å or 12.4 keV. The wafer substrates with lipid thin films were placed within an environment chamber filled with humidified helium. Due to the reproducibility of the spin coated films the beam was able to be placed at a grazing incident angle of pitch -0.25° .

The testing of the automated humidity control using mass flow controllers used a beam wavelength of 0.88 Å or 14 keV. The wafer substrates with lipid thin films were placed within an environment chamber filled with humidified helium. Due to the reproducibility of the spin coated films the beam was able to be placed at a grazing incident angle of pitch -0.3° .

Films were created from 80 % (w/w) ethanol solutions.

2.3.2.3 Diamond I07

A GISAXS and Grazing Incidence Wide Angle X-ray Scattering (GIWAXS) experiment took place on the I07 beamline at Diamond Light Source, UK. The camera length was changed between the GISAXS and GIWAXS experiments. SAXS patterns were analysed in ImageJ software with the custom macro

YAXs. ?? Lipid phases and lattice parameters were determined from q values using the python script in Appendix E 1.

A beam wavelength of 0.855 Å or 14.5 keV was used. The wafer substrates with lipid thin films were placed within an environment chamber filled with humidified helium which was constantly at <95 % humidity. Due to the reproducibility of the spin coated films the beam was able to be placed at a grazing incident angle of pitch -0.3° . Films were created from 80 % 50 % and 40 % (w/w) ethanol solutions.

2.3.2.4 GISANS Experiments

The GISANS experiments took place at ISIS Neutron and Muon Source, UK. The camera length was 4 m. Lipid phases and lattice parameters were determined from q values using the python script in Appendix E 1.

The process of dissolving the lipids and glycerol and coating the wafers was the same as the GISAXS experiments. Monoolein, monopalmitin, and cholesterol were mixed in 8:1:1 molar ratios before being dissolved in 80 % (w/w) ethanol. The resulting solution was mixed with contrast matched glycerol in a 30 % (v/v) ratio. Solutions using contrast matched monoolein were created in the same manner with h-glycerol. Both deuterated monoolein and deuterated glycerol when used were contrast matched to D₂O in the ratios in Table 2.6.

Films were spin coated at 1000 rpm onto a quarter of 76 mm wafers. The wafer substrates with lipid thin films were placed within an environment chamber filled with humidified helium which was constantly at 80 % humidity. The humidity was generated using the Raspberry Pi humidity control system and D₂O bubblers. D₂O was provided by ISIS Neutron and Muon Source, UK.

Compound	SLD	Contrast match to D ₂ O
D ₂ O	$6.38 * 10^{-6}$	-
H ₂ O	$-5.6052 * 10^{-7}$	-
d-monoolein	$6.4882 * 10^{-6}$	98.3 %
h-monoolein	$2.0958 * 10^{-7}$	1.7 %
d-glycerol	$7.4821 * 10^{-6}$	84 %
h-glycerol	$6.1243 * 10^{-7}$	16 %
h-cholesterol	$2.164 * 10^{-7}$	-
h-monopalmitin	$1.304 * 10^{-7}$	-

Table 2.6: Scattering Length Density (SLD) and percentage weight to contrast match to D₂O of compounds used in GISANS experiments.

2.3.3 Thin Film Capillaries

Thin films in capillaries are created similarly from the same lipid/glycerol in ethanol solutions as those used for spin coating. The lipid and glycerol are dissolved in 80 % (w/w) ethanol then mixed in appropriate (v/v) ratios dependent on desired phase. The glycerol ratios required for the phases of monoolein and Cithrol are found in Table 2.5. The mixed ethanol solution is then pipetted into an open-ended capillary. The excess is then removed so that the capillary can be seen through. This is accomplished via pipetting out the excess and then tapping the capillary onto blue roll.

The capillary is then left in a < 70 % RH environment, such as a plastic box, of sufficiently large volume overnight. The capillaries are then sealed for SAXS analysis as is or filled with aqueous solution before sealing.

SAXS experiments were done on the Bruker Nanostar at the University of Reading, the SAXSLAB Ganesha 300XL at the University of Bristol and the Xenocs Nano-inXider SAXS/WAXS system at ISIS Neutron and Muon Source. Each had a copper x-ray source of 1.54 Å. The SAXS set-up is calibrated from a known diffraction spacing of silver behenate ($d_1 = 58.3$ Å).[?] SAXS patterns were analysed in ImageJ software with the custom macro YAXs.^{??}

2.3.4 Capillary Flow Through

Capillaries were filled with molten Cithrol and the excess removed. To ensure an even coating the capillary was tapped onto blue roll until it could be clearly seen through. A syringe was then coupled to the capillary and 2 ml of air

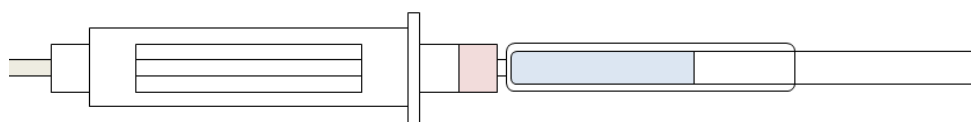


Figure 2.7: Schematic drawing of the capillary connected to a syringe via a HPLC connection. A tube at the other end was connected to remove the waste solutions.

was pushed through the capillary to ensure a smooth layer of molten Cithrol. Water was immediately added to form the Q_{II}^D phase.

Before the addition of any new solution, the capillary was cleared of excess solution by slowly pushing air through the capillary. Aqueous solutions were then added to the capillary. Aqueous solutions were the detergent LDAO, 603 μ M SMALPS (SMA2000) with DMPC in 50mM sodium phosphate (Na_2HPO_4) pH 8.0 and 0.2 M sodium chloride, 603 μ M styrene maleic acid co-polymer (SMA2000) in the buffer 50 mM sodium phosphate (Na_2HPO_4) pH 8.0 and 0.2 M sodium chloride, and the buffer 50mM sodium phosphate (Na_2HPO_4) pH 8.0 and 0.2 M sodium chloride. Air was again pushed through the capillary before water was added.

2.3.4.1 SAXS

The aqueous nanodisc solution SAXS measurements were taken on B21 at Diamond Light Source, UK. The detector was placed at 3.9 m and the wavelength was 0.99 Å or 12.4 keV. The capillary of Q_{II}^D phase was placed in the beam and SAXS patterns taken at appropriate intervals. The addition of aqueous solutions was done on the beamline by coupling a syringe to the capillary. SAXS patterns were taken at regular intervals until the lipid had stopped changing phase. Lipid phases and lattice parameters were determined from q values using the python script in Appendix E 1.

The addition of OmpF and LDAO experiments were done on i22 at Diamond Light Source, UK. The wavelength was 0.88 Å or 14 keV. The capillary of Q_{II}^D phase was placed in the beam and SAXS patterns taken at appropriate intervals. The addition of aqueous solutions was done via a syringe pump. This allowed for the addition of the aqueous solution to be viewed via SAXS instantaneously with no time delay. Data processing was performed using the DAWN software package^{??} and a set of pipelines developed at Diamond Light Source.

2.3.5 Raman

The Raman spectra were collected using a Renishaw inVia Raman microscope at the University of Bath. A 532 cm^{-1} excitation laser was used and the microscope was calibrated using a silicon wafer using the peak 520.6 cm^{-1} .

Samples were either deposited onto silicon wafers or within quartz capillaries. The microscope was focused then a scan was taken between 500 cm^{-1} - 4000 cm^{-1} of a duration of 10 seconds.

Chapter 3

Lipid Domain Orientation

For surface aligned lipid thin films, glycerol was found to prevent the dehydration of lipid thin films.[?] The thin films were created by spin coating a lipid/glycerol solution dissolved in the organic solvent ethanol. Using this simple method, uniaxially orientated lipid films of the L_α , Q_{II}^G , and Q_{II}^D phases of monoolein and phytantriol^{??} were reproducibly created. The uniaxial orientations of the Q_{II}^D and Q_{II}^G phases were simulated and matched predictions^{???} of uniaxial orientation [1,1,1] and [1,1,0]. It was hypothesised that this approach could be used to create and analyse other lipid phases.

In this chapter I first present new ways of data analysis for 2D diffraction patterns whereby lattice parameters of uniaxially orientated lipid phases are generated. Secondly I created lipid films of the Q_{II}^P phase, the micellar cubic Fd3m, and the H_{II} phase. I extend the analysis of Richardson et al.[?] to include these phases and simulate their uniaxial orientation. I have also extended the simulations to the 3D micellar hexagonal phase although no experimental data has yet been acquired. Finally I also present a new method for creating orientated films within capillaries and investigate the stability of the orientation under water.

3.1 Prediction of Uniaxial Orientation

A peak simulation for the uniaxially orientated lipid domains of both the Q_{II}^D and Q_{II}^G phase was created by Richardson et al.^{??} This consisted of generating all the (h,k,l) values for each phase and their corresponding peak positions.

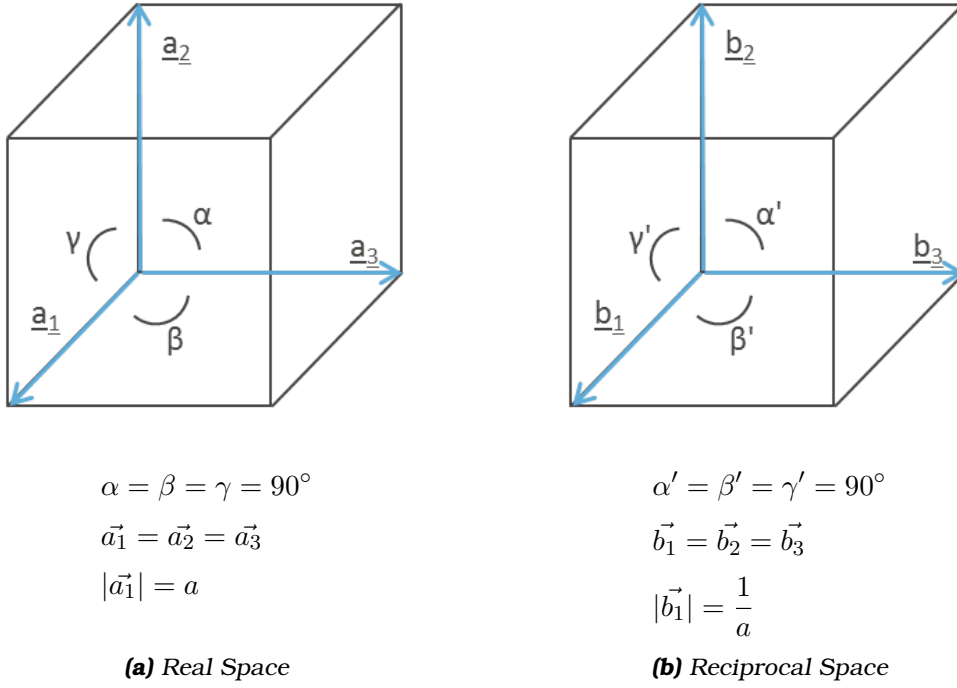


Figure 3.1: Q_{II} lattice vectors

In brief, the cubic lattice is unique in that all the vectors are orthogonally equidistant to each other, as shown in Figure 3.1. The lattice parameter equation^{??} is:

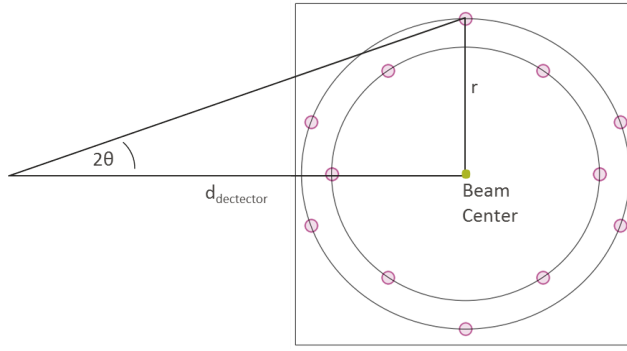
$$d_{hkl} = \frac{a}{\sqrt{(h^2 + k^2 + l^2)}} \quad (3.1)$$

For GISAXS experiments, the x-ray beam is perpendicular to the surface normal of the thin film. This corresponds to the axis of rotational symmetry or uniaxial axis and can be defined by a real space vector $\vec{a} = (h\vec{a}_1 + k\vec{a}_2 + l\vec{a}_3)$. Considering an x-ray reflection from a set of planes given by the reciprocal Miller indices $(h'k'l')$, for small-angle scattering, there will be a diffraction peak when the reciprocal lattice vector $\vec{b} = (h'\vec{b}_1 + k'\vec{b}_2 + l'\vec{b}_3)$ also lies approximately in the plane of the detector. The relationship between the two vectors is $\vec{a} \cdot \vec{b} = 2\pi$.[?] The azimuthal angle χ of the reflection is equivalent to the angle between these two vectors:

$$\cos \chi = \frac{(h\vec{a}_1 + k\vec{a}_2 + l\vec{a}_3) \cdot (h'\vec{b}_1 + k'\vec{b}_2 + l'\vec{b}_3)}{|(h\vec{a}_1 + k\vec{a}_2 + l\vec{a}_3)| |(h'\vec{b}_1 + k'\vec{b}_2 + l'\vec{b}_3)|} \quad (3.2)$$

For a cubic lattice this then becomes:

$$\cos \chi = \frac{hh' + kk' + ll'}{\sqrt{h^2 + k^2 + l^2} \sqrt{h'^2 + k'^2 + l'^2}} \quad (3.3)$$



$$r = \frac{d_{\text{detector}}}{\tan 2\theta}$$

where :

$$\sin \theta = \frac{\lambda}{2r}$$

Figure 3.2: Radial geometry of the SAXS set-up with regards to the diffraction pattern and the incident beam at a distance d_{detector} .

The radial geometry is calculated in pixels using the calibration from silver behenate requiring the beam center and the distance to the detector in pixels.

$$\begin{aligned} x &= x_{\text{center}} + r \sin \chi \\ y &= y_{\text{center}} + r \cos \chi \end{aligned} \quad (3.4)$$

3.2 Experimental Details

Lipids and gramicidin were each dissolved in 80 % (w/w) ethanol or chloroform before being mixed with glycerol dissolved in 80 % (w/w) ethanol or chloroform. The lipid and glycerol solutions were then mixed to appropriate (v/v) ratios[?] for the required phase.

The mixed solutions were spin coated onto hydrophobic silicon wafers, plain silicon wafers or glass slides in a 1000 rpm for 20 s, 1500 rpm for 60 s then 6000 rpm for 60 s cycle. The wafer was then placed on a beamline in a high humidity chamber for GISAXS. Data was collected on both i22 and i07 beamlines at Diamond Light Source, UK.

3.2.1 Ratios of Cithrol/Glycerol

Based on previous work using Rylo, another commercial monoolein, done by Richardson et al.[?] the lipid phases for set Cithrol/glycerol ratios were proposed and confirmed at low humidity < 25 % RH and are listed in Table 3.1.

% (v/v) Cithrol	% (v/v) glycerol	Phase
100	0	L_α
95	5	L_α
90	10	Q_{II}^G
85	15	Q_{II}^G
80	20	Q_{II}^G
75	25	Q_{II}^D
70	30	Q_{II}^D

Table 3.1: Lipid phases of Cithrol at different glycerol concentrations at low (< 25 % RH).

3.3 Updating the Peak Simulation

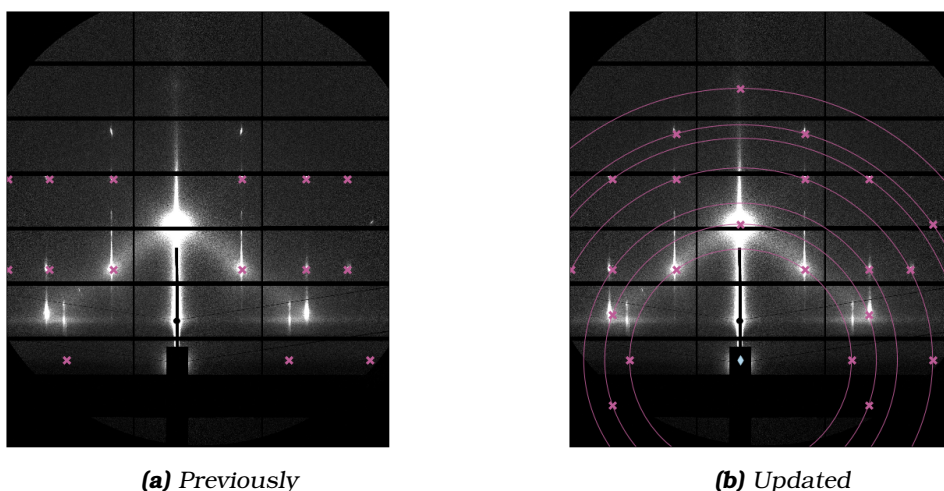


Figure 3.3: Prediction of Q_{II}^D phase of $[1,1,1]$ orientation. **(a)** The previous python script created by Sam Richardson and **(b)** the updated script including the addition of 2 more reflections. The lipid film is spin coated from a 70/30 (v/v) solution of Cithrol and glycerol dissolved in 80 % (w/w) ethanol.

Upon reviewing the Python script used to generate the peak simulations for the Q_{II}^D and Q_{II}^G phases, a small mistake due to the nature of mathematical operations in Python was found and corrected. As shown in Figure 3.3a, the mistake had resulted in the two on axis peaks for $\sqrt{3}$ reflection not being predicted in the $[1,1,1]$ uniaxial orientation despite them being present in the (h,k,l) values calculated. The updated simulation is shown in Figure 3.3b. The number of reflections being predicted was also increased from 5 to 7.

3.4 Indexing from a 2D Diffraction Pattern

Next the Python script was updated to allow for the automatic calculation of the lattice parameter from the 2D diffraction pattern. Beforehand a 1 dimensional radial profile would be created separately in ImageJ and the corresponding d_{hkl} for each peak would be used to assign the correct phase and lattice parameter. However using Python it is possible to index the lipid phase straight from the 2D diffraction pattern.

Initially the Python script worked by:

1. Generating all (h,k,l) values for the $\text{Q}_{\text{II}}^{\text{D}}$ or $\text{Q}_{\text{II}}^{\text{G}}$ phase
2. Calculating azimuthal angles using a given uniaxial orientation
3. Calculating the radial geometry
4. Calculating the (x,y) coordinates in pixels
5. Plotting the peaks on the diffraction pattern

A step was added at the beginning which involved finding peaks of high intensity in the diffraction pattern and then a calculation of the lipid lattice parameter from those peaks. To find peaks of high intensity, first any intensity from the beam center and the bright on axis reflections has to be masked so as to not to interfere with the calculations of the lattice parameter. Therefore a simple binary mask was created in ImageJ by the macro YAXs^{??} for a group of diffraction patterns of the same beam center and wafer position.

Second a blob detection algorithm was applied to the grayscale of the image. Blobs are considered to be regions of an image in which some properties are constant or approximately constant. The detection of blobs focuses on regions of an image which differ in either brightness or colour compared to the surrounding regions. This can be done either by differential methods based on the derivatives of a function with respect to position or methods based around local extrema. The particular algorithm used is called a difference of Gaussians. It is well suited to finding blobs of high intensity in a diffraction image as it removes high frequency noise or artefacts as well as enhancing edges of details present.

The difference of Gaussians involves the subtraction of one blurred grayscale image with a slightly less blurred grayscale image. The blurred images are obtained by combining the original image with Gaussian kernels of differing

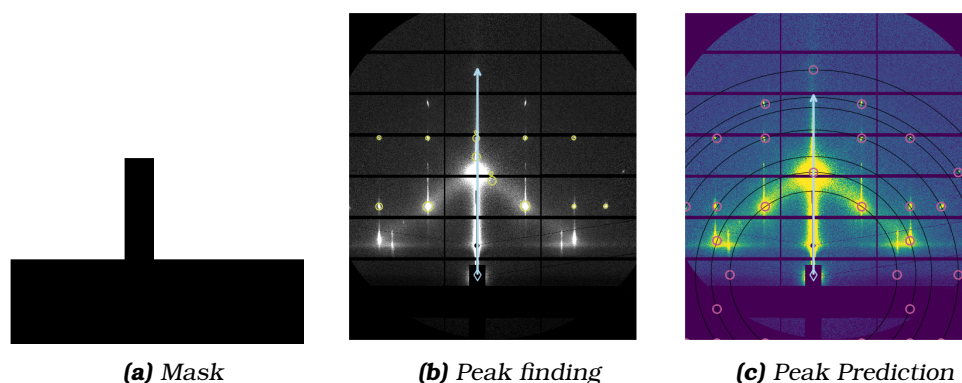


Figure 3.4: The binary mask **(a)** was used for the peak finding in **(b)**. The lattice parameter was found to be 84 \AA . The diffraction pattern was that of Cithrol in the Q_{II}^D phase with uniaxial orientation $[1,1,1]$ **(c)**. The mask is required to mask intensity near the beam center and the on axis intensity not covered by the beam stop. The beam center is marked with a small diamond.

standard deviations. The blurring of the image will suppress high frequency information while the subtraction preserves the spatial information in the frequencies between the images. The method used returns an array of the blobs coordinates in pixels and the standard deviation of the Gaussian kernel that detected the blob. Using the standard deviation as an indication of the size of the blob, as a radius of a circle, the blobs found can then be plotted on top of the image as in Figure 3.4b. The number of blobs, and their sizes can be tuned via three parameters: the minimum standard deviation for the Gaussian kernel, the maximum standard deviation for the Gaussian kernel, and the threshold at which local maxima are ignored. For each experiment or groups of similar diffraction images it is necessary to tune these parameters.

To index the diffraction pattern it is not required to 'find' all the diffraction peaks as blobs. What is required is that the closest blob to the beam center is a genuine diffraction peak, which is in part why masking the image around the beam center is crucial. The distance from each blob to the beam center is calculated and from the smallest radial distance (the closest blob) the indexing will progress.

Using the smallest radial distance as r_1 or if the closest blob is in the second or third ring r_2 or r_3 respectively, the lattice parameter is calculated using Equation 3.1 and the reflection values for a particular phase. A complete table of reflections for each phase can be found in Chapter 2.1, (pg. 29). Although the method is not as accurate as using the average of all peaks from a 1D diffraction pattern, it was found that the lattice parameter was in good agreement to 0.5 \AA . Therefore, especially for large quantities of data

where quick mass data analysis is desired, this method can confidently be used to give lattice parameters to the nearest Å.

3.5 New Uniaxial Q_{II} Phases

The uniaxial orientation of the Q_{II}^D and Q_{II}^G phase of lipid thin films is known to be [1,1,0] and [1,1,1] respectively.^{??} The creation and analysis were extended to other lipid Q_{II} phases,. The Q_{II}^P phase[?] and the micellar cubic Fd3m phase^{??} have the characteristic diffraction reflections listed in Equation 3.5 and Equation 3.6 respectively.

$$[hkl] = (h^2 + k^2 + l^2) = 2, 4, 6, 8, 10, 12, 14 \quad (3.5)$$

$$[hkl] = (h^2 + k^2 + l^2) = 3, 8, 11, 12, 16, 19, 24 \quad (3.6)$$

3.5.1 Q_{II}^P Phase

The Q_{II}^P phase is a less common Q_{II} phase than that the Q_{II}^D or Q_{II}^G phases as it most typically appears in ternary lipid/ additive/ water mixtures.[?] The Q_{II}^P phase was formed at high humidity < 96 % RH from 30 % (v/v) Cithrol, 24.75 % (v/v) phytantriol, and 5.25 % (v/v) polyoxyethylene surfactant (10) cetyl ether (Brij-56) all in 80 % (w/w) ethanol mixed with glycerol in 80 % (w/w) ethanol at a 60/40 total lipid to glycerol ratio. The Q_{II}^P phase is uniaxially orientated in the [1,0,0] direction, as shown in Figure 3.5 with a lattice parameter of 132 Å. The azimuthal angles of the [1,0,0] uniaxial orientation of the Q_{II}^P phase are provided in Appendix B.1.

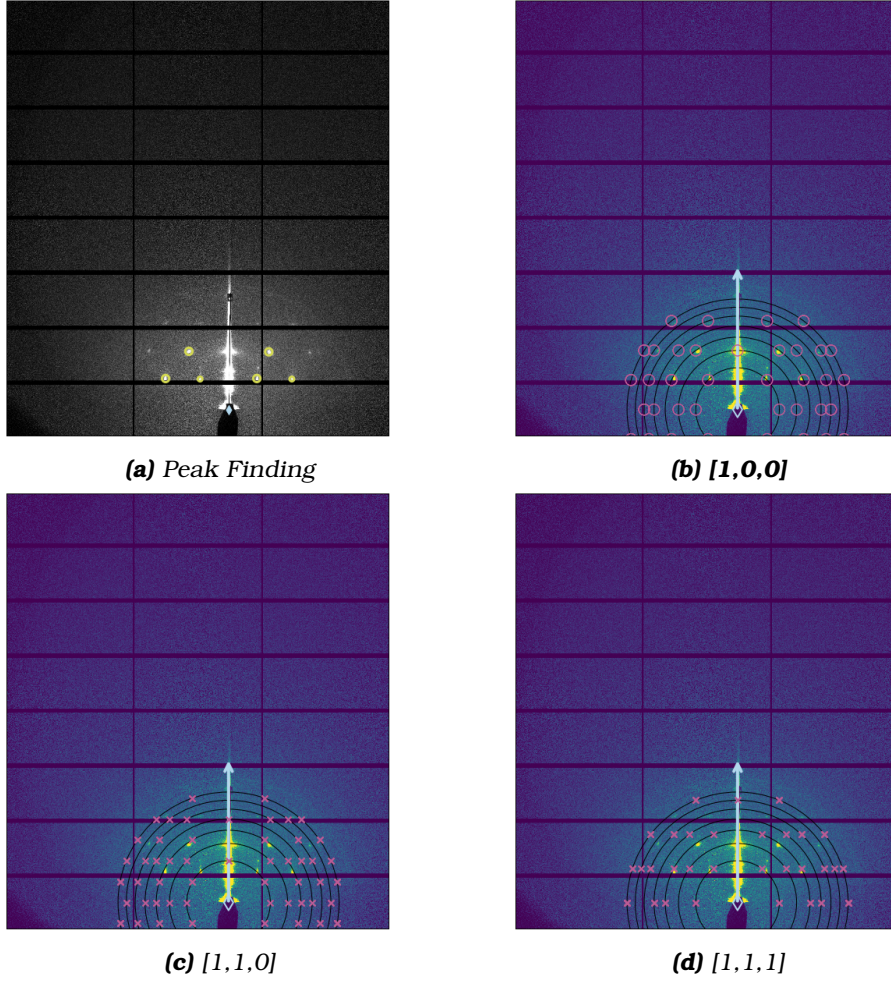


Figure 3.5: Q_{II}^P phase made from spin coating the ternary mixture 30 % (v/v) Cithrol, 24.75 % (v/v) phytantriol, and 5.25 % (v/v) Brij-56 all in 80 % (w/w) ethanol mixed with glycerol in 80 % (w/w) ethanol at a 60/40 total lipid to glycerol ratio. (b) - (d) Simulations of expected vertical uniaxial orientation corresponding to $[1,0,0]$, $[1,1,0]$, $[1,1,1]$.

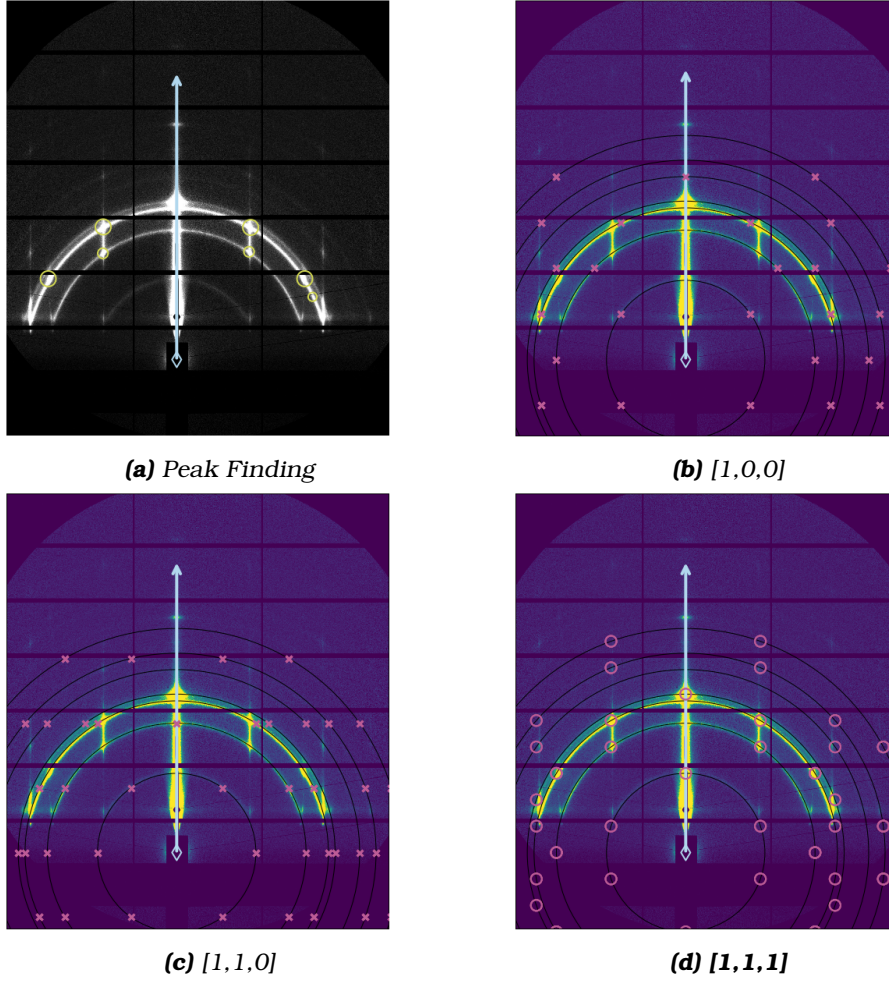


Figure 3.6: *Fd3m* micellar phase of lattice parameter 142 Å made from a DOPC / OA molar ratios 20/80 in 80 % (w/w) ethanol mixed with glycerol 20 % (v/v) also in 80 % (w/w) ethanol. **(b)** - **(d)** Simulations of expected vertical uniaxial orientation corresponding to $[1,0,0]$, $[1,1,0]$, $[1,1,1]$.

3.5.2 Micellar Cubic, *Fd3m*

The micellar cubic *Fd3m* phase was formed from DOPC and oleic acid[?] in molar ratios of 20:80 dissolved together in 80 % (w/w) ethanol. This was mixed with 20 % (v/v) glycerol in 80 % (w/w) ethanol. There were no bright enough spots on the first ring of the *Fd3m* micellar phase, so the peak finding code instead used the second reflection to calculate the lattice parameter. The micellar cubic *Fd3m* phase is uniaxially orientated in the $[1,1,1]$ direction as shown in Figure 3.6 with a lattice parameter of 142 Å. The azimuthal angles of the $[1,1,1]$ uniaxial orientation of the micellar *Fd3m* cubic phase are provided in Appendix B.2.

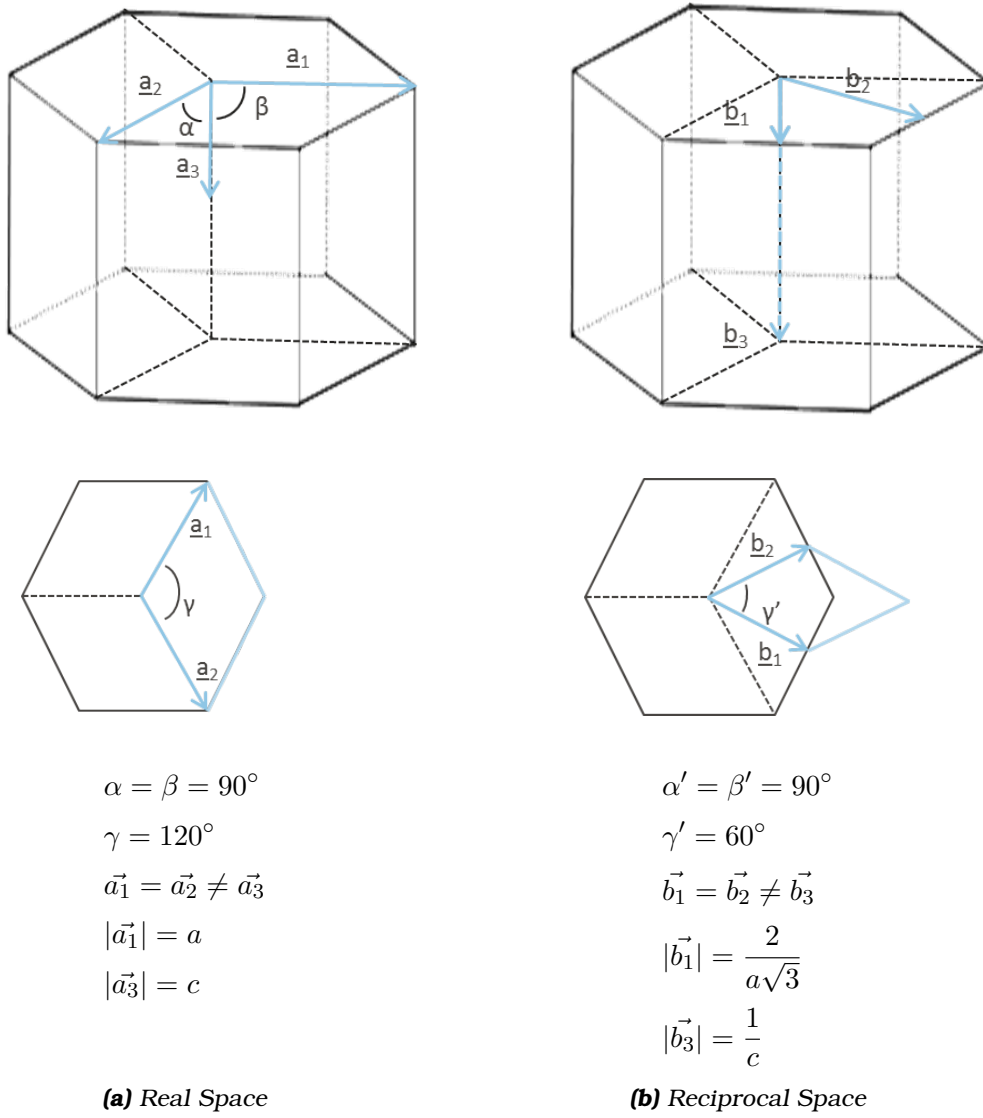


Figure 3.7: Hexagonal lattice vectors

3.6 Hexagonal Phases with Uniaxial Orientation

3.6.1 The Hexagonal Lattice

The prediction script was then extended to the lipid hexagonal lattice phases. The hexagonal lattice is so called because when three parallelepiped unit cells stack together they form a hexagonal prism. The real and reciprocal vectors are shown in Figure 3.7 and their relationship is $\vec{a} \cdot \vec{b} = \frac{\pi}{6}$. The lattice parameter equation is: ?

$$d_{hkl} = \frac{\sqrt{3}a}{2\sqrt{(h^2 + k^2 + 2hkl)}} + \frac{c}{l} \quad (3.7)$$

3.6.2 H_{II} Phase

For the H_{II} phase, the 2D diffraction pattern is initially analysed in exactly the same way as a Q_{II} phase, though using the H_{II} lattice parameter equation^{??} where the cylinders are considered infinite:

$$d_{hkl} = \frac{\sqrt{3}a}{2\sqrt{(h^2 + k^2 + 2hk)}} \quad (3.8)$$

However the generation of all [hk] values and corresponding azimuthal angles is different due to the different crystallographic symmetries. Therefore a new model to generate the uniaxial orientation for hexagonal lattices was created. The reflections for the H_{II} phase are:^{??}

$$[hk] = (h^2 + k^2 - 2hk) = 1, 3, 4, 7, 9, 12, 13 \quad (3.9)$$

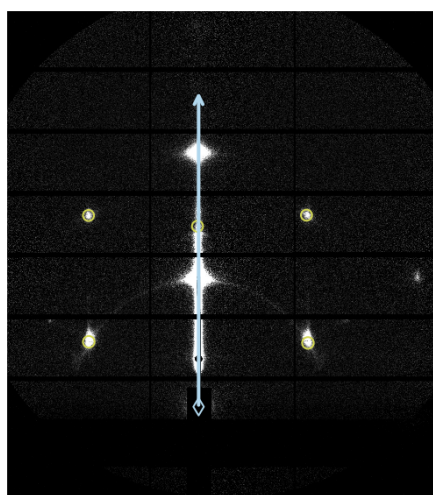
Solving Equation 3.2 with regards to the hexagonal real and reciprocal vectors gives:

$$\cos \chi = \frac{hh' + kk' + ll'}{\sqrt{h^2 + k^2 - 2hk} \sqrt{\frac{4}{3}(h'^2 + k'^2 + h'k')}} \quad (3.10)$$

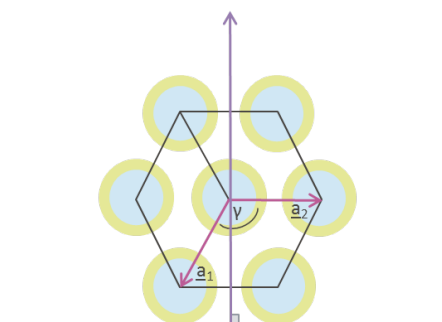
3.6.2.1 Example

Monoolein and phytantriol only form the H_{II} phase at elevated temperatures or with additives^{???} though other lipids are known to form H_{II} phases at fully hydrated conditions such as DOPE,[?] shown in Figure 3.8. The H_{II} phase has also been formed from gramicidin/monoolein mixtures where at > 95 % RH gramicidin > 15 % (w/w) in monoolein or at lower humidities < 50 % RH at > 9 % (w/w) gramicidin in monoolein. All the samples were mixed with 30 % (v/v) lipid/glycerol in 80 % (w/w) ethanol solution before spin coating. The H_{II} phase also formed from monoolein/dioleoyl-phosphatidic acid (DOPA)/cholesterol in both 68:2:30 and 65:5:30 molar ratios mixed with 30 % (v/v) glycerol in 80 % (w/w) ethanol solutions.

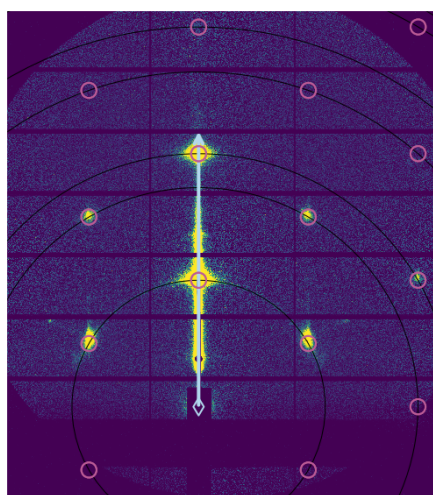
The H_{II} phase is uniaxially orientated in the [1,0] direction as shown in Figure 3.8 with a lattice parameter of 66 Å. The azimuthal angles of the [1,0] uniaxial orientation of the H_{II} phase are provided in Appendix B.3.



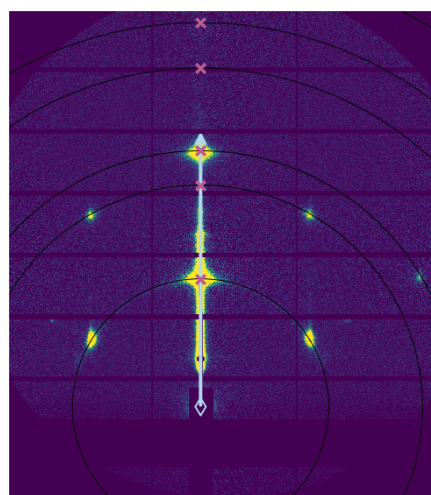
(a) Peak Finding



(b) Schematic [1,0]



(c) [1,0]



(d) [1,1]

Figure 3.8: H_{II} phase of lattice parameter 66 \AA made from a DOPE spin coated with 30 % (v/v) glycerol. It is uniaxially orientated in the [1,0] direction.

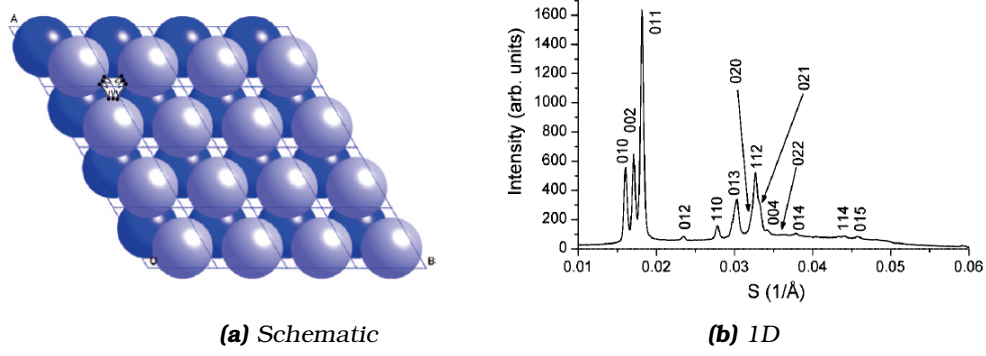


Figure 3.9: Schematic (a) and 1D pattern (b) of the $P63/mmc$ micellar phase. Reproduced from Shearman et al.[?]

3.6.3 $P63/mmc$ Micellar Phase

In 2009 Shearman et al.[?] found a 3D hexagonally packed inverse micellar phase with the space group $P63/mmc$. A simulation of uniaxial orientation was created although no experimental data has been acquired yet. The lattice parameter is calculated using Equation 3.7, and the predictions were created using the published lattice parameters $a=71.5$ Å and $c=116.5$ Å.

The reflections have $[hkl]$ values of $[010]$, $[002]$, $[011]$, $[012]$, $[110]$, $[013]$, $[020]$. Therefore the acceptable $[hkl]$ values are calculated using Equation 3.11 and Equation 3.12.

$$[hk] = (h^2 + k^2 - 2hk) = 1, 0, 1, 1, 3, 1, 4 \quad (3.11)$$

$$[l] = (l^2) = 0, 4, 1, 4, 0, 9, 0 \quad (3.12)$$

In Figure 3.10 the simulations for the $[1,0,0]$, $[1,1,0]$, $[0,0,1]$ and $[1,1,1]$ are presented. However without any experimental or theoretical calculations there is no indication for which uniaxial orientation the $P63/mmc$ micellar phase will have. When uniaxially orientated samples are created in the future, the Python code can accommodate and predict any orientation.

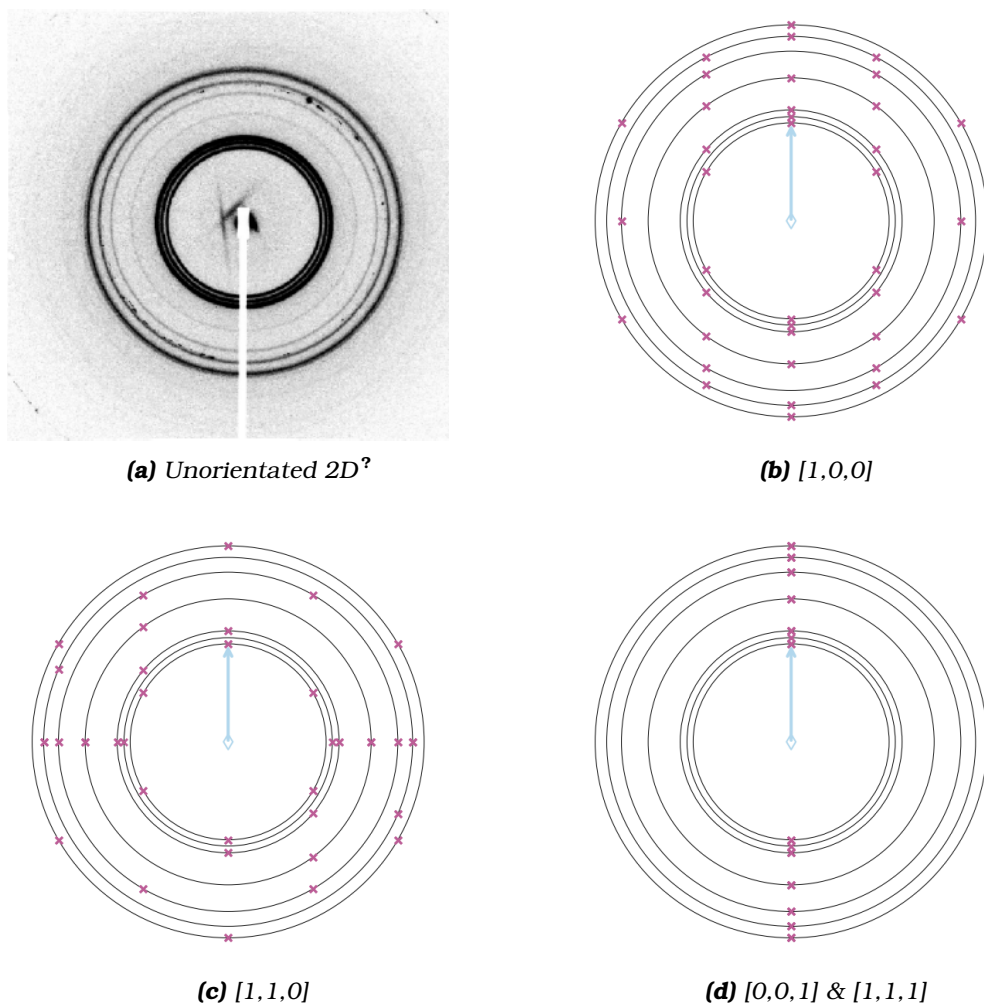


Figure 3.10: (a) Experimental data for the $P63/mmc$ micellar phase reproduced from Shearman et al.[?] (b)-(d) Predictions for the $P63/mmc$ micellar phase.

3.7 Orientation in Capillaries

The applications of orientated lipid systems, discussed in Chapter 1.4 (pg. 19), is not restricted to the simple lipid/water binary. Not all additive components, such as membrane proteins, can be dissolved in an organic solvent in order to be spin coated. The addition of different components after the creation of an orientated film needed to be investigated. Oka has previously shown that L-arginine can be added to a single crystal Q_{II}^D phase of monoolein through the phase change into a single crystal Q_{II}^P phase.[?] As such to investigate the addition of components to uniaxially orientated films, the orientation would need to be stable under aqueous conditions.

The addition of water droplets to spin coated films produced smeared patterns with continuous deterioration of the orientation of the films. Therefore a new method was devised to create orientated films within capillaries to investigate the effect of aqueous environments on orientation.

3.7.1 Experimental Details

Similar to the spin coated thin films; Cithrol and glycerol were dissolved in 80 % (w/w) ethanol before being mixed. The lipid/glycerol solutions were then pipetted into open-ended borosilicate capillaries (diameter 1.5mm) that had been glued into metal holders. The excess was tipped out and the capillaries tapped onto blue roll until the capillaries could be seen through. Capillaries were left to dry overnight in a humidified box to produce a thin orientated lipid film. SAXS was taken in transmission mode on the lab SAXS machines; Bruker Nanostar at the University of Reading, the SAXSLAB Ganesha 300XL at the University of Bristol and the Xenocs Nano-inXider SAXS/WAXS at ISIS Neutron and Muon Source.

3.7.2 Capillary Uniaxial Orientation

An orientated thin film forms from a glycerol content greater than 25 % (v/v). A glycerol content lower than 25 % (v/v) produced unorientated films. The phases produced at specific glycerol percentages are, as expected, the same as those produced when spin coated. The 2D diffraction patterns of different glycerol percentages is shown in Figure 3.11.

At over 25 % (v/v) the Q_{II}^D phase forms in a uniaxial orientation of [1,1,0] as shown in Figure 3.12. The capillary axis is the axis of rotational symmetry or uniaxial axis. The [1,1,0] orientation is different than the predicted thermodynamically favourable[?] [1,1,1] which is formed in spin coated Q_{II}^D

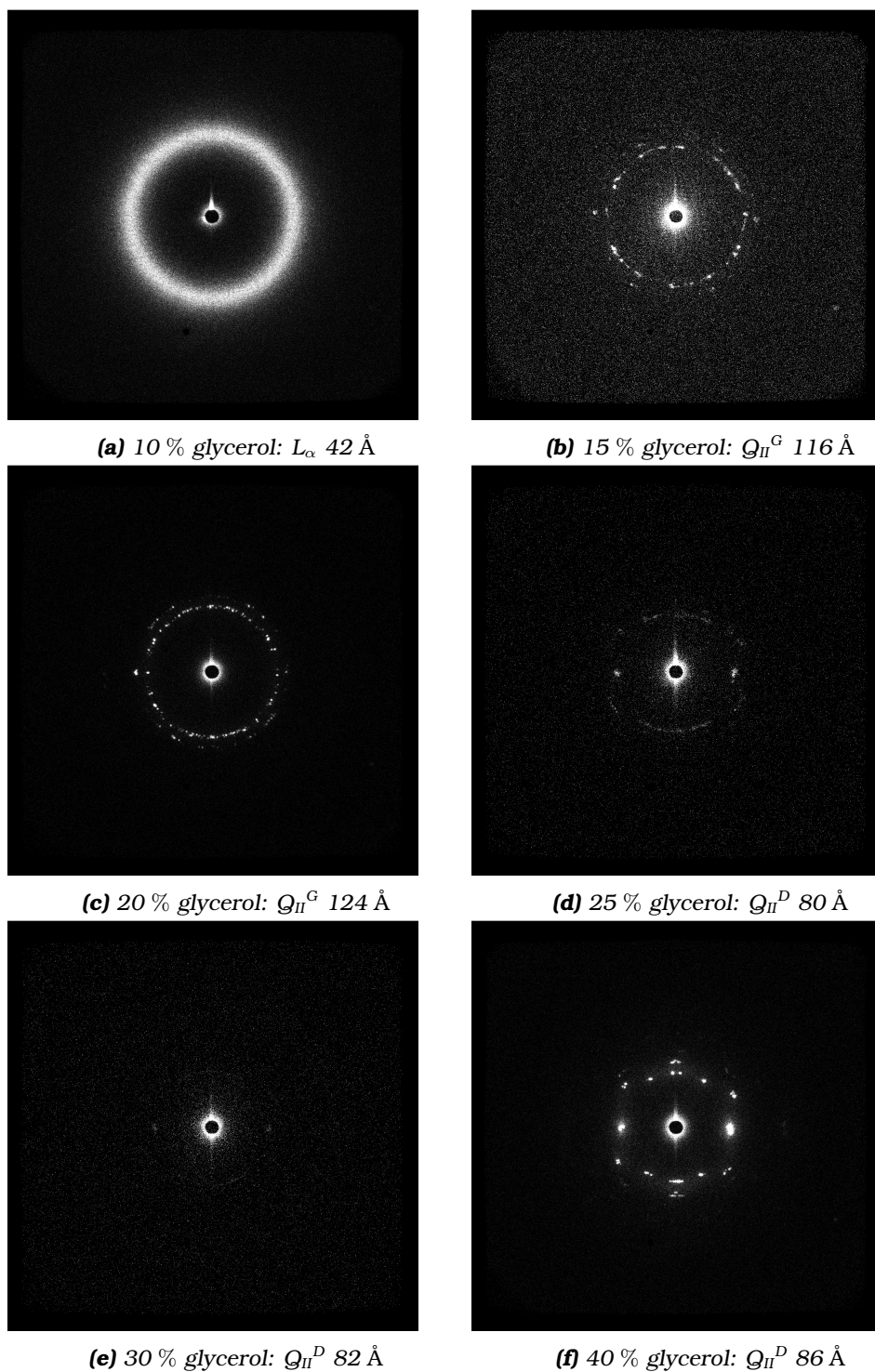


Figure 3.11: Effect of the ratio of glycerol on the thin film formed in a capillary from Cithrol/glycerol. The thin films were made from Cithrol mixed with glycerol (v/v) in 80 % (w/w) ethanol.

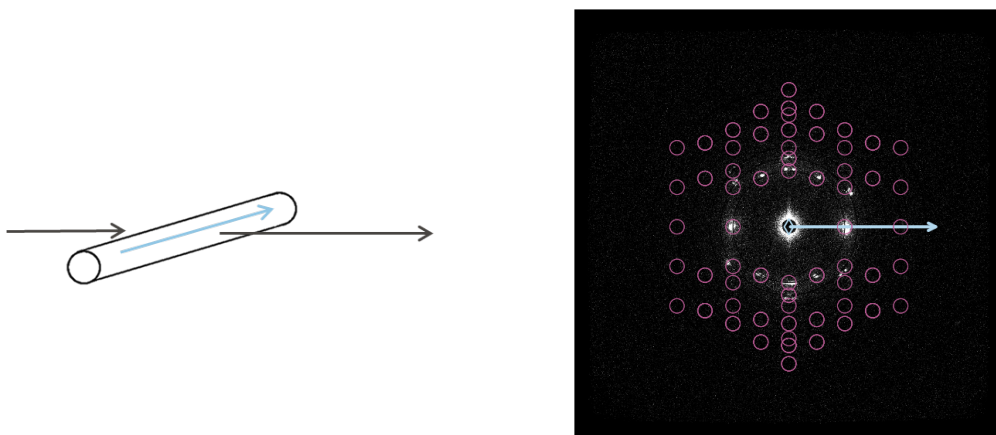


Figure 3.12: The Q_{II}^D thin film within a capillary is uniaxially orientated in the $[1,1,0]$ direction. The thin film was made from Cithrol mixed with 40 % (v/v) glycerol in 80 % (w/w) ethanol. A schematic showing the capillary normal is included on the left.

thin films.[?] It has been suggested that the use of different surface materials, such as glass instead of silicon, might be the determining factor for the crystallographic orientation of thin films.[?] However I propose that it is more complex than this.

In Q_{II}^D spin coated films, I have produced the $[1,1,1]$ uniaxial orientation on both glass slides and silicon wafers. This was created from solutions where the glycerol percentage was greater than 25 % (v/v) at all humidities. At lower glycerol percentages and changes in humidity, it is possible to produce other orientations for both the Q_{II}^G and Q_{II}^D phases. These orientations are the $[2,1,1]$ and the $[1,1,0]$ respectively and are shown in Figure 3.13. This is consistent with work by Rittman et al.[?] which had both orientations in samples of phytantriol and monoolein. Therefore given the glycerol percentage in the capillaries is greater than 25 % (v/v), I propose that something other than the surface orientation from the substrate is affecting the crystallographic orientation in the capillaries.

In shear experiments within capillaries Squires et al.^{??} created orientated Q_{II}^D films aligned in the direction parallel to the flow. This corresponded to an alignment in the axis of the capillary in the $[1,1,0]$. The phase diagram of monoolein/water/ethanol[?] suggests that with the evaporation of ethanol there is a micellar to sponge phase L_3 to Q_{II}^D phase transformation. At lower glycerol percentages, equating to lower water content,[?] there would be a micellar to L_3 to L_α to Q_{II}^D phase transformation. Applying the theory that the alignment comes from a gradient change,^{??} I hypothesis in the lipid/glycerol capillaries that the orientation is from the diffusion of ethanol and gradient

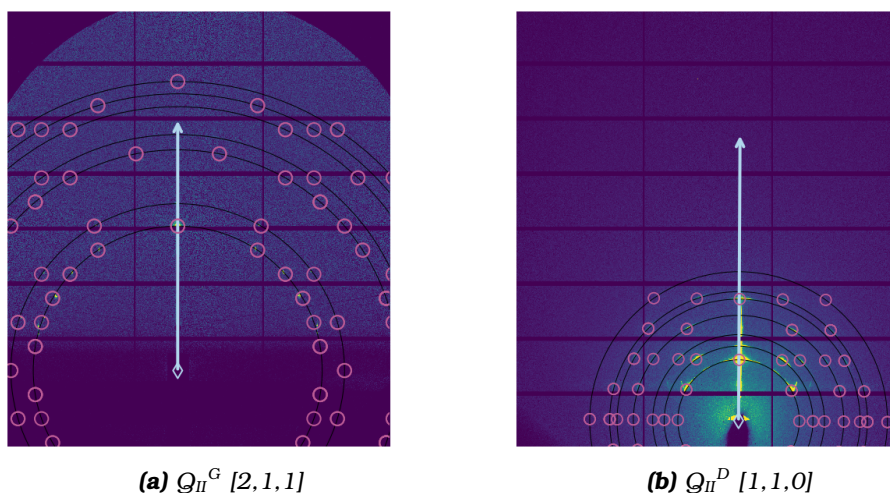


Figure 3.13: GISAXS patterns of spin coated samples from (a) Cithrol mixed with 20 % (v/v) glycerol in 80 % (w/w) ethanol at 25 % RH. (b) Cithrol mixed with 15 % (v/v) glycerol in 80 % (w/w) ethanol at <96 % RH

change in humidity. Certainly if the ethanol is vacuumed off only a broad micellar ring is present.

3.7.3 Addition of Water

To investigate the stability of the orientation in aqueous conditions, after a uniaxial film was formed in the capillaries water was added. The orientation remained unchanged upon the addition of water. The capillary was then left for two weeks, and the orientation still remained unchanged as shown in Figure 3.14. The increased number of reflections and higher intensity than before the addition of water (shown in Figure 3.11f) is attributed to the washing out of glycerol. Glycerol is known to suppress x-ray signals.?

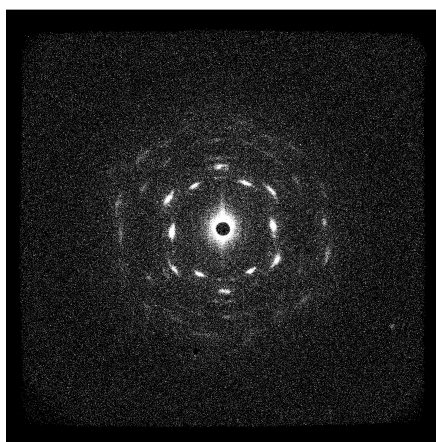


Figure 3.14: Diffraction pattern of Figure 3.11f, a uniaxially orientated [1,1,0] film in a capillary, after being filled with water for two weeks.

3.8 Summary of Data Analysis

The final Python script generated for the data analysis of 2D diffraction patterns of lipids can generate the lattice parameter for the $\text{Q}_{\text{II}}^{\text{G}}$, $\text{Q}_{\text{II}}^{\text{D}}$, $\text{Q}_{\text{II}}^{\text{P}}$, the micellar Fd3m, and the H_{II} phase. It can also produce simulations of the uniaxial orientation of all of these phases and the micellar $P63/mmc$ hexagonal phase. The script can be found in the Appendix E 2. It requires the calibration data of the beam center, detector distance and wavelength. At the moment it also requires the phase and proposed uniaxial orientation. It is possible to run the script with multiple phases and/or uniaxial orientation options but the correct indexing is still reliant on the person analysing the data. With regards to mass data analysis, should the phase be the same for multiple diffraction patterns, the script can run through a folder of diffraction patterns and generate a list of lattice parameters and indexed images.

In summary the code can (optional functions in italics):

1. *Find peaks in the 2D diffraction pattern*
2. *Calculate the lattice parameter*
3. Generate all (h,k,l) values for the $\text{Q}_{\text{II}}^{\text{G}}$, $\text{Q}_{\text{II}}^{\text{D}}$, $\text{Q}_{\text{II}}^{\text{P}}$, the micellar Fd3m, the H_{II} phase, and the micellar hexagonal phase.
4. Calculate azimuthal angles using a given uniaxial orientation
5. Calculate the radial geometry
6. Calculate the (x,y) coordinates in pixels
7. Plot the predicted peaks onto the diffraction pattern

3.9 Conclusions

A small error in the data analysis for uniaxially orientated $\text{Q}_{\text{II}}^{\text{D}}$ and $\text{Q}_{\text{II}}^{\text{G}}$ phases was corrected. The analysis script was extended to find peaks in a 2D diffraction pattern and calculate a lattice parameter from them. Uniaxially orientated $\text{Q}_{\text{II}}^{\text{P}}$ phases and the Fd3m micellar phases were created and the analysis of orientation extended. The phases were found to be [1,0,0] and [1,1,1] uniaxially orientated respectively.

The prediction analysis for uniaxially orientated thin films was extended to hexagonal lattices. A uniaxially orientated H_{II} phase was created and found

to be [1,0] orientated. The prediction was extended to the *P63/mmc* micellar phase though no experimental data has been obtained.

Uniaxially orientated Q_{II}^D films were created within capillaries with an orientation of [1,1,0]. The orientation remains in the capillary after two weeks filled with water.

3.10 Future Work

In the future a uniaxially oriented *P63/mmc* micellar phase could be created and the prediction of the uniaxial orientation tested.

3.10.1 Adaptation of Analysis

The data analysis could be adapted to simultaneously predict two phases and in doing so it could be used to monitor phase transitions such as those caused by humidity, temperature, or pressure. Phase transitions in thin films have applications in encapsulation and release of molecules^{???} or biosensors.^{??} The analysis could also be modified to monitor *in-situ* metal growth.^{????}

The analysis is also not limited to lipids but can be applied to other uniaxially oriented systems. In systems such as block co-polymers other lattices and more complex space groups can be created. The script could be extended to predict the orientations of these systems.

3.10.2 Addition of Aqueous Components

The creation of thin films within capillaries means that studies of the addition of compounds such as membrane proteins, detergents or those that induce phase changes dissolved within aqueous systems can be studied using uniaxially orientated films. Further discussion of this takes place in later chapters.

Chapter 4

Additions to a Q_{II}^D Phase

As a highly viscous, stiff, and sticky gel, handling the Q_{II} phase presents certain challenges and limitations. Given the many applications (discussed in Chapter 1.1.5) which use the Q_{II} phase as a host/vehicle for different functional molecules, one can imagine how desirable it would be to preferentially work with a liquid before transforming it into a Q_{II} phase gel. The liquid could either be the lipid in its pure molten form or dissolved in an organic solvent before converting into a functional Q_{II} phase. However if this were the case many additives, such as proteins, would then need to be incorporated into the Q_{II} phase after its formation. Such would be the case with the orientated phases discussed in the previous chapter, which are spin coated from an organic solvent that would denature most proteins. Therefore the incorporation of different types of additives into the Q_{II} phase needs to be investigated.

In this chapter I use SAXS and Raman to monitor the incorporation of several additives, including the membrane protein OmpF, into the Q_{II}^D bilayer of monoolein in excess water conditions. This work culminated with the incorporation of the detergent LDAO into an orientated Q_{II}^D thin film of monoolein causing a transformation into an orientated Q_{II}^P phase.

4.1 SAXS and Raman

There are several methods used to monitor additives in lipid phases however many are type specific or involve the inclusion of additional components. Some examples include monitoring the colour saturation of the usually clear lipid for coloured membrane proteins such as bacteriorhodopsin[?] or the coloured photosynthetic reaction centre from *Rhodobacter sphaeroides*.[?] A

fluorescent dye can be mixed with the protein and monitored via fluorescence.^{???} For detergents, specific assays can exist using radio labelled detergents,[?] Fourier transform infrared spectroscopy,[?] or the phenol-sulphuric acid reaction for sugar containing detergents.^{??}

Therefore SAXS in conjunction with Raman spectroscopy has been chosen to monitor the phase behaviour of the lipid as well as the incorporation of additives without any molecular changes. SAXS is the primary technique for the characterisation of lipid phase behaviour. Raman was chosen as it is a non-invasive, non-destructive optical technique which as it is insensitive to water compared to infrared spectroscopy has been extensively used to probe biological samples.[?] Both lipids and proteins have characteristic features (Techniques and Methods 2.1.3 pg. 31) in Raman spectroscopy which allow for the analysis of complex biological samples. One such example is where Raman has been used to probe the lipid organization and protein secondary structure in synthetic human skin.[?] Another is where both IR and Raman were used to assess the functionality of bacteriorhodopsin within a crystal created using the *in meso* method.[?]

4.2 Prediction of Phase Behaviour

The incorporation of several different additive systems into the Q_{II}^D phase of monoolein was investigated: polymer nanodiscs, the membrane protein OmpF and its solubilising detergent OG, and the detergent LDAO. The phase behaviour from the incorporation of the polymer nanodiscs and the detergents was predicted and is discussed. Though OmpF has been successfully crystallised[?] using the *in meso* method, there have been no studies published regarding the protein's effect on lipid phase behaviour and as such its effect was unknown.

4.2.1 Nanodiscs

Styrene maleic acid co-polymers have been successfully combined with the cell line to purify a membrane protein of interest.^{??} They have been shown to spontaneously self-assemble into particles with well-defined size and discoidal shape called nanodiscs in the presence of phospholipids and $pH > 8.0$.^{??} The removal of the extraction, subsequent purification, and solubilisation steps for membrane proteins is of particular interest in crystallisation. Indeed bacteriorhodopsin has recently been crystallised from SMALPS using the *in meso* method.[?] However as a rather stable membrane protein of which 72 of its 164 crystal structures within the Protein Data Bank (PDB) are

crystals produced using the *in surfo* method further experiments are needed with more challenging membrane proteins for the nanodiscs to be used as a substitution in the *in meso* method.

The current theory postulated for crystallisation using SMALPS nanodiscs is that the nanodiscs partition into the lipid bilayer of the cubic phase and the transfer of the protein into the lipid Q_{II}^D phase which is triggered by the excess monoolein present.[?] It was decided to investigate this theory further. It has been proved that between a polymer nanodisc and a lipid monolayer, lipid exchange will take place.[?] The hypothesis is that by using a type 1 lipid such as DMPC to form nanodiscs that a lattice parameter change or phase change towards a less curved phase can be seen from the exchange of lipids with a monoolein Q_{II}^D phase.

4.2.2 Detergents

Currently the established practise for solubilising membrane proteins is via a solubilising detergent within a buffer solution where the detergent type and concentration changes dependent on the membrane protein. It has already been proven that the detergents in sufficient concentrations will induce phase changes in bulk lipid mixtures.^{???} Both the detergents OG, used to solubilise OmpF, and LDAO induce a phase change from the Q_{II}^D phase to the L_α phase[?] in bulk mixtures. For OG, the phase transition from the Q_{II}^D phase takes place at a concentration of 0.05 M or 0.015 g mL⁻¹. Therefore at the concentrations used for solubilising OmpF of 0.03 mg/ml the L_α phase is expected. For LDAO the phase transition from the Q_{II}^D phase takes place at a concentration of 1.1 M or 0.25 g mL⁻¹ and a phase change is also expected for the concentration used.

4.3 SAXS Flow Through Experiments

To investigate the incorporation of the three different additive systems into the Q_{II}^D phase, flow through experiments were devised. A capillary was coated with a thin coating of the commercial monoolein, Cithrol, and then filled with water to form the excess water Q_{II}^D phase. The additive solution was then added and the effect on the Q_{II}^D noted. Finally the additive was flushed out and water added. This was done to determine whether the additive irreversibly interacted with the bilayer such as by incorporation or simply changed the hydration of the lipid while present in the aqueous solution.

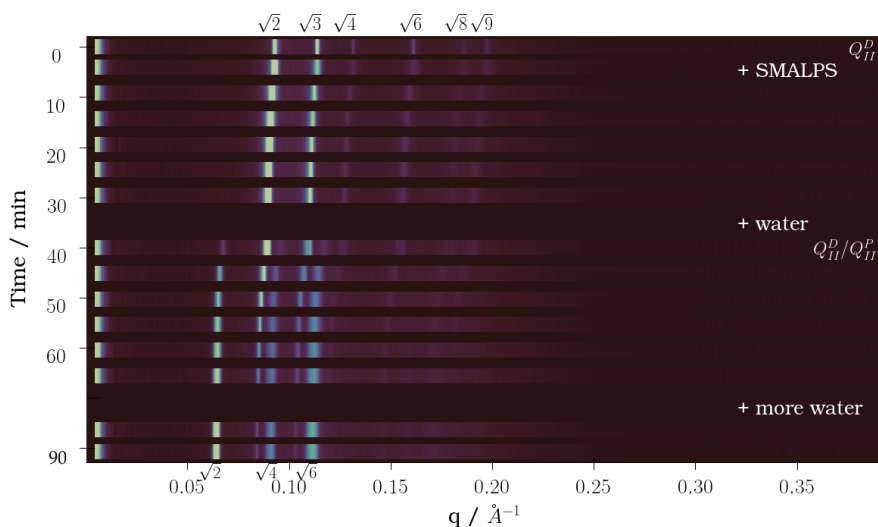


Figure 4.1: The change in the lipid Q_{II}^D phase due to the addition of SMALPS and then a flush through with water. The original Q_{II}^D film had a lattice parameter of 96 Å which swells upon the addition of the polymer to 99 Å. Upon addition of water there is a coexisting Q_{II}^P phase with lattice parameter of 132 Å.

4.3.1 SMA2000 Nanodiscs

The SMALPS nanodiscs used in the following experiment were provided by Stephen Hall from the University of Birmingham and used as received. For the purpose of this thesis the formation, composition and characterisation of SMALPS nanodiscs is not gone in depth. The SMALPS provided were 603 μM styrene maleic acid co-polymer nanodiscs (SMA2000) with the phospholipid DMPC in a buffer solution of 50 mM sodium phosphate pH 8.0 and 0.2 M sodium chloride.

The effect of three different components was investigated and then compared: the nanodiscs in buffer, the polymer in buffer, and the buffer alone. This was to separate the different effects on the Q_{II}^D phase from the buffer, the polymer and then the nanodiscs containing phospholipids.

4.3.1.1 SMALPS Nanodiscs

Firstly the effect of SMALPS nanodiscs made with DMPC lipid on the Q_{II}^D phase of monoolein was investigated. It was expected that lipids would exchange between the Q_{II}^D phase and the nanodiscs creating a swollen lattice or a phase change to a less curved phase. After creating an excess water Q_{II}^D phase, 603 μM styrene maleic acid co-polymer nanodiscs (SMA2000) with the phospholipid DMPC in a buffer solution of 50 mM sodium phosphate pH

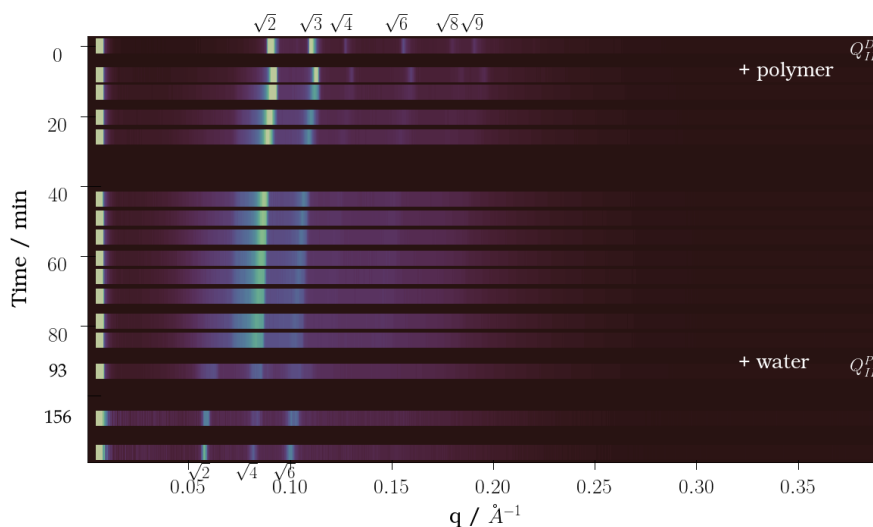


Figure 4.2: The change in the lipid Q_{II}^D phase due to the addition of styrene maleic acid co-polymer and then a flush through with water. The original Q_{II}^D film had a lattice parameter of 99 Å which swells upon the addition of the polymer to 107 Å. Upon addition of water there is a phase change to the Q_{II}^P phase with lattice parameter of 154 Å.

8.0 and 0.2 M sodium chloride was added. As Figure 4.1 shows, upon the addition of the nanodiscs there is a very slight swelling of the lattice parameter from 96 Å to 99 Å in 30 minutes. Once the SMALPS solution was removed and water added, a coexisting Q_{II}^D/Q_{II}^P phase with a Q_{II}^P lattice parameter of 132 Å was present. The addition of more water had no effect on the film.

4.3.1.2 SMA2000 Polymer

Secondly the effect of the SMA2000 polymer on the Q_{II}^D phase of monoolein was investigated. It was expected that the polymer would self-insert into the bilayer and potentially form nanodiscs. After creating an excess water Q_{II}^D phase, 603 μ M styrene maleic acid co-polymer (SMA2000) in the buffer of 50mM sodium phosphate pH 8.0 and 0.2 M sodium chloride was added. As Figure 4.2 shows the addition of the polymer smears the Bragg peaks from the Q_{II}^D phase. The shift towards smaller q is due to a shift in lattice parameter from the incorporation of the polymer into the Q_{II}^D phase before the potential formation of soluble nanodiscs. The overall decrease in intensity of the Bragg peaks, more clearly shown in Figure 4.3, also illustrates that the polymer is dissolving the monoolein and possibly that soluble nanodiscs are forming. Should nanodiscs be forming, it would be to my knowledge the first recorded monoolein-SMA nanodisc formation. Previous studies have focused on phospholipids and the solubilisation of membranes for the incorporation of proteins into nanodiscs.

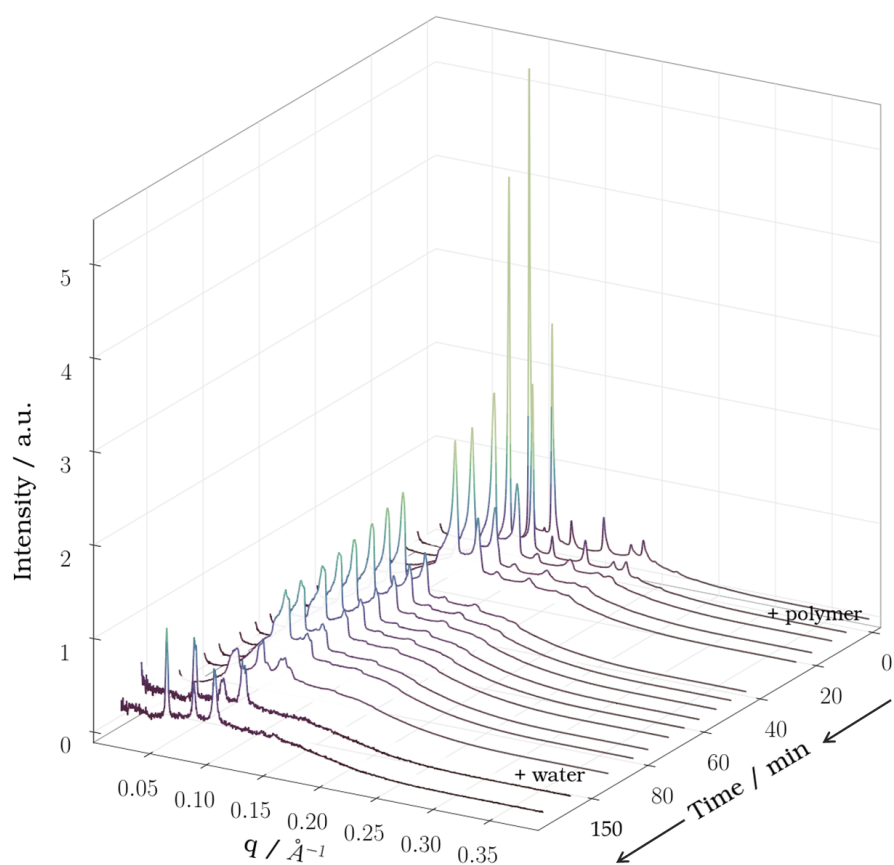


Figure 4.3: Intensity change of the monoolein film in Figure 4.2 due to the addition of styrene maleic acid co-polymer.

After an hour and thirty minutes the polymer solution was removed and the capillary was filled with water. This caused an immediate change to the Q_{II}^P phase with two distinctive lattice parameters of 146 Å and 151 Å. After another hour the film settles to a single Q_{II}^P phase with a lattice parameter of 154 Å. Upon the addition of water, the two initial Q_{II}^P phase lattice parameters suggest that the polymer penetration is inhomogeneous through the coating of the Q_{II}^D phase and that the phase change to the Q_{II}^P phase is not due to any exchange of lipids between the DMPC SMALPS and the monoolein bilayer in the previous experiment.

The inhomogeneity of penetration of the polymer into the monoolein coating is unsurprising as the lipid is in excess of the polymer concentration. That the lattice parameter should change from 99 Å to 107 Å shows that the polymer inserts itself readily into the curved bilayer. However, as the water channels for the Q_{II}^D phases are 21.8 Å and 23.5 Å respectively (equations taken from Kulkarni et al.[?]) the solubilisation of the monoolein SMALPS most likely is restricted to the interface of the lipid coating due to the probable size of the nanodiscs formed. In phospholipid bilayers, SMALPS are between 12 - 30 nm[?] depending on the molar ratio of polymer to lipid.

4.3.1.3 Buffer Solution

Lastly, the effect of the buffer, 50 mM sodium phosphate pH 8.0 and 0.2 M sodium chloride, on the Q_{II}^D phase of monoolein was investigated. It was expected that there would be no effect from the low concentrations of salts on the bilayer due to the tolerance of the phase behaviour of monoolein.[?] After creating an excess water Q_{II}^D phase, the buffer of 50mM sodium phosphate pH 8.0 and 0.2 M sodium chloride was added. As Figure 4.4 shows upon the addition of the buffer there is a slight swelling of the lattice parameter from 98 Å to 101.5 Å in 45 minutes. Once the buffer solution was removed and water added a coexisting Q_{II}^D/Q_{II}^P phase was formed which then settles into a single Q_{II}^P phase of lattice parameter 136 Å.

At higher concentrations above 1 M both sodium chloride[?] and sodium phosphate^{??} decrease the lattice parameter of bulk Q_{II}^D phase of monoolein in excess hydration conditions. At such low concentrations of 50 mM sodium phosphate pH 8.0 and 0.2 M sodium chloride it was unexpected that the buffer had an effect on the Q_{II}^D phase. It is unlikely that the swelling of the lattice parameter isn't due to the buffer solution as the Q_{II}^D phase had fully equilibrated before the addition of the buffer solution.

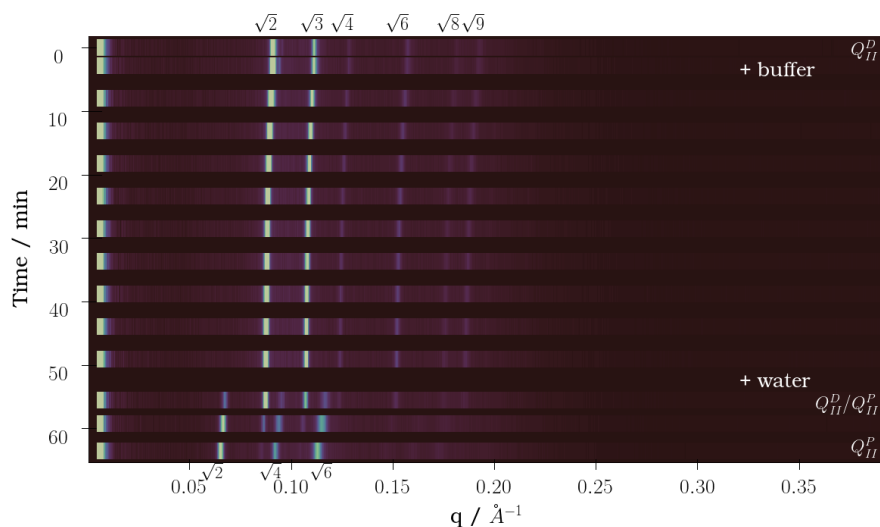


Figure 4.4: The change in the lipid Q_{II} phase due to the addition of buffer solution and then flush through with water. The original Q_{II}^D film had a lattice parameter of 98 Å which swells upon the addition of the polymer to 101.5 Å. Upon addition of water there is a phase change to the Q_{II}^P phase with lattice parameter of 136 Å.

4.3.1.4 Discussion

It was found that in the time scale of the experiments there was little effect from the interactions of the nanodiscs with the Q_{II}^D phase but the polymer ate away at the lipid film. The buffer, as expected, on its own does not change the Q_{II}^D phase due to the fact that monoolein can tolerate large concentrations of salts (~ 1.0 M depending on the salt) before a phase change is triggered.[?] Interestingly once each additive solution was removed a phase change to the Q_{II}^P phase was triggered upon the addition of water into the capillary.

The adoption of the Q_{II}^P phase from the buffer alone suggests that the transformation is due to the salts or removal of salts rather than any affect from the nanodiscs or polymer. This was surprising as monoolein does not adopt the Q_{II}^P phase in the binary lipid/water system. The Q_{II}^P has greater hydration than the Q_{II}^D phase (which is greater than the Q_{II}^G phase)[?] which implies that the removal of the salt exhibits an osmotic effect on the lipid bilayer.

The buffer containing SMA2000 polymer upon removal transforms the lipid bilayer into a Q_{II}^P phase with a lattice parameter 18 Å larger than the Q_{II}^P phase created with just the buffer solution or the buffer solution containing nanodiscs. This confirms that the solubilisation of monoolein nanodiscs only takes place at the interface and that that there is still polymer inserted into

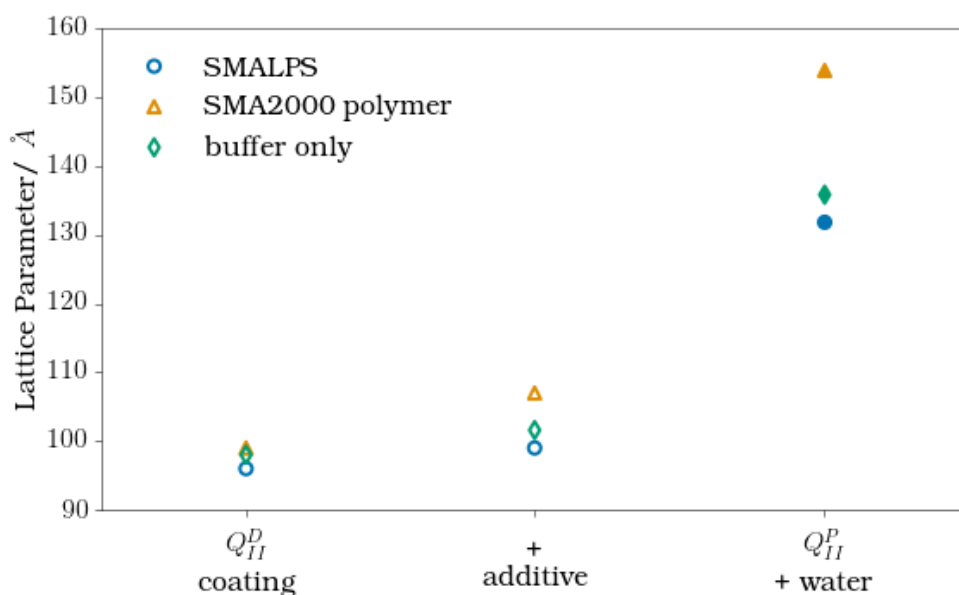


Figure 4.5: Lattice parameter changes from flow through experiments of SMALPS nanodiscs. The experiments begin with a Q_{II}^D coating in a capillary in which an aqueous solution is added. After some time the aqueous solution is removed and water added to the capillary. Error bars are not plotted as they do not exceed the marker size.

the lipid bilayer. Despite the initial inhomogeneity of penetration into the lipid bilayer the polymer is able to move freely. A comparison of the overall lattice parameter changes, shown in Figure 4.5, for all three solutions suggests that if there is any lipid exchange from the nanodiscs with DMPC lipids it is too small compared to the effect of the buffer on the lipid bilayer. Also the insertion of the polymer has a larger effect on the Q_{II}^P phase at 18 Å than the Q_{II}^D phase at 5.5 Å.

4.3.2 Detergent: LDAO

The effect of the detergent, LDAO, on the Q_{II}^D phase of monoolein was investigated. After creating an excess water Q_{II}^D phase of lattice parameter 91.7 Å, the detergent 0.1 % LDAO in 20mM tris buffer (the solubilising solution for the reaction center of *Rhodobacter sphaeroides*) was added. As Figure 4.6 shows, upon the addition of the detergent there was a phase change to the Q_{II}^P phase with a lattice parameter of 138.8 Å. The removal of the detergent and then addition of water gave no further change implying the phase change is due to the insertion of the LDAO into the lipid bilayer.

The phase change to the Q_{II}^P phase was unexpected. In bulk mixtures, monoolein mixed with LDAO forms a L_α phase at over 0.25 g mL⁻¹.[?] In

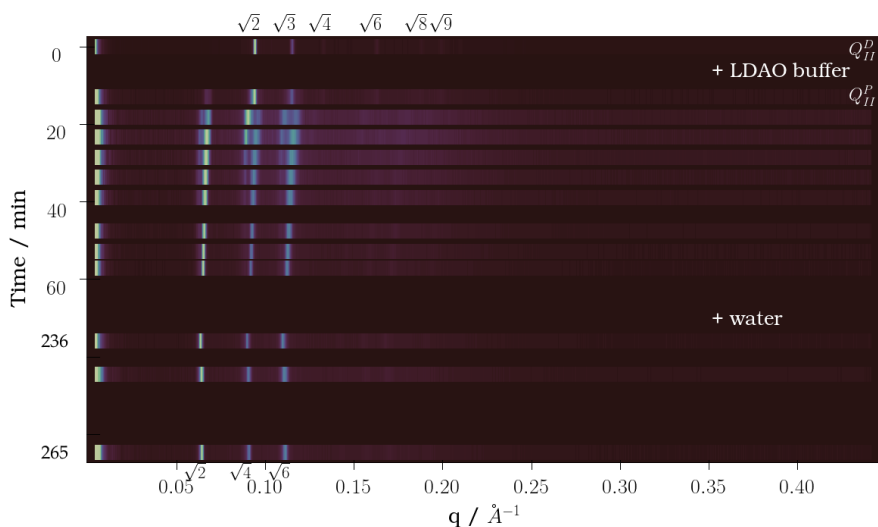


Figure 4.6: The change in the lipid Q_{II} phase due to the addition of LDAO buffer solution and then flushing through with water. The original Q_{II}^D film had a lattice parameter of 94.9 Å. Upon addition of LDAO buffer there is a phase change to the Q_{II}^P phase with lattice parameter of 138.3 Å. For each scan the intensity is normalised to the highest peak.

this case the zwitterionic surfactant LDAO behaved like a charged lipid, increasing the hydration of monoolein's head groups upon insertion.^{??} The insertion of LDAO would force monoolein's head groups apart, reducing the hydrogen bonding between adjacent monoolein molecules. This results in the increased hydration of the head groups which induces a phase change to the Q_{II}^P phase. This behaviour is most likely due to electrostatic interactions^{??} as the head group of LDAO is very small.

4.3.3 Protein: OmpF

The effect of the membrane protein, OmpF, on the Q_{II}^D phase of monoolein was investigated. After creating an excess water Q_{II}^D phase, the protein 4.4 mg mL⁻¹ OmpF in 3 % (w/w) OG 20 mM Tris pH 8.0, 1 mM ethylenediamine tetraacetic acid (EDTA) was added via syringe pump at a rate of 5 µL/min. As Figure 4.7 shows upon the addition of OmpF there is a phase change from the Q_{II}^D phase to the Q_{II}^P phase. The continuous addition of protein solution continually changed the lattice parameter, which before the addition of water was 170.8 Å. Water was flushed through the capillary at a rate of 5 µL/min which caused no change in phase, but did shrink the lattice parameter to 151.7 Å. The faintness of the Q_{II}^P phase peaks could either be from the solubilisation by excess OG detergent or from multiple lattice parameters smearing the signal.

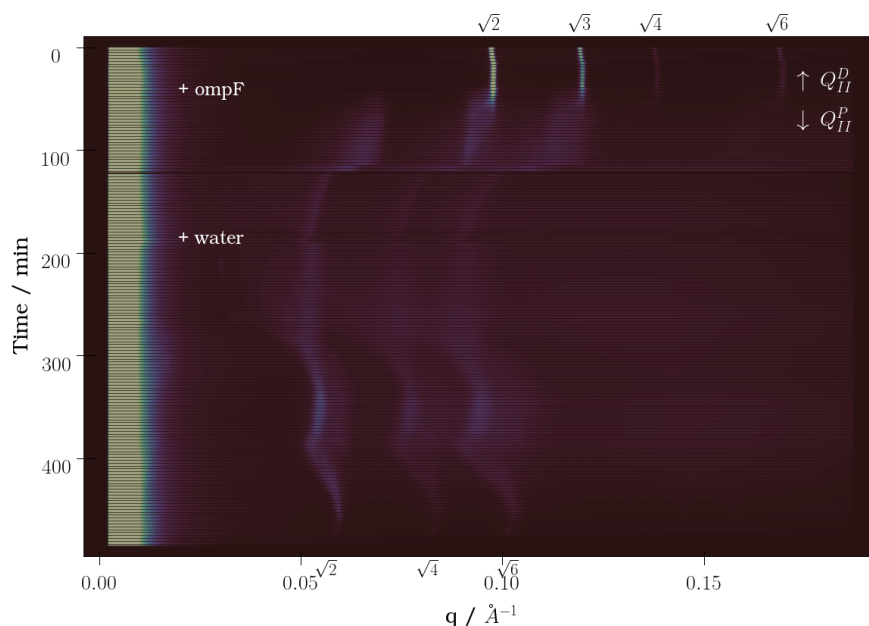


Figure 4.7: The change in the lipid Q_{II} phase due to the addition of OmpF solution and then flushing through with water. The original Q_{II}^D film had a lattice parameter of 91.7 Å. Upon addition of OmpF solution there is a phase change to the Q_{II}^P phase with lattice parameter of 170.8 Å which settled to 151.7 Å after the addition of water.

4.3.3.1 Detergent: OG

The effect of the solubilising detergent solution for OmpF on the Q_{II}^D phase of monoolein was investigated. After creating an excess water Q_{II}^D phase, the detergent 3 % (w/w) OG 20 mM Tris pH 8.0, 1 mM EDTA was added. As Figure 4.8 shows upon the addition of the detergent there was a smearing of the Bragg peaks towards low q . After the removal of the detergent, the addition of water and being left overnight the coating settles to a multi-lattice parameter Q_{II}^D phase around 109 Å. A static capillary of 20 mM Tris pH 8.0, 1 mM EDTA showed that there was no phase change due to the buffer therefore the changes shown in Figure 4.8 are singularly due to the OG.

A phase change from the Q_{II}^D phase to either the Q_{II}^G phase or the L_α phase based on the behaviour in bulk[?] was expected from the concentration of OG used. The lack of phase change implies that the addition of OG is not in sufficient quantities to induce a phase change. Therefore the required amount needed to induce phase changes isn't concentration dependent but rather quantitative. The multiple lattice parameters forming in the first hour after the addition of OG implies the insertion of OG into the bilayer isn't homogeneous or fast, unlike the detergent LDAO. The persistence of multiple

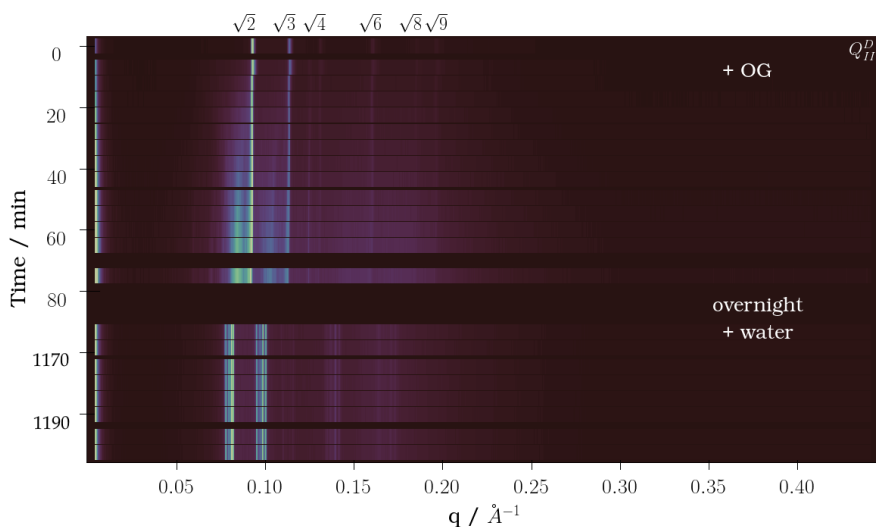


Figure 4.8: The change in the lipid Q_{II} phase due to the addition of OG solution and then flushing through with water. The original Q_{II}^D film had a lattice parameter of 94.9 Å. For each scan the intensity is normalised to the highest peak

lattice parameters after the addition of water supports the theory that OG does not move as freely through the bilayer as LDAO.

4.3.3.2 Discussion

The lack of phase change from the detergent or buffer means that the phase change to the Q_{II}^P phase from the OmpF solution is due to the insertion of the membrane protein into the lipid bilayer. Unlike OG on its own, the induced phase change to the Q_{II}^P happens instantaneously as the membrane protein preferentially inserts into the Q_{II} phase bilayer rather than remaining in the detergent micelles. Wallace et. al[?] also found that the reaction centre from *Rhodobacter sphaeroides* incorporates into a lipid bolus which was monitored via changes in colour saturation. If proteins preferentially reconstitute into a lipid bilayer this has implications for *in meso* crystallisation where excess detergent can create problems.

4.4 Raman

SAXS is a powerful technique to show the phase changes from additives to binary lipid/water system. Though as the previous examples show, the insertion into the bilayer is mainly inferred and the systems can be complex. Therefore a complimentary technique was used, Raman, to detect the incorporation of membrane proteins and the polymer used to form nanodiscs into

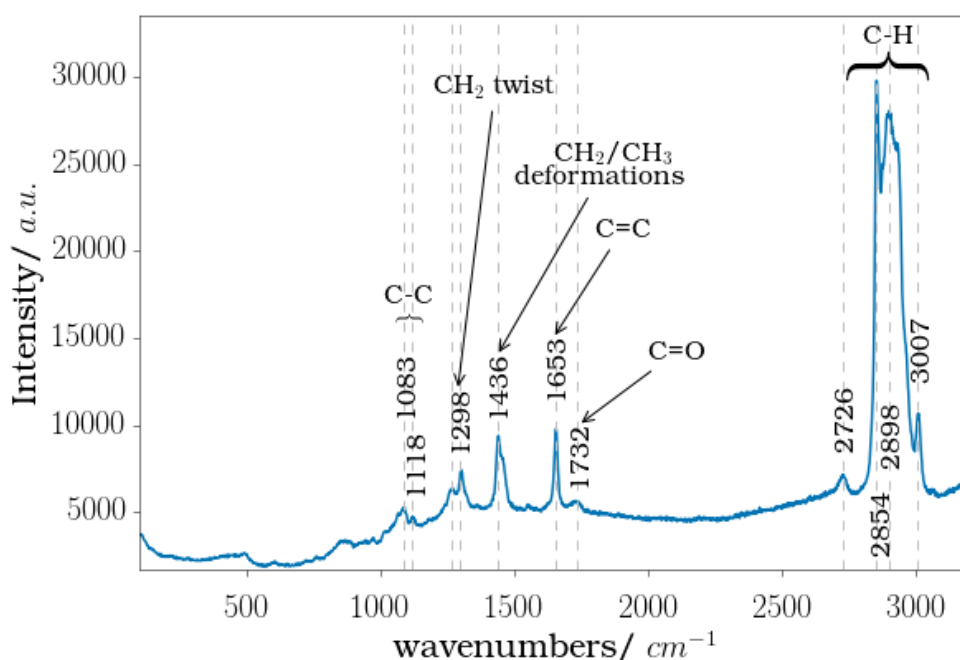


Figure 4.9: Raman spectra of the Q_{II}^D phase of Cithrol. Spectra taken from a capillary coating of Cithrol filled with water to produce the excess water Q_{II}^D phase. Characteristic vibrational modes for acyl chains of lipid are noted.

a lipid Q_{II}^D phase of the commercial monoolein, Cithrol. A unique signal from the additive is monitored upon the incorporation of the additive into the Q_{II}^D phase.

4.4.1 Raman of the Q_{II}^D phase

Firstly the Raman spectra of Cithrol Q_{II}^D phase over the wavenumber range 100 - 3200 cm^{-1} was investigated and is presented in Figure 4.9. It shows the characteristic lipid peaks for the acyl chains.[?] These are the bands for the C-C stretching at 1083 and 1118 cm^{-1} , the CH_2 twist at 1298 cm^{-1} , the CH_2 scissoring at 1436 cm^{-1} , and the C-H stretching bands between 2726 - 3007. The bands for monoolein's C=C stretching and C=O stretching are at 1653 and 1732 respectively. The spectra is consistent with the Raman spectra of pure monoolein[?] and does not show any additional peaks due to impurities in Cithrol.

This consistency between the impure commercial Cithrol and pure monoolein is expected. The spectra of monoolein is very similar to that of oleic acid[?] which is very similar to triolein with the addition of the vibrational band for the ester at 1730 cm^{-1} . As the most likely quoted impurity by the suppliers is oleic acid there would be no additional vibrational modes.

4.4.2 Styrene Maleic Acid Co-Polymer

The first additive investigated using Raman for the incorporation into the Q_{II}^D phase was the polymer used to form nanodiscs, styrene maleic acid co-polymer. Styrene maleic acid co-polymer has characteristic strong vibrational bands⁹ at 1000 cm^{-1} , 1031 cm^{-1} , 1583 cm^{-1} and 1602 cm^{-1} doublet, and 3060 cm^{-1} of which the 1000 cm^{-1} vibrational mode can clearly be distinguished from the lipid, as shown in Figure 4.10. The polymer was used instead of the fully formed SMALPS nanodiscs so as not to introduce other vibrational modes from the phospholipids incorporated within.

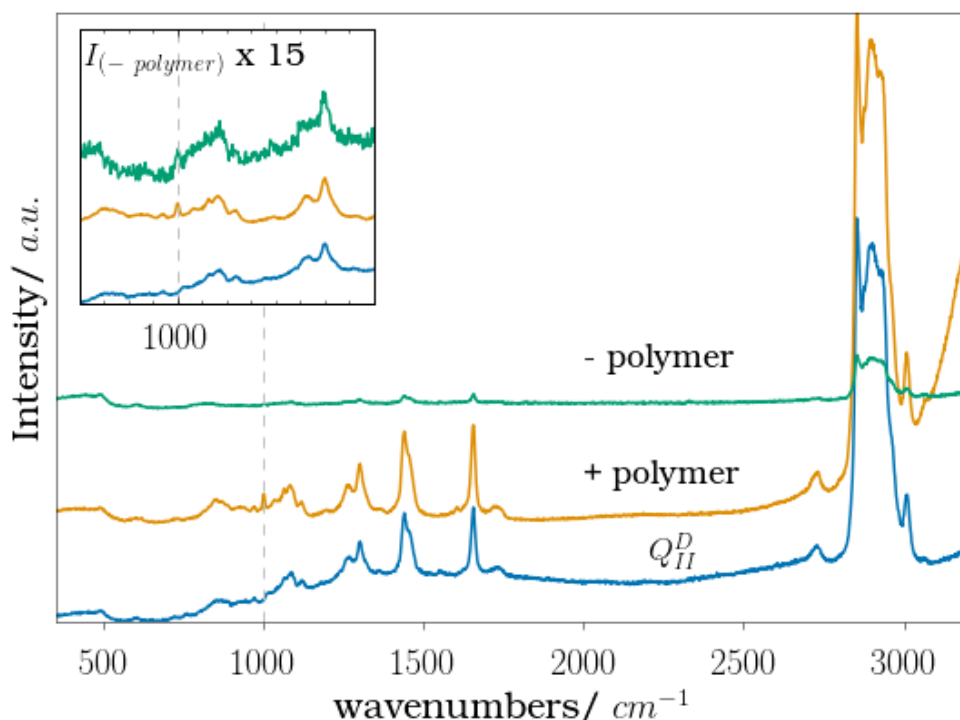


Figure 4.10: Raman spectra was first taken of a Cithrol Q_{II}^D phase coating in a capillary in excess water, second Styrene maleic acid co-polymer solution was added and a spectra taken. Third the polymer solution was removed after 2 hours and another spectra taken.

The incorporation into the lipid bilayer was tested by creating a Q_{II}^D film in a capillary to which the polymer was added and then removed after 2 hours before the capillary was filled with water. At each stage a Raman spectra focusing on the lipid film was taken between $100 - 3200\text{ cm}^{-1}$. Figure 4.10 shows the incorporation of the polymer as seen by the vibrational mode at 1000 cm^{-1} from styrene. Upon removal of the polymer the overall Raman signal decreases due to the dissolving of the bilayer by the polymer and possible formation of SMALPS. This is consistent with the SAXS data. If the signal is

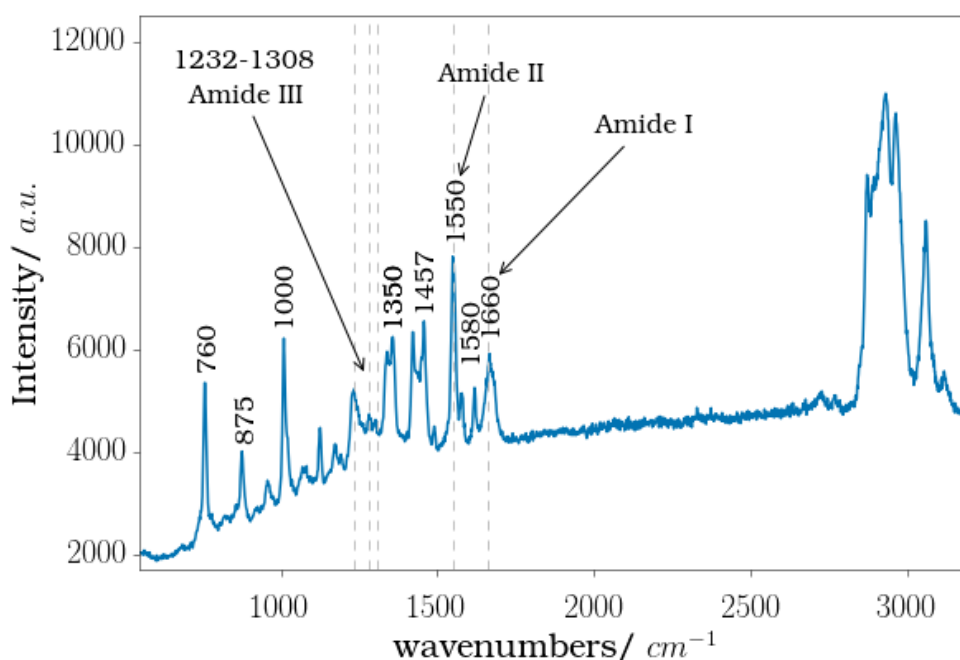


Figure 4.11: Raman of gramicidin powder. Characteristic vibrational modes for proteins are noted.

increased by a factor of 15, as in the insert of Figure 4.10, it can be seen that there is no longer a peak due to styrene within the Q_{II}^D phase.

As the Raman laser is focused on the lipid film rather than the center of the capillary it can be definitively said that the polymer is incorporated into the Q_{II}^D phase and upon flushing with water is washed away upon removal of the remaining solution.

4.4.3 Membrane Proteins

4.4.3.1 Gramicidin

Proteins have a variety of strong characteristic vibrational modes which shouldn't be hidden by the vibrational bands from the lipid. This phenomenon was first investigated for the peptide gramicidin, of which the Raman of pure gramicidin between the wavenumbers 550 - 3200 cm^{-1} is presented in Figure 4.11. The characteristic peptide backbone vibrational modes known as Amide I, Amide II and Amide III are highlighted. It is these Raman signals which are expected to be unique within the Q_{II}^D phase of the lipid.

Raman spectra between 550 - 2300 cm^{-1} were taken of Q_{II}^D phases of Cithrol with 3 % (w/w) and 10 % (w/w) gramicidin mixed in. The Q_{II}^D phases were created by mixing Cithrol with gramicidin and then water to a lipid/water

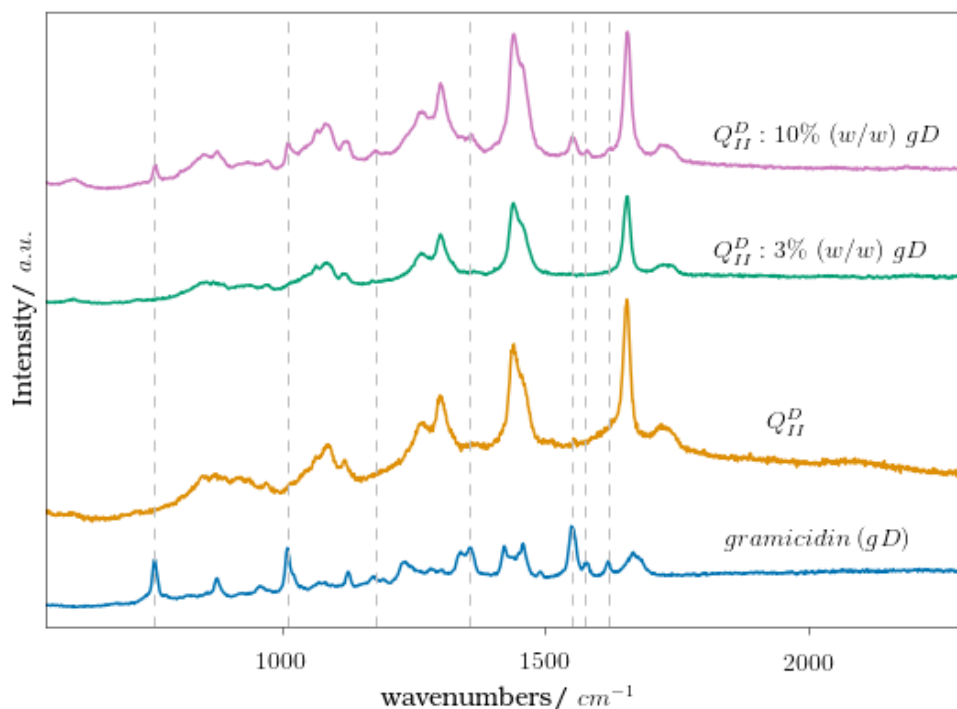


Figure 4.12: Comparative Raman spectra of powdered gramicidin, Cithrol Q_{II}^D phase, a coating of cithrol containing 3 % (w/w) gramicidin, and a coating of cithrol containing 10 % (w/w) gramicidin. Unique vibrational modes for gramicidin are highlighted.

ratio of 50/50 (w/w). Figure 4.12 shows that with increasing concentration more vibrational modes can be distinguished from the lipid spectra. At 3 % (w/w) gramicidin 3 bands can be seen at 1660 cm^{-1} (Amide I), 1350 cm^{-1} , and 1000 cm^{-1} . At 10 % (w/w) gramicidin there are seven distinct bands including the Amide II (1550 cm^{-1}) from the incorporation of gramicidin into the Q_{II}^D phase. Therefore the incorporation of membrane proteins into the Q_{II}^D phase can be monitored using a vibrational mode characteristic to a particular composition of the protein.

4.4.3.2 OmpF

Protein incorporation was further investigated via the addition of the membrane protein OmpF into the Q_{II}^D phase. However, as Figure 4.13 shows, the OmpF solution lacks the characteristic vibrational modes of a protein. The concentration of the protein was checked via a UV-vis spectra at 280 nm, and was found to be large at 7.9 mg mL^{-1} . The Raman of pure OG and the protein solution was then compared, as shown in the insert in Figure 4.13. It seems as if the signal from the OG masks that of the protein. All the bands in the OmpF solution can also be found in the detergent spectra, though there are

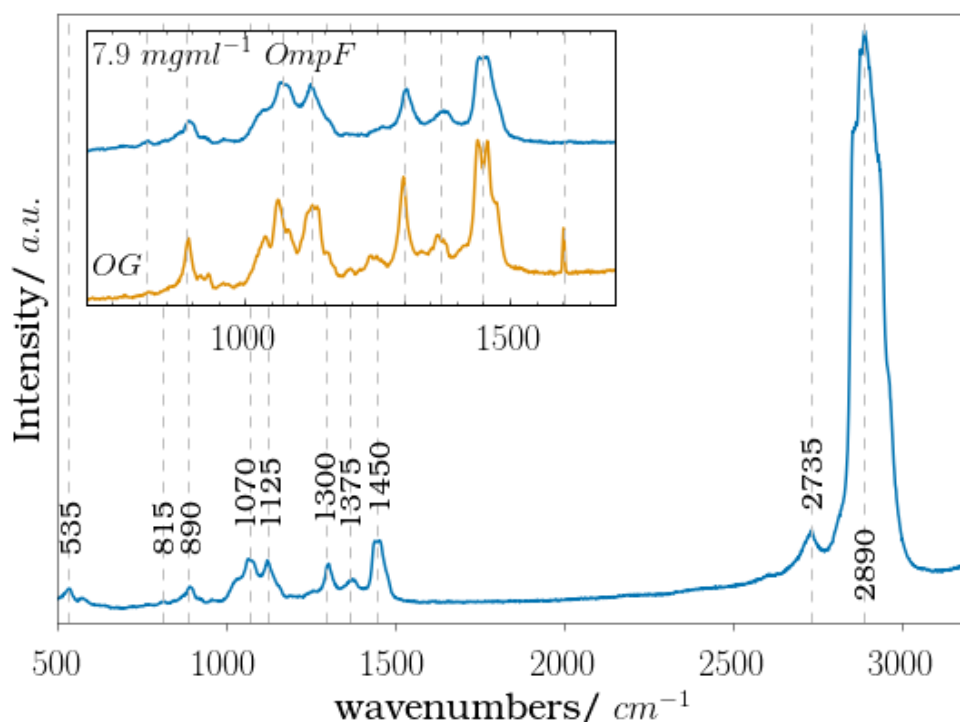


Figure 4.13: RAMAN spectra of OmpF. OmpF is solubilised in OG detergent in 20 mM Tris pH 8.0, 1 mM EDTA protein buffer.

slight differences between the two spectra, most notably the doublet at 1450 cm^{-1} and the bands at 1070 cm^{-1} and 1125 cm^{-1} . While it is possible to sort out the contributions within a band? ? ? it is beyond the scope of this work.

Despite the masking of the protein by the detergent, it is still possible to distinguish separate vibrational modes from the OmpF solution from that of the Q_{II} phase. Raman spectra were taken between $100 - 2000\text{ cm}^{-1}$ of the Q_{II} phase with increasing OmpF concentration. Figure 4.14 highlights six bands at 420 cm^{-1} , 535 cm^{-1} , 815 cm^{-1} , 895 cm^{-1} , 1070 cm^{-1} , and 1370 cm^{-1} which are unique to the OmpF solution. These peaks are indicative of the incorporation of the solution into the Q_{II} phase but it does not give any information on the incorporation of the protein. Therefore this means that through Raman alone it is not possible to prove the incorporation of OmpF into the Q_{II} phase. As such, coupling Raman with SAXS should give a more comprehensive view of the incorporation of molecules into the Q_{II} phase.

Overall, it can be concluded that Raman is a useful technique in detecting the incorporation of additives into a lipid Q_{II} phase. It is possible to distinguish between separate signals from the lipid and an additive such as a polymer, membrane protein, or membrane protein solution. The ability to focus only

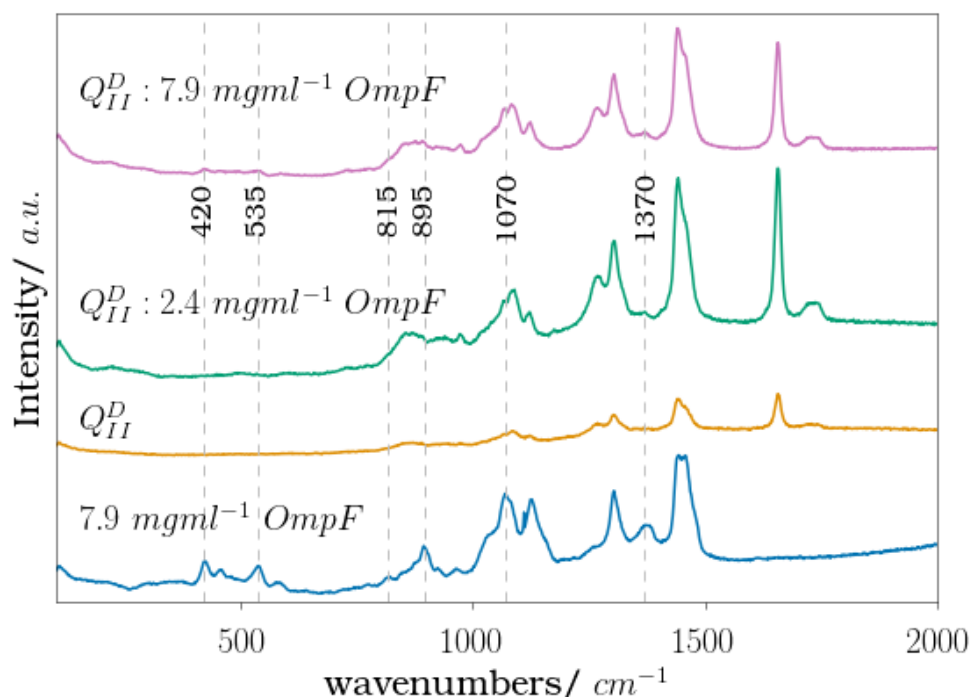


Figure 4.14: Comparative Raman spectra for OmpF solution, the Q_{II}^D phase of Cithrol, and Q_{II}^D phases made with OmpF solutions.

on the lipid layer within a capillary allows for the specific monitoring of the incorporation into a Q_{II} phase.

4.5 Aligned Lipid Phase Change

Given the success of the addition of molecules into the bulk Q_{II} phase, the incorporation of the detergent LDAO was attempted into an aligned Q_{II}^D phase in a capillary. A thin film of Q_{II}^D phase was created using the solvent vapour procedure described in Chapter 3.7 (pg. 57) from 70/30 (v/v) Cithrol/glycerol solution in 50% (w/w) ethanol. After confirmation of an orientated film, Figure 4.15a, 0.1 % LDAO in 20mM tris buffer was added which induced a phase transformation to the Q_{II}^P phase, Figure 4.15c. The Q_{II}^D phase has a lattice parameter of 84 Å and the Q_{II}^P phase has a lattice parameter of 144 Å.

A transformation pathway for the Q_{II}^D phase to the Q_{II}^P phase has been proposed using data of a single crystal region of Q_{II}^D phase of monoolein transformed to a single crystal of the Q_{II}^P phase with 20 mM L-arginine.[?] Unfortunately the phase change in Figure 4.15 cannot be used to investigate this transformation. The first reason is the films are of unknown alignment. To produce thicker films within the capillary the lipid and glycerol were dissolved

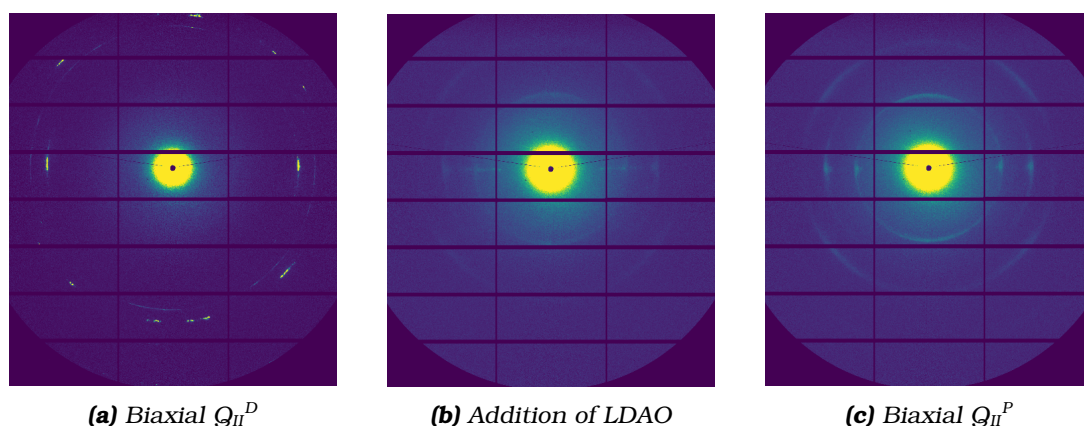


Figure 4.15: Phase change of an orientated capillary of Q_{II}^D to Q_{II}^P upon the addition of LDAO buffer solution. The lipid film was made from Cithrol/glycerol 70/30 (v/v) and coated from a 50 % ethanol solution.

in less ethanol (50 % rather than 80 %) and as such have produced films that are not uniaxially orientated. The orientations shown in Figure 4.15 do not fit any uniaxial prediction for the Q_{II}^D and Q_{II}^P phase respectively nor is this a single crystal. Interestingly, this difference of orientation is different to spin coated films which produce the [1,1,1] orientation for the Q_{II}^D phase with as little as 40 % (w/w) ethanol (discussed in Chapter 5.1.1 pg. 86).

The second reason is that for the phase change to progress through a Bonnet transformation, the mechanism of Infinite Periodic Minimal Surface (IPMS) transformation, the ratio between the lattice parameters of Q_{II}^P/Q_{II}^D should be 1.28.^{??} The ratio of Oka et al.[?]’s single crystal had this ratio, however the aligned phase gives a ratio of 1.71. The previous bulk Q_{II}^D film phase change with LDAO also has a larger ratio at 1.51. This further suggests that LDAO influences the curvature of the lipid bilayer through electrostatic interactions like the charged lipids dioleoyl-phosphatidylserine (DOPS) and dioleoyl-phosphatidylglycerol (DOPG)[?] which also have larger ratios between the Q_{II}^P/Q_{II}^D lattice parameters.

4.6 Conclusions

The incorporation of the SMALPS nanodiscs, SMA2000 polymer, the detergents LDAO and OG, and the membrane proteins OmpF and gramicidin were monitored by SAXS and Raman. The insertion of additives into previously made coatings of the Q_{II}^D phase was confirmed.

The phase behaviour of bulk lipid coatings isn’t the same as bulk lipid mixtures. The removal of the buffer solution of 50mM sodium phosphate pH 8.0

and 0.2 M sodium chloride caused a phase change to the Q_{II}^P phase. Neither of the two detergents, LDAO or OG produced the expected phase transitions to the Q_{II}^G phase or the L_α phase respectively. LDAO produced a Q_{II}^P phase and OG only changed the lattice parameter of the Q_{II}^D phase.

The membrane protein OmpF was found to preferentially insert into a Q_{II}^D phase lipid bilayer rather than remaining in detergent micelles.

It is possible to incorporate biomolecules into an orientated lipid film and the orientation of the film remains. This was monitored through a Q_{II}^D to Q_{II}^P phase transition through the addition of LDAO.

4.7 Future Work

4.7.1 Mechanism of Q_{II}^P Phase Transformation

The transformation from a Q_{II}^D phase to Q_{II}^P phase from the removal of the buffer 50mM sodium phosphate pH 8.0 and 0.2 M sodium chloride was unexpected. The mechanism and stability of this transformation should be investigated. The hypothesis put forward in this work is that of osmotic stress but further study would be recommended.

4.7.2 Renaturing Membrane Proteins

Traditionally membrane proteins have been mixed with two syringes to form a bulk lipid phase. In this way membrane proteins have been successfully re-natured by mixing with dry monoolein to form a Q_{II} phase and removing the denaturant by diffusion.[?] With proteins reconstituting in Q_{II}^D phases spontaneously, in future it should be possible to renature proteins by using a Q_{II}^D phase with no mechanical mixing. As subsequent or continuous reconstitution is possible the concentration of the membrane protein in the lipid bilayer could also be maximised. Not only would renaturing membrane proteins be of use in the lab to maximise the shelf-life of membrane proteins but it has implications for any applications requiring high concentrations of membrane proteins such as membrane protein crystallisation or vaccine development.

To test this hypothesis, the flow through experiments can be repeated but with a denatured protein. The particular denatured protein would need to have a specific activation assay attributed to it to check for the active conformation within the lipid bilayer such as diacylglycerol kinase,^{??} radio-labelled ligand-binding for dopamine 2 Long receptor and histamine H1 receptor,[?] or vitamin B12 binding to outer membrane cobalamin transporter.[?]

4.7.3 Membrane Proteins with Orientated Phases

With the successful incorporation of the detergent LDAO into an aligned Q_{II} phase, the next step would be the incorporation of membrane proteins into an orientated phase. The implications of this work are described more fully in the next chapter.

Chapter 5

A Question of Curvature

Current theory states that in a lipid bilayer, proteins and other molecules are free to diffuse within the plane of the bilayer.[?] In fact much of *in meso* membrane protein crystallisation is built on this model. Yet, this does not mean that the bilayer is strictly homogeneous. In cell membranes different lipid species are asymmetrically distributed throughout the bilayer.[?] The composition and thickness of the lipid bilayer can also influence protein organisation in the plane of the membrane and hence their function.^{??} The mechanisms involved in protein-lipid interactions are non-specific and non-chemical in nature, thus it is easy to imagine the partitioning of an additive within a more curved bilayer into sections of higher or lower curvature potentially due the hydrophobic match[?] of a protein.

Lipid rafts, of which one of the main components is cholesterol, are known to form laterally segregated microdomains in cell membranes[?] which have been linked to the liquid phase separation in model membranes.^{??} Liquid phase separation pertains to the separation of the typical liquid disordered phase L_d of most lipid phases and the liquid ordered phase L_o . The L_o phase arises upon the addition of cholesterol or other molecules which increase the orientational order and decrease the rate of motion of the hydrocarbon chain of the lipid phases.^{??} Cholesterol preferentially interacts with saturated lipids so in mixed lipid bilayers the cholesterol will laterally segregate with these lipids forming cholesterol rich L_o and cholesterol poor L_d domains.

Phase separation, including the conformation of inserted peptides,^{????} has been extensively studied in L_α model membranes.^{???} Yet the Q_{II} phases also play a vital role *in vivo*[?] and little work has gone into studying the lateral inhomogeneity in such phases. Given the many applications that the

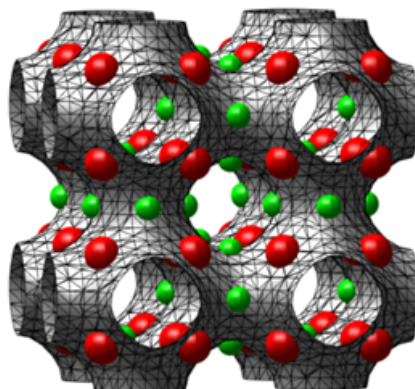


Figure 5.1: A visualisation of regions of flatter (small green balls) and highly curved (larger red balls) of a Q_{II}^P phase bilayer.

Q_{II} phases are used in, it is crucial to understand the location of proteins, peptides, and other biomolecules within the Q_{II} phase bilayer.

The Gaussian curvature of the Q_{II} phases constantly varies from 0 at the flat points to the most negative curvature at the saddle points. A depiction of flatter and highly curved regions of the bilayer is shown in Figure 5.1 using the easy to visualise Q_{II}^P phase. As biomolecules are free to diffuse laterally through the bilayer^{??} the theory is that they will preferentially partition into flatter or more curved regions of the Q_{II} phase.^{??} Recently the partitioning of two peptides^{??} was investigated in the bulk Q_{II}^D phase using SANS. However, no evidence was found of preferential partitioning for either peptide.

As such, in this Chapter I present two different methods, simultaneous GISAXS-GIWAXS and GISANS, which were used to investigate the partitioning of a hydrophobic peptide and the L_o phase within a uniaxially orientated Q_{II}^D phase. This work culminated in the use of GISANS, a modification on the SANS method used previously,^{??} to confirm that monopalmitin and cholesterol preferentially partition into the flatter regions of the Q_{II}^D bilayer.

5.1 Simultaneous GISAXS-GIWAXS

Wide Angle X-ray Scattering (WAXS) focuses on the signal from molecular form factors such as the liquid packing or protein structures, Table 5.1 shows their q values. Information on the molecular tilt of a peptide has been found by using orientated lipid L_α samples and the anisotropy in the GIWAXS signal.^{??} By orientating Q_{II} phases, the bilayer normal or inter-lipid packing from different regions of curvature of the bilayer will have different preferred directions. This preferred direction was hypothesised to be able to be mea-

sured by anisotropy in the WAXS signal of the guest biomolecules.

	$q / \text{\AA}^{-1}$
L_o	1.5 [?]
L_d	1.4 [?]
Gramicidin β helix	1.37 [?]
β sheet	1.25
α helix	1.16

Table 5.1: WAXS peaks for different structures.

Simultaneous GISAXS-GIWAXS experiments should provide information on the phase and lattice parameter of a lipid (GISAXS) and also the guest biomolecules preferential partitioning within the bilayer (GIWAXS). The two additives are the hydrophobic peptide gramicidin which has a β helical pitch at $4.7 \pm 0.2 \text{\AA}$ [?] or $q = 1.37 \text{\AA}^{-1}$ and the potential L_o phase separation of monoolein, the saturated lipid monopalmitin, and cholesterol.

5.1.1 Obtaining a WAXS Signal

Before investigating the anisotropy of a WAXS signal, a WAXS signal from an orientated thin film of the Q_{II}^D phase was required. Therefore an experiment where both SAXS, which would confirm the lipid phase and uniaxial orientation of the film, and a concurrent WAXS signal was designed. It was possible to set both beamlines i22 and i07 at Diamond Light Source to obtain simultaneous GISAXS-GIWAXS patterns, though the data presented in this Chapter is from i07.

Mixtures of lipids, gramicidin, monopalmitin, and cholesterol were dissolved in a particular (w/w) ethanol concentration. These ethanol solutions were then mixed with glycerol dissolved in the same concentration of ethanol in a ratio of 70/30 (v/v) total lipid to glycerol. The mixed solution was then spin coated onto a silicon wafer in the three spin-cycle method. Deposition was at 1000 rpm for 20 s, drying at 1500 rpm for 60 s then final 6000 rpm for 60 s. The wafer was then placed on a beamline in a high humidity chamber.

To obtain a defined lipid L_d signal at 1.4\AA^{-1} , the thickness of film was varied. The thickness of film was controlled via the percentage of ethanol that the lipid and glycerol were dissolved in.[?] Cithrol, a commercial monoolein, and glycerol were dissolved in different percentages of ethanol and mixed in a lipid/glycerol ratio of 70/30 (v/v). At 30 % (w/w) and below, both Cithrol

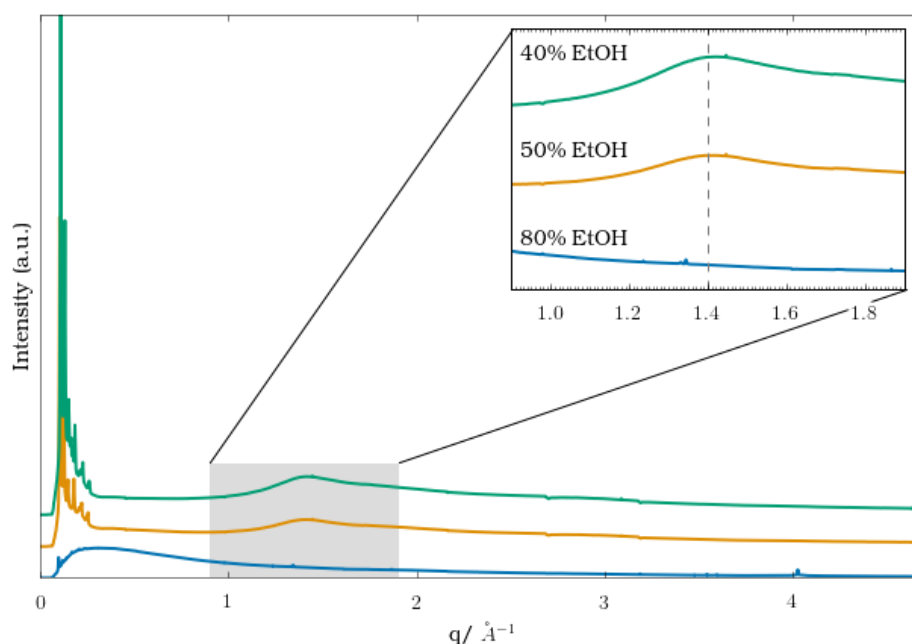


Figure 5.2: Thickness of Q_{II}^D film as controlled by percentage of ethanol. The thickness increases with decreasing amount of ethanol. The films are Cithrol/glycerol mixed in a 70/30 (v/v) ratio.

and glycerol will dissolve in ethanol however the combined mixture is quite viscous and does not spin coat a uniform film at the deposition speed used (1000 rpm). As Figure 5.2 shows for 50 % and 40 % (w/w) ethanol the $1.4 \text{ \AA}^{-1} L_d$ peak can be perceived. For films spin coated from 80 % (w/w) the lipid signal is too weak to be distinguished from the background therefore for films investigating additives within the Q_{II}^D phase 40 % (w/w) ethanol was used.

5.2 Gramicidin

The first additive investigated was the peptide gramicidin with a WAXS value of 1.37 \AA^{-1} .[?] Gramicidin was investigated because as a stable hydrophobic peptide it can be dissolved in ethanol with no loss of active conformation?[?] and then spin coated.

5.2.1 The ratio of Gramicidin to Cithrol

To begin with the amount of gramicidin that Cithrol can tolerate was investigated. The amount of gramicidin pure monoolein can tolerate before inducing a phase change to the more curved H_{II} phase is known?[?] at 5 mol % gramicidin to monoolein. However although Cithrol has the same phase behaviour with regards to water content it has a reduced H_{II} phase transition temper-

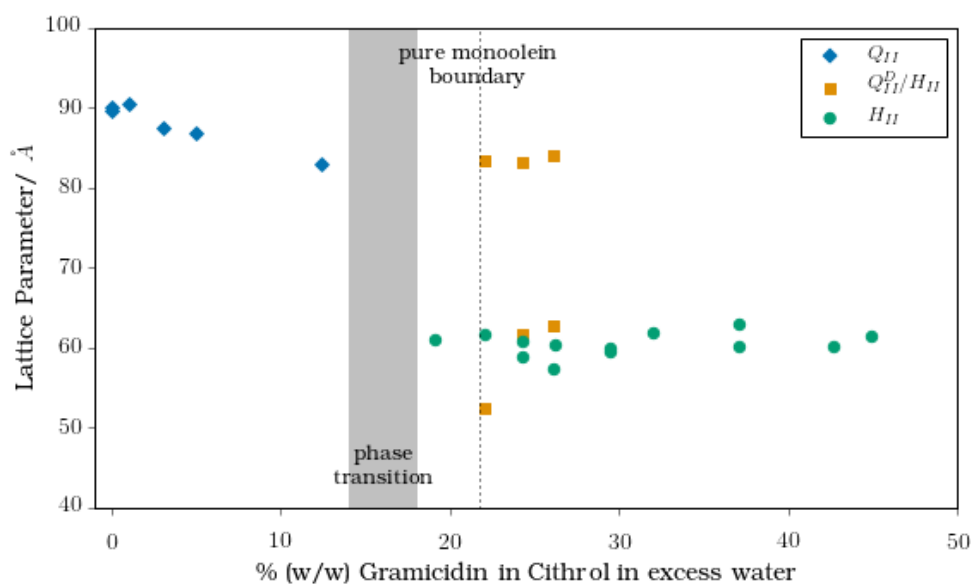


Figure 5.3: The percentage loading of gramicidin in Cithrol was tested in excess water. The phase change occurred between 14-18 % (w/w) gramicidin. The phase boundary for gramicidin in pure monoolein is also plotted at 21.7 % (w/w).

ature (Appendix A pg. 166). It was hypothesised that Cithrol might tolerate less gramicidin before a phase change from the Q_{II}^D phase was induced, and as such this was investigated.

Solid gramicidin was weighed out and mixed with the appropriate weight of molten Cithrol. The mixture was then sonicated at room temperature for 15 minutes before being mixed with water in a 60/40 (w/w) lipid/water ratio to form excess water phases. The gel was then syringed into screw cap capillaries and SAXS patterns taken on the Bruker Nanostar at the University of Reading. The phase change, shown in Figure 5.3, occurs between 14 - 18 % (w/w) in Cithrol. For pure monoolein the phase change happens at 5 mol % gramicidin to monoolein, which corresponds to a 21.7 % (w/w). Cithrol, therefore, tolerates less gramicidin than pure monoolein at about 4 - 8 % less or only 3-4 mol %. All future studies involving gramicidin and Cithrol remained below 13 % (w/w) so as to remain in the Q_{II}^D phase.

5.2.2 Raman on a Thin Film

Raman spectra presented in the previous Chapter 4.4.3.1 (pg.77) showed that the signal for gramicidin can be distinguished from the Q_{II} phase. The experiment was repeated for thin films of Q_{II}^D phase containing gramicidin to confirm the presence of gramicidin in the spin coated films of the Q_{II}^D

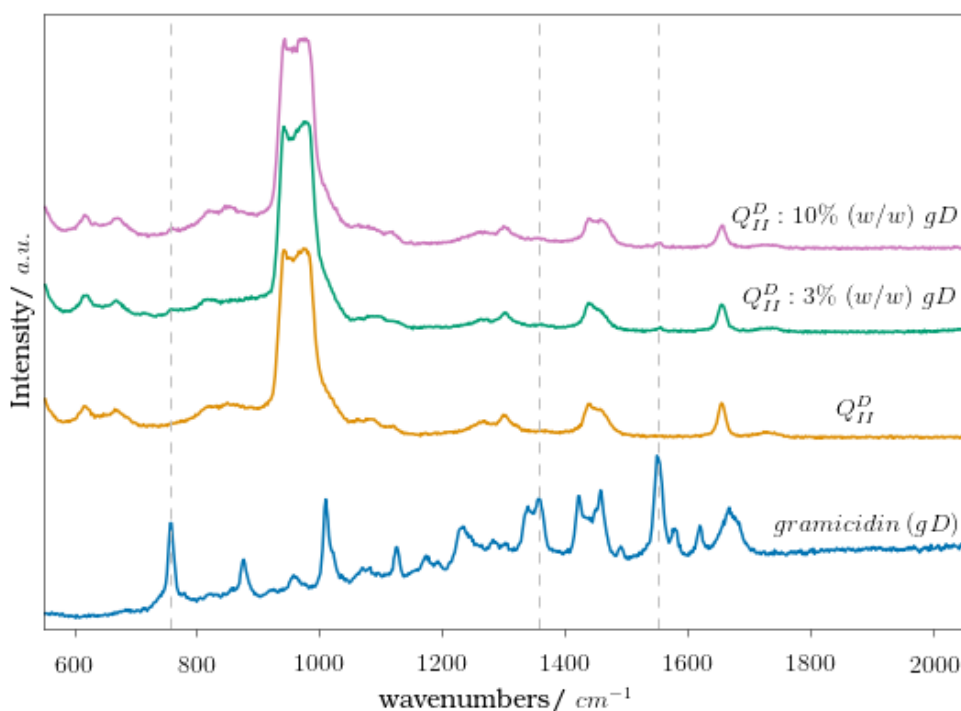


Figure 5.4: Raman of spin coated films of gramicidin in Cithrol. Characteristic gramicidin vibrational modes are noted.

phase. Gramicidin was mixed with molten Cithrol to a desired concentration. As molten Cithrol is viscous, the actual concentration was confirmed by weight before the mixture was dissolved in 50 % (w/w) ethanol. The gramicidin/Cithrol solution was mixed with glycerol dissolved in 50 % (w/w) ethanol in a 70/30 (v/v) ratio. The mixed solution was then spin coated onto a silicon wafer in a three spin-cycle method. Deposition was at 1000 rpm for 20 s, drying at 1500 rpm for 60 s then final 6000 rpm for 60 s. Raman spectra were then taken between the wavenumbers 550 - 3200 cm^{-1} .

As Figure 5.4 shows gramicidin signals can be distinguished from the $\text{Q}_{\text{II}}^{\text{D}}$ phase in a thin film. The bands highlighted are those for the Amide II at 1550 cm^{-1} , the Amide I bands at 1350 cm^{-1} , and the band at 760 cm^{-1} . As expected the glycerol present within the thin film does not have a separate signal due to the corresponding signal from the glycerol head group of monoolein. The large doublet at 950 cm^{-1} and 970 cm^{-1} is due to the silicon substrate. The signal from gramicidin is less intense and other bands were not able to be distinguished from the $\text{Q}_{\text{II}}^{\text{D}}$ phase than in the bulk seen in Figure 4.12. However this was expected as the spin coated films are much thinner than the capillary coatings. The ability to distinguish gramicidin from the Q_{II} phase of monoolein in a thin film is indicative that the incorporation

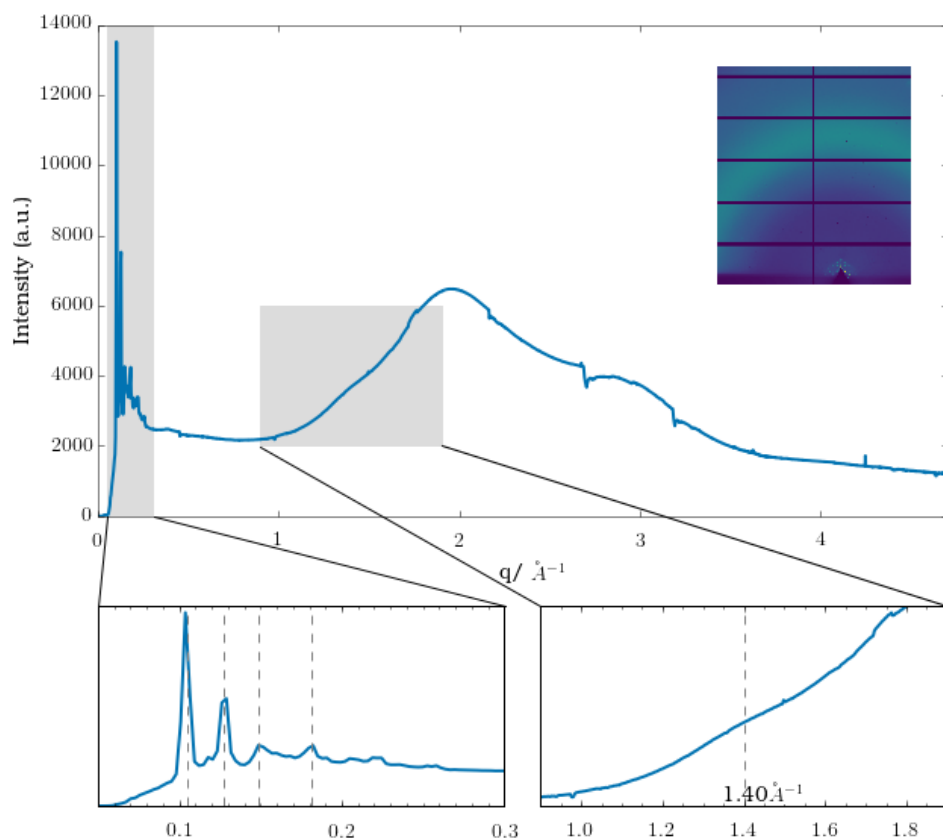


Figure 5.5: A 5 % (w/w) gramicidin in Cithrol spin-coated with 30 % (v/v) glycerol. The thin film was Q_{II}^D phase with a lattice parameter of 84\AA and orientated in the $[1,1,1]$ direction. The large WAXS peak was from the absorption of water in the high humidity ($<95\%$ RH) environment.

of additives to the Q_{II} phase via aqueous solution, as discussed in Chapter 4 (pg. 63), can be monitored via Raman in orientated thin films.

5.2.3 GISAXS-GIWAXS of Gramicidin

Multiple experiments were attempted to perceive the possible GIWAXS signal from gramicidin at 1.37\AA^{-1} . Gramicidin was mixed with molten Cithrol then dissolved in 50 % (w/w) ethanol. The solution was mixed with glycerol dissolved in 50 % (w/w) ethanol in a 70/30 lipid/glycerol ratio then spin coated into a thin film. Deposition was at 1000 rpm for 20 s, drying at 1500 rpm for 60 s then final 6000 rpm for 60 s. The wafers were then placed on the i07 beamline at Diamond Light Source, UK.

Firstly the simultaneous GISAXS-GIWAXS pattern of a Q_{II}^D phase containing gramicidin was confirmed. Figure 5.5 shows the diffraction pattern of 5 % (w/w) gramicidin in the Q_{II}^D phase. The lattice parameter in high humidity, $<$

95 % RH, is 84 Å. Before the anisotropy of the WAXS signal was investigated, confirmation of a peak from the gramicidin at 1.37 Å^{-1} was sought. However the absorption of water at 2.0 Å^{-1} ? obscures both the 1.4 Å^{-1} lipid peak and any possible 1.37 Å^{-1} peak. The experiments were conducted before the completion of the humidity control systems discussed in Chapter 6 (pg. 109) and as such only two humidities were available, high > 95 % RH or low < 25 % RH. Unfortunately at low humidity, the gramicidin containing films contained the H_{II} phase as well as the Q_{II}^D phase. Therefore it was decided that until humidity control was achieved, analysing the WAXS signals of gramicidin containing Q_{II}^D phases was of little value but the presence of the β helix peak might be confirmed in the H_{II} and L_α phases.

5.2.4 Gramicidin in the H_{II} Phase

To investigate the possibility of a gramicidin WAXS peak at 1.37 Å^{-1} at lower humidities but with higher concentrations of gramicidin the lipid DOPE was used. DOPE forms the H_{II} phase in excess water conditions at room temperature? and therefore the addition of gramicidin would not effect the phase behaviour, regardless of humidity. Gramicidin and DOPE were dissolved in 70 % (w/w) ethanol then mixed with glycerol in 70 % (w/w) ethanol. 5 %, 10 %, and 30 % (w/w) gramicidin in DOPE were created. As Figure 5.6 shows there is no discernible peak from gramicidin at 1.37 Å^{-1} even at 30 % (w/w) gramicidin. It is mostly likely that either the peak at 1.37 Å^{-1} is indiscernible from the lipid peak or that it does not exist within the H_{II} phase due to too weak a signal. To determine which was the case, the superstructure of gramicidin in the L_α phase was confirmed and the WAXS signal investigated.

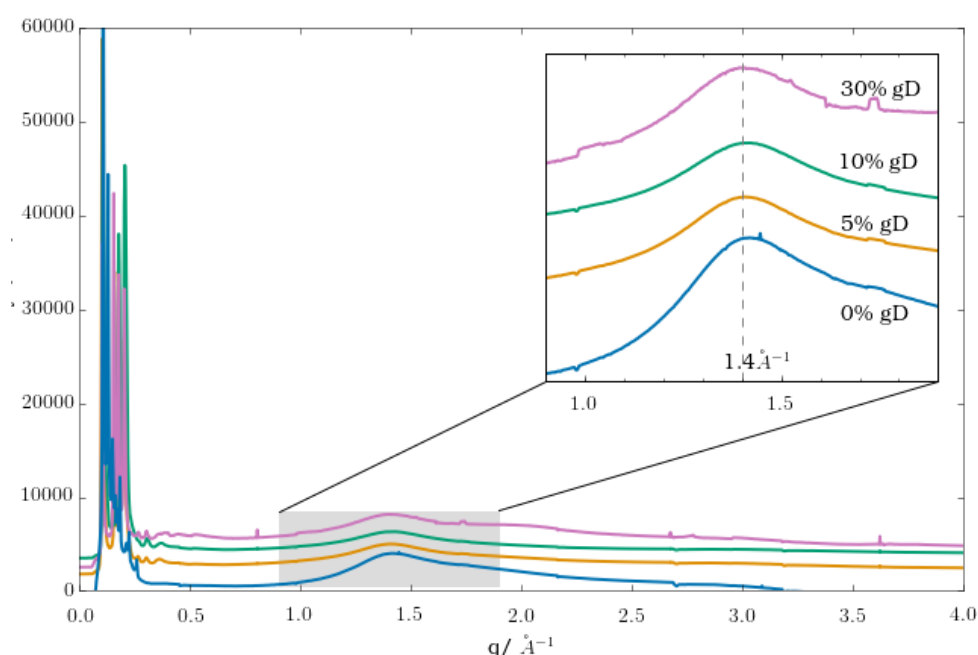


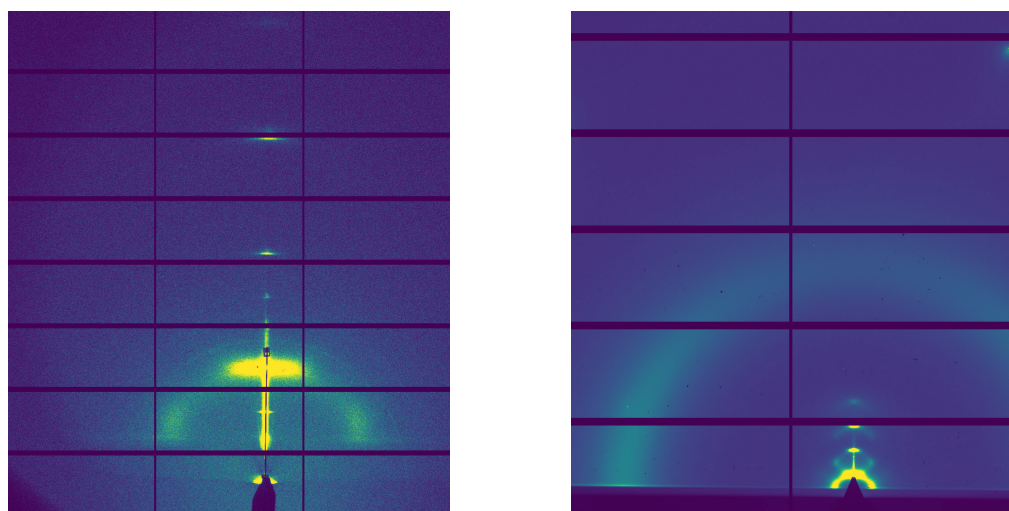
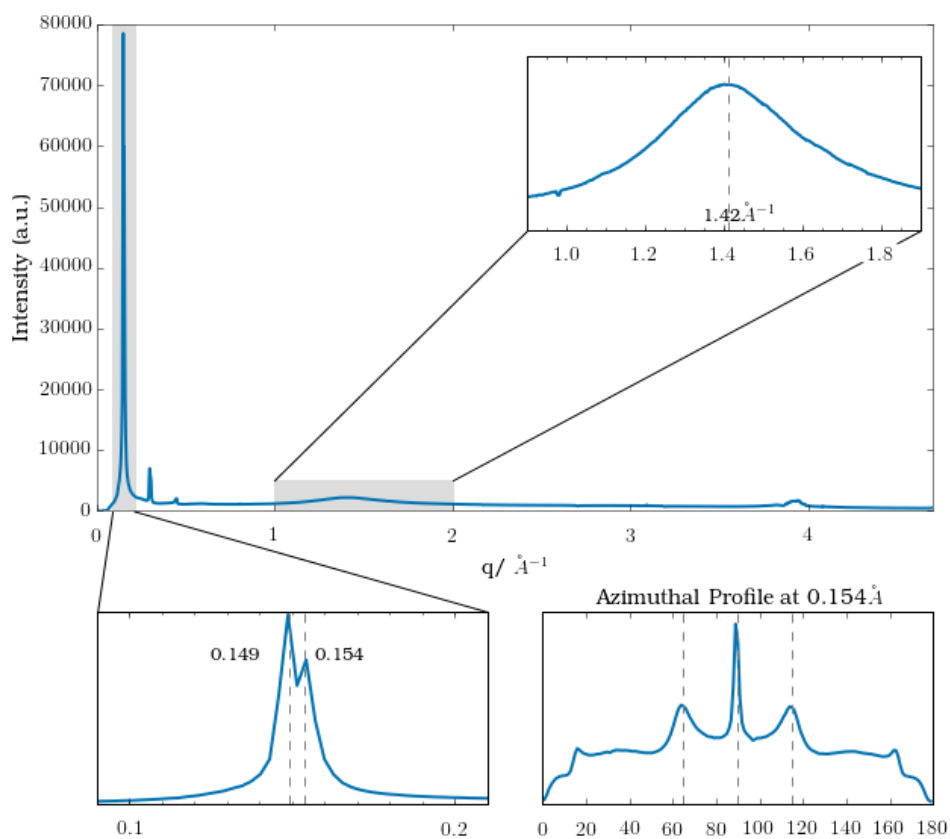
Figure 5.6: Gramicidin in DOPE of H_{II} phase with lattice parameter 70 Å. The lipid peak at 1.4 Å^{-1} is marked. The small peak around 1.7 Å^{-1} was determined to be from an artefact and present in every sample

5.2.5 Superstructure in the L_{α} Phase

The superstructure of peptides in the L_{α} phase has been previously studied using GIWAXS. A lateral correlation of membrane inserted structures such as the pore arrangements can be detected and characterised from superstructure peaks at low q . Gramicidin's superstructure was probed within monoolein L_{α} bilayers using GISAXS-GIWAXS and the presence of a WAXS peak investigated. 30 % (w/w) gramicidin was mixed with molten Cithrol and dissolved in 50 % (w/w) ethanol then spin coated onto a silicon substrate. The SAXS pattern was taken at low humidity (< 25 % RH) and a L_{α} phase is formed with a lattice parameter of 41 Å.

As Figure 5.7 shows, a peak due to the gramicidin superstructure in the monoolein bilayer can be seen at $q = 0.154 \text{ Å}^{-1}$ at a 25° from vertical. The gramicidin superstructure was not seen in L_{α} bilayers of DOPE with a lattice parameter 70 Å. This is potentially due to too great a hydrophobic mismatch. The peak position gives to rough estimate of the outer pore size of 41 Å which is consistent of a hexamer with limited size. Further analysis of the hexamer size was not the focus of this study but the process has been described by Constantin et al. for the peptide alamethicin.

As expected in the L_{α} bilayers, the result of the inclusion of gramicidin can

(a) L_α : Cithrol(b) L_α :30% gramicidin in Cithrol

(c) 30 % gramicidin 1D pattern

Figure 5.7: (b) 30 % (w/w) gramicidin in Cithrol was spin-coated and a L_α phase of lattice parameter 41.3 Å was formed at low humidity (<25 % RH). The off axis diffuse peak at q 0.154 Å⁻¹ is due to Gramicidin pores. A comparison of the L_α phase is provided in (a)

also be seen in the shift of the WAXS lipid peak from 1.4 \AA^{-1} to 1.42 \AA^{-1} . The restriction of the configuration of lipid chains around the peptide results in some lipid ordering[?] which causes the peak shift. However the peak from the gramicidin cannot be separately discerned. Therefore for future work, either the signal for gramicidin must be increased, such as by the inclusion of thallium ions,^{??} or a new system investigated.

5.3 Monoolein, Monopalmitin, Cholesterol

The second additive system investigated was the model membrane system monoolein, monopalmitin and cholesterol with a potential phase separation of the liquid peaks. The liquid peaks would have a WAXS signal the L_o at 1.5 \AA^{-1} and the L_d at 1.4 \AA^{-1} . A Q_{II} phase can be created with high cholesterol content upon the addition of both cholesterol and the saturated lipid monopalmitin, where upon the cholesterol should preferentially phase separate with monopalmitin and form a segregated L_o phase.

5.3.1 Orientated GISAXS

A Q_{II}^D phase with high cholesterol content was required. Monoolein, monopalmitin, and cholesterol in different molar ratios were dissolved in 80 % (w/w) ethanol and mixed with glycerol dissolved in 80 % (w/w) ethanol in a 70/30 (v/v) lipid/glycerol ratio. A 70/30 (v/v) lipid/glycerol ratio was used as the phase behaviour of monoolein dominates so the film will be in the excess water condition. The resulting solutions were then spin coated onto a silicon wafer in a three spin-cycle method. Deposition was at 1000 rpm for 20 s, drying at 1500 rpm for 60 s then final spin 6000 rpm for 60 s. Monoolein, monopalmitin, and cholesterol in a 80:10:10 molar ratio produced a Q_{II}^D phase in excess water conditions, as shown in Figure 5.8. The Q_{II}^D phase was formed at 50 % humidity with a lattice parameter 89.6 \AA with a uniaxial orientation in the $[1,1,1]$ direction.

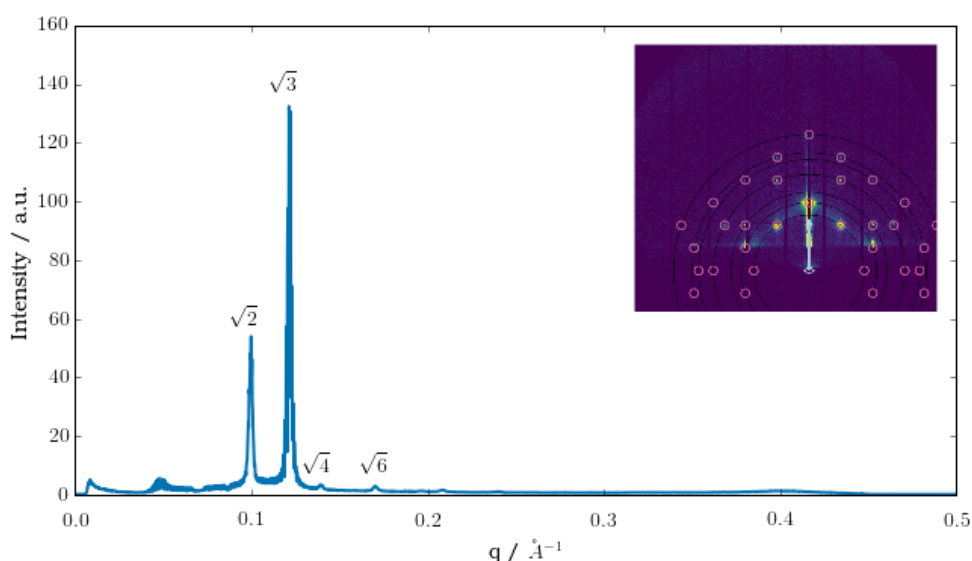


Figure 5.8: Q_{II}^D monoolein, monopalmitin, and cholesterol in a 80:10:10 molar ratio spin coated with 30 % (v/v) glycerol with a lattice parameter of 89.6 Å and a uniaxial orientation of [1, 1, 1].

5.3.2 GIWAXS

Multiple experiments were attempted to see the possible phase separation of the tertiary system of monoolein, monopalmitin, and cholesterol at a molar ratio of 80:10:10. For the Q_{II}^D phase monoolein, monopalmitin, and cholesterol were dissolved in 50 % (w/w) ethanol and mixed with glycerol dissolved in 50 % (w/w) ethanol in a ratio of 70/30 lipid/glycerol. The solution was then spin coated onto a silicon wafer in a three spin-cycle method. Deposition was at 1000 rpm for 20 s, drying at 1500 rpm for 60 s then final spin 6000 rpm for 60 s.

As Figure 5.9 shows, a Q_{II}^D phase of lattice parameter 89.6 Å formed with a uniaxial orientation of [1, 1, 1]. At low humidity (< 25 %) a WAXS peak for the L_d phase is present, however there is no evidence of a peak for the L_o phase. If there had been phase separation, the L_d/L_o chain correlation peaks would have been able to be separated.[?] There is also no evident anisotropy in the WAXS. Therefore there is no way to determine the formation or localisation of the L_o phase in the Q_{II}^D phase using GIWAXS.

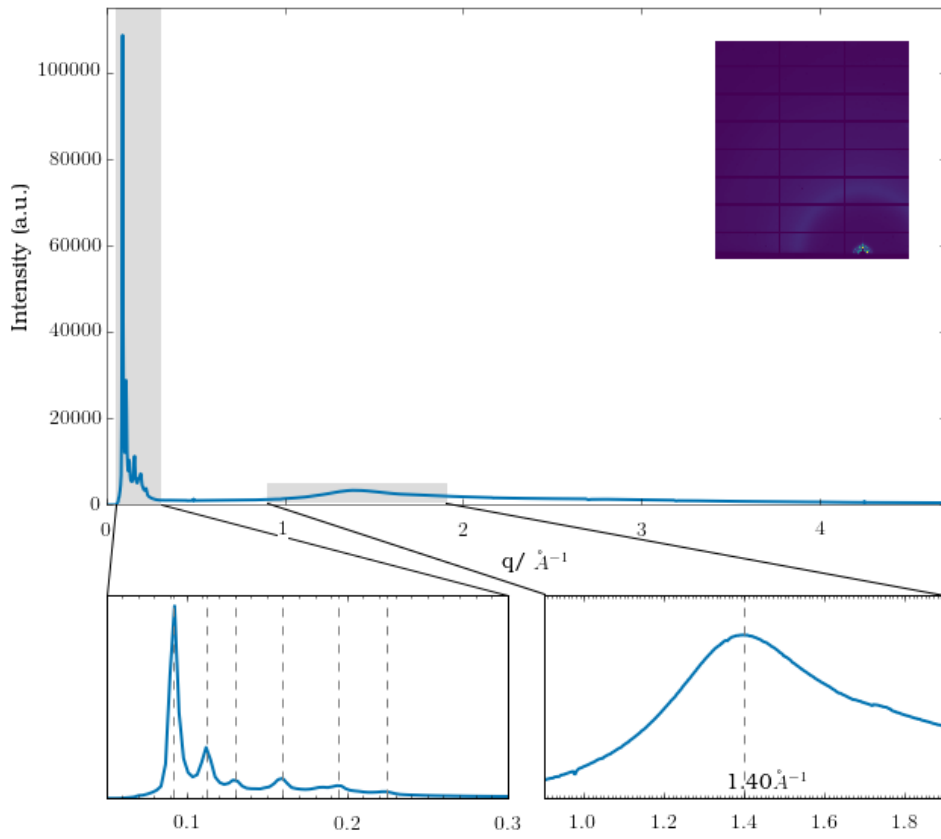


Figure 5.9: Q_{II}^D monoolein, monopalmitin, and cholesterol in a 80:10:10 molar ratio spin coated with 30 % (v/v) glycerol with a lattice parameter of 89.6\AA and a uniaxial orientation of $[1,1,1]$.

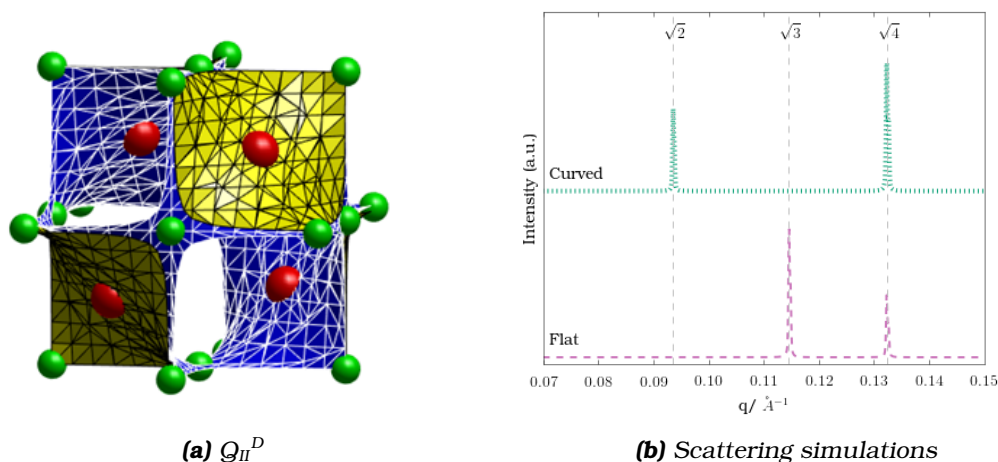


Figure 5.10: Scattering simulation done in VESPA[?] of the flatter (large red balls) and the more curved (small green balls) regions of the bilayer. A visualisation of the Q_{II}^D phase is provided, (a).

5.4 GISANS

After the failure of seeing anything in the wide angle a new method was devised to investigate preferential partitioning in the Q_{II} phases. Recently in 2016 van 't Hag et al.[?] published that by contrast matching lipids, the preferential partitioning of the hydrophobic peptide WALP21 was investigated. The host lipid signal of the bulk Q_{II} phase gel was contrast matched to D_2O , leaving only the SANS signal from the peptide remaining. It was found that the peptide WALP21, and in later work the peptide gramicidin,[?] do not preferentially partition within the Q_{II}^D phase. By combining this method of contrast matching lipids with the method of creating uniaxially orientated lipid thin films, a GISANS experiment was created to investigate the partitioning of lipids within a Q_{II}^D phase. The use of orientated Q_{II}^D phases should drastically reduce the signal to noise ratio[?] and allow the use of very small samples.

5.4.1 Prediction: Curved or Flat Regions

Scattering simulations, shown in Figure 5.10, show that the intensity ratio of the first two Bragg reflections will give information of the preferential locations of guest biomolecules. If guest biomolecules in perfectly contrast matched systems were to sit in the flatter regions of the bilayer than the scattering will be dominated by the second $\sqrt{3}$ Bragg reflection rather than the first $\sqrt{2}$ Bragg reflection. If the guest biomolecules were to sit in the more curved regions of the bilayer than the opposite would be true and the first $\sqrt{2}$ Bragg reflection will dominate over the second $\sqrt{3}$ Bragg reflection.

5.4.2 Methodology

The system investigated was the monoolein, monopalmitin and cholesterol at a molecular ratio of 80:10:10. Gramicidin, at low concentrations, has very recently been found to not preferentially partition by van t'Hag et al.[?] using SANS therefore it was not investigated.

Deuterated d-monoolein was synthesised by Dr. Tamin Darwish at ANSTO, Australia and was used as received.

Monoolein, d-monoolein, monopalmitin, and cholesterol were each dissolved in 80 % (w/w) ethanol. These ethanol solutions were then mixed with glycerol or d-glycerol dissolved in the same concentration of ethanol in a ratio of 60/40 (v/v) total lipid to glycerol. A higher glycerol content over the excess water boundary was chosen as there is a small difference in hydration between hydrogenated and deuterated samples.[?] The mixed solution was then spin coated onto a silicon wafer in a three spin-cycle method. Deposition was at 1000 rpm for 20 s, drying at 1500 rpm for 60 s then final 6000 rpm for 60 s. The wafer was then placed on the SANS2D beamline at ISIS Neutron and Muon Source, UK in a humid D₂O atmosphere. The D₂O atmosphere was created by using the Raspberry Pi humidity control described in Chapter 6. The maximum recorded humidity was only 80% RH despite the wet line running on full and the dry line being off. This was probably due to the large chamber size as well as the differences in vapour pressure for H₂O and D₂O.

5.4.3 Orientated GISANS of Monoolein

To begin with, a GISANS pattern from just the host lipid was acquired. Monoolein was spin coated with d-glycerol in 80 % ethanol. As Figure 5.11 shows, it formed a Q_{II}^D phase of lattice parameter 94 Å and uniaxial orientation of [1,1,1]. To our knowledge, this is the first orientated lipid GISANS diffraction pattern. Neutrons go through silicon so both sides of the diffraction pattern can be seen despite the GISANS set-up. Unfortunately this leads to the splitting of reflections in the generated 1D diffraction pattern due to the distortion in reflection position from top half and the bottom half of the diffraction pattern.

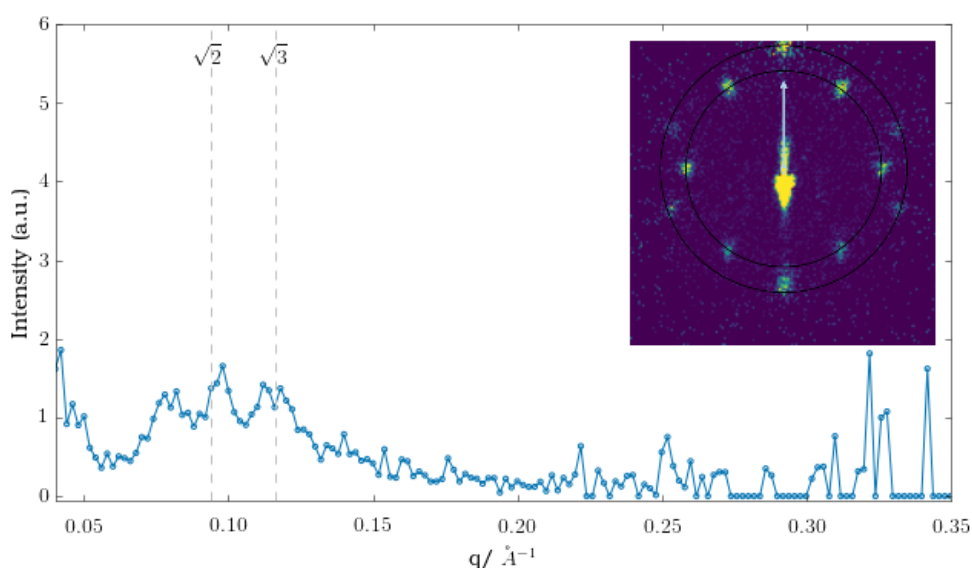


Figure 5.11: 2D GISANS pattern of monoolein spin coated with d-glycerol/h-glycerol in a D_2O environment. The glycerol ratio was chosen to contrast match D_2O . The lattice parameter is 94 \AA and calculated from the middle of the second reflection rather than the split first reflection.

5.4.3.1 Successful Contrast Matching of d-Monoolein

Next, the contrast matching of the lipid film to the D_2O environment was confirmed. Both d-monoolein and d-glycerol were successfully contrast matched. The percentages for the contrast matching can be found in the Techniques and Methods 2.3.2.4 (pg. 39) and were calculated using the equations found in van 't Hag et al.⁷ Figure 5.12 shows the successful contrast matching of a d-monoolein and d-glycerol film in a 60/40 (v/v) ratio. As the film was spin coated in a normal H_2O atmosphere, there was a some doubt that the film would not be perfectly contrast matched. However as the thinness of the film would suggest the diffusion exchange proved quick and the lipid film was successfully contrast matched. To check the lipid formed the correct phase, the film was placed in a H_2O atmosphere and a GISANS pattern acquired. The film was found to be a Q_{II}^D phase with a lattice parameter of 97 \AA . The successful contrast matching allowed for the isolating of the scattering contribution of the hydrogenated monopalmitin and cholesterol.

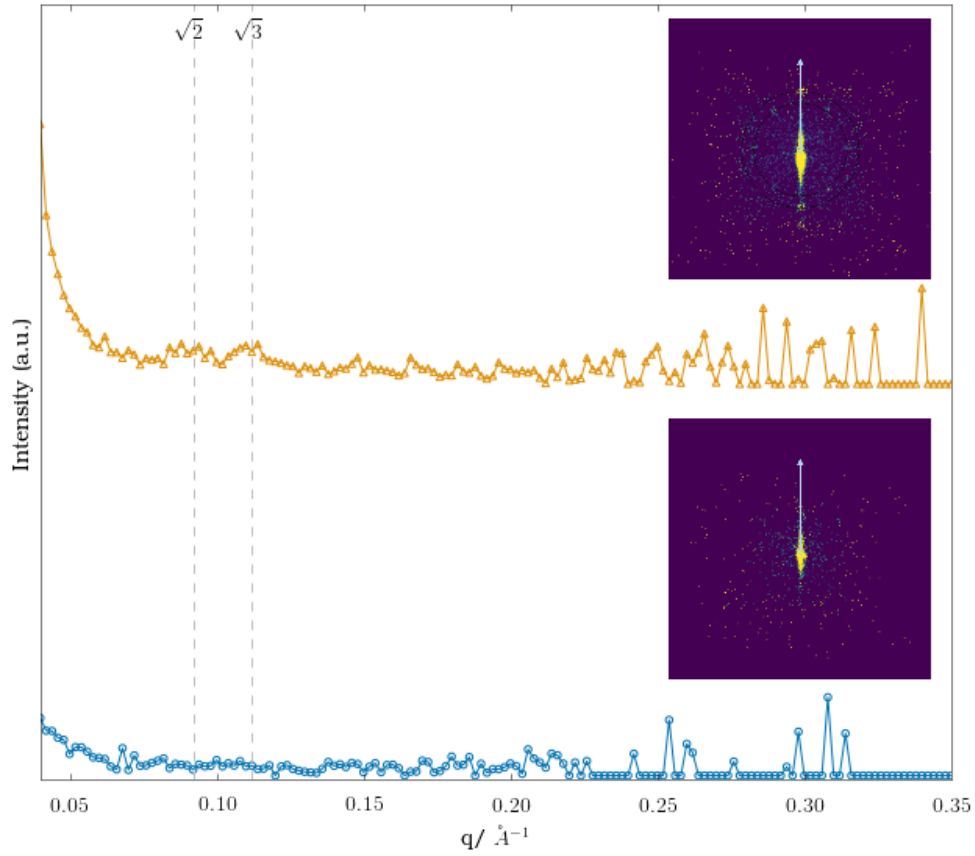


Figure 5.12: *d*-Monoolein was successfully contrast matched to D₂O (bottom). To check that *d*-monoolein formed the right phase, the wafer was put in a H₂O atmosphere (top). When no longer contrast matched the Q_{II}^D phase can be seen with a lattice parameter of 97 Å.

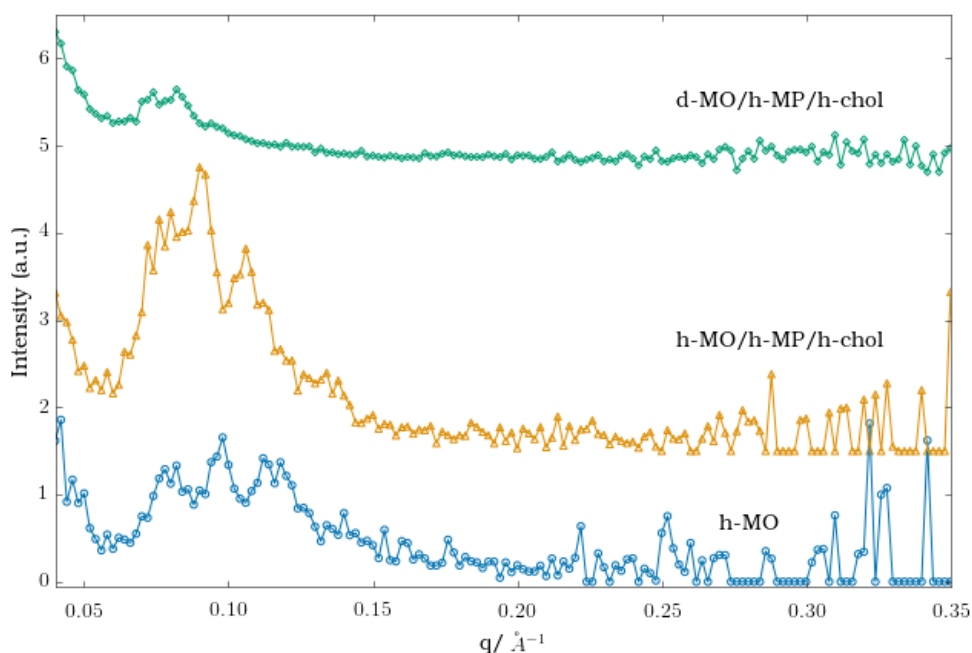


Figure 5.13: The 1D GISANS patterns of several spin coated thin films of lipid/glycerol mixtures. Despite the increase of signal to noise ratio from the orientated lipid film it is still hard to differentiate between the first and second reflections. Especially in the deuterated lipid sample where only one peak is visible. By contrast the peaks are quite distinguishable in the 2D patterns.

5.4.3.2 Signal to Noise of GISANS

The use of GISANS on domain orientated lipids means that the signal to noise ratio is reduced compared to SANS.[?] Figure 5.13 shows the 1D patterns of several of the films later discussed. For each a sample volume of 40 μL was spin coated which corresponded to a lipid content of 5 mg for each spin coated wafer. As deuterated lipid is very expensive this means that a lot more samples can be investigated. Of particular note is that even with the host lipid monoolein contrast matched out, monopalmitin and cholesterol produce enough signal in a sample for analysis into their position within the $\text{Q}_{\text{II}}^{\text{D}}$ phase.

5.4.4 Monoolein, Monopalmitin, Cholesterol

To view the preferential location of the guest biomolecules of monopalmitin and cholesterol, comparison films using h-monoolein and d-monoolein were created with h-monopalmitin and h-cholesterol in a 80:10:10 molar ratio. The resulting diffraction patterns are shown in Figure 5.14. For monopalmitin and cholesterol in the contrast matched d-monoolein the only signal in Figure 5.14b is from them and there is still a noticeable $\text{Q}_{\text{II}}^{\text{D}}$ phase of [1,1,1]

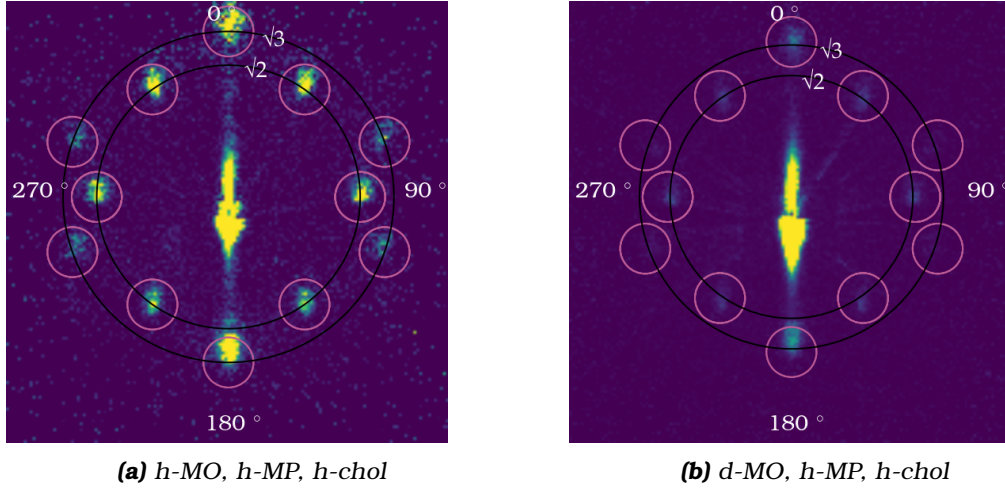


Figure 5.14: Monoolein(MO), Monopalmitin (MP), and cholesterol(chol) in a 80:10:10 molar ratio dissolved in 80 % (w/w) ethanol and mixed d-glycerol in 80 % (w/w) ethanol in a 60/40 (v/v) ratio. The d-MO and d-glycerol was contrasted matched to D_2O .

uniaxial orientation. The diffraction patterns were not taken over the same time frame and not of absolute intensity so analysis was done to normalise the signals from each Bragg reflection.

5.4.4.1 Normalisation of the $\sqrt{3}$ to the $\sqrt{2}$ reflection

First the intensities of each peak were recorded by taking a value of *area * intensity* of a box containing the reflection in ImageJ. An average value was calculated with standard deviation σ . The weighted mean, Equation 5.1, was then generated for the two Bragg reflections.

$$weighted\ mean = \frac{\sum(Intensity * Area)/\sigma^2}{\sum 1/\sigma^2} \quad (5.1)$$

The $\sqrt{3}$ reflections were split into two categories. The on axis (0° and 180°) peaks were six times the intensity than the four other peaks at 71° , 109° , 251° , and 289° and as such they were separated. The full table of intensities can be found in Appendix C.

To separate the contributions from the flatter regions from the more curved regions the intensity of the $\sqrt{3}$ reflections was normalised to the $\sqrt{2}$, Equation 5.2.

$$normalised\ intesity = \frac{weighted\ mean\ \sqrt{3}}{weighted\ mean\ \sqrt{2}} \quad (5.2)$$

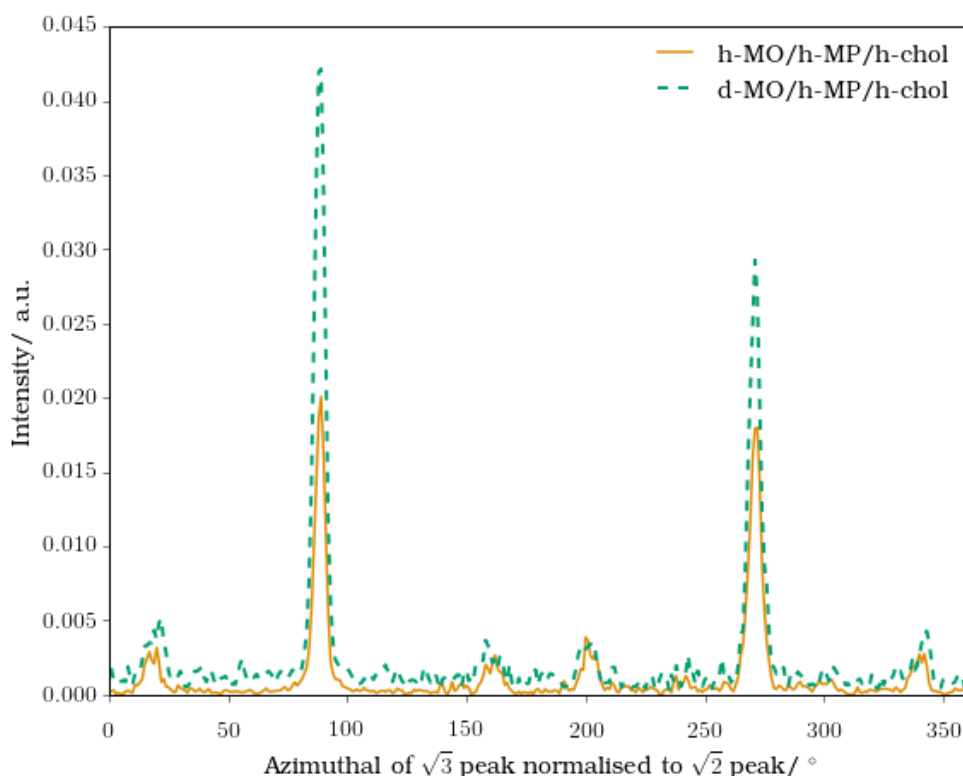


Figure 5.15: Azimuthal profile of the $\sqrt{3}$ reflection normalised to the $\sqrt{2}$ reflection. The difference in intensity between the deuterated and non-deuterated samples can be clearly seen in the on axis peaks.

Graphically this can be seen in Figure 5.15 where the azimuthal angle around the $\sqrt{3}$ Bragg reflection was normalised to the $\sqrt{2}$. This clearly shows that for the d-monoolein sample the contribution from the $\sqrt{3}$ Bragg reflection is greater than that of the h-monoolein sample. This corresponds to the prediction in which if monopalmitin and cholesterol are sitting in the flatter regions the intensity of the $\sqrt{3}$ should be greater relative to the $\sqrt{2}$. As the only signal in the deuterated sample comes from the monopalmitin and cholesterol it can be stated that these biomolecules have partitioned to the flatter regions of the bilayer.

5.4.5 Dynamic Non-contrast Matching

To further validate the results, a process I have called dynamic un-contrast matching was undertaken. This is where the d-monoolein, monopalmitin, and cholesterol film is exposed to H_2O and a new diffraction pattern taken. This process takes advantage of the quick vapour exchange between D_2O and H_2O within the film. Though given the time constraints that were present in the experiment, I do not suppose that a full exchange was able to take place.

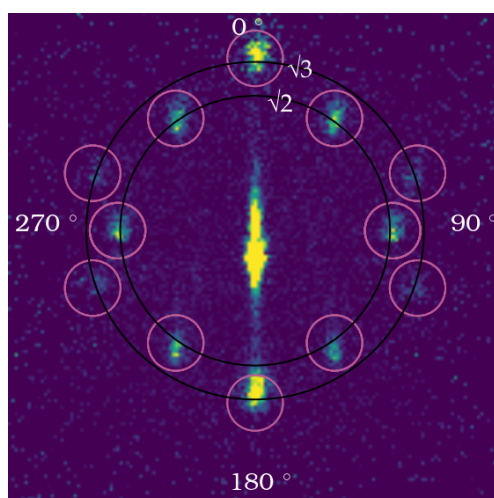


Figure 5.16: *d-MO/h-MP/h-chol* in a 80:10:10 molar ratio dissolved in ethanol and mixed with 30% (v/v) glycerol in ethanol solution in a H_2O environment

However as Figure 5.16 shows, with the lack of contrast matching there is a clear increase in intensity. The hypothesis is the difference in intensity relative to each Bragg reflection will decrease.

5.4.6 Monopalmitin and Cholesterol sit in the Flatter Regions of the Q_{II}^D Phase

Quantifying the ratio of Bragg reflections for all three samples gives Figure 5.17. The ratio of Bragg reflections is greater for the contrast matched monoolein system, which then decreases upon dynamic un-contrast matching. The decrease in reflection ratios upon the addition of H_2O further confirms that monopalmitin and cholesterol preferentially partition into the flatter regions of a Q_{II}^D bilayer.

Therefore monopalmitin and cholesterol within the Q_{II}^D phase of monoolein phase separate and preferentially locate at the flatter regions of the bilayer. This suggests that L_o/L_d phase separation takes place within the Q_{II}^D phase. The results shows how powerful a technique GISANS is with regards to investigating guest biomolecules within the Q_{II} phases.

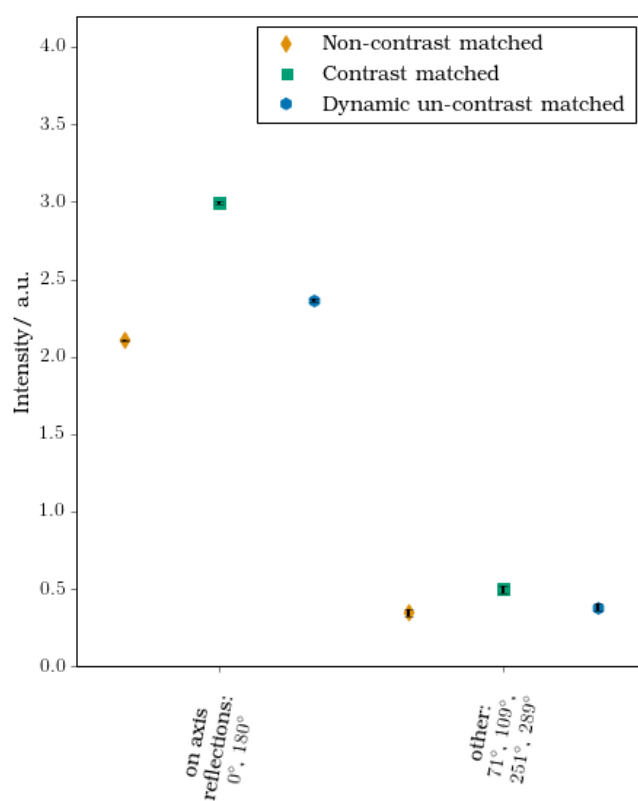


Figure 5.17: Normalisation of the $\sqrt{3}$ reflections to the $\sqrt{2}$ reflections. The on axis peaks are separated from the other $\sqrt{3}$ reflections due to the 6 times greater intensity. The ratio of intensity is greater for the contrast matched system.

5.5 Conclusions

Currently neither gramicidin nor L_o liquid separation can be seen in the WAXS of a Q_{II}^D phase. Although the formation of the gramicidin hexamer in a monoolein L_α phase has been confirmed.

The use of GISANS proves to be a promising technique to investigate the preferential partitioning within curved phases. Monopalmitin and cholesterol were found to localise within the flatter regions of a Q_{II}^D bilayer which is an indication of L_o phase separation within a Q_{II}^D phase. This was done by successfully contrast matching the host lipid monoolein to a humid D_2O environment. A process of un-contrast matching the lipid thin film, whereby the humid environment was swapped for H_2O , allowed further validation of the localisation within the Q_{II}^D phase.

5.6 Future Work

5.6.1 GIWAXS

Neither gramicidin nor the effect of cholesterol and monopalmitin could be perceived in the wide angle. Though no information was found about the partitioning of guest molecules within Q_{II} phases, each experiment revealed some shortcomings of the experimental design. Gramicidin on its own does not have a strong enough WAXS signal, even in concentrations which show the hexamer superstructure in the SAXS pattern. Gramicidin has a high affinity for binding two thallium ions[?] and work by Constantin et al[?] has shown that the addition of thallium can enhance the x-ray signal from gramicidin. Therefore it might be possible to increase the WAXS signal by introducing thallium ions into the experiment.

Another shortcoming is the previous lack of reliable humidity control. With the creation of both the Raspberry Pi system and the mass flow controller system (Chapter 6 pg. 109) the peak due to the absorption of water could be controlled so that it doesn't overwhelm the WAXS.

The 80:10:10 molar ratio of monoolein, monopalmitin, and cholesterol was settled on for the high cholesterol content that formed the Q_{II}^D phase in excess water conditions. However the liquid phase separation of this system has not yet been confirmed. Some attempt to investigate the phase separation in the L_α phase was made however a GIWAXS pattern including the lipid peak has not yet been achieved. It would be my suggestion to confirm the

liquid phase separation in the L_α phase before further investigation of this system using GIWAXS.

5.6.2 GISANS

5.6.2.1 Other Phases

Given the success of GISANS for probing the preferential location of monopalmitin and cholesterol within the Q_{II}^D phase, this could be extended to other Q_{II} phases. At lower hydration monoolein, monopalmitin and cholesterol form the Q_{II}^G phase, and with the control of the humidity within the chamber a phase transition is possible. Different lipid combinations will also form different phases and the localisation of these lipids could be investigated.

The contributions of monopalmitin and cholesterol could be separated by contrast matching out both monoolein and one of these lipids. The signal left would be of the other lipid, though the experimental time may need to be extended due to the reduction of hydrogenated material.

5.6.2.2 Other Biomolecules

The incorporation within the Q_{II} phase of other guest biomolecules should be investigated. Molecules which are stable in organic solvents can be spin coated with monoolein or phytantriol. Phytantriol as another Q_{II} phase forming lipid has also been successfully fully deuterated.[?] Some suggestions would be detergents used for *in meso* crystallisation,^{???} or molecules of interest in drug delivery using the Q_{II} phase.^{??}

5.6.2.3 Addition of Aqueous Components

In Chapter 4.5 the addition of the LDAO to an aligned Q_{II}^D phase was proved via SAXS from the phase change to the Q_{II}^P phase. This addition of molecules, specifically proteins, to orientated phases could be extended with contrast matched Q_{II} phases and GISANS to investigate the preferential localisation of membrane proteins or other biomolecules within aqueous solutions.

Recently at the ESRF, France, we succeeded in incorporating OmpF using the sample cell created by Robert Barker (University of Kent). A GISANS diffraction pattern was collected from OmpF in a contrast matched monoolein Q_{II}^P phase and analysis is currently ongoing. The concentration of OmpF used was 0.04 mg mL^{-1} and volume was 1.5 mg. For *in meso* crystallisation a concentration greater than 25 mg mL^{-1} is suggested. This means that experiments to determine the preferential localisation of the membrane protein

within a Q_{II} phases would not be as limited like crystallisation experiments due to concentration requirements.

The experimental set-up involved soaking the spin coated film of contrast matched lipid in OmpF hydrogenated aqueous solution before flushing with D_2O to provide the contrast matching. With the successful GISANS from the addition of aqueous biomolecules this could be extended to other membrane proteins such as enzymes used in biosensors.^{???} The interaction of SMALPS with the Q_{II}^D phase could further be investigated including the possibility of lipid exchange[?] and the mechanism of protein incorporation[?] as the components which are not incorporated into the bilayer would be flushed away.

Chapter 6

Humidity Control

Humidity is important to everyday life, for example in contexts such as in types of agriculture or the production of rust. As a measure of the water content in air, controlling humidity is relevant in a variety of scientific processes. Examples include the manufacturing of silicon chips,[?] the degradation and thus restoration of canvas paintings,[?] the electrical performance of semi-conductors,[?] the efficiency of fuel cells,[?] the production of polymer films,[?] and the growth of fungus.[?] Essentially any system studied or material made that is susceptible to dehydration or water uptake will require the need for precise control of humidity.

Many academic research groups, for whom humidity control may be crucial to their research, tend to create in house systems or work arounds for their specific requirements. While it is certainly possible to buy a neatly packaged commercial humidity control system, it can come at a significant cost of more than £10,000.[?] In-house systems can range from complex environment chambers^{??} to simple salt solutions,[?] such as those famously used by Rosalind Franklin to find the hydrated structure of DNA.^{??}

Here I present two separate automated humidity control systems. The first is a low cost, portable, chamber independent humidity control system powered and controlled from a Raspberry Pi which can be used in multiple environments and has no need for calibration to a specific chamber or environment with each use. The second is a fully automated system calibrated to a chamber for use at Diamond Light Source with different gases. The chamber was designed for use in GISAXS experiments. The control systems were successfully used in the GISANS in Chapter 5.4 (pg. 97) and other GISAXS experiments on lyotropic lipid systems in this thesis.

6.1 Relative Humidity

Humidity refers to the amount of water vapour present in the air. It can be measured on a variety of scales; absolute, relative, or specific humidity. The humidity sensors discussed below all operate using relative humidity (RH). Relative humidity is the ratio of partial pressure of water vapour in a specific volume p_{H_2O} , to the partial pressure of water vapour in the air above a body of pure water at equilibrium $p_{H_2O}^o$ for any given temperature.

$$RH \% = \frac{p_{H_2O}}{p_{H_2O}^o} * 100 \quad (6.1)$$

6.2 First Prototype: Manual Humidity Control

My first attempt at creating a humidity controlled system, which highlighted the need for automated humidity control, was directly related to experiments at Diamond Light Source on i22 for lipid thin film GISAXS. The requirements included remote viewing of the humidity, a chamber for a helium atmosphere, and some sort of variable humidity. With this in mind a hand-held humidity and temperature sensor was purchased from Maplin. For the chamber a rectangular screw top box had holes strategically drilled into it. A picture of the set up can be seen in Figure 6.1.

The required humidity was created by mixing dry and "wet" helium. Wet helium was created by bubbling the gas through a water filled bubbler. The bubbler was simply made from a plastic 50 mL centrifuge tube filled with water and afterwards the two gas lines were connected to create a single input gas flow. The flow rate was achieved through manual control of the two flow taps. The humidity was monitored via a webcam.

The box proved adequate for purpose. Data was acquired that showed structural phase changes for lipid thin films such as that in Figure 6.2. However the humidity sensor kept timing out and turning off midway through a data run. This often led to a complete loss of humidity reading for an experiment or only a start and end estimate acquired once someone could re-enter the experimental hutch to turn on the sensor. This was particularly frustrating if phase changes occurred later in the data run where no specific humidity was able to be recorded. The manual control of the humidity also meant that only rough regions of humidity could be targeted as no calibration or quick change was possible. Therefore a reliable automated humidity control system was envisioned, for both use in the lab and at a national facility.

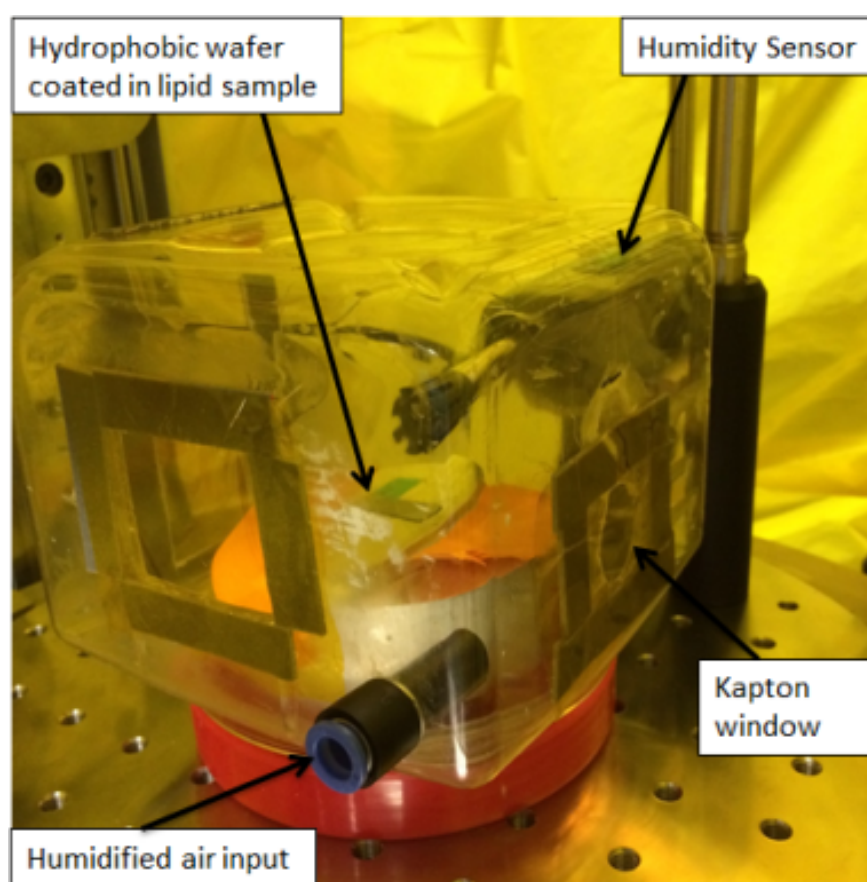


Figure 6.1: Photograph of the first iteration of humidity control used on the beamline i22 at Diamond Light Source. Consisting of a modified plastic box, the air input was at the bottom and the humidity sensor was placed just above the sample wafer. All other holes or windows were covered in Kapton.

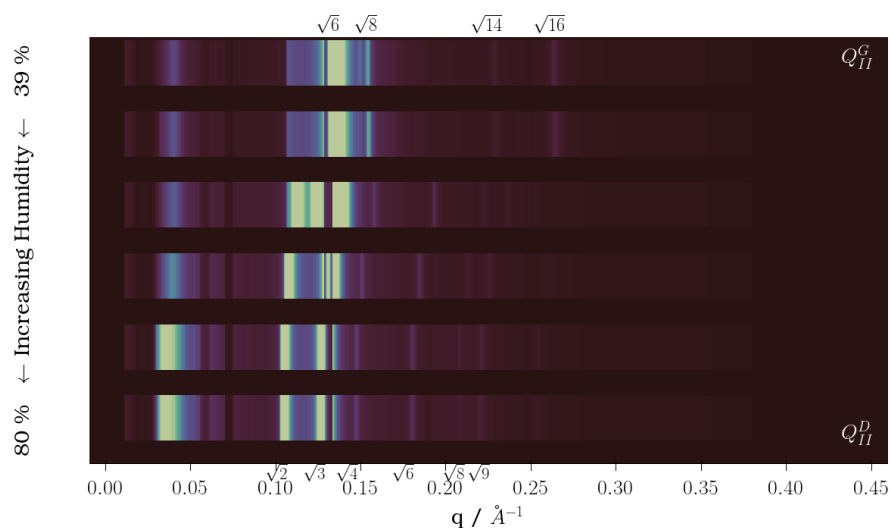


Figure 6.2: Thin film of Cithrol and glycerol mixture 80/20 (v/v) spin coated from 80 % (w/w) ethanol solution in which a phase change from Q_{II}^G to Q_{II}^D occurs with increasing humidity.

6.3 The Raspberry Pi System

It quickly became apparent that it would be prudent to separate the humidity control for different input gases. Humidity control requiring pressurised gas, such as helium or nitrogen, would be much more expensive. In part this is due to their reliance on mass flow controllers compared to humidity controllers which could be used with ambient air. For everyday lab use especially, it would be more practical for a variety of reasons not to rely on pressurised gases. As such a low cost, portable, humidity control system was developed by a Masters student, Ben Laurence, under my supervision. The advantages of the system were that it runs independent of a sample environment. Humidity control is achieved by two 5V pumps which are controlled and powered via a Raspberry Pi. The humidity is read by an Arduino which is also powered by the Raspberry Pi.

The Raspberry Pi system relies on digital pulses to turn on and off two fish tank air pumps, and has created humidities between 20 % and 95 % with an accuracy of ± 2 %. The system can maintain a constant relative humidity within 0.2 %. One air pump is run through desiccator beads and the other through a bubbler. The maximum and minimum humidity is in part limited by the size and sealing of the chamber or container the humidity is pumped into.

By no means the first digital humidity system to be created, we propose ours is one of the easiest to assemble and run. One such system previously developed[?] used a duty cycle of two fans to vary the humidity within a chamber. The average speed was controlled to give humidity control in one direction from the ambient room humidity. The direction of control was determined by either a container of water or a desiccator being placed in front of one of the fans. Our system instead uses low power (5V) fish tank air pumps to which are then pulsed to create either a dehumidifying or humidifying stream of air which is not attached to a specific chamber.

The control of the pumps relies on user input through a simple General User Interface (GUI). The GUI contains functions for live-plotting of the humidity and several ways to input a target humidity. The whole control system is written in Python and as such could be easily adapted or modified in future.

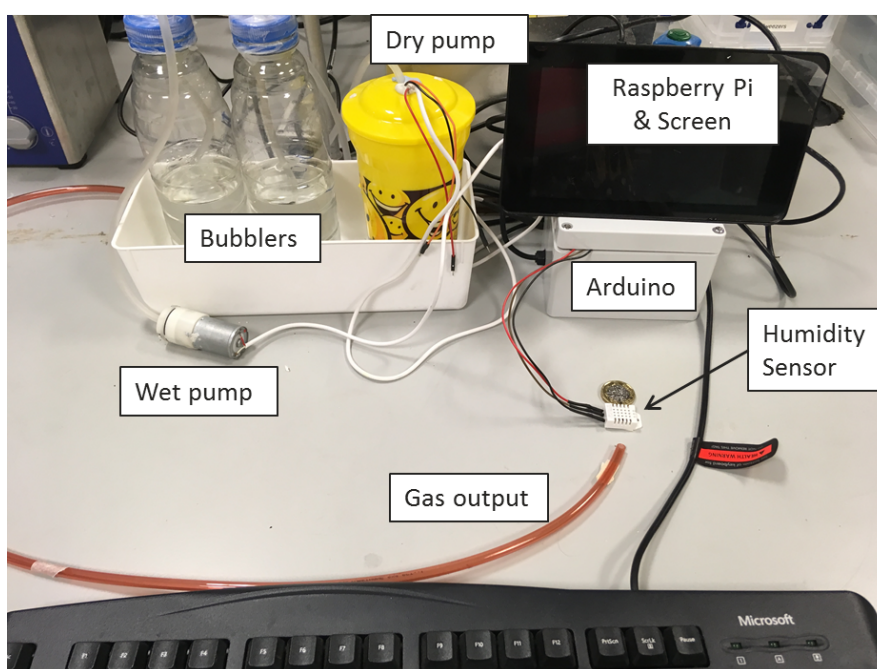
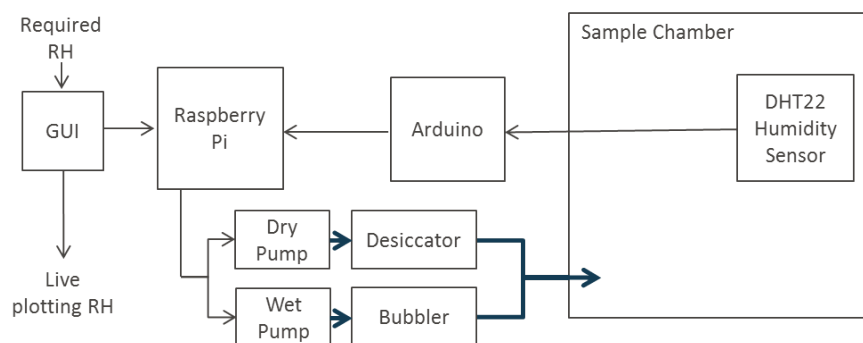


Figure 6.3: (above) Schematic of the Raspberry Pi set up. **(below)** Photograph of the Raspberry Pi set up. In this iteration to achieve the top range of higher humidities a second bubbler was added. The bright yellow cup contains desiccator beads and the dry pump. For scale a pound coin is next to the humidity sensor.

Component	Approximate Price
Raspberry Pi	£32
Arduino Uno	£18
Fish tank pumps x2 (with tubing and diffuser)	£22
Sensors (x2)	£6
Power supply	£8
500 ml Plastic bottle	£1
Cup for desiccator	£1
Dehumidifier beads	£2
Ethernet cable	£2
(if using RPi 1 or 2)	
Minor electronic components:	< £20
Transistors, stripboard, wires, connectors	
Total	< £112

Table 6.1: List of components and their prices as of 2018

6.3.1 Hardware

The total cost of building the humidity controller was £112 in 2018. Built on a Raspberry Pi 3 and an Arduino Uno, the cost of building the system will decrease with time as these components will become cheaper as newer versions become available. The system can also be run from a Raspberry Pi 1, 2 or any computer running Python.

6.3.1.1 Raspberry Pi and Arduino

A Raspberry Pi is a credit card sized single board computer originally designed to promote the study of computing. The first version was developed in 2012 bringing the power of 1990s computer at around £30. It had 2 USB ports, an Ethernet port and a Micro USB card slot, a 3.5 mm audio input, a HDMI input and 26 Graphical Purpose Input/Output (GPIO). It is these GPIOs, situated on an integrated circuit board, which send and receive data through digital pulses that have allowed the Raspberry Pi to become incredibly popular in both the scientific community and general populace. A huge range of devices can be controlled from the GPIO including LEDs, cameras,

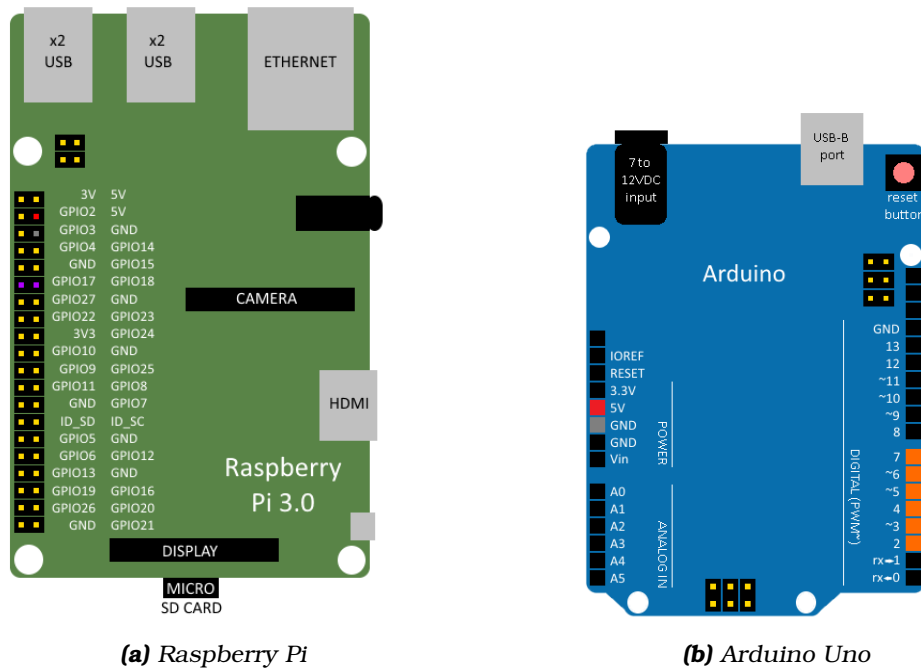


Figure 6.4: The design and set up of both the Raspberry Pi 3.0 and Arduino Uno. The pins used are coloured red (5V), grey (ground), purple for the fish tank pumps, and orange for the humidity sensors. The Raspberry Pi powers the Arduino Uno through a USB to USB-2 cable. The 5V and ground cables from the Arduino Uno are attached to the humidity sensor along with one cable into a digital pin.

simple motors, or in the case of the humidity controller: fish tank pumps.

The set-up in Figure 6.4 and the pricing in Table 6.1 corresponds to a Raspberry Pi 3.0, however the system can easily be adapted for future advancements should the positions of the GPIO change. Currently the system code assumes that the fish tank pumps are plugged into the GPIO 17 and 18 and the power for the pumps comes from the 5V and ground.

As well as the pumps, the Raspberry Pi is used to power the Arduino through a USB to USB-B cable. The Arduino is a microcontroller which can be programmed by a computer and is often used as an analogue to digital converter. The Arduino was used to control and read the humidity sensors. Currently the code assumes the sensors can be plugged into the digital ports 2 - 7. The chamber humidity readings come from ports 4, 5, 6, or 7.

6.3.1.2 Other components

The 5V pumps were mini silicone USB 5V aquarium fish tank air pumps from which the USB connector was removed and the neutral and positive wires exposed. The neutral wire was attached to a ground GPIO of the Raspberry Pi and the positive wire was soldered to a transistor before being attached to the 5V GPIO.

To create a wet line a 5V pump was connected to a bubbler. In keeping with the cheap theme, an ordinary drinks bottle was used with holes cut in the lid and a connector inserted. The input air tube had a diffuser at the end to ensure maximum humidity. To create a dry line a dehumidifier was made using a cheap plastic cup filled with desiccating beads and with the pump inserted. Small holes were drilled around the bottom of the bottle to allow for input air flow.

The DHT 22 sensors are humidity and temperature sensors with a humidity range of 0 to 100 % RH with an accuracy of 2-5 % and a temperature range of -40 to 80 °C with an accuracy of ± 0.5 °C. Currently the code can support a maximum of 6 humidity sensors wired into the Arduino; 4 for the chamber, 1 for the dry line, and 1 for the wet line. While not required for the code, which can function with as little as one humidity sensor in the chamber, the suggestion behind the wet and dry readings is to procure a maximum and minimum humidity value by placing these sensors in the bubbler/desiccator respectively. The chamber humidity is non-specific to chamber size so the idea of having more than one humidity sensor is to check the mixing and average humidities for a particular sample environment.

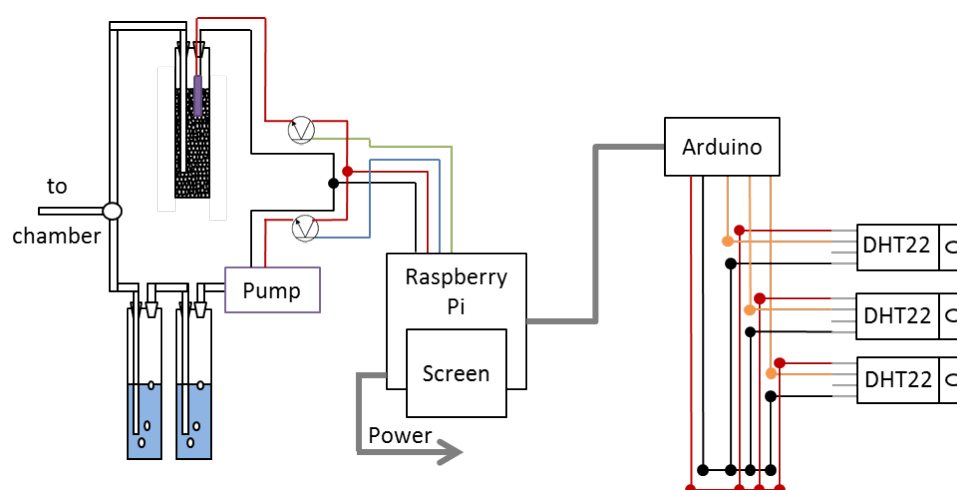


Figure 6.5: Full circuit diagram of the humidity control system. The positive (5V) wires are labelled in red and the neutral (ground) wires are labelled in black. The pumps are purple while the wires going to them from the pins are green and blue. The humidity sensors are connected to the Arduino by an orange wire into the digital pins.

A circuit diagram of the whole system can be found in Figure 6.5.

6.3.2 Software

The software set-up is included in the Python code. The full code to run the Raspberry Pi humidity control system can be found in Appendix E (pg.186). A brief summary of the process is described below.

The aim of the code is to ask for a target humidity and to achieve and maintain that humidity. This is done by reading the humidity before adjusting the pump ratios to then achieve the desired humidity. To begin with this is achieved by turning on one pump in the direction of humidity change. Within 5 % of the desired humidity a proportionality gain control loop kicks in to change the ratio of the wet and dry pumps. This means that within the minimum and maximum range of humidities the target humidity is achieved in between 2 and 5 minutes depending on the sample environment size and the humidity step change. There is also the ability to script a series of humidity changes at set time points or intervals into the program.

6.3.2.1 The GUI

Once loaded and running, user interaction with the python code is done through a GUI. Initially the program starts up by recording the humidities from the sensors and live plotting the data. Though dependent on the number of sensors connected, the live plotting can include a line for the wet, dry and

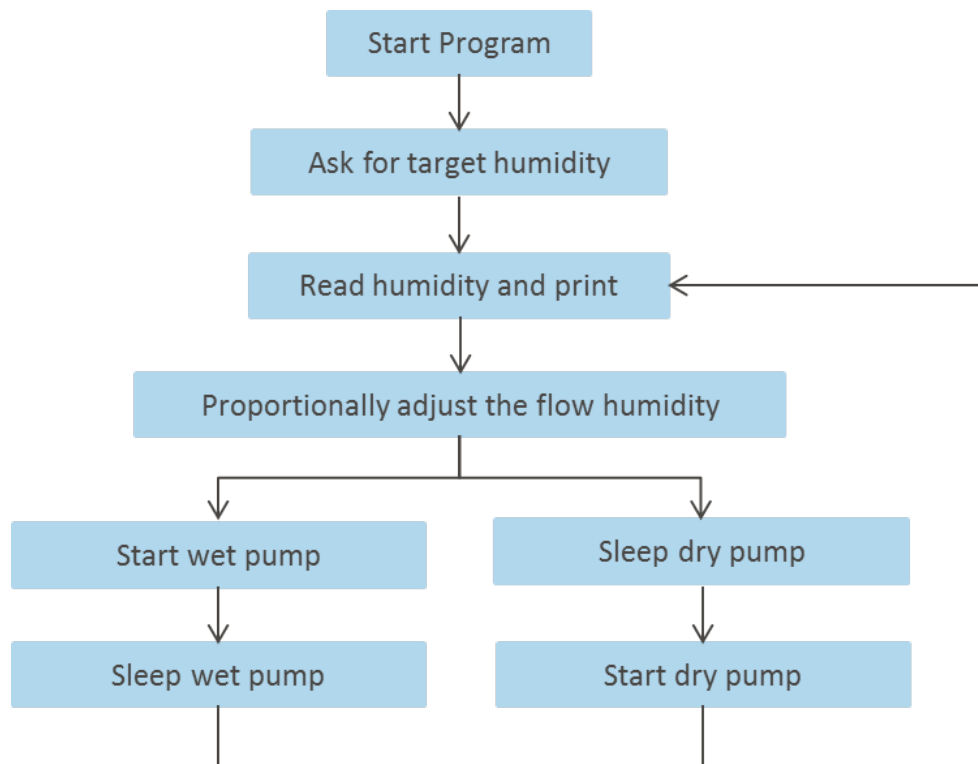


Figure 6.6: Schematic representation of the operations of the Raspberry Pi software written in Python.

chamber humidities. If there is more than one sensor for the chamber, the chamber humidity value is an averaged humidity for all chamber sensors.

The GUI has two ways to control the humidity, either by inputting a percentage RH or inputting a pump ratio. Inputting a pump ratio is much simpler in that it is directly transmitted through the Raspberry Pi to the pumps. Inputting the percentage RH starts by reading the initial chamber humidity and then creating a digital pulse for each pump to follow. A few iterations were created following this method before the final one was decided on.

6.3.2.2 Controlling the pumps

Initially the digital pulse consisted of splitting a second into on or off for each pump where the ratio depended on the desired humidity. This was changed when threading was used to run multiple processes including saving the data and changing the humidity without restarting the python code. The digital pulse then became a on/off switch for the pumps where both were able to be 'on' at the same time. Threading also had the advantage of increased air inflow and mixing therefore decreasing the time taken to reach the desired humidity.

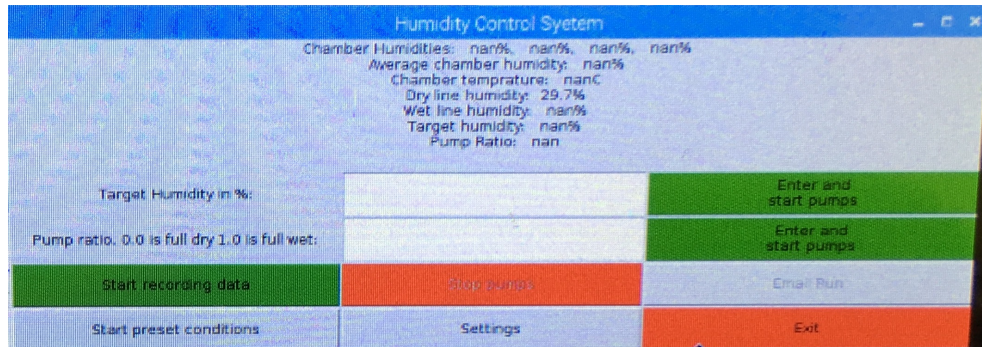


Figure 6.7: The GUI for the Raspberry Pi controlled humidity system. The target humidity or pump ratio can be imputed manually or through a preset conditions file, the settings can be controlled as can the recording of data through the GUI.

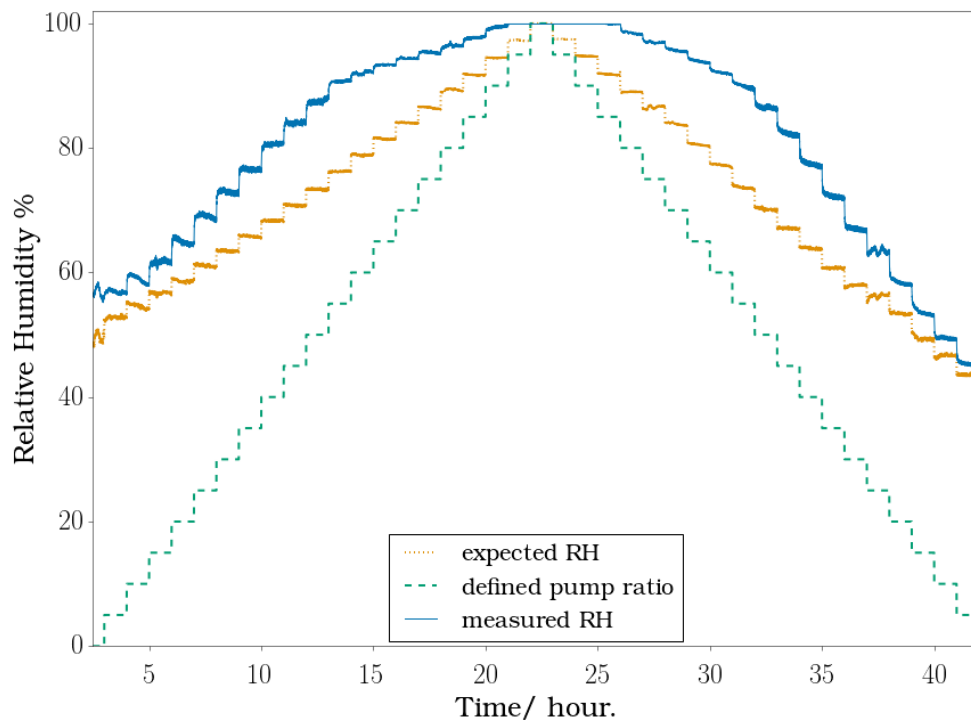


Figure 6.8: The relative humidity and expected relative humidity are plotted as a function of time with regards to changing pump ratio. The expected humidity is defined in Equation 6.4

With both pumps having the ability to be 'on' a new pump ratio was defined where one pump is constantly 'on' and the other is 'on' for a fraction of that time. For example if the wet pump was constantly 'on' and the dry pump for 50 % of the time, the pump ratio is 0.66. By defining the pump ratio, the amount of time that the pumps should be running was calculated using Equation 6.2 and Equation 6.3 depending whether the read humidity was above or below 50 % where t_{wet} and t_{dry} are the percentage of a second that the wet and dry pumps, respectively, would be running.

$$t_{wet} = \frac{1}{\frac{1}{ratio} - 1} \quad (6.2)$$

$$t_{dry} = \frac{1}{\frac{1}{1-ratio} - 1} \quad (6.3)$$

The humidity was monitored for a systematic change to the pump ratio over 24 hours from 0.0 to 1.0 and back in 0.1 intervals every hour where 1.0 is 100 % wet pump only and 0.0 is 100 % dry pump only. Figure 6.8 shows the difference between the recorded humidity and the expected humidity with regards to changing pump ratio. The expected humidity h_{exp} is the starting minimum humidity h_{min} scaled linearly with to maximum humidity h_{max} of 100 % is also plotted. The difference in expected humidity and recorded humidity turned out to be quite variable so a control loop was implemented, Equation 6.4.

$$h_{exp} = h_{min} + ratio (h_{max} - h_{min}) \quad (6.4)$$

6.3.2.3 Control Loop

A control loop is a script that keeps a variable constant by monitoring and adjusting the input variables. For the case of the Raspberry Pi the control loop monitors the relative humidity and adjusts the pump ratio once the humidity leaves a predetermined value or range. For the final iteration an adapted proportional controller was implemented. The proportional controller adjusts the output change δu by the difference (or error) between the desired value v_d and the recorded value v_r multiplied by the proportionality-gain K_p . The controller for the system can be calibrated to a sample environment by changing the K_p . The higher the gain, the faster the system will react to change. However if the K_p value is too large the recorded value will start to oscillate around the desired value. For smaller sample environments a value of 0.002 was found to work well.

$$\delta u = K_p(v_p - v_r) \quad (6.5)$$

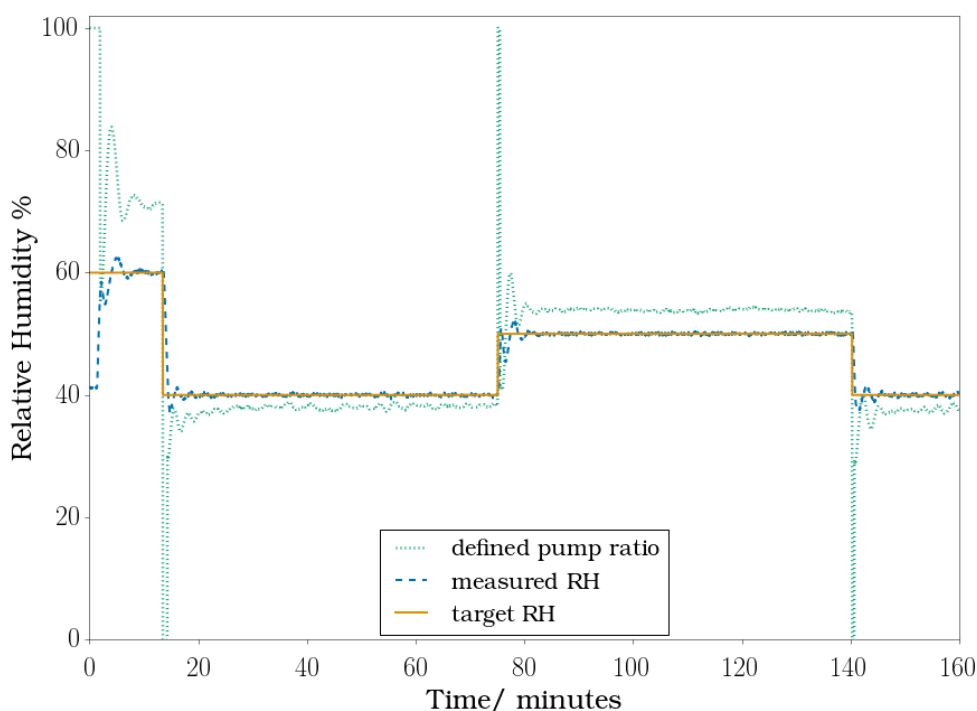


Figure 6.9: Using the control loop, the target humidity and actual relative humidity are plotted as a function of time with regards to changing pump ratio.

The proportional control was adapted as it ended up being too slow in changing the humidity. To increase the humidity change, at the initial point of change the pumps are set to 0.0 (full dry) or 1.0 (full wet) depending on the required humidity. Once the recorded humidity was within 5 % of the target, the proportional controller would take over to produce a pump ratio which achieved and maintained the required humidity. This means that the Raspberry Pi controller is able to change humidities and keep within a ± 1 % range of the target humidity within 2 to 5 minutes depending on the relative size of the change, as shown in Figure 6.9.

6.3.3 Examples of Use

The portable humidity control system has successfully been used for multiple experiments in both the lab and at national facilities where air was permissible for the experiment.

6.3.3.1 Integration with a Raspberry Pi Camera

As part of his Master's dissertation Ben Laurence integrated the humidity control system with a Raspberry Pi camera. This was to give a preliminary phase diagram for the lipids Cithrol and phytantriol using the anisotropy of

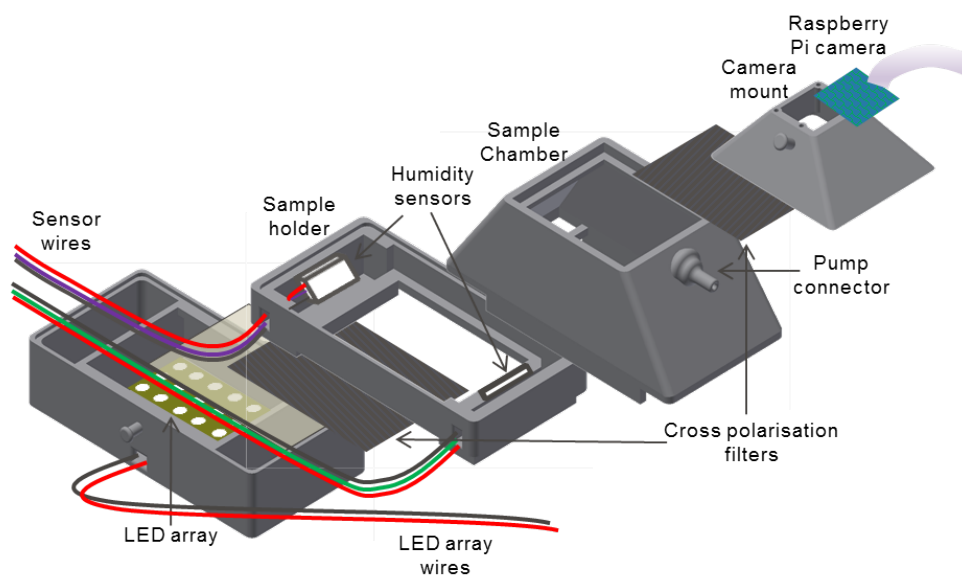


Figure 6.10: 3D printed box for the Raspberry Pi camera containing cross polarisers. The matt grey chamber was printed in black plastic to hold the camera at a distance to observe the phase changes of lipids under cross-polarised light. The camera and humidity sensors were both powered by the Raspberry Pi.

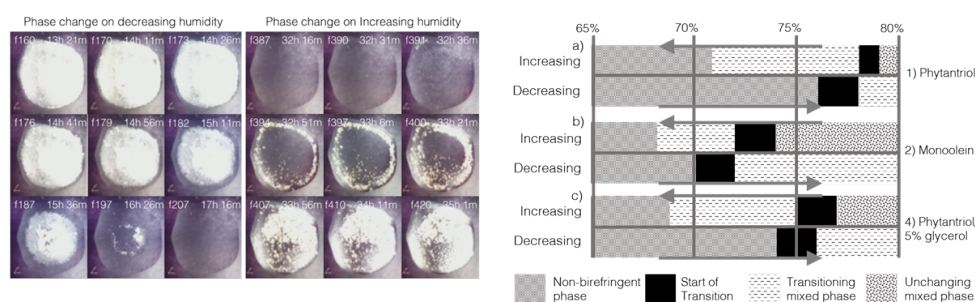


Figure 6.11: Phase changes of the two lipids monoolein and phytantriol, documented via changes in birefringence.

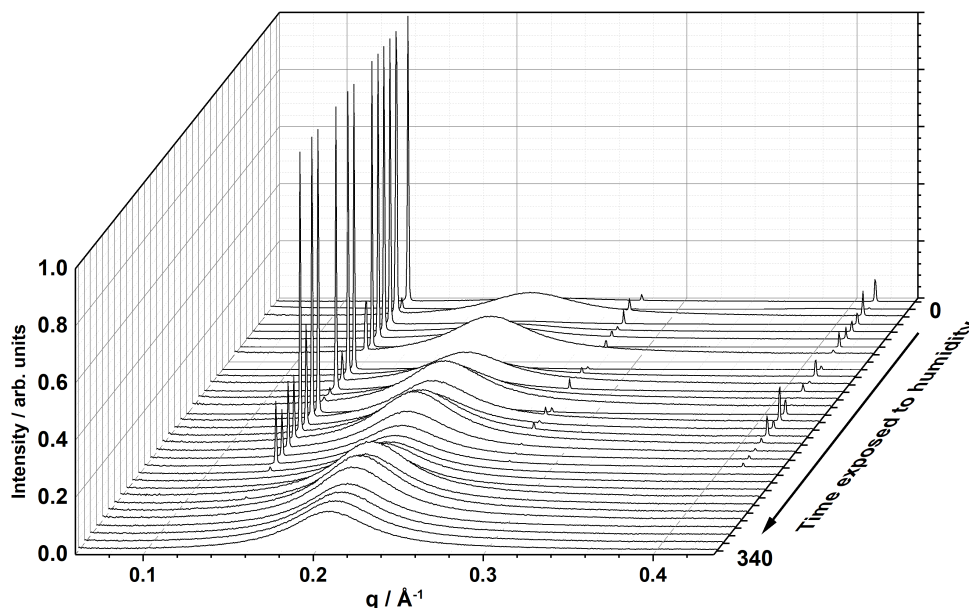


Figure 6.12: Phase change from L_α to micellar in oleic acid/sodium oleate mixture induced by elevated humidity levels (>90 %) in an levitated droplet.

the L_α phase under cross-polarisers compared to the isotropic Q_{II} phase. The camera was coupled with a 3D printed box, Figure 6.10, which contained two sheets of polarising plastic at 90° to each other. The box is lit from underneath with a LED grid of light. It was possible to record images at set time points documenting the changes in birefringence of the lipid. The phase changes recorded using the camera of the lipids monoolein and phytantriol are shown in Figure 6.11.

6.3.3.2 Acoustic Levitation at Diamond Light Source

Collaborators at the University of Birmingham successfully used the Raspberry Pi humidity control at Diamond Light Source for an acoustic levitation SAXS experiment on the beamline i22. The humidity control system was used in the investigation of high humidity on the macroscopic structure of several different acoustically levitated samples. An example of a phase change induced by high levels of humidity, from the L_α to the micellar phase, is shown in Figure 6.12.

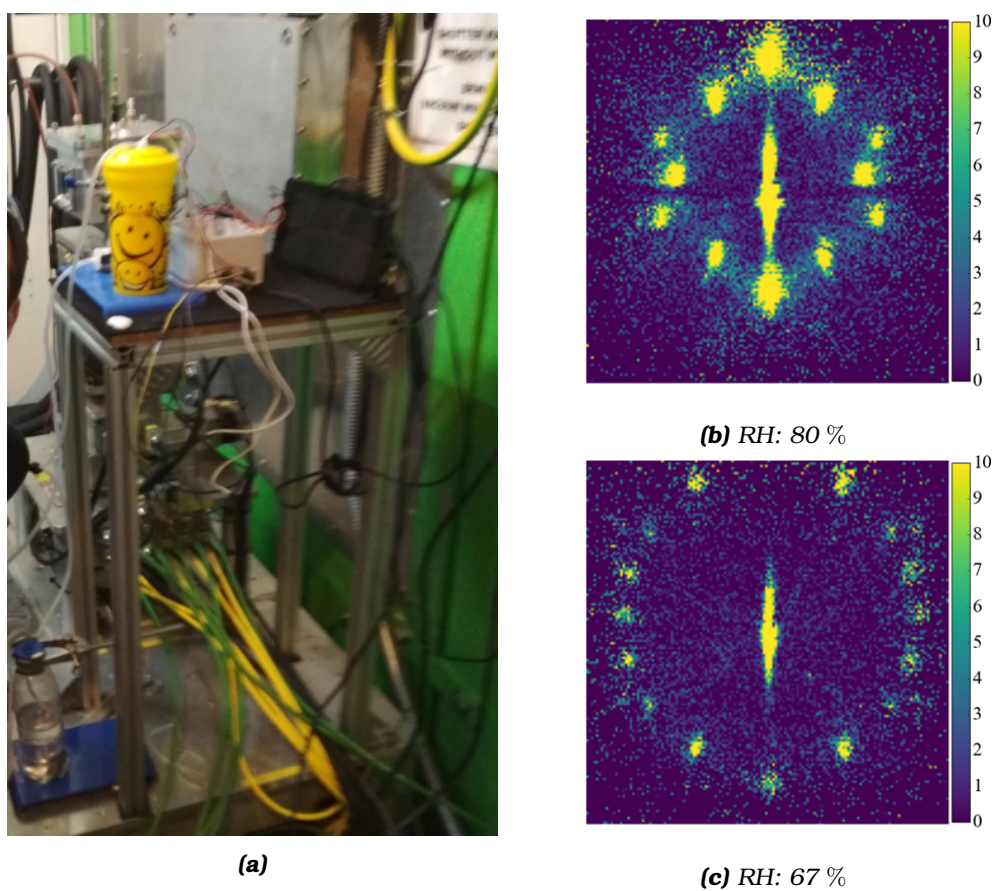


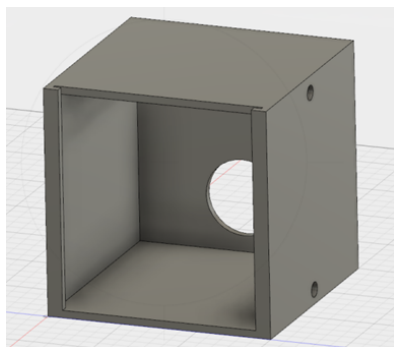
Figure 6.13: (a) Photograph of the Raspberry Pi system in use on ISIS Neutron and Muon Source's SANS2D beamline. Phase change from the Q_{II}^D (b) to the Q_{II}^G (c) phase due to reduction of humidity of a 20 % (w/w) Brij in phytantriol with 20 % (v/v) glycerol spin coated on a silicon substrate.

6.3.3.3 GISANS at ISIS Neutron and Muon Source

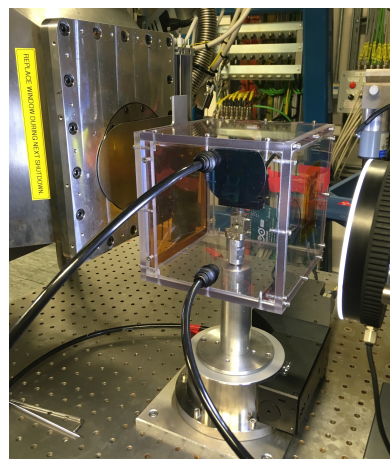
The Raspberry Pi humidity control was used at ISIS Neutron and Muon Source to bubble D_2O into a chamber containing lipid thin films. The humidified D_2O provided the aqueous environment for contrast matching as well as keeping the samples at the correct humidity for the required lipid phases. Figure 6.13 shows a phase change for the lipid thin film of phytantriol with 20% (w/w) Brij from the Q_{II}^D phase to the Q_{II}^G phase by decreasing the humidity in the sample chamber from 80 % to 67 %.

6.4 Other Gases: Mass Flow Controllers

For sample systems needing other gases, such as GISAXS with large air gaps needing helium, mass flow controllers are required to handle the pressurised gases. A system was designed to be integrated into the current controls of the beamlines at Diamond Light Source using Python. A chamber was also



(a) Design



(b) On the beamline

Figure 6.14: Humidity chamber concept and execution on the beamline. There are three gas flow input/outputs. One of which has been used to thread the humidity sensor cables through and then blocked off. For helium gas the input was placed at the bottom while for Nitrogen gas the input was at the top.

designed and created to be calibrated with the system.

Mass flow controllers control the gas flow via a control box, which in turn can be run remotely from a computer via serial commands. A simple system to reach and maintain target humidities was created to be further integrated into the main Diamond control system at a later date. As such, unlike the Raspberry Pi system, the Python code has not been designed to be controlled by a GUI but rather left in modular sections of code to be used in conjunction with taking data acquisition on the beamline. The system has been successfully, though separately, used on the beamline of i22.

6.4.1 Chamber Design

A sample environment was envisioned and designed for future GISAXS work. The box is 10 cm by 10 cm by 10 cm, with a volume of 1 L. As it is made out of perspex with Kapton windows for the X-rays, the chamber cannot be used with reactive gases or solvent vapours, even though the mass flow controllers allow for these uses. The box can be attached to any sample stage through a screw on the base. For the preliminary testing of the humidity control system, the box was mounted on a rotation stage so that GISAXS could be done on a vertically mounted wafer.

An example of the GISAXS diffraction pattern taken with the box and previous i22 GISAXS data is shown in Figure 6.15c. With the smaller air gap dis-

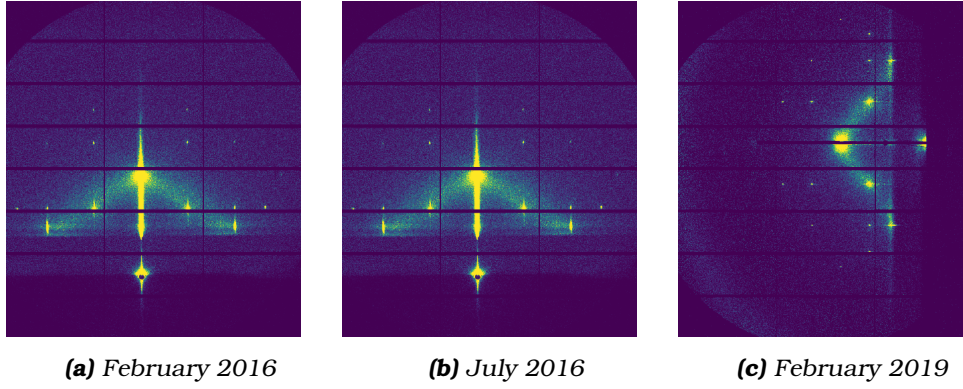


Figure 6.15: Comparison of different sample environments on i22 GISAXS data using a Q_{II}^D phase thin film uniaxially orientated in the $[1,1,1]$ direction spin-coated from cithrol/glycerol 75/25 (v/v) in 80 % (w/w) ethanol. For (a) and (b) a large air gap between beam, sample, and detector was created by the hexapod. (a) The initial iteration of humidity control was used in air. For (b) the air gap scatter was aimed to be decreased by creating a helium 'balloon' between the beam and detector. Humidity control was poor due to such large volumes and small bubblers. (c) was collected on a vertical wafer (hence the rotation of spots) in the 1L sample box created where the air gap was minimised due to lack of hexapod.

tance and controlled environment the GISAXS data is much improved from previous data collections with lower background scattering. The samples shown are of a thin film Q_{II}^D phase of Cithrol. Presented alongside is the initial attempt at humidity control Figure 6.15a and an attempt at minimising the air scatter by filling a large 'balloon' sealed around the detector and beam Figure 6.15b. The intensities cannot be directly compared due to the differences in attenuation but it is worth noting the sharpness of the spots in Figure 6.15c and Figure 6.15a with the humidity control boxes full of helium.

6.4.2 Hardware Set-up

Mass flow controllers were sourced from a previously envisioned and abandoned humidity control system for the beamline i22. The MKS mass flow controllers were of model GM50A and size 50 slm. The control range was between 0.01 standard litres per minute (slm) to 50 slm calibrated in nitrogen gas and a quoted accuracy of ± 1 % between 20-100 % and ± 0.2 % for 2-20 %. The mass flow controllers have a 15 pin analogue connector to which the control box powers and controls from. There is a 30 minute warm-up time and the typical settling time is less than 750 ms.

A chamber of size 10 cm x 10 cm x 10 cm with a volume of 1 L was designed and created for GISAXS experiments. The maximum flow of the gas

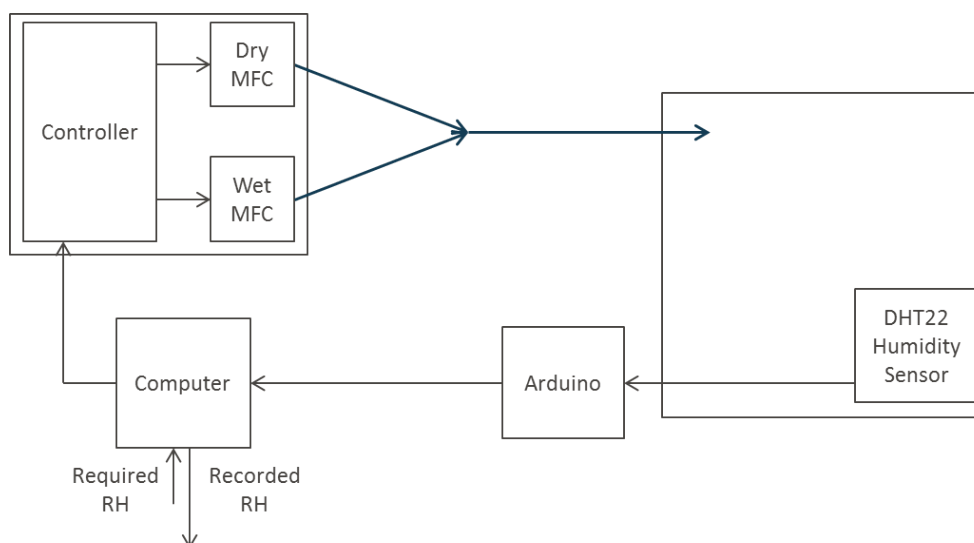


Figure 6.16: Schematic representation of the set up of the mass flow controller system.

was therefore limited so as not to introduce pressure into the chamber. For future experiments the scripts for controlling the mass flow controllers were written in such a way to allow for the swapping to smaller flow rate mass flow controllers by simply changing a single number in the initial set-up stage.

Two mass flow controllers were set up though the control box had the possibility to control up to four. The mass flow controller 1 (channel 1 on the control box) was denoted as the dry line and mass flow controller 2 (channel 2) the wet line which led to a bubbler. The bubbler must be installed after the mass flow controller as it is explicitly noted that these mass flow controllers cannot handle high humidities.

To read the humidity, a similar set-up to the Raspberry Pi system was used with an Arduino Uno and DHT22 humidity sensor with a slightly different polling system set-up. The Arduino was powered via the computer and controlled using a serial Python script. The full code to run the mass flow controller's humidity control system can be found in Appendix E.

6.4.2.1 Initialising the Mass Flow Controllers

Every time the control box for the mass flow controllers is turned on or reset, the initial parameters unique to the mass flow controllers must be initialised with a set-up either manually or through the automated script. The parameters the control box needs to correctly input the right commands to the mass flow controllers are the maximum flow or size of the mass flow controllers,

the type of gas for a gas correction factor, the upper and lower trip limits of the mass flow controllers and if the mass flow controllers are independent or linked (slave) to each other. After the initial parametrisation the mass flow controller's valves will need to be opened before any gas can flow.

6.4.3 Flow Rate Control

As the control box was used previously on i22 for detector gas control and is many years older than the mass flow controllers, an initial systems test was performed to determine if the two were compatible with each other and controllable from a computer. A series of serial commands were transmitted via the control box, which involved changing the amount of gas through each mass flow controller and noting whether the flow rate was as it should be. The mass flow controllers read flow rate as a percentage of the maximum flow rate of the mass flow controllers, in this case 50 slm, allowing for the control box to be calibrated to many different flow rates of mass flow controller.

The mass flow controllers are quoted as having a leak integrity[?] of less than 1 % however it was found that once connected to the control box and as such powered up the 50 slm mass flow controllers were 'leaking' at a rate between 4 to 5 slm or around 10 % of the total flow. Due to the fact that when the power was disconnected the mass flow controllers did not leak at all, it was determined that they weren't simply broken. It is hypothesised instead that due to the difference in age and that they weren't explicitly bought to interface with each other that there was a miscommunication between the newer mass flow controllers and the old control box. The mass flow controllers had a pin to accept a parameter called "Zero Flow" which the control box had no way of providing. This was less than ideal as not only does it waste gas, which in the case of helium is expensive, but it restricts the humidities that can be achieved as the system can never fully turn off either mass flow controller.

Due to the non-zero flow the old mass flow controllers of 0.01 slm that were originally used with the control box were considered and tested. However these proved to have no discernible humidity change over 15 minutes from the wet line on full flow and the dry line off. Therefore the 50 slm mass flow controllers were re-installed and the rate of change for different humidity jumps was monitored where the maximum flow into the chamber was set to 25 slm. Despite the non-zero flow the mass flow controllers were able to change and maintain the humidity rapidly, as Figure 6.17 shows. While it wasn't surprising given the large flow volume in only a 1 L box, it was reassuring for the potential humidity control.

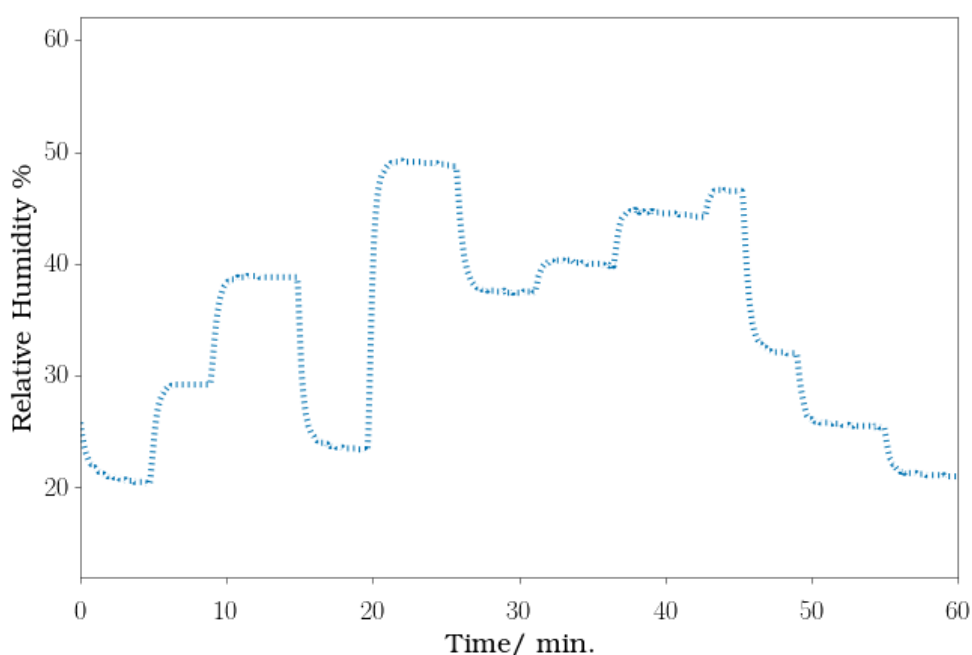


Figure 6.17: Change of humidity over time for changing flow rates of the 50 slm mass flow controllers

6.4.4 Recording the Humidities

There are four functions to read the humidity. The full code can be found in Appendix E. The basic principles for each remain the same: read and save the humidity and temperature from the Arduino with it's corresponding times-tamp to a csv file. The four columns are listed below where the `DateTime` refers to human readable time whereas the `PythonTime` is the time in days since 0001-01-01 00:00:00 and is plottable in python.

<code>DateTime</code>	<code>PythonTime</code>	<code>RH</code>	<code>Temperature</code>
-----------------------	-------------------------	-----------------	--------------------------

The first function `SingleRH(sensors)` is only used in the calibration of the mass flow controllers to the box as it simply outputs and prints the relative humidity. Its input is the number of sensors it needs to read. Currently the Arduino and script for reading the Arduino is only able to handle two sensors though adding more is possible.

```
SingleRH(sensors)
ContrRH()
SaveRH(sensors)
RunRH(filename, sensors)
```

The second function `ContrRH()` allows for the continuous reading and printing of humidity until stopped with a `KeyboardInterrupt`. The data for the hu-

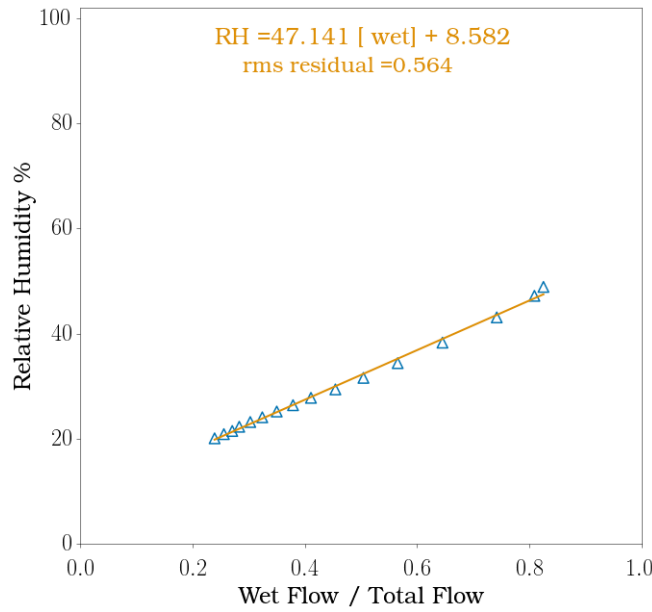


Figure 6.18: Manual calibration of the flow rate to humidity for the 50 slm mass flow controllers. The flow rates of each mass flow controller were changed sequentially and the box was left to equilibrate for 5 minutes before the humidity was read as were the actual flow rates.

midity and temperature are then plotted as a graph against time. The third `SaveRH(sensors)` and forth `RunRH(filename, sensors)` functions are the main functions used for experiments. The main difference between the two is where the data is saved. `SaveRH(sensors)` saves the data in a generic `RH.csv` file while the `RunRH(filename, sensors)` saves the data in a file of `filename` where `filename` is the date and time in `YY-MM-DD-HH-MM.csv`. Both functions can have the number of sensors as either 1 or 2.

6.4.5 Calibration

A calibration was successfully run for the flow rates with regards to humidity in a box. A total volume of 20 slm was used as a limiting maximum flow for the mass flow controllers. The 20 slm maximum flow was decided on to give a reasonable humidity range given the non-zero flow of 4 slm. The flow ratio for the mass flow controllers was calculated from the read wet flow over the read total flow volume. Initially the calibration was done manually using compressed air, shown in Figure 6.18, where every 5 minutes the flow rate to the mass flow controllers was changed. The flow ratio and humidity were read before each change. A straight line fit gave a calibration between the

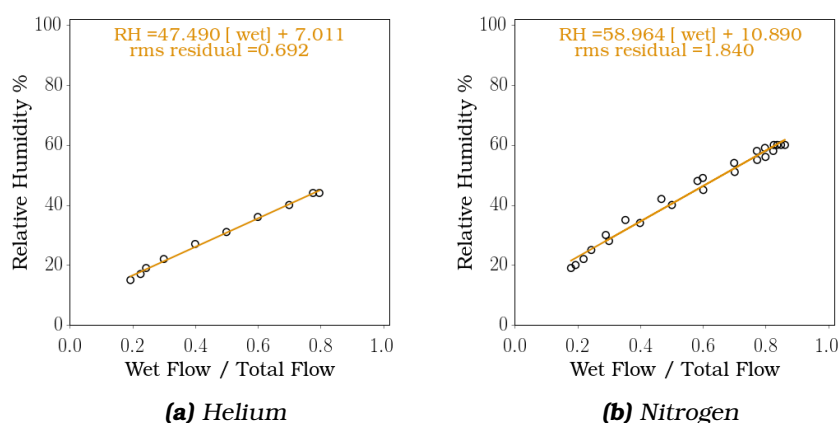


Figure 6.19: Automatic calibration of the flow rate to humidity for the 50 slm mass flow controllers capped at a 20 slm total volume through the box. The flow rates of each mass flow controller were changed sequentially in 0.1 increasing then decreasing steps. The box was left to equilibrate for 5 minutes (helium) or 3 minutes (nitrogen) before the humidity was read along with the actual flow rates for each mass flow controller.

0.23 to 0.84 flow ratio and 20 and 49 % humidity.

$$flow\ ratio = \frac{wet\ flow}{total\ flow} \quad (6.6)$$

6.4.5.1 Automatic Calibration

An automatic calibration was set up so that for each new project folder or set-up the calibration of the chamber to mass flow controllers will be automatic. This is accomplished via a script checking for a specific csv file with the saved calibration data from the straight line fit. The data is generated from a calibration of flow ratios between 0 (full dry, zero wet) to 1 (zero dry, full wet) and then back to 0 in user defined step sizes before pausing for a user defined wait time and then reading the actual flow rates of the mass flow controllers and the humidity from the sensors. The data is saved continuously in the below format:

flow ratio	dry flow	wet flow	RH
------------	----------	----------	----

The script saves both the gradient and intercept from the straight line fit into a csv file called `currentCalibration`. Currently only the data from the first sensor is used in the calibration if multiple sensors are available, though all data is saved. In the future it is suggested to make an average of the humidity data from all the sensors to create a calibration.

In this way a calibration was found for both helium and nitrogen gas for the

chamber with the 50 slm mass flow controllers set to a maximum of 20 slm. The calibration data is presented as saved from the script in Figure 6.19. The helium calibration had a step size of 0.1 and a wait time of 5 minutes. The nitrogen calibration had a step size of 0.1 also but a reduced wait time of 3 minutes. The nitrogen gas calibration also had a release valve fitted after the dry line mass flow controller which constantly vented 4 slm to compensate for the non-zero flow. Therefore higher humidities were reached than for the helium gas calibration. While the flow ratio is incorrect for the gas within the chamber, the flow ratio needed for the control box is the correct value and as such does not affect the calibration for achieving desired humidities.

6.4.6 Humidity Control

Once a calibration has been acquired, setting the humidity can be controlled with two functions:

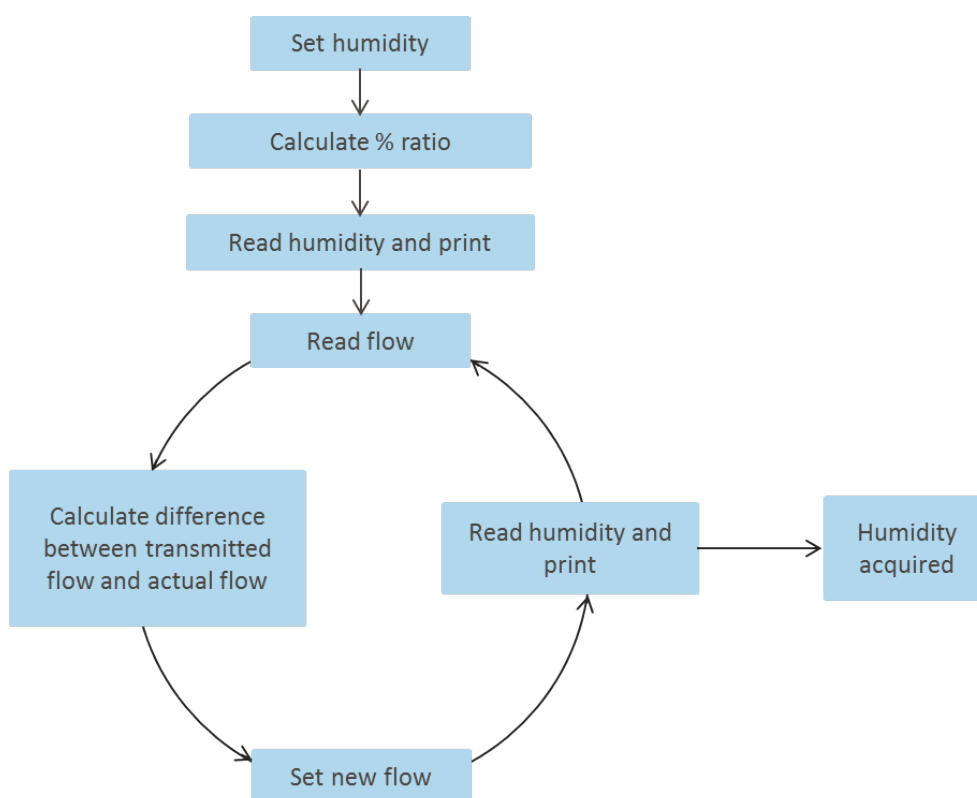
```
setHumidity(humidity)
runHumidity(startHum, stopHum, stepHum, TimeSec)
```

Both rely on the same method to set and retain the correct humidity, shown in the schematic Figure 6.20b. To start the required flow rate is calculated using the calibration equation. The humidity is then read and saved, followed by the reading the actual flow rates. If the humidity is not within 1 % of the target humidity then the difference between the transmitted flow rate and the actual flow rate is calculated. A new flow is then set from the required flow rate minus the difference. The humidity and flow rates are then read again. This continues cycles until the measured humidity is within 1 % of the target humidity.

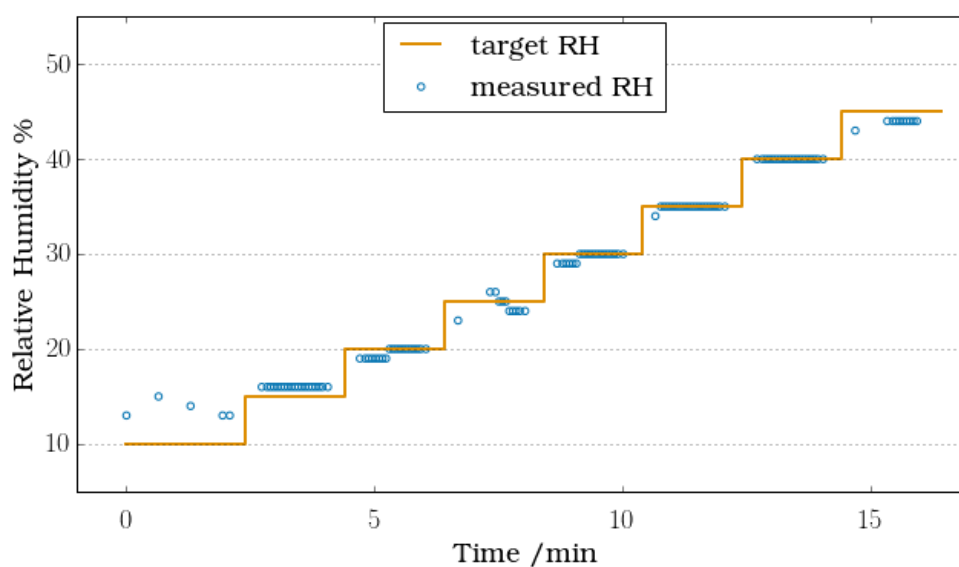
The data presented in Figure 6.21 is representative of the humidity control possible. A set of humidity jumps were separately inputted between 30 % humidity and 70 % humidity in increasing then decreasing steps. The humidity change induces a phase change for a spin coated thin film of Cithrol/glycerol in a 80:20 (v/v) ratio from the Q_{II}^G phase to the Q_{II}^D phase then back to finally settle in the fluid isotropic micellar phase.

6.4.6.1 Humidity Ramps

The second function `runHumidity(startHum, stopHum, stepHum, TimeSec)` runs a humidity ramp and incorporates two more loops into the function. The humidity ramp is defined by a starting humidity `startHum` an end humidity `stopHum` and how large the steps in-between `stepHum`. At the beginning of



(a) Schematic of how the script achieves the correct humidity.



(b) Measured humidity plotted against target humidity.

Figure 6.20: Humidity control using the mass flow controllers using the loops in the schematic **(a)**. The data plotted in **(b)** was produced where the tolerance for the target humidity was 1 %. However less than 15 % humidity is currently unachievable due to the non-zero flow of the mass flow controllers.

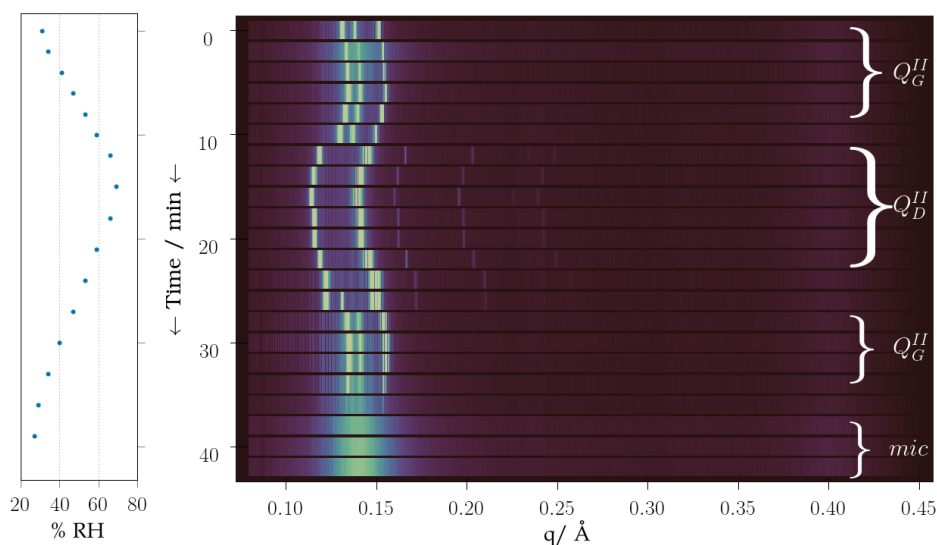
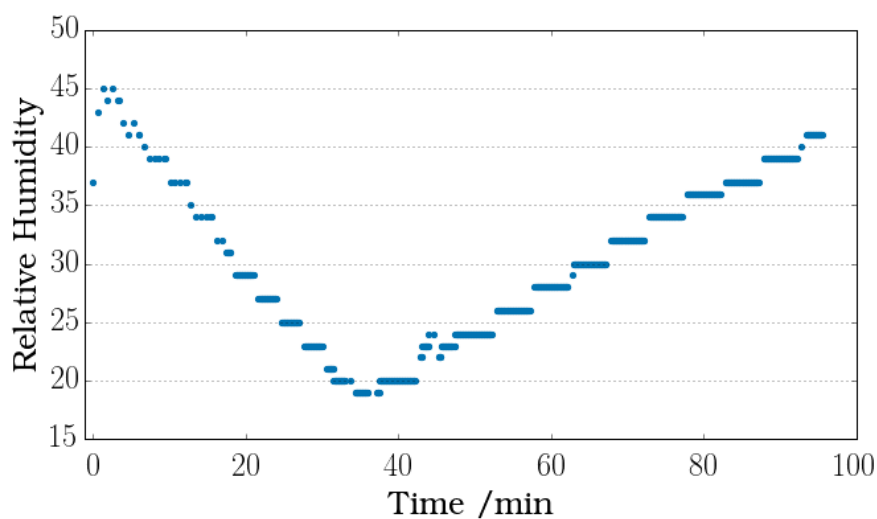


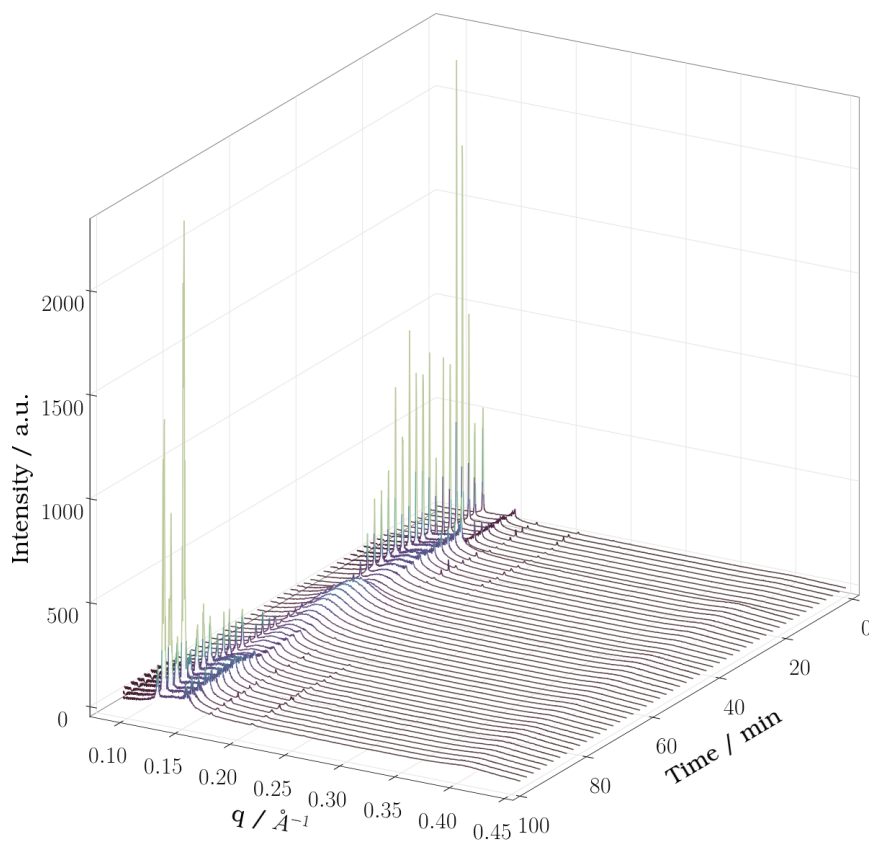
Figure 6.21: The 1D diffraction data for a thin film of cithrol/glycerol of 80:20 (v/v) ratio. Humidity control using Nitrogen gas was used to induce phase changes by first increasing the humidity then decreasing it. A phase change from the Q_{II}^G phase to the Q_{II}^D phase takes place with increasing humidity. With decreasing humidity the film changes back to the Q_{II}^G phase and then to the micellar phase.

the humidity ramp an initial start time is set in seconds. The humidity loop is then implemented until the target humidity is reached or the time between steps TimeSec is rundown. Should the required humidity be achieved before the end of the time for that step then the humidity is simply read until the end of the set time. After the time for the step is finished the target humidity is changed to the next step and the loop started again.

Several humidity ramps were run on i22 to test the humidity control system. An example of the data is show in Figure 6.22 with corresponding lipid phase changes due to changes in humidity. The film is a cithrol/glycerol of 75:25 (v/v) ratio which starts in the Q_{II}^D phase. With decreasing humidity the micellar phase begins to appear, seen by the broad peak between the $\sqrt{2}$ and $\sqrt{3}$ peaks. Below 20 % humidity only the micellar phase is present. Upon re-humidifying the lipid film, the Q_{II}^D phase begins to reappear though the micellar phase has not completely disappeared by 40 % humidity.



(a) Humidity ramp using helium gas from 45 % to 18 % in 2 % steps every 2 minutes then from 20 % in 2 % steps every 5 minutes and stopped at 41 %.



(b) 1D diffraction data for the humidity ramps plotted as a function of time. Diffraction patterns were taken every 2 minutes

Figure 6.22: Phase change of a thin film of cithrol/glycerol of 75:25 (v/v) ratio from the Q_{II}^D phase to the micellar phase due to changes in humidity.

6.5 Conclusions

Two humidity control systems have been designed and created which can reliably change and maintain humidity: the first is Raspberry Pi controlled and the second uses mass flow controllers. Each has successfully been used in several different experiments.

6.5.1 Raspberry Pi Control System

The Raspberry Pi humidity control system is low cost, portable, and chamber independent. The control system is able to reliably change and keep the humidity with ± 1 % of a target within 2 to 5 minutes dependent on the start humidity and size of change. The lower limit of humidity available is dependent on how dry the air (dry line) and the upper limit is 98 % with two sequential bubblers.

The Raspberry Pi has been used with experiments at Diamond Light Source, ISIS Muon and Neutron Source and has been used in-house with connection with a Raspberry Pi camera.

6.5.2 Mass Flow Control System

The mass flow controller humidity control system is a fully automated and calibrated chamber for use at Diamond Light Source, and can integrate with a large number of gases. The range of humidities possible is currently between 15 % and 70 % with non-zero flow of the mass flow controllers. The disconnect between the control box and the mass flow controllers is contributing to a large non-zero flow of gas which isn't currently practical. It is hypothesised that should this be fixed then a larger range of humidities would be available.

The mass flow controller humidity control system has been successfully tested on the i22 beamline at Diamond Light Source to produce phase changes in uniaxially orientated lipid thin films.

6.5.3 Future Improvements

6.5.3.1 Mass Flow Controllers

A major improvement would be to acquire different mass flow controllers. For the 1 L box, 50 slm mass flow controllers are too large, either 1 slm or even 0.5 slm mass flow controllers should be used instead. MKS offers support for legacy mass flow controllers from 0.001 slm to 20 slm. It would be possible to buy the previous model which interfaced well with the current control box

but at a larger flow volume which should eliminate the problem with the non-zero flow at the zero point. Once the mass flow controllers were switched out, it would simply require a change in number for the `set_up()` function to calibrate the control box.

One check that should be implemented with new mass flow controllers would be to note the time taken to change the humidity within a required box size. Ideally this wouldn't be below 10 % per minute. The range of available humidities would also change if there was no leaking due to the non-zero flow. It would be interesting to see if the higher humidities could be reached. Previous work using the Raspberry Pi controller has shown by adding another bubbler in sequence higher humidities (greater than 95%) can be achieved. This should be tested with the mass flow controller system once the non-zero flow is fixed.

6.5.3.2 Control Box

Should it be necessary, MKS Instruments has two suggested replacements for the controller or the multi-channel flow ratio/pressure controller type 647C. These are the PAC 100/MFC Module Programmable Automation Control or the 946 Vacuum System Controller. The PAC 100 is part of modular system control and would need a power supply module as well. Another module can also be bought to interface with LabView if necessary. The PAC 100 has matching pins to 50 slm mass flow controllers. The 946 Vacuum System, on the other hand, has the advantage of having a separate manual interface. It claims to also be able to interface with the GM50A mass flow controllers. The control commands are quoted to be a universal control standard and as such should be able to be run with the current python control.

While this is a possible alternative to fixing the non-zero flow problem, it is not one that I would recommend. While the modular automation control comes with many options, it is unlikely that it will be able to run using the Python scripts created. MKS Instruments does provide software to control the mass flow controllers however it would still need to be integrated with any sort of humidity control system. Other than the possibility of fixing the non-zero flow and the ability to interface with the current 50 slm mass flow controllers, the 946 Vacuum System does not provide any particular advantages. Therefore unless a larger box is required for which 50 slm mass flow controllers are necessary it is suggested that it is the mass flow controllers that are swapped rather than the control box.

6.5.3.3 Addition of More Sensors

In the future more sensors can be added to the system by modifying the Arduino code and the python control for the Arduino. The Arduino Uno can accommodate up to 12 sensors. This is not particularly necessary in the 1 L box as it was found with the current set-up that the humidity did not vary with position in the box. However this may change with a larger box or indeed with different size mass flow controllers.

With the addition of more sensors all the read humidity functions should be re-written to take into account the average box humidity. Instead of saving each humidity sensor data separately, they could all be saved into one file including the average humidity. By changing the way that the Arduino and python functions read and save the humidity data the calibration script can be modified to take the average chamber humidity, providing a more accurate description of the humidity within a particular chamber.

6.5.4 Interchangeable Chambers

The mass flow controller system has the ability to be integrated with other chambers. Currently the chamber is made from plastic and as such could not be used with other vapours such as some solvents. Should a chamber be made out of another material such as steel, wherein the limiting factor would then be the Kapton windows, solvents such as ethanol or acetone could be used instead of water. The sensors are calibrated to quote the relative humidity of water but this can be modified in the script by adding a multiplication factor so that the solvent vapour present could be correctly recorded.

With the use of solvents, the mass flow controller system could be used to investigate solvent annealing processes, particularly for investigating the kinetics of thin films, such as the capillary lipid thin films discussed in Chapter 3.

The chamber can also be integrated with other apparatus at Diamond Light Source, for example the doctor blade at Diamond Light Source or temperature control. For temperature experiments, the bubblers can be heated to produce heated humidified air as necessary. Though it should be noted that the humidity sensors are only accurate between -40 °C and 80 °C so for higher temperatures other sensor would need to be acquired and integrated into the system.

Chapter 7

Micelles

The prediction of structures formed by self-assembly of lipids can be quite difficult due to the many previously discussed factors which influence it. Even in simple binary systems the creation of a complete theoretical model is complicated due to the large numbers of molecules required to form nanoscale structures. This is especially true of the Q_{II} phases which have inherent complexity in modelling the inverse highly curved bilayers.

Therefore we propose the use of inverse micelles of relaxed curvature as a method of determining curvature elastic modelling parameters which can be used to model lipid self-assembly. Inverse micelles are spherical aggregates formed by surfactants or lipids in organic solvents either in the presence of water or without.[?] As such I have experimentally determined using SAXS the size of different relaxed curvature lipid micelles and the sizes of their aqueous cores. These are then used to determine the average number of lipids within a micelle, the position of a modelling parameter called the neutral surface, and it's relaxed curvature. All three of these are used within theoretical modelling.

7.1 Modelling the Q_{II} Phase

7.1.1 Molecular Dynamics

For lipids, the most popular form of molecular modelling is molecular dynamics. Molecular dynamics simulations are a subset of atomistic simulations where upon Newton's forces are resolved in an infinite periodic box.[?] Though often limited to small system sizes over short time frames due to the computational power required to make all the calculations, this approach

has proven very successful in modelling the L_α and gel phases.^{??} Currently atomistic simulations are in the order of a few microseconds, for box lengths of tens of nanometres with complex lipid mixtures.^{??}

A common way to model lipids, in part to minimise the required computational power, is by coarse graining. Coarse graining is a technique by which atoms are grouped together into a bead where all their associated behaviour, reactivity and forces are approximated together. A classic example of this is CH_3 or H_2O being grouped together with the latter including a dipole moment to simulate the electrostatics.[?] The two models of the $\text{Q}_{\text{II}}^{\text{D}}$ phase published^{??} both utilise coarse-graining.

The first of these two models, published in 2001^{??} could not self-assemble the $\text{Q}_{\text{II}}^{\text{D}}$ phase. Rather it started by having the lipids placed upon the Diamond IPMS and then imposed constraints to get the lipids to remain in the $\text{Q}_{\text{II}}^{\text{D}}$ phase. The need for constraints to maintain the $\text{Q}_{\text{II}}^{\text{D}}$ phase indicates that the model is insufficient. The second method, published over ten years later in 2012,^{??} has successfully self-assembled the $\text{Q}_{\text{II}}^{\text{D}}$ phase from a mixed water and monoolein box, though it too required constraints to do so.

7.1.2 Continuum Models

Biological functions, in which the properties and structures of lipid membranes play a part, often take place at much larger distances than molecular size and a time scale much longer than molecular vibrational bonds.[?] Continuum models, therefore, are useful at describing macroscopic phenomena by modelling the membrane as a smooth continuous surface based on the frameworks of fluid dynamics, elastic theory, and statistical membranes.^{????}

The starting point for a mathematical description of a lipid bilayer is the Helfrich equation Equation 1.5, discussed in Chapter 1.1.3 (pg. 5). The Helfrich equation describes the curvature energetics of a thin fluid sheet.^{??} When modelling a L_α phase the mathematical surface for the lipid bilayer can essentially be placed dependent on what properties are modelled. However for Q_{II} phases the energetics of the surface cannot be defined at either the interface nor the mid-plane (IPMS) due to some dependence on traverse forces.[?] Instead the monolayers are each defined at what is called the neutral surface.

7.1.3 The Neutral surface

The neutral surface is a surface defined within the amphiphilic monolayer whose area does not change due to bending. Bending or flexing may occur due to change in hydration represented by changes in unit cell or from a series of phase changes to more curved phases such as the H_{II} or Q_{II} phases. This means that at the neutral surface, the cross-sectional area of the lipid remains unchanged with hydration or phase. As the formation of curved phases is driven by both the hydrophobic effect and the balance between packing energy and elastic curvature stress^{??} the cross-sectional area change is assumed to be more complex with regards to temperature. As the phase boundaries are not purely vertical, one of the curvature elastic parameters is temperature dependent.

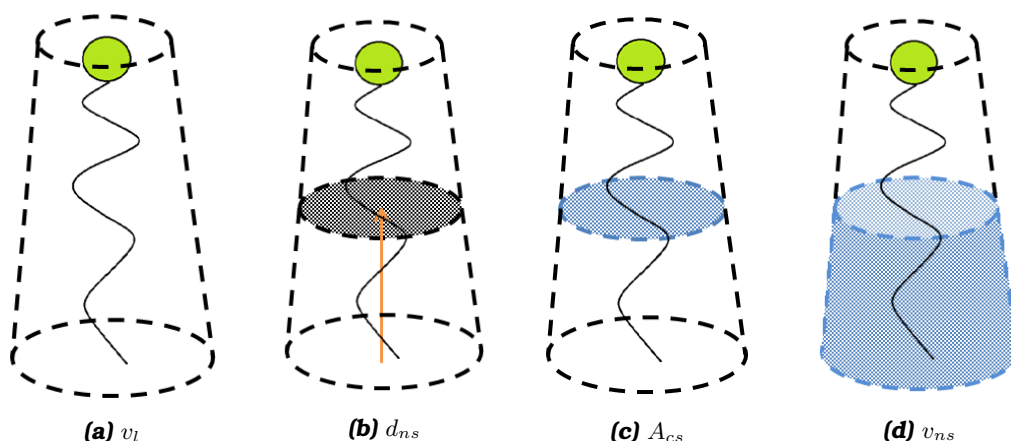


Figure 7.1: Schematic representations of properties of the neutral surface. **(a)** The molecular volume. **(b)** Distance from the center of the bilayer to the neutral surface. **(c)** Cross-sectional area per lipid at the neutral surface. **(d)** Volume per lipid underneath the neutral surface. By definition both the cross-sectional area and the volume underneath the neutral surface are invariant whilst the distance to the neutral surface will change.

The neutral surface is paramount in curvature elastic models as the assumption is that the elastic parameters remain constant whilst being bent. This is only true for lipids if the system modelled has pure bending around the neutral surface.[?]

7.2 From the Q_{II} Phase to a Micelle

For computational modelling, micelles have many advantages over Q_{II}^D phases. For molecular dynamics simulations, micelles are a much smaller system to model and spheres are much easier to computationally evaluate than a IPMS.

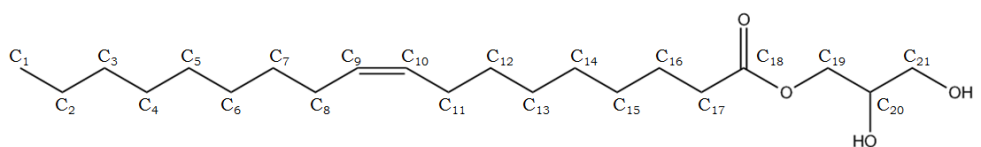
For continuum models the cross-sectional area and volume of the neutral surface are required to model any curved phase. It has already previously been shown how the neutral surface can be used to predict the dimensions of the hexagonal phase and Q_{II}^G phases.[?] We hypothesise that by calculating the neutral surface from a series of short solution SAXS experiments the properties of lipids and lipid mixtures can be predicted and modelled as well.

7.3 SAXS Experiments

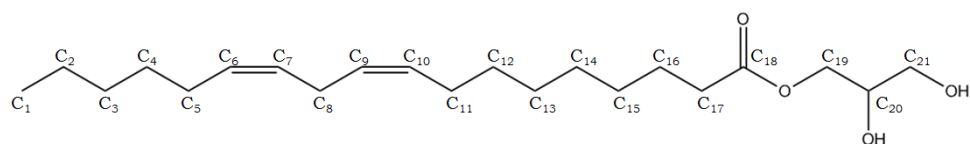
Type II lipids can form inverse micelles when dissolved in a mixture of organic solvent and water. For the critical packing parameter to be unconstrained, an excess of water is required. This allows for the micelles to form with relaxed curvature and not be constrained by water content.[?]

Four lipids were used to create inverse micelles, three of which have well defined phase behaviour including forming the Q_{II}^D phase in excess water. Monoolein[?] and phytantriol[?] were the primary lipids chosen. Both the monoolein (Cithrol) and phytantriol used were commercial versions. Monolinolein[?] was chosen for its similar structure to monoolein. They have the same head group but differ in the tail as monolinolein has a second double bond in the tail at C6-C7 as well as C9-C10. Carbon backbone labelling and representations of the molecules are shown in Figure 7.2. Finally a new synthetic lipid similar to phytantriol, which had been found to form the Q_{II}^D phase in excess water was used. Phytantetrol is structurally similar to phytantriol with another alcohol group on the head group and was synthesised by Masters students at the University of Reading.

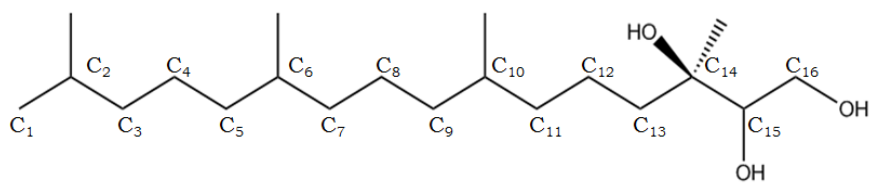
A set of solution SAXS experiments was designed to determine the size of the different lipid micelles and their aqueous cores at different temperatures. A dilution series for each lipid in an organic solvent was used to remove inter-micelle scattering effects. Different aqueous cores were created using salt solutions to provide different electron densities within the aqueous core for modelling. The scattering profiles were modelled as a core shell and the size of the lipid layer and aqueous core extracted.



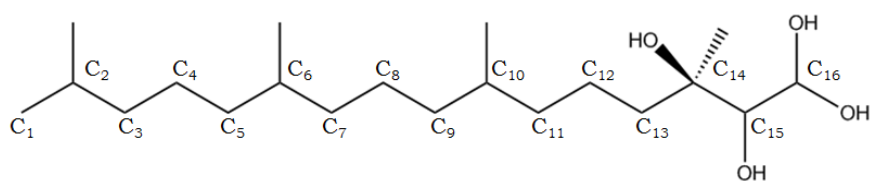
(a) Monoolein



(b) Monolinolein



(c) Phytantriol



(d) Phytantetrol

Figure 7.2: Skeleton drawings of the lipids used to create inverse micelles. The carbon backbones are labelled in each.

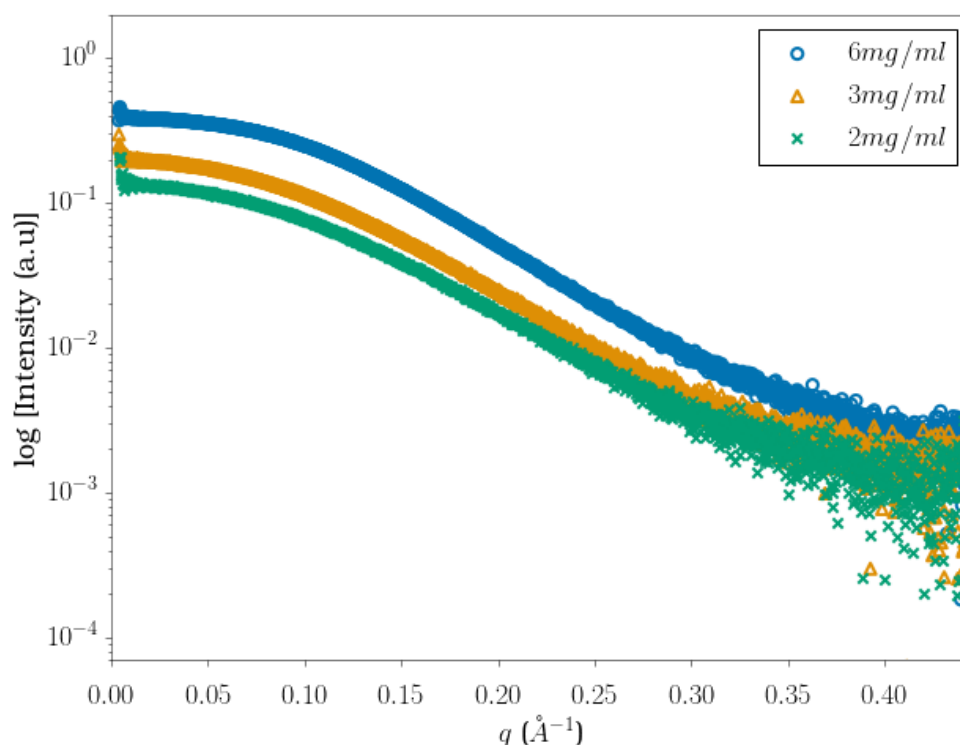


Figure 7.3: Background subtracted 1D SAXS patterns for Cithrol micelles in hexadecane created with water and incubated and run at 30 °C

7.3.1 Creation of the Micelles

Full details of the experiment can be found in the Techniques and Methods 2.3.1.

In short, inverse micelles were created using the organic solvent hexadecane.?? The lipids were dissolved in hexadecane to a concentration of 6 mg mL⁻¹. For the water or aqueous salt solution was then added in a 9:1 ratio organic to aqueous and the final solution vortexed. This mixture was left to stand for at least 30 minutes before solution scattering data was collected. Two layers were formed with the larger top organic layer containing the inverse micelles.?

For the temperature runs of 30 °C and 37 °C, the vials were incubated at the required temperature for at least 4 hours before being transferred to well plates which were also at the required temperature.

Solution scattering data was collected at Diamond Light Source on beamline B21. Micelles were pipetted from the middle of the organic layer into well plates to be loaded onto the beam by the BioSAXS robot.

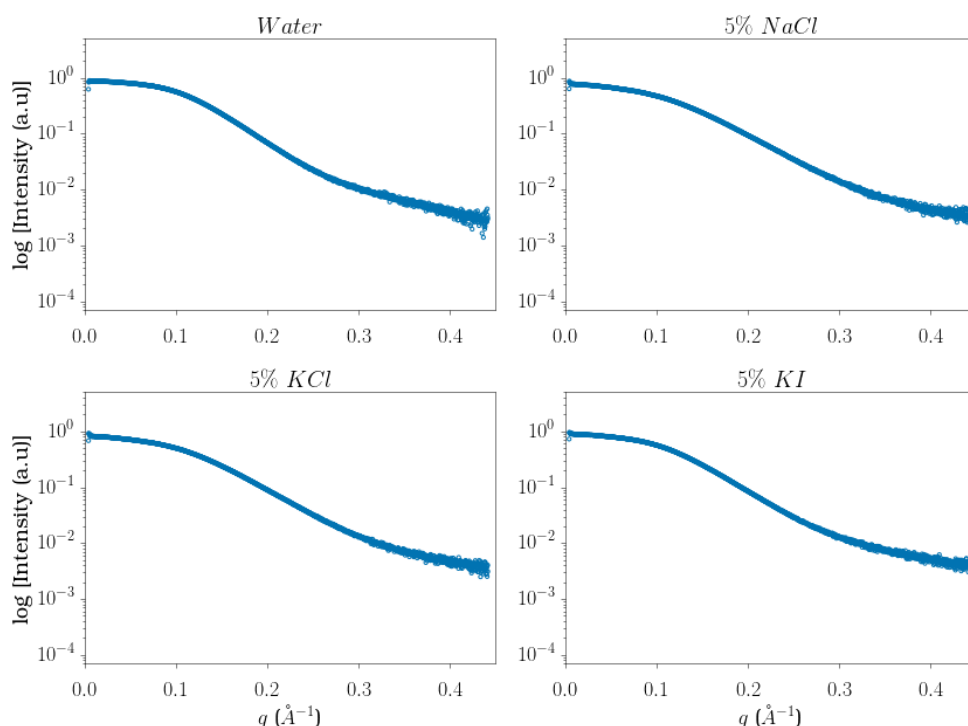


Figure 7.4: The 1D background subtracted scattering patterns for micelles of phytantriol of a concentration of 10mg/ml

Raw data was background subtracted in ScÅtter, a program created by Rob Rambo for the B21 beamline. An example of the background subtracted data for the dilution series of Cithrol is shown in Figure 7.3.

7.3.2 The Differences Between Salts

Three different salts were considered to provide different scattering length densities for the aqueous core of the micelle. These three salts were sodium chloride, potassium chloride, and potassium iodide. At low concentrations the phase behaviour of monoolein and phytantriol is unaffected by sodium chloride, potassium chloride and potassium iodide salt solutions.^{??} It was indeed found that the size of micelle formed by phytantriol was unaffected by the presence of salt in the aqueous solution. However this was not the case for the lipids containing an ester bond in the head group.

Monoolein, Cithrol and monolinolein were all seen to visibly react with potassium iodide by changing colour and eventually monolinolein gains an orange precipitate. Initially the organic layer is cloudy upon vortexing, however for these three lipids, this soon changed to a slight yellow colour instead of settling into two colourless layers. The colour change, shown in Figure 7.5, became more pronounced over 24 hours, surpassing that of the initial potas-

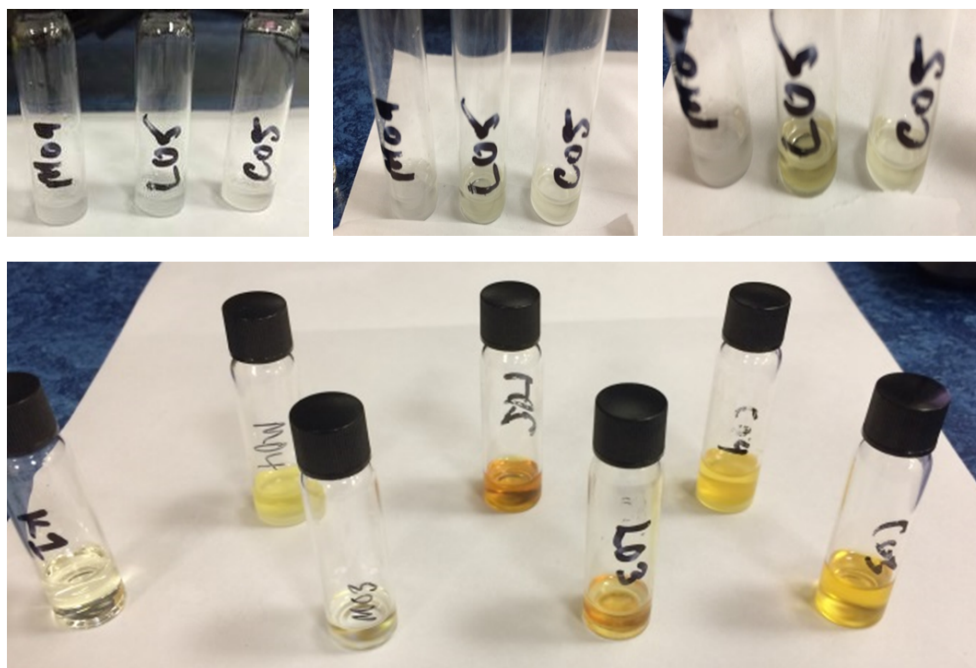


Figure 7.5: Photograph of the change in colour due to potassium iodine in the different ester bond containing lipids used to form micelles. The organic layers containing micelles of monoolein (M), monolinolien (L) and Cithrol (C) turned a yellow/orange colour where the deepness of the colour depends on the unsaturation of the tail.

sium iodide solution. After 24 hours the organic layer of monolinolein, (LO3), which had produced an orange precipitate had no scatter pattern and as such does not contain any micelles.

Potassium chloride has a slightly greater difference in scattering length density to water than sodium chloride, 1.64×10^{-5} to 1.79×10^{-5} respectively to water's 9.44×10^{-6} . Therefore potassium chloride was used to change the scattering length density of the aqueous core of the micelles.

7.3.3 Modelling the Data

Molecule	Molecular formula	Density g cm ⁻³	SLD
Water	H ₂ O	0.9970	9.44*10 ⁻⁶
Potassium Chloride	KCl	1.98	1.64*10 ⁻⁵
10 % KCl Solution	KCl _(aq)	1.10	1.00*10 ⁻⁵
5 % KCl Solution	KCl _(aq)	1.05	9.74*10 ⁻⁶
3 % KCl Solution	KCl _(aq)	1.03	9.63*10 ⁻⁶
Monoolein	C ₂₁ H ₄₀ O ₄	0.942	8.9*10 ⁻⁶
Monolinolein	C ₂₁ H ₃₈ O ₄	0.875 [?]	8.2*10 ⁻⁶
Phytantriol	C ₂₀ H ₄₂ O ₃	0.94 [?]	9.0*10 ⁻⁶
Phytantetrol	C ₂₀ H ₄₂ O ₄	0.94	8.9*10 ⁻⁶
Hexadecane	C ₁₆ H ₃₄	0.773	7.5*10 ⁻⁶

Table 7.1: Calculated SLD for micelles

Two different models were considered for the micelle solution scattering data. First was the basic sphere model where the micelles are considered a monodisperse spherical particle consisting of uniform SLD. The model deals with only 5 parameters of scale, radius of the sphere, the sphere's SLD, the solvent's SLD, and a background constant. As the scattering patterns were not corrected for in absolute scale, the scale parameter does not reference the volume fraction of the particles rather the volume fraction scaled by some factor. The second model was a core shell model where the micelles are considered spherical particles consisting of a central aqueous core and surrounded by a lipid shell. This model uses 7 parameters of which scale, the solvent's SLD, and background are the same as the sphere model. The other additional parameters are the core radius, the thickness of the shell, the core's SLD, and the shell's SLD. A more comprehensive description of the solution SAXS models can be found in Techniques and Methods 2.3.1.2.

The core shell model was chosen over the sphere model as the sphere model could not fit all the data. Additionally the core shell model allowed for separate values of the aqueous core to the thickness of the lipid layer to be extracted from the model[?] which are important for the later neutral surface calculations.

The calculated SLD of the different aqueous solutions and lipid is provided in Table 7.1. As there is no recorded value for the density of phytantetrol, it was assumed to be the same as phytantriol at 0.94 g cm⁻³. These values were

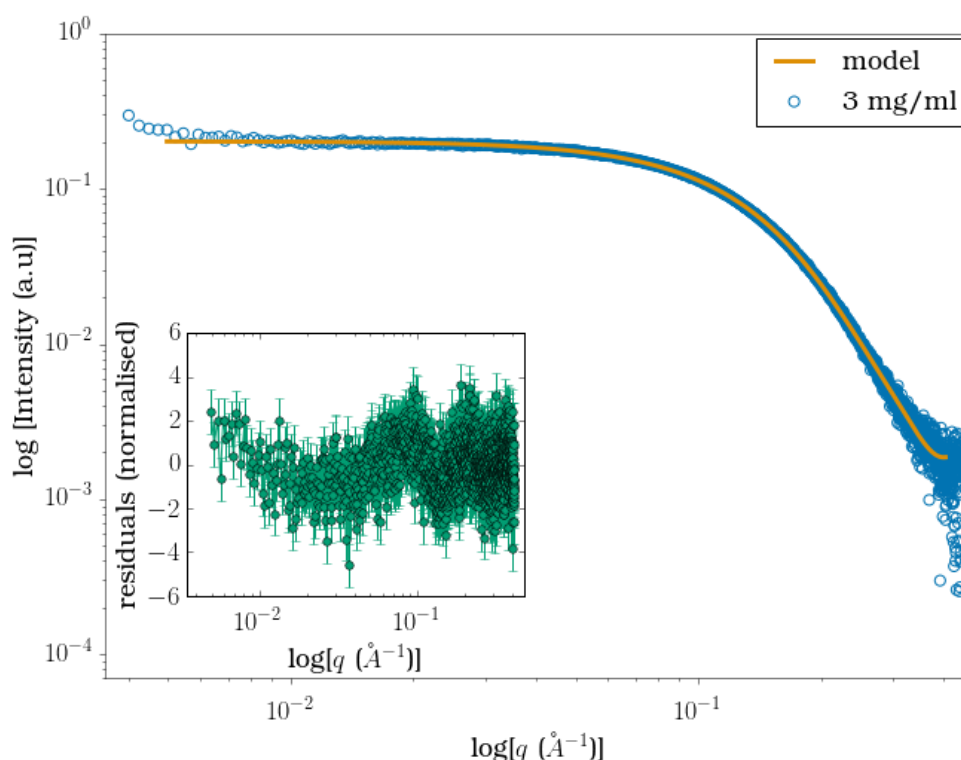


Figure 7.6: Core shell model of micelles of Cithrol 3 mg mL⁻¹ with a water core at 30 °C. The χ^2 value was 1.36

used to constrain the parameters for the SLD of the solvent, hexadecane, and the relevant aqueous cores. The lipid's SLD however were not constrained. This mainly due to the fact that not all the lipids used were of 100 % purity. Interestingly the SLD for all lipids was modelled to be between $7.6 \cdot 10^{-6}$ and $7.8 \cdot 10^{-6}$ for every data set despite the calculated differences.

The data was modelled using SasView. A good fit for a model is a flat as possible residual graph and a minimum χ^2 value. An example of the core shell model fitting the data is shown in Figure 7.6. The data is plotted on a log/log scale with the fitted model plotted on top. The residuals are plotted beneath. The fit between the model and the data was reasonable.

7.3.4 Micelle Size

Serial dilutions of were created for each of the lipids. It was expected and confirmed that the overall size of the micelle did not change as the aqueous solution was added in excess. The lipids encompassed as much water as needed to form their preferred micelle size with relaxed curvature.

Models were created of each concentration and aqueous solution and the r_{lipid}

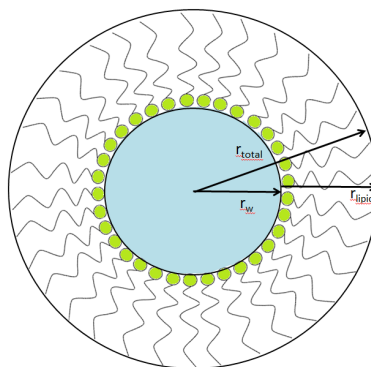


Figure 7.7: Schematic drawing of a micelle with the radius of the water core r_w and the thickness of the shell or length of the lipid r_{lipid} marked.

	Temperature	$r_{lipid} / \text{\AA}$	$r_w / \text{\AA}$	$r_{total} / \text{\AA}$
Cithrol	20 °C	15.0 ± 0.2	13.8 ± 0.2	28.7 ± 0.4
	30 °C	12.4 ± 0.3	11.6 ± 0.3	24.0 ± 0.3
	37 °C	12.1 ± 0.3	11.1 ± 0.2	23.2 ± 0.4
Monolinolein	20 °C	17.3 ± 0.7	15.5 ± 0.1	32.9 ± 0.7
Phytantriol	20 °C	15.3 ± 0.8	12.4 ± 0.2	27.6 ± 0.7
	30 °C	13.2 ± 0.2	10.3 ± 0.1	23.5 ± 0.2
	37 °C	11.7 ± 0.4	9.8 ± 0.1	21.5 ± 0.5
Phytantetrol	20 °C	29.6 ± 2.1	19.1 ± 1.1	48.7 ± 3.0

Table 7.2: Lipid lengths r_{lipid} and the radius of the aqueous core r_w for inverse micelles created in hexadecane

and r_w were extracted. The total size of the micelle was calculated for each as there were initial problems with micelle stability due to disruption from needle of the robot. Therefore any anomalous micelles were not included in the average r_{lipid} and r_w shown in Table 7.2. The fits of all the data used can be found in Appendix D (pg. 184).

7.4 Lipid Length of Monoolein

The lipid lengths for the micelles of monoolein were compared to those from lattice parameters published by Briggs et al.[?] and calculated using Equation 7.1 for the L_α phase and Equation 7.2[?] for the Q_{II} phases for the temperatures 20 °C, 30 °C, and 40 °C. For the L_α phase the lipid length or monolayer thickness is found by the lattice parameter of the L_α phase a_{lam}

minus the water channel distance d_w halved. For the \mathcal{Q}_{II} phases the lipid length is found by using the Euler-Poincaré characteristic χ , the ratio of the minimal surface in a unit cell to the quantity (unit cell volume) $^{2/3}$ σ , and the lattice parameter a of the \mathcal{Q}_{II} phase.[?] The χ and σ for each \mathcal{Q}_{II} phase is listed in Table 7.3.

$$d_l = 0.5(a_{lam} - d_w) \quad \text{where } d_w = \phi_w a_{lam} \quad (7.1)$$

$$\phi_l = 2\sigma \left(\frac{l}{a}\right) + \frac{4}{3}\pi\chi \left(\frac{l}{a}\right)^3 \quad (7.2)$$

Minimal Surface	Cubic Phase	χ	σ
Diamond	\mathcal{Q}_{II}^D	-2	1.919
Primitive	\mathcal{Q}_{II}^P	-4	2.345
Gyroid	\mathcal{Q}_{II}^G	-6	3.091

Table 7.3: Minimal surface characteristics

The calculated lipid length data is plotted in Figure 7.8. As expected, when the curvature increases from the L_α to the \mathcal{Q}_{II}^G to the \mathcal{Q}_{II}^D phase the lipid length decreases. The monoolein inverse micelles have smaller still average lipid lengths at 15.0 Å, 12.4 Å, 12.1 Å for 20 °C, 30 °C, and 37 °C respectively which can be explained by the further increased curvature of the inverse micelles. Therefore the lipid lengths of the inverse micelles are in reasonable agreement with the calculated values for the phases of monoolein.

For all phases and the inverse micelles, the decrease in lipid length due to temperature is consistent at roughly 3 Å. The large decrease between 20 °C and 30 °C in all phases and the inverse micelles is attributed to the fact that for monoolein 20 °C is right on the cusp of the phase boundary between L_α and L_c phases.

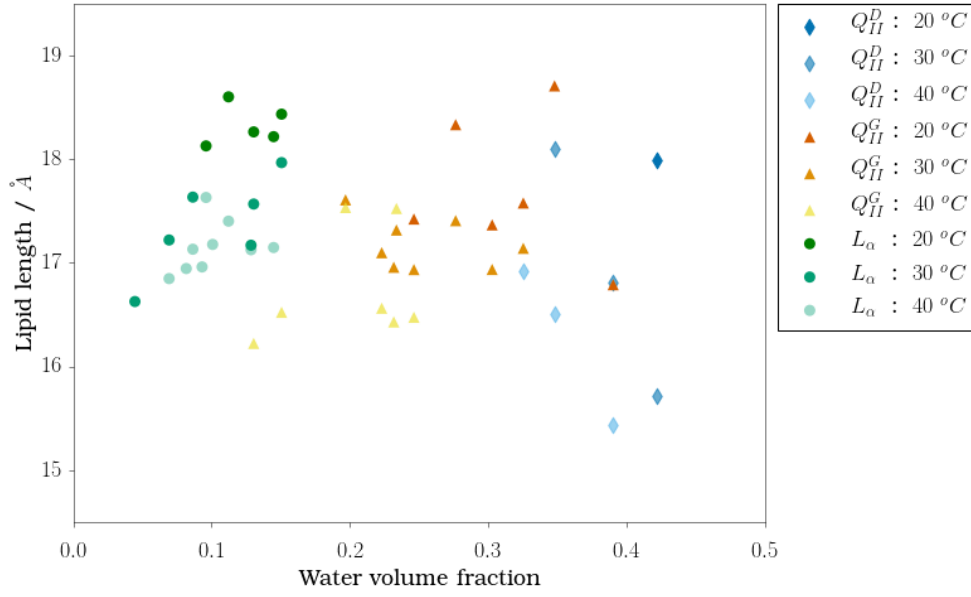


Figure 7.8: The lipid length calculated from Equation 7.2 for the Q_{II} phases and Equation 7.1 for the L_{α} phase plotted as a function of temperature (20 °C, 30 °C, 40 °C) against water volume fraction. Data obtained from Briggs et al.⁷

7.5 The Neutral Surface of a Micelle

By definition the neutral surface is the area which does not change due to bending from hydration or dehydration regardless of phase. Therefore despite the third component of the solvent, for an inverse micelle the neutral surface will also be located somewhere within the lipid layer, as shown in Figure 7.9. Calculating the neutral surface then is based around the equations of a sphere.

$$V_{sphere} = \frac{4}{3}\pi r^3 \quad A_{sphere} = 4\pi r^2$$

First the number of lipids n_{lipids} in a micelle is calculated from the volume of the lipid shell of the micelle and divided by the molecular volume of a single lipid, Equation 7.3. The molecular volume can be calculated using Equation 7.4 where the mass of one molecule of lipid m or the molecular weight M_W of the lipid divided by Avogadro's constant A_V is divided by the density of the lipid ρ_l . The number of lipids is also useful for molecular dynamic simulations of inverse micelles.

$$n_{lipids} = \frac{\frac{4}{3}\pi(r_{total} - r_w)}{v_l} \quad (7.3)$$

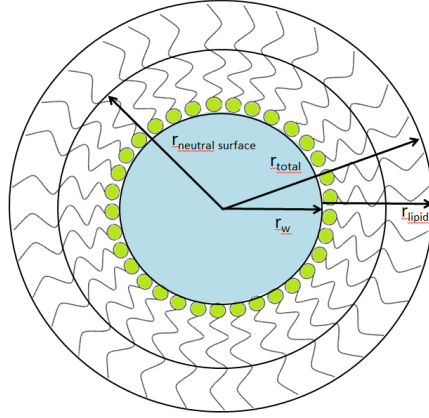


Figure 7.9: Schematic drawing of a micelle with the radius of the water core r_w and the thickness or the shell or length of the lipid r_{lipid} marked.

$$v_l = \frac{m}{\rho_l} = \frac{(M_w/A_v)}{\rho_l} \quad (7.4)$$

Next the area of the neutral surface is calculated by multiplying n_{lipids} by cross-sectional area per lipid molecule A_{cs} at the neutral surface, Equation 7.5.

$$A_{ns} = n_{\text{lipids}} A_{cs} \quad (7.5)$$

The cross-sectional area per lipid at the neutral surface comes from the L_α phase area of a lipid, Equation 7.6, for by definition the cross-sectional area at the neutral surface is invariant. Equation 7.6 assumes that as a flat bilayer the lipid molecules stack evenly and as such the molecular volume molecular volume of a lipid molecule v_l is a cylinder.

$$A_{cs} = \frac{v_l}{d_l} \quad (7.6)$$

Using the area of a sphere it possible to calculate the radius of the neutral surface sphere r_{ns} using Equation 7.7. Conventionally the tail end of the lipid is referred to as being underneath the neutral surface, as in pure aqueous/lipid mixtures the distance to the neutral surface is notated from the center of the bilayer. As such, for comparative purposes the distance underneath the neutral surface is $d_{ns} = r_{\text{total}} - r_{ns}$.

$$r_{ns} = \sqrt{\frac{A_{ns}}{4\pi}} \quad (7.7)$$

The volume of a single molecule underneath the neutral surface v_{ns} is then calculated by subtracting the volume of of the neutral surface from the total micelle volume and then dividing by the total number of lipids, as in Equa-

tion 7.8.

$$v_{ns} = \frac{\frac{4}{3}\pi(r_{total} - r_{ns})}{n_{lipids}} \quad (7.8)$$

The v_{ns} cannot simply be calculated from the area at the neutral surface multiplied by the distance on the hydrophobic side of the neutral surface as a regular shape cannot be assumed. Consider a r_{total} of 30.7 Å and a r_{ns} of 22 Å, the calculated v_{ns} is 454 Å³ while the cross-sectional area, 36 Å², multiplied by the distance underneath the neutral surface, 8.7 Å gives a neutral surface volume of 314 Å³. At 140 Å³ this is a rather large difference in volume.

7.5.1 The Neutral Surfaces of Monoolein, Phytantriol and Monolinolen

7.5.1.1 Cross-sectional Area of the L_α Phase

	M_w /g mol ⁻¹	ρ_l /g cm ⁻³	M_V /Å ³	A_{cs} Å ²
Cithrol	356.6	0.942	628.5	37
Monolinolein	354.5	0.875 [?]	672.7	35
Phytantriol	330.6	0.94 [?]	583.9	21

Table 7.4: The molecular weight M_w , density ρ_l , molecular volume v_l , and cross-sectional area A_{cs} of each lipid.

It has been noted in the literature that temperature has little effect on the cross-sectional area of the neutral surface[?] when calculated using the parallel interface model. Certainly if the cross-sectional area of the monoolein is calculated from L_α data from Briggs et al.[?] for 20 °C, 30 °C, 40 °C this gives cross-sectional values of 36.7 ± 1 Å², 36.2 ± 0.9 Å², and 36.7 ± 0.5 Å². Averaging this to 37 Å² introduces less than 1 % variance in the molecular volume on the hydrophobic side of the neutral surface and as such has been deemed an acceptable approximation for the cross-sectional area.

The cross-sectional area for monolinolein was taken from the literature, 35 Å².[?] The cross-sectional area for phytantriol was calculated from previous work by Dr. Samina Akbar[?] in the Squires Group in which the L_α bilayer thickness was 28.3 Å giving a cross-sectional area of 21 Å².

7.5.1.2 Hydrophobic Volume from the Neutral Surface

	n_{lipids}	$d_{ns} / \text{\AA}$	$v_{ns} / \text{\AA}^3$	v_{ns}/v_l
Cithrol	141.7 ± 5.8	8.38 ± 0.02	454 ± 5	0.72 ± 0.01
	81.7 ± 6.0	8.49 ± 0.02	517 ± 7	0.82 ± 0.01
	74.1 ± 5.6	8.43 ± 0.03	524 ± 7	0.83 ± 0.01
Monolinolein	196.5 ± 16.0	9.40 ± 0.13	479 ± 15	0.71 ± 0.02
Phytantriol	138.8 ± 16.4	12.47 ± 0.12	535 ± 10	0.92 ± 0.02
	85.3 ± 3.4	11.56 ± 0.07	554 ± 2	0.94 ± 0.01
	64.5 ± 4.9	11.1 ± 0.11	572 ± 5	0.95 ± 0.01

Table 7.5: The number of lipids in the inverse micelles created in hexadecane, the calculated distance on the hydrophobic side of the neutral surface d_{ns} and volume on the hydrophobic side of the neutral surface v_{ns} , and the ratio of the v_{ns} and the molecular volume v_l .

The number of lipids in the micelles, the distance on the hydrophobic side of the neutral surface d_{ns} , and the volume underneath the neutral surface v_{ns} were calculated for Cithrol, phytantriol, monolinolein at each temperature. The results are shown in Table 7.5. The code used to calculate the results can be found in Appendix E 6 (pg.186).

The number of lipids in an inverse micelle is proportional to the total size and both decrease with temperature. The volume of the neutral surface v_{ns} is similar for monoolein and monolinolein. For fluid lipid phases the approximate volumes[?] for CH_3 is 54\AA^3 and for CH_2 is 27\AA^3 . This places the neutral surface for monoolein at about C_{15} for 20°C , increasing to about C_{17} at 37°C . The labelling of the molecule is drawn in Figure 7.2 and the C_{17} is next to the ester head group. The C_{15} position corresponds to the previously calculated chain position[?] which was predicted to exert the greatest outward pressure and therefore be the most incompressible part of the chain. The theoretical calculations for the position of the neutral surface of Templer.[?]

Taking the same approximate volumes for CH_3 and CH_2 gives the position of the neutral surface of monolinolein at around C_{16} for 20°C . The similarity of the position to monoolein suggests that the additional double bond has only a small impact on the neutral surface. This is further cemented by calculating the ratio of the v_{ns} to the molecular volume v_l which at 0.72 to 0.71 for monoolein and monolinolein is nearly identical.

The ratio between volumes under the neutral surface and total volume also emphasises the difference in the position of the neutral surface between the

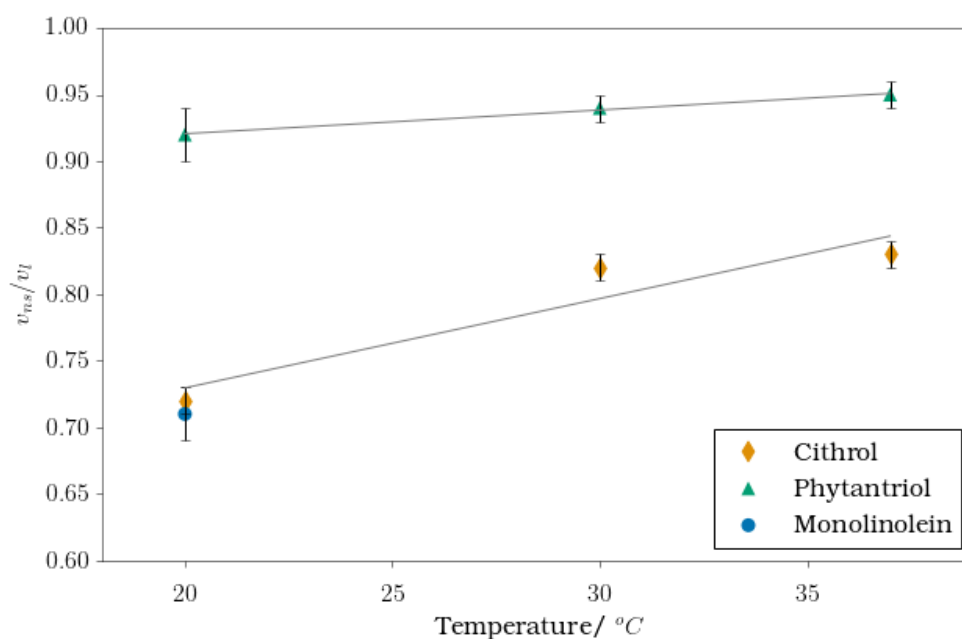


Figure 7.10: The ratio of the volume on the hydrophobic side of the neutral surface v_{ns} to the molecular volume v_l of the micelles plotted against temperature.

ester bonded lipids and phytantriol. The neutral surface for phytantriol sits almost at the interface at 92-95 % volume of the lipid.

The effect of temperature on the neutral surface is shown Figure 7.10. While the ratio of volume under the neutral surface to total volume decreases with temperature for both monoolein and phytantriol, this is more pronounced in monoolein. This difference is interesting because the lipid length decreased similarly for monoolein and phytantriol at 2.9 Å and 3.6 Å respectively. It would be worth investigating this difference in temperature more thoroughly to investigate any link to the super cooling phase behaviour of monoolein.

7.6 Comparisons with the Literature for Monoolein and Monolinolein

7.6.1 Published Values for Monoolein

There are published values for the distance to the neutral surface from the bilayer midplane d_{ns} and the v_{ns} for the Q_{II} phase of monoolein. The d_{ns} was calculated by Chung et al.[?] from a series of minutely precise experiments measuring the lattice parameter at incremental hydration values at 25°C. The cross-sectional area was calculated along the length of a lipid molecule and the point at which this does not change was determined due to hydration.^{??}

This method assumed the bilayer thickness does not change throughout the Q_{II} phase and therefore the lipid chain length is analogous to the monolayer thickness.

Chung et al.⁷ found the distance to monoolein's neutral surface in the Q_{II}^G phase to be at $8.8 \pm 1.0 \text{ \AA}$ and a cross-sectional area of $35 \pm 0.5 \text{ \AA}^2$ where they equated the weight fraction of water C_w to the lipid volume fraction ϕ_l and all the densities were all approximated to 1.00 g cm^{-3} . I have created a python script, Appendix E 5 (pg. 186), using the same analysis and equations. The script reproduced the graph and data shown in Figure 7.11.

Adjusting the values of ρ_l and density of water ρ_w to 0.942 g cm^{-3} and 0.9970 g cm^{-3} which also changes the ϕ_l gives Figure 7.12. The d_{ns} shifts to $9.7 \pm 0.8 \text{ \AA}$ with a cross-sectional area at the neutral surface of $36 \pm 0.5 \text{ \AA}^2$. This value for the cross-sectional area is identical to that of the L_α phase previously calculated at 36 \AA^2 . The changes in values are due to the change in molecular volume from $5.92 \cdot 10^{-28} \text{ m}^{-3}$ to $6.29 \cdot 10^{-28} \text{ m}^{-3}$ rather than any effect from the change in ϕ_l (from 0.2306 - 0.334 to 0.2207 - 0.3321) and hence the lipid length (17.2 to 17.6 \AA).

The fact that the d_{ns} varies due to changes in density highlights some significant drawbacks in calculating the distance to the neutral surface using this method. As Templer⁷ was quick to point out, assuming the distance to the neutral surface remains constant is inconsistent with the geometry of the phases. It is the amount of matter below the neutral surface as well as its cross-sectional area per molecule which remains constant rather than the distance to the neutral surface. If the distance is constant despite changes in hydration this would imply that the amount of matter above and below this point would be varying, which is false.

A purely mathematical determination⁷ of the neutral surface was proposed based around the concept that the neutral surface is a parallel interface to the minimal surface. This allowed the d_{ns} to vary and a value of $v_{ns} = 451 \pm 53 \text{ \AA}^3$ with a cross-sectional area of $32.6 \pm 12.2 \text{ \AA}^2$ to be obtained. These values were obtained using the same data and assumptions as Chung et al. however it is beyond the scope of this work to delve into the mathematics behind these values. Though it is still pertinent to note that the difference in cross-sectional area from the L_α phase which calls into question the accuracy of this method as well.

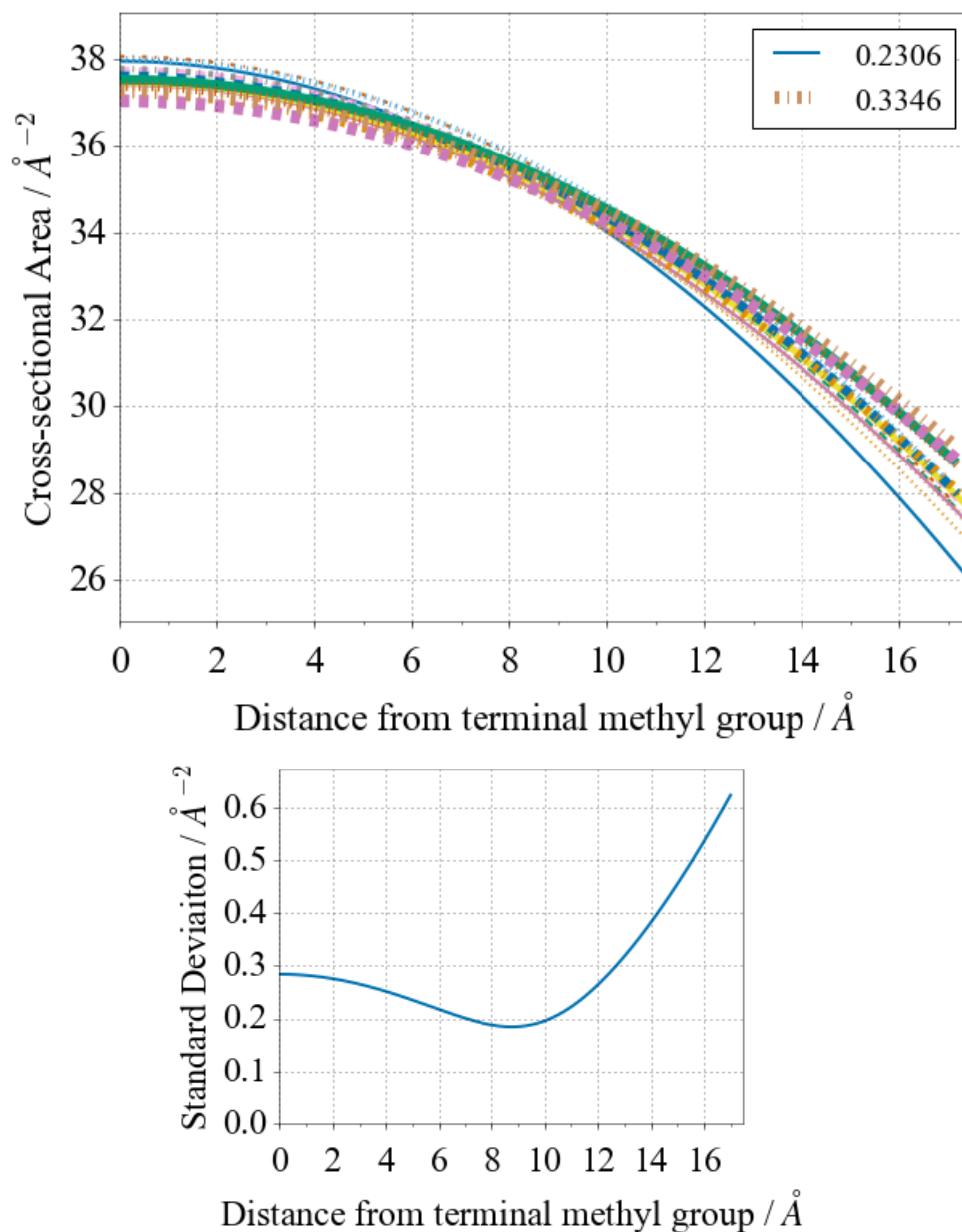


Figure 7.11: Cross-sectional area as a function of the distance from the tail terminal methyl group. There are 16 separate hydrations levels plotted in the Q_{II}^G phase of which the driest and wettest are labelled on the graph as a weight ratio. The point at which the cross sectional area is the same for all the different hydration samples is where the neutral surface resides. The data was reproduced from values provided in Chung and Caffrey?

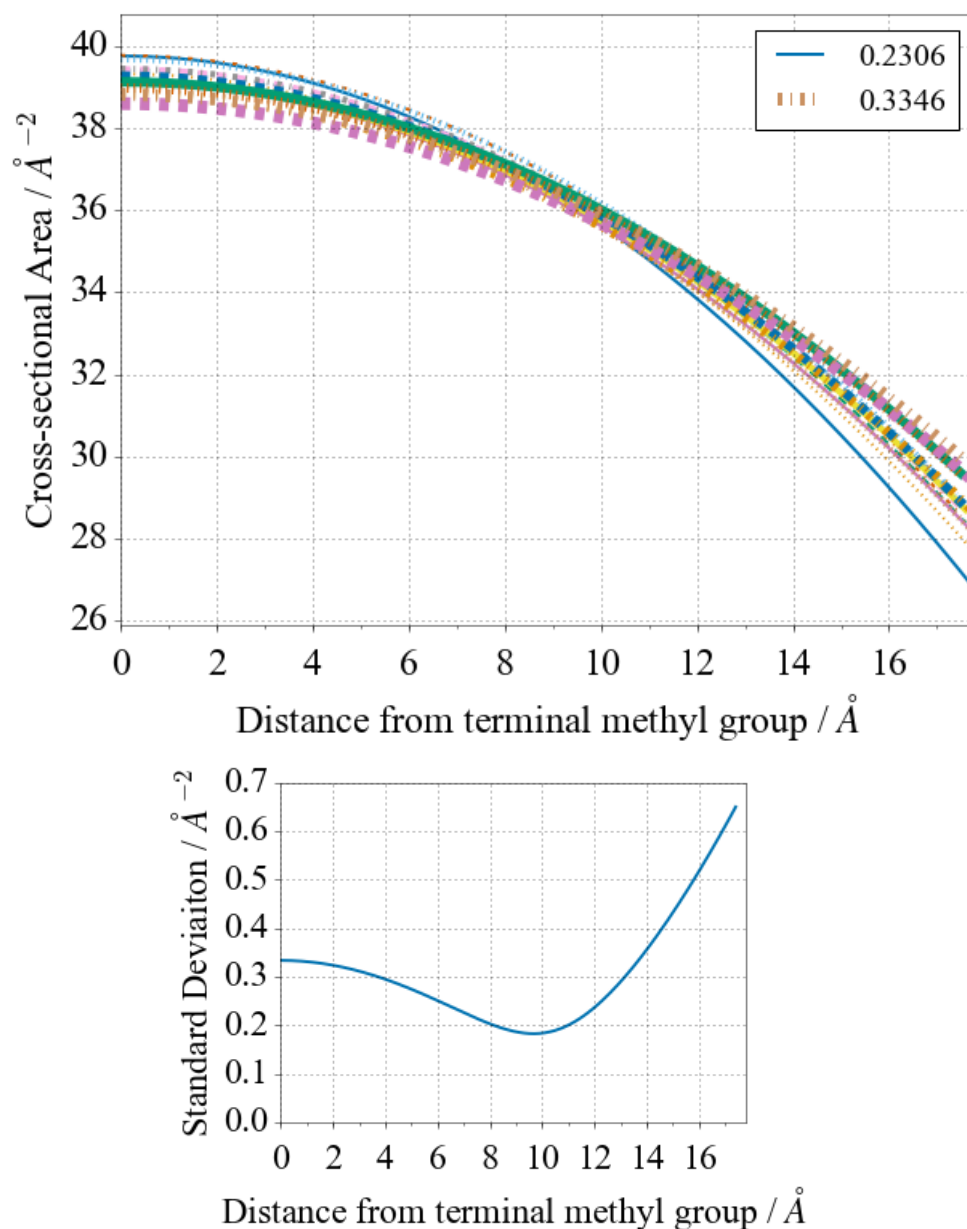


Figure 7.12: Cross-sectional area as a function of the distance from the tail terminal methyl group. There are 16 separate hydrations levels plotted of which the driest and wettest are labelled on the graph as a weight ratio. The data was reproduced from values provided in Chung and Caffrey⁷ but with corrected lipid and water density values.

7.6.2 Comparisons

	Chung [?]	Adjusted	Templer [?]	m: 20 °C	m: 30 °C
$\rho_l / \text{g cm}^{-3}$	1.00	0.942	1.00	0.942	0.942
$\rho_w / \text{g cm}^{-3}$	1.00	0.9971	1.00	0.9971	0.9971
$M_V / \text{\AA}^3$	592.1	628.5	592.1	628.5	628.5
Phase	$\text{Q}_{\text{II}}^{\text{G}}$	$\text{Q}_{\text{II}}^{\text{G}}$	$\text{Q}_{\text{II}}^{\text{G}}$	micelles	micelles
$l / \text{\AA}$	17.2	17.6	17.2	15.0 ± 0.2	12.4 ± 0.3
$d_{ns} / \text{\AA}$	8.8 ± 1.0	9.7 ± 0.8	n/a	8.38 ± 0.02	8.49 ± 0.02
$A_{cs} / \text{\AA}^2$	35 ± 0.5	36 ± 0.5	32.6 ± 12.2	36.7 ± 1	36.7 ± 1
$v_{ns} / \text{\AA}^3$	n/a	n/a	451 ± 53	454 ± 5	571 ± 7
d_{ns}/l	0.516	0.55	n/a	0.56	0.68
v_{ns}/M_V	n/a	n/a	0.76	0.72	0.82

Table 7.6: Calculations for the neutral surface of monoolein.

A comparison of the published parameters of the neutral surface of monoolein and the micelles is shown in Table 7.6. The d_{ns} of the micelles is less than that of the adjusted values, however as previously pointed out the distance to the neutral surface from the bilayer or the distance on the hydrophobic side of the neutral surface d_{ns} changes with phase. The ratio of d_{ns} and the lipid length l however is in good agreement for the micelles and the adjusted values.

While the v_{ns} of Templer at 25 °C and the micelles at 20 °C is very similar, the differences in molecular volume make it hard to compare the two values. Taking the ratio between the volume underneath the neutral surface and the molecular volume v_{ns}/M_V places the Templer value between the values for the micelles at 20 °C and 30 °C which at 25 °C it should be. Even given the discussed shortcomings of the previous methods, I believe that these comparisons suggest that using inverse micelles with relaxed curvature can determine the elastic curvature modelling parameters.

7.6.3 Monolinolein

The area at the neutral surface, the ratio of the volume underneath the neutral surface, and the molecular volume were found using the $\text{Q}_{\text{II}}^{\text{G}}$ phase of monolinolein.[?] These parameters were calculated by modelling the constant mean curvature model and the parallel interface model. The v_{ns}/M_V values

were calculated for different temperatures and pressures. It was found that, similar to the micelles, there was an increase of v_{ns}/M_V with a temperature increase. The value for v_{ns}/M_V was 0.79 ± 0.8 . The value for the inverse micelles is 0.71, which is in the lower value for error and as such in good agreement.

7.7 Phytantriol and Phytantetrol Neutral Surfaces

To my knowledge, the values for the v_{ns} of 535 ± 10 Å and the v_{ns}/M_V of 0.92 are the first values for the neutral surface of phytantriol..

Phytantetrol forms a Q_{II}^D phase in excess water with a lattice parameter of 87.7 ± 0.3 Å² which is larger than phytantriol at 68 Å² but smaller than monoolein at 98 Å². Phytantetrol has a larger head group coupled to the branched carbon chain compared to phytantriol. This may help account for the fact the micelles of phytantetrol were much larger than phytantriol at 48.7 ± 3.0 Å compared to 21 Å. The number of lipids in a micelles also increases by a factor of 5.4 from 138 ± 16.4 to 743.3 ± 138.1 for phytantriol to phytantetrol. Comparing this change to the change in size from monoolein to monolinolein where the tail chain gains an unsaturated bond, suggests that the change in head group has a much larger effect on the relaxed curvature. Intuitively this would make sense with regards to the change in shape of the molecule. However without further assumptions, any quantifiable change was unable to be investigated.

	Phytantriol	Phytantetrol
$\rho_l / \text{g cm}^{-3}$	0.94 [?]	0.94
$M_V / \text{\AA}^3$	583.9	611.7
$\Theta_{II}^D a_{excess H_2O} / \text{\AA}$	68 [?]	87.7 ± 0.3 [?]
$A_{cs} / \text{\AA}^2$	21 [?]	21
n_{lipids}	138 ± 16.4	743.3 ± 138.1
$r_{lipid} / \text{\AA}$	15.3 ± 0.8	29.6 ± 2.1
$d_{ns} / \text{\AA}$	12.48 ± 0.12	13.46 ± 0.24
$v_{ns} / \text{\AA}^3$	535 ± 10	404 ± 25
d_{ns}/r_{lipid}	0.81	0.46
v_{ns}/M_V	0.92	0.66

Table 7.7: Calculations for the neutral surface of phytantriol and phytantetrol at 20 °C.

The molecular weight of phytantetrol is 346.3 g mol^{-1} . If the density of phytantetrol is assumed to be the same as phytantriol at 0.94 g cm^{-3} the molecular volume is 611.7 \AA^3 . Assuming the cross-sectional area of phytantetrol is also the same at 21 \AA^2 ,[?] the number of lipids in a micelle is 743.3 ± 138.1 , the d_{ns} is $13.46 \pm 0.24 \text{ \AA}$ and the v_{ns} is $404 \pm 25 \text{ \AA}^3$ as well as the ratio of the volume underneath the neutral surface to total volume of 0.66. A comparison of the values for phytantetrol to phytantriol is given in Table 7.7.

Unfortunately without a L_α lattice parameter to calculate the cross-sectional area at the neutral surface it isn't possible to calculate more accurate values for the elastic curvature parameters. The values for d_{ns} , v_{ns} , and v_{ns}/v_l as a function of A_{ns} are plotted in Figure 7.13. This shows that a larger cross-section area than phytantriol will decrease the hydrophobic volume of the neutral surface and a smaller cross-section area will increase the hydrophobic volume of the neutral surface compared to phytantriol.

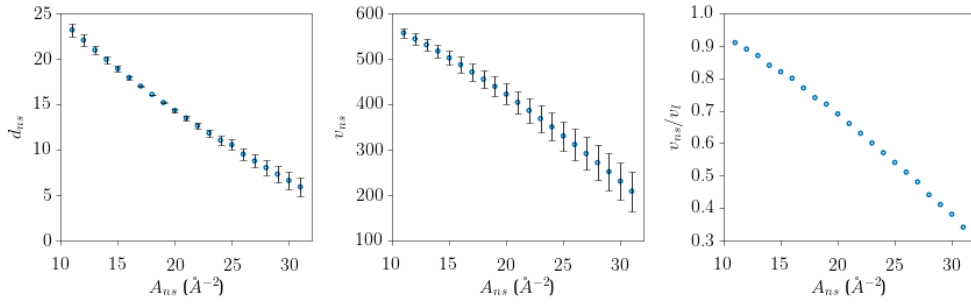


Figure 7.13: Values for distance on the hydrophobic side of the neutral surface d_{ns} , the volume on the hydrophobic side of the neutral surface v_{ns} , and the ratio of v_{ns} to the molecular volume v_l as a function of cross-sectional area A_{ns}

7.8 Relaxed Curvature

The relaxed curvature H_o was calculated for each lipid, shown in Table 7.8. The relaxed curvature from the Helfrich equation,^{??} (Chapter 1.1.3 pg. 5) is $H_o = 1/R$ where R is considered the radius from the center of the water core to the neutral surface. Therefore for a micelle this is:

$$R = \text{total radius} - d_{ns} \quad (7.9)$$

The relaxed curvature of monoolein has previously been calculated using the H_{II} phase of DOPE[?] to be $0.054 \pm 0.003 \text{ \AA}^{-1}$ at 25 °C which is in good agreement of the relaxed curvatures of the micelles. Other examples of calculations of the relaxed curvature include Vacklin et al.[?] 0.05 \AA^{-1} at 37 °C using the H_{II} phase of monoolein with cis-tricosene and 0.008 \AA^{-1} by Chung et al.[?] However as the flaws in the analysis by Chung et al. have already been discussed,^{??} I shall not do so here. One advantage of using micelles to calculate the relaxed curvature is that unlike Dymond et al.[?] it isn't assumed that H_o is temperature independent.

Lipid	Temperature	$R / \text{\AA}$	$H_o / \text{\AA}^{-1}$
Monoolein	20 °C	20.32 ± 0.42	0.049 ± 0.001
	30 °C	15.51 ± 0.32	0.064 ± 0.002
	37 °C	14.77 ± 0.43	0.068 ± 0.002
Monolinolein	20 °C	23.5 ± 0.83	0.043 ± 0.002
Phytantriol	20 °C	15.13 ± 0.82	0.066 ± 0.004
	30 °C	11.94 ± 0.27	0.084 ± 0.002
	37 °C	10.14 ± 0.61	0.094 ± 0.006
Phytantetrol	20 °C	35.24 ± 3.24	0.038 ± 0.003

Table 7.8: The relaxed curvature of the micelles. The d_{ns} of Phytantetrol is calculated from a A_{ns} of phytantriol.

Comparing the values for the relaxed curvature between monoolein, monolinolein, and phytantriol, phytantriol has the greatest relaxed curvature and monolinolein the least. Phytantretrol is discounted from the comparison due to the assumptions made in acquiring the values for the neutral surface. Overall it seems as if the relaxed curvature increases with regards to temperature, with an increase of 0.19 for monoolein and 0.28 for phytantriol.

7.9 Conclusions

The values of the hydrophobic volume from the neutral surface, the position of the neutral surface in a micelle, and the number of lipids in a micelle was calculated from simple solution SAXS experiments for three lipids. These lipids were monoolein, monolinolein, and phytantriol. The values for monoolein and monolinolein were found to be in good agreement with previously published values in the literature. The values for phytantriol were the first calculated to my knowledge.

Micelles were also formed for Q_{II}^D phase forming lipid analogue of phytantriol, phytantetrol, and the values of the hydrophobic volume from the neutral surface, the position of the neutral surface in a micelle, and the number of lipids in a micelle were estimated.

Finally the relaxed curvatures were also calculated and the values for monoolein were found to be in good agreement in the literature.

7.10 Future Work

Firstly a lamellar phase of set water composition of phytantetrol should be acquired so that accurate values for the neutral surface and the relaxed curvature could be obtained.

In the future this new method for calculating the neutral surface of a inverse micelle can be applied and further tested to different lipid or surfactant systems.

To investigate the effect of temperature on the relaxed curvature and neutral surface further temperatures could easily be attempted. This would especially be of value to for monolinolein where comparisons could be made to the data published by Tang et al.[?]

Vacklin et al.[?] found that there were differences in the relaxed curvature of monoolein between the unsaturated and saturated cis-tricosene and tricosane. This could be further investigated by forming micelles in other hydrophobic systems such as cis-tricosene, tetradecane,[?] or decahydronaphthalene.[?]

The effect of amphiphilic molecules such as detergents on the relaxed curvature of lipids could be investigated using inverse micelles. From the effect on the relaxed curvature, the effects on the phase behaviour of the host lipid could be predicted.

The numbers generated for the number of lipids could be used to better refine molecular dynamic simulations of the self-assembly of inverse micelles as well as a model system for the Q_{II} phase.

Chapter 8

Summary

In summary this thesis describes the culmination of the successful creation of a method of analysis for the preferential partitioning of biomolecules in curved lipid nanostructures. This new method uses a combination of orientated lipid nanostructures called phases and Grazing Incidence Small Angle Neutron Scattering (GISANS). It was able to confirm the preferential partitioning of monopalmitin and cholesterol in a host monoolein Q_{II}^D phase. Steps have been made towards extending the method to investigating the preferential partitioning of membrane proteins in curved Q_{II} phases.

As part of this work two separate humidity control systems were designed and created. One for the use with compressed gases and the other a portable system which uses humid air.

A separate study was carried out investigating the calculation of the area and volume of the neutral surface of a lipid using inverse micelles in hydrophobic solutions. It concluded in a new quicker method for calculating these values which provided good agreement with previously published data.

Appendix A

Phase behaviour of Cithrol

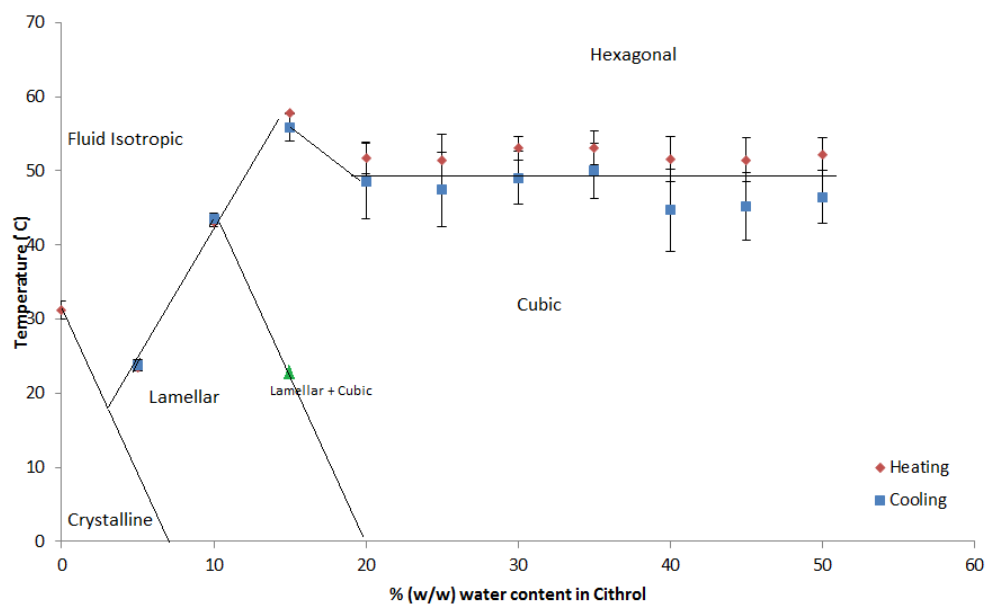


Figure A.1: Phase diagram of Cithrol determined using Hot Stage Microscopy. The samples were heated and cooled at a rate of 2°C/min. The Q_{II} phase and fluid isotropic phase are isotropic and appear black under cross polarisers. The L_{α} and H_{II} phases are anisotropic and are birefringent.

Appendix B

Uniaxial Orientation Azimuthal Angles

B.1 $\mathbf{Q}_{\Pi}^{\text{P}}$ Phase

Reflections	h	k	l	χ
2	-1	-1	0	135
2	-1	-1	0	315
2	-1	0	-1	135
2	-1	0	-1	315
2	-1	0	1	135
2	-1	0	1	315
2	-1	1	0	135
2	-1	1	0	315
2	0	-1	-1	90
2	0	-1	-1	270
2	0	-1	1	90
2	0	-1	1	270
2	0	1	-1	90
2	0	1	-1	270
2	0	1	1	90
2	0	1	1	270
2	1	-1	0	45
2	1	-1	0	225
2	1	0	-1	45
2	1	0	-1	225
2	1	0	1	45
2	1	0	1	225
2	1	1	0	45
2	1	1	0	225

Reflections	h	k	l	χ
4	-2	0	0	180
4	-2	0	0	360
4	0	-2	0	90
4	0	-2	0	270
4	0	0	-2	90
4	0	0	-2	270
4	0	0	2	90
4	0	0	2	270
4	0	2	0	90
4	0	2	0	270
4	2	0	0	0
4	2	0	0	180
6	-2	-1	-1	145
6	-2	-1	-1	325
6	-2	-1	1	145
6	-2	-1	1	325
6	-2	1	-1	145
6	-2	1	-1	325
6	-2	1	1	145
6	-2	1	1	325
6	-1	-2	-1	114
6	-1	-2	-1	294
6	-1	-2	1	114
6	-1	-2	1	294
6	-1	-1	-2	114
6	-1	-1	-2	294
6	-1	-1	2	114
6	-1	-1	2	294
6	-1	1	-2	114
6	-1	1	-2	294
6	-1	1	2	114
6	-1	1	2	294
6	-1	2	-1	114
6	-1	2	-1	294
6	-1	2	1	114
6	-1	2	1	294
6	1	-2	-1	66
6	1	-2	-1	246
6	1	-2	1	66
6	1	-2	1	246
6	1	-1	-2	66
6	1	-1	-2	246
6	1	-1	2	66
6	1	-1	2	246

Reflections	h	k	l	χ
6	1	1	-2	66
6	1	1	-2	246
6	1	1	2	66
6	1	1	2	246
6	1	2	-1	66
6	1	2	-1	246
6	1	2	1	66
6	1	2	1	246
6	2	-1	-1	35
6	2	-1	-1	215
6	2	-1	1	35
6	2	-1	1	215
6	2	1	-1	35
6	2	1	-1	215
6	2	1	1	35
6	2	1	1	215
8	-2	-2	0	135
8	-2	-2	0	315
8	-2	0	-2	135
8	-2	0	-2	315
8	-2	0	2	135
8	-2	0	2	315
8	-2	2	0	135
8	-2	2	0	315
8	0	-2	-2	90
8	0	-2	-2	270
8	0	-2	2	90
8	0	-2	2	270
8	0	2	-2	90
8	0	2	-2	270
8	0	2	2	90
8	0	2	2	270
8	2	-2	0	45
8	2	-2	0	225
8	2	0	-2	45
8	2	0	-2	225
8	2	0	2	45
8	2	0	2	225
8	2	2	0	45
8	2	2	0	225
10	-3	-1	0	162
10	-3	-1	0	342
10	-3	0	-1	162
10	-3	0	-1	342

Reflections	h	k	l	χ
10	-3	0	1	162
10	-3	0	1	342
10	-3	1	0	162
10	-3	1	0	342
10	-1	-3	0	108
10	-1	-3	0	288
10	-1	0	-3	108
10	-1	0	-3	288
10	-1	0	3	108
10	-1	0	3	288
10	-1	3	0	108
10	-1	3	0	288
10	0	-3	-1	90
10	0	-3	-1	270
10	0	-3	1	90
10	0	-3	1	270
10	0	-1	-3	90
10	0	-1	-3	270
10	0	-1	3	90
10	0	-1	3	270
10	0	1	-3	90
10	0	1	-3	270
10	0	1	3	90
10	0	1	3	270
10	0	3	-1	90
10	0	3	-1	270
10	0	3	1	90
10	0	3	1	270
10	1	-3	0	72
10	1	-3	0	252
10	1	0	-3	72
10	1	0	-3	252
10	1	0	3	72
10	1	0	3	252
10	1	3	0	72
10	1	3	0	252
10	3	-1	0	18
10	3	-1	0	198
10	3	0	-1	18
10	3	0	-1	198
10	3	0	1	18
10	3	0	1	198
10	3	1	0	18
10	3	1	0	198

Reflections	h	k	l	χ
12	-2	-2	-2	125
12	-2	-2	-2	305
12	-2	-2	2	125
12	-2	-2	2	305
12	-2	2	-2	125
12	-2	2	-2	305
12	-2	2	2	125
12	-2	2	2	305
12	2	-2	-2	55
12	2	-2	-2	235
12	2	-2	2	55
12	2	-2	2	235
12	2	2	-2	55
12	2	2	-2	235
12	2	2	2	55
12	2	2	2	235
14	-3	-2	-1	143
14	-3	-2	-1	323
14	-3	-2	1	143
14	-3	-2	1	323
14	-3	-1	-2	143
14	-3	-1	-2	323
14	-3	-1	2	143
14	-3	-1	2	323
14	-3	1	-2	143
14	-3	1	-2	323
14	-3	1	2	143
14	-3	1	2	323
14	-3	2	-1	143
14	-3	2	-1	323
14	-3	2	1	143
14	-3	2	1	323
14	-2	-3	-1	122
14	-2	-3	-1	302
14	-2	-3	1	122
14	-2	-3	1	302
14	-2	-1	-3	122
14	-2	-1	-3	302
14	-2	-1	3	122
14	-2	-1	3	302
14	-2	1	-3	122
14	-2	1	-3	302
14	-2	1	3	122
14	-2	1	3	302

Reflections	h	k	l	χ
14	-2	3	-1	122
14	-2	3	-1	302
14	-2	3	1	122
14	-2	3	1	302
14	-1	-3	-2	106
14	-1	-3	-2	286
14	-1	-3	2	106
14	-1	-3	2	286
14	-1	-2	-3	106
14	-1	-2	-3	286
14	-1	-2	3	106
14	-1	-2	3	286
14	-1	2	-3	106
14	-1	2	-3	286
14	-1	2	3	106
14	-1	2	3	286
14	-1	3	-2	106
14	-1	3	-2	286
14	-1	3	2	106
14	-1	3	2	286
14	1	-3	-2	74
14	1	-3	-2	254
14	1	-3	2	74
14	1	-3	2	254
14	1	-2	-3	74
14	1	-2	-3	254
14	1	-2	3	74
14	1	-2	3	254
14	1	2	-3	74
14	1	2	-3	254
14	1	2	3	74
14	1	2	3	254
14	1	3	-2	74
14	1	3	-2	254
14	1	3	2	74
14	1	3	2	254
14	2	-3	-1	58
14	2	-3	-1	238
14	2	-3	1	58
14	2	-3	1	238
14	2	-1	-3	58
14	2	-1	-3	238
14	2	-1	3	58
14	2	-1	3	238

Reflections	h	k	l	χ
14	2	1	-3	58
14	2	1	-3	238
14	2	1	3	58
14	2	1	3	238
14	2	3	-1	58
14	2	3	-1	238
14	2	3	1	58
14	2	3	1	238
14	3	-2	-1	37
14	3	-2	-1	217
14	3	-2	1	37
14	3	-2	1	217
14	3	-1	-2	37
14	3	-1	-2	217
14	3	-1	2	37
14	3	-1	2	217
14	3	1	-2	37
14	3	1	-2	217
14	3	1	2	37
14	3	1	2	217
14	3	2	-1	37
14	3	2	-1	217
14	3	2	1	37
14	3	2	1	217

B.2 Micellar Fd3m Phase

Reflections	h	k	l	χ
3	-1	-1	-1	0
3	-1	-1	-1	180
3	-1	-1	1	109
3	-1	-1	1	289
3	-1	1	-1	109
3	-1	1	-1	289
3	-1	1	1	71
3	-1	1	1	251
3	1	-1	-1	109
3	1	-1	-1	289
3	1	-1	1	71
3	1	-1	1	251
3	1	1	-1	71
3	1	1	-1	251
3	1	1	1	0
3	1	1	1	180
8	-2	-2	0	145
8	-2	-2	0	325
8	-2	0	-2	145
8	-2	0	-2	325
8	-2	0	2	90
8	-2	0	2	270
8	-2	2	0	90
8	-2	2	0	270
8	0	-2	-2	145
8	0	-2	-2	325
8	0	-2	2	90
8	0	-2	2	270
8	0	2	-2	90
8	0	2	-2	270
8	0	2	2	35
8	0	2	2	215
8	2	-2	0	90
8	2	-2	0	270
8	2	0	-2	90
8	2	0	-2	270
8	2	0	2	35
8	2	0	2	215
8	2	2	0	35
8	2	2	0	215
11	-3	-1	-1	151
11	-3	-1	-1	331

Reflections	h	k	l	χ
11	-3	-1	1	121
11	-3	-1	1	301
11	-3	1	-1	121
11	-3	1	-1	301
11	-3	1	1	100
11	-3	1	1	280
11	-1	-3	-1	151
11	-1	-3	-1	331
11	-1	-3	1	121
11	-1	-3	1	301
11	-1	-1	-3	151
11	-1	-1	-3	331
11	-1	-1	3	80
11	-1	-1	3	260
11	-1	1	-3	121
11	-1	1	-3	301
11	-1	1	3	59
11	-1	1	3	239
11	-1	3	-1	80
11	-1	3	-1	260
11	-1	3	1	59
11	-1	3	1	239
11	1	-3	-1	121
11	1	-3	-1	301
11	1	-3	1	100
11	1	-3	1	280
11	1	-1	-3	121
11	1	-1	-3	301
11	1	-1	3	59
11	1	-1	3	239
11	1	1	-3	100
11	1	1	-3	280
11	1	1	3	29
11	1	1	3	209
11	1	3	-1	59
11	1	3	-1	239
11	1	3	1	29
11	1	3	1	209
11	3	-1	-1	80
11	3	-1	-1	260
11	3	-1	1	59
11	3	-1	1	239
11	3	1	-1	59
11	3	1	-1	239

Reflections	h	k	l	χ
11	3	1	1	29
11	3	1	1	209
12	-2	-2	-2	0
12	-2	-2	-2	180
12	-2	-2	2	109
12	-2	-2	2	289
12	-2	2	-2	109
12	-2	2	-2	289
12	-2	2	2	71
12	-2	2	2	251
12	2	-2	-2	109
12	2	-2	-2	289
12	2	-2	2	71
12	2	-2	2	251
12	2	2	-2	71
12	2	2	-2	251
12	2	2	2	0
12	2	2	2	180
16	-4	0	0	125
16	-4	0	0	305
16	0	-4	0	125
16	0	-4	0	305
16	0	0	-4	125
16	0	0	-4	305
16	0	0	4	55
16	0	0	4	235
16	0	4	0	55
16	0	4	0	235
16	4	0	0	55
16	4	0	0	235
19	-3	-3	-1	158
19	-3	-3	-1	338
19	-3	-3	1	131
19	-3	-3	1	311
19	-3	-1	-3	158
19	-3	-1	-3	338
19	-3	-1	3	98
19	-3	-1	3	278
19	-3	1	-3	131
19	-3	1	-3	311
19	-3	1	3	82
19	-3	1	3	262
19	-3	3	-1	98
19	-3	3	-1	278

Reflections	h	k	l	χ
19	-3	3	1	82
19	-3	3	1	262
19	-1	-3	-3	158
19	-1	-3	-3	338
19	-1	-3	3	98
19	-1	-3	3	278
19	-1	3	-3	98
19	-1	3	-3	278
19	-1	3	3	49
19	-1	3	3	229
19	1	-3	-3	131
19	1	-3	-3	311
19	1	-3	3	82
19	1	-3	3	262
19	1	3	-3	82
19	1	3	-3	262
19	1	3	3	22
19	1	3	3	202
19	3	-3	-1	98
19	3	-3	-1	278
19	3	-3	1	82
19	3	-3	1	262
19	3	-1	-3	98
19	3	-1	-3	278
19	3	-1	3	49
19	3	-1	3	229
19	3	1	-3	82
19	3	1	-3	262
19	3	1	3	22
19	3	1	3	202
19	3	3	-1	49
19	3	3	-1	229
19	3	3	1	22
19	3	3	1	202
24	-4	-2	-2	161
24	-4	-2	-2	341
24	-4	-2	2	118
24	-4	-2	2	298
24	-4	2	-2	118
24	-4	2	-2	298
24	-4	2	2	90
24	-4	2	2	270
24	-2	-4	-2	161
24	-2	-4	-2	341

Reflections	h	k	l	χ
24	-2	-4	2	118
24	-2	-4	2	298
24	-2	-2	-4	161
24	-2	-2	-4	341
24	-2	-2	4	90
24	-2	-2	4	270
24	-2	2	-4	118
24	-2	2	-4	298
24	-2	2	4	62
24	-2	2	4	242
24	-2	4	-2	90
24	-2	4	-2	270
24	-2	4	2	62
24	-2	4	2	242
24	2	-4	-2	118
24	2	-4	-2	298
24	2	-4	2	90
24	2	-4	2	270
24	2	-2	-4	118
24	2	-2	-4	298
24	2	-2	4	62
24	2	-2	4	242
24	2	2	-4	90
24	2	2	-4	270
24	2	2	4	19
24	2	2	4	199
24	2	4	-2	62
24	2	4	-2	242
24	2	4	2	19
24	2	4	2	199
24	4	-2	-2	90
24	4	-2	-2	270
24	4	-2	2	62
24	4	-2	2	242
24	4	2	-2	62
24	4	2	-2	242
24	4	2	2	19
24	4	2	2	199

B.3 H_{II} Phase

Reflections	h	k	χ
1	-1	0	180
1	-1	0	360
1	-1	1	180
1	-1	1	360
1	0	-1	120
1	0	-1	300
1	0	1	120
1	0	1	300
1	1	-1	60
1	1	-1	240
1	1	0	60
1	1	0	240
3	-2	1	210
3	-2	1	390
3	-1	-1	150
3	-1	-1	330
3	-1	2	150
3	-1	2	330
3	1	-2	90
3	1	-2	270
3	1	1	90
3	1	1	270
3	2	-1	30
3	2	-1	210
4	-2	0	180
4	-2	0	360
4	-2	2	180
4	-2	2	360
4	0	-2	120
4	0	-2	300
4	0	2	120
4	0	2	300
4	2	-2	60
4	2	-2	240
4	2	0	60
4	2	0	240
7	-3	1	199
7	-3	1	379
7	-3	2	199
7	-3	2	379
7	-2	-1	161
7	-2	-1	341

Reflections	h	k	χ
7	-2	3	161
7	-2	3	341
7	-1	-2	139
7	-1	-2	319
7	-1	3	139
7	-1	3	319
7	1	-3	101
7	1	-3	281
7	1	2	101
7	1	2	281
7	2	-3	79
7	2	-3	259
7	2	1	79
7	2	1	259
7	3	-2	41
7	3	-2	221
7	3	-1	41
7	3	-1	221
9	-3	0	180
9	-3	0	360
9	-3	3	180
9	-3	3	360
9	0	-3	120
9	0	-3	300
9	0	3	120
9	0	3	300
9	3	-3	60
9	3	-3	240
9	3	0	60
9	3	0	240
12	-4	2	210
12	-4	2	390
12	-2	-2	150
12	-2	-2	330
12	-2	4	150
12	-2	4	330
12	2	-4	90
12	2	-4	270
12	2	2	90
12	2	2	270
12	4	-2	30
12	4	-2	210
13	-4	1	194
13	-4	1	374

Reflections	h	k	χ
13	-4	3	194
13	-4	3	374
13	-3	-1	166
13	-3	-1	346
13	-3	4	166
13	-3	4	346
13	-1	-3	134
13	-1	-3	314
13	-1	4	134
13	-1	4	314
13	1	-4	106
13	1	-4	286
13	1	3	106
13	1	3	286
13	3	-4	74
13	3	-4	254
13	3	1	74
13	3	1	254
13	4	-3	46
13	4	-3	226
13	4	-1	46
13	4	-1	226

Appendix C

GISANS Peak Intensities

Sample	Ring	Azimuthal Angle	Average: <i>Area * Mean</i>	σ	σ %
h-Mo/ h-MP/ h-chol	$\sqrt{2}$	35	1843.60	12.98	0.70
		90	1527.39	62.34	4.08
		145	1112.97	61.41	5.52
		215	1057.43	82.65	7.82
		270	1486.35	17.85	1.20
		325	1888.79	48.11	2.55
	$\sqrt{3}$	0	3290.76	28.53	0.87
		70	717.22	105.99	14.78
		109	588.39	33.08	5.62
		180	4237.45	43.75	1.03
		251	616.56	30.32	4.92
		289	582.04	16.86	2.90
d-Mo/ h-MP/ h-chol	$\sqrt{2}$	35	298.60	6.53	2.19
		90	257.55	5.24	2.04
		145	208.52	6.22	2.98
		215	216.19	12.44	5.76
		270	249.41	18.45	7.40
		325	253.35	21.07	8.32
	$\sqrt{3}$	0	619.78	47.06	7.59
		70	116.68	12.43	10.66
		109	127.93	11.03	8.62
		180	863.22	42.47	4.92
		251	147.43	6.00	4.07
		289	79.72	8.76	10.99
d-Mo/ h-MP/ h-chol (H ₂ O)	$\sqrt{2}$	35	1031.37	11.89	1.15
		90	794.39	24.89	3.13
		145	681.48	21.44	3.15
		215	782.75	50.24	6.42
		270	802.30	33.96	4.23

Sample	Ring	Azimuthal Angle	Average: $Area * Mean$	σ	$\sigma \%$
		325	976.07	37.11	3.80
	$\sqrt{3}$	0	2102.97	29.11	1.38
		70	378.11	10.58	2.80
		109	401.78	43.30	10.78
		180	2368.10	52.63	2.22
		251	343.04	6.77	1.97
		289	310.45	15.46	4.98

Appendix D

Micelle Sizes

D.1 Cithrol

Temperature	Concentration	Aqueous	χ^2	Thickness	Radius	Total Size
20	3	H ₂ O	3.05	14.80	13.53	28.33
20	3	H ₂ O	3.28	14.63	13.62	28.26
20	2	H ₂ O	3.07	15.14	14.09	29.23
20	2	H ₂ O	2.87	15.14	13.94	29.08
20	2	3 % KCl	2.99	15.29	14.08	29.38
20	2	5 % KCl	2.12	14.69	13.31	28.00
20	2	5 % KCl	2.68	14.98	13.74	28.72
30	6	H ₂ O	22.68	11.67	12.47	24.14
30	3	H ₂ O	1.37	12.20	11.31	23.51
30	3	H ₂ O	1.35	12.20	11.32	23.52
30	2	H ₂ O	1.18	12.58	11.41	23.99
30	2	H ₂ O	0.68	12.82	11.62	24.45
30	2	5 % KCl	1.23	12.51	11.30	23.81
30	2	5 % KCl	0.60	12.67	11.58	24.25
37	2	H ₂ O	0.98	12.46	11.06	23.51
37	2	H ₂ O	1.10	12.86	11.47	24.33
37	3	H ₂ O	1.16	11.79	10.85	22.64
37	3	H ₂ O	1.18	12.07	11.10	23.17
37	3	H ₂ O	1.24	12.04	11.17	23.21
37	3	H ₂ O	0.95	11.70	10.73	22.42
37	2	H ₂ O	0.89	12.47	11.26	23.74
37	3	3 % KCl	1.12	11.88	11.15	23.03
37	2	3 % KCl	0.93	12.05	11.03	23.08
37	2	3 % KCl	1.20	12.17	11.26	23.44
37	2	5 % KCl	1.00	11.86	10.85	22.71
37	2	5 % KCl	1.24	12.24	11.37	23.60

D.2 Phytantriol

Temperature	Concentration	Aqueous	χ^2	Thickness	Radius	Total Size
20	2	H ₂ O	2.57	16.07	12.30	28.38
20	3	3 % KCl	4.51	13.96	12.62	26.58
20	2	3 % KCl	3.05	15.68	12.62	28.30
20	3	5 % KCl	4.78	15.43	12.49	27.92
20	3	5 % KCl	4.48	14.88	12.47	27.35
20	2	5 % KCl	2.86	16.08	12.44	28.52
20	2	5 % KCl	2.94	15.35	12.47	27.82
30	3	H ₂ O	1.12	12.89	10.26	23.14
30	3	H ₂ O	0.74	13.32	10.41	23.73
30	2	H ₂ O	1.11	13.26	10.13	23.40
30	2	H ₂ O	0.67	13.63	10.38	24.01
30	3	3 % KCl	1.21	13.09	10.30	23.39
30	3	3 % KCl	0.72	13.16	10.38	23.54
30	2	3 % KCl	1.23	13.15	10.20	23.36
30	2	3 % KCl	0.55	13.49	10.35	23.84
30	3	5 % KCl	1.19	12.78	10.19	22.97
30	3	5 % KCl	0.58	13.17	10.40	23.57
30	2	5 % KCl	1.12	13.22	10.22	23.44
37	2	H ₂ O	0.99	11.95	9.76	21.72
37	3	H ₂ O	1.01	11.70	9.85	21.55
37	3	H ₂ O	1.06	12.31	10.07	22.39
37	3	H ₂ O	0.96	11.54	9.81	21.34
37	2	H ₂ O	1.09	12.07	9.85	21.92
37	2	H ₂ O	0.91	12.10	9.84	21.94
37	3	3 % KCl	0.99	11.19	9.76	20.95
37	3	3 % KCl	0.94	10.82	9.60	20.42
37	2	3 % KCl	1.00	11.93	9.88	21.81
37	2	3 % KCl	1.04	12.22	9.99	22.21
37	2	3 % KCl	0.86	11.92	9.87	21.79
37	3	5 % KCl	1.04	11.17	9.85	21.02
37	2	5 % KCl	1.00	11.65	9.85	21.49
37	2	10 % KCl	0.95	10.84	9.75	20.59

Appendix E

Python Code

Due to the length of the scripts, I have not included the code in print. Instead all python code used in this thesis is currently hosted on git-hub at:

<https://github.com/EleonoreM/phd-appendix-code>

At the time of publishing the repository is private. It is the plan to soon make the code public, however until such a time please use the enclosed account to view the code.

Username: EM-PhD-Appendix

Email: EM-phd-appendix@outlook.com

Password: emphdappendixcode

The scripts contained are:

1. Lipid Phase and Lattice Parameter Determination
2. Orientated 2D GISAXS data
3. Raspberry Pi Humidity Control
4. Mass Flow Controllers Humidity Control
5. Parameters of a Q_{II} Phase
6. Neutral Surface of a Micelle

Any trouble viewing the code please email: *EM-phd-appendix@outlook.com*

Bibliography

.

List of Figures

1.1	Schematic of types of shapes of lipid molecules. Type 1 (a) are cone like, type 0 (b) are cylindrical, and type 2 (c) are wedge like.	3
1.2	Principal curvatures C_1 and C_2 of a surface. Reproduced from Liu et al. [?]	4
1.3	Schematic representation of packing frustration in type 2 lipids. The cross-sectional grey areas show potential voids from the cylindrical geometry which must be filled by the deformation of the hydrocarbon chains. Reproduced from Shearman et al. [?]	6
1.4	Lipid mesostructures, the green sphere represents the head group of the lipid and the wiggly line the tail. In the Q_{II} phases (d-f) the green surface represents the surface of the bilayer and grey area is inside. In (g) the bilayer midplane is represented and for (h) the black dots represent micelles. (g-h) are reproduced from Kulkarni et al. [?]	7
1.5	Chemical structure of monoolein	10
1.6	Phase diagram of monoolein, reproduced from Qiu et al. [?]	10
1.7	Chemical structure of phytantriol	11
1.8	Phase diagram of phytantriol reproduced from Barauskas et al. [?] . .	11
1.9	The levels of protein structure beginning with amino acids forming a peptide chain as a primary structure. The secondary structure is the stacking of peptide chains to form α helixes or β sheets. Combinations of these form the tertiary structure of the protein. multiple proteins together are macromolecular complexes with quaternary structure. .	12
1.10	Cell membrane with component parts, reproduced from OpenStax. [?] Lipids are represented as brown ball head groups with yellow tail chains.	13
1.11	Cartoon representation of the proposed mechanism for <i>in meso</i> crystallisation reproduced from. [?] The protein is first reconstituted in the Q_{II} phase. Once a precipitant is added, the equilibrium is shifted away from stability and a phase separation occurs. The protein molecules diffuse from the Q_{II} phase to lock into the crystal lattice by way of a L_α portal. The Q_{II}^P phase is shown for ease of viewing.	15
1.12	The structure of gramicidin dimer reproduced from Hoefer et al. [?] and the ompF trimer reproduced from Efremov et al. [?] with a from the bilayer view (top) and into the channel (bottom).	17
1.13	Shear orientation schematic, including the 2D Small Angle X-ray Scattering (SAXS) patterns produced, reproduced from Squires et al. [?] . .	20

1.14	Single crystal orientation schematic, including the 2D SAXS patterns produced, reproduced from Oka et al. [?] The top red bar represents the concentration of 1,4-butanediol in the sample while the bottom bar of the capillary represents the phase present.	20
1.15	Single crystal transformation from the Q_{II}^D phase to the Q_{II}^P phase using L-arginine (Arg), reproduced from Oka et al. [?] The sponge phase L_3 phase was created from t-butyl alcohol (tBA) which was diluted out before the capillary cut at the end of the single crystal region. The capillary was then placed in Arg solution to induce a phase change to the Q_{II}^P phase.	21
1.16	(a) The identity of phases present of the phytantriol-glycerol system with respect to humidity, reproduced from Richardson et al. [?] The white dotted line represents the upper limit measured and black dotted line is the lower limit measured. (b) GISAXS images of phytantriol/glycerol films showing different phases, reproduced from Richardson et al. [?]	22
2.1	(a) Graphical representation of a parallelepiped with side lengths a , b , c and a lattice plane (1,1,1). (b) Graphical representation of the relationship between parallel diffraction planes with a distance d apart.	25
2.2	Graphical representation of the vector normal of a lattice plane. The corresponding trigonometric \cos relationship for each plane vertex is listed on the right.	26
2.3	X-ray scattering from two different lattice planes. The distance between planes is d_{hkl} . The second ray travels further by $\vec{r}\vec{q} + \vec{q}\vec{s}$ or $2d_{hkl} \sin \theta$. As $\theta_{in} = \theta_{out}$ the change in wave vector \vec{k} is 2θ with a momentum change of $\Delta\vec{k}$. [?]	27
2.4	Simplified schematic of corresponding 2D diffraction patterns from lipid micro-domains and domain orientation	30
2.5	Metal capillary holders	34
2.6	Schematic of spin-coating	37
2.7	Schematic drawing of the capillary connected to a syringe via a HPLC connection. A tube at the other end was connected to remove the waste solutions.	41
3.1	Q_{II} lattice vectors	44
3.2	Radial geometry of the SAXS set-up with regards to the diffraction pattern and the incident beam at a distance $d_{detector}$	45
3.3	Prediction of Q_{II}^D phase of [1,1,1] orientation. (a) The previous python script created by Sam Richardson and (b) the updated script including the addition of 2 more reflections. The lipid film is spin coated from a 70/30 (v/v) solution of Cithrol and glycerol dissolved in 80 % (w/w) ethanol.	46

3.4	The binary mask (a) was used for the peak finding in (b) . The lattice parameter was found to be 84 Å . The diffraction pattern was that of Cithrol in the Q_{II}^D phase with uniaxial orientation [1,1,1] (c) . The mask is required to mask intensity near the beam center and the on axis intensity not covered by the beam stop. The beam center is marked with a small diamond.	48
3.5	Q_{II}^P phase made from spin coating the ternary mixture 30 % (v/v) Cithrol, 24.75 % (v/v) phytantriol, and 5.25 % (v/v) Brij-56 all in 80 % (w/w) ethanol mixed with glycerol in 80 % (w/w) ethanol at a 60/40 total lipid to glycerol ratio. (b) - (d) Simulations of expected vertical uniaxial orientation corresponding to [1,0,0], [1,1,0], [1,1,1].	50
3.6	Fd3m micellar phase of lattice parameter 142 Å made from a DOPC / OA molar ratios 20/80 in 80 % (w/w) ethanol mixed with glycerol 20 % (v/v) also in 80 % (w/w) ethanol. (b) - (d) Simulations of expected vertical uniaxial orientation corresponding to [1,0,0], [1,1,0], [1,1,1].	51
3.7	Hexagonal lattice vectors	52
3.8	H_{II} phase of lattice parameter 66 Å made from a dioleoyl-phosphatidylethanolamine (DOPE) spin coated with 30 % (v/v) glycerol. It is uniaxially orientated in the [1,0] direction.	54
3.9	Schematic (a) and 1D pattern (b) of the $P63/mmc$ micellar phase. Reproduced from Shearman et al. [?]	55
3.10	(a) Experimental data for the $P63/mmc$ micellar phase reproduced from Shearman et al. [?] (b)-(d) Predictions for the $P63/mmc$ micellar phase.	56
3.11	Effect of the ratio of glycerol on the thin film formed in a capillary from Cithrol/glycerol. The thin films were made from Cithrol mixed with glycerol (v/v) in 80 % (w/w) ethanol.	58
3.12	The Q_{II}^D thin film within a capillary is uniaxially orientated in the [1,1,0] direction. The thin film was made from Cithrol mixed with 40 % (v/v) glycerol in 80 % (w/w) ethanol. A schematic showing the capillary normal is included on the left.	59
3.13	Grazing Incidence Small Angle X-ray Scattering (GISAXS) patterns of spin coated samples from (a) Cithrol mixed with 20 % (v/v) glycerol in 80 % (w/w) ethanol at 25 % RH. (b) Cithrol mixed with 15 % (v/v) glycerol in 80 % (w/w) ethanol at <96 % RH	60
3.14	Diffraction pattern of Figure 3.11f, a uniaxially orientated [1,1,0] film in a capillary, after being filled with water for two weeks.	60
4.1	The change in the lipid Q_{II}^D phase due to the addition of styrene maleic acid co-polymer lipid particles (SMALPS) and then a flush through with water. The original Q_{II}^D film had a lattice parameter of 96 Å which swells upon the addition of the polymer to 99 Å. Upon addition of water there is a coexisting Q_{II}^P phase with lattice parameter of 132 Å.	66

4.2	The change in the lipid Q_{II}^D phase due to the addition of styrene maleic acid co-polymer and then a flush through with water. The original Q_{II}^D film had a lattice parameter of 99 Å which swells upon the addition of the polymer to 107 Å. Upon addition of water there is a phase change to the Q_{II}^P phase with lattice parameter of 154 Å.	67
4.3	Intensity change of the monoolein film in Figure 4.2 due to the addition of styrene maleic acid co-polymer.	68
4.4	The change in the lipid Q_{II} phase due to the addition of buffer solution and then flush through with water. The original Q_{II}^D film had a lattice parameter of 98 Å which swells upon the addition of the polymer to 101.5 Å. Upon addition of water there is a phase change to the Q_{II}^P phase with lattice parameter of 136 Å.	70
4.5	Lattice parameter changes from flow through experiments of SMALPS nanodiscs. The experiments begin with a Q_{II}^D coating in a capillary in which an aqueous solution is added. After some time the aqueous solution is removed and water added to the capillary. Error bars are not plotted as they do not exceed the marker size.	71
4.6	The change in the lipid Q_{II} phase due to the addition of LDAO buffer solution and then flushing through with water. The original Q_{II}^D film had a lattice parameter of 94.9 Å. Upon addition of LDAO buffer there is a phase change to the Q_{II}^P phase with lattice parameter of 138.3 Å. For each scan the intensity is normalised to the highest peak.	72
4.7	The change in the lipid Q_{II} phase due to the addition of outer membrane protein F (OmpF) solution and then flushing through with water. The original Q_{II}^D film had a lattice parameter of 91.7 Å. Upon addition of OmpF solution there is a phase change to the Q_{II}^P phase with lattice parameter of 170.8 Å which settled to 151.7 Å after the addition of water.	73
4.8	The change in the lipid Q_{II} phase due to the addition of OG solution and then flushing through with water. The original Q_{II}^D film had a lattice parameter of 94.9 Å. For each scan the intensity is normalised to the highest peak	74
4.9	Raman spectra of the Q_{II}^D phase of Cithrol. Spectra taken from a capillary coating of Cithrol filled with water to produce the excess water Q_{II}^D phase. Characteristic vibrational modes for acyl chains of lipid are noted.	75
4.10	Raman spectra was first taken of a Cithrol Q_{II}^D phase coating in a capillary in excess water, second Styrene maleic acid co-polymer solution was added and a spectra taken. Third the polymer solution was removed after 2 hours and another spectra taken.	76
4.11	Raman of gramicidin powder. Characteristic vibrational modes for proteins are noted.	77

4.12	Comparative Raman spectra of powdered gramicidin, Cithrol Q_{II}^D phase, a coating of cithrol containing 3 % (w/w) gramicidin, and a coating of cithrol containing 10 % (w/w) gramicidin. Unique vibrational modes for gramicidin are highlighted.	78
4.13	RAMAN spectra of OmpF. OmpF is solubilised in OG detergent in 20 mM Tris pH 8.0, 1 mM ethylenediamine tetraacetic acid (EDTA) protein buffer.	79
4.14	Comparative Raman spectra for OmpF solution, the Q_{II}^D phase of Cithrol, and Q_{II}^D phases made with OmpF solutions.	80
4.15	Phase change of an orientated capillary of Q_{II}^D to Q_{II}^P upon the addition of LDAO buffer solution. The lipid film was made from Cithrol/glycerol 70/30 (v/v) and coated from a 50 % ethanol solution.	81
5.1	A visualisation of regions of flatter (small green balls) and highly curved (larger red balls) of a Q_{II}^P phase bilayer.	85
5.2	Thickness of Q_{II}^D film as controlled by percentage of ethanol. The thickness increases with decreasing amount of ethanol. The films are Cithrol/glycerol mixed in a 70/30 (v/v) ratio.	87
5.3	The percentage loading of gramicidin in Cithrol was tested in excess water. The phase change occurred between 14-18 % (w/w) gramicidin. The phase boundary for gramicidin in pure monoolein is also plotted at 21.7 % (w/w).	88
5.4	Raman of spin coated films of gramicidin in Cithrol. Characteristic gramicidin vibrational modes are noted.	89
5.5	A 5 % (w/w) gramicidin in Cithrol spin-coated with 30 % (v/v) glycerol. The thin film was Q_{II}^D phase with a lattice parameter of 84 Å and orientated in the [1,1,1] direction. The large WAXS peak was from the absorption of water in the high humidity (<95 % RH) environment. . .	90
5.6	Gramicidin in DOPE of H_{II} phase with lattice parameter 70 Å. The lipid peak at 1.4 Å^{-1} is marked. The small peak around 1.7 Å was determined to be from an artefact and present in every sample	92
5.7	(b) 30 % (w/w) gramicidin in Cithrol was spin-coated and a L_{α} phase of lattice parameter 41.3 Å was formed at low humidity (<25 % RH). The off axis diffuse peak at $q \text{ } 0.154 \text{ Å}^{-1}$ is due to Gramicidin pores. A comparison of the L_{α} phase is provided in (a)	93
5.8	Q_{II}^D monoolein, monopalmitin, and cholesterol in a 80:10:10 molar ratio spin coated with 30 % (v/v) glycerol with a lattice parameter of 89.6 Å and a uniaxial orientation of [1,1,1].	95
5.9	Q_{II}^D monoolein, monopalmitin, and cholesterol in a 80:10:10 molar ratio spin coated with 30 % (v/v) glycerol with a lattice parameter of 89.6 Å and a uniaxial orientation of [1,1,1].	96
5.10	Scattering simulation done in VESPA [?] of the flatter (large red balls) and the more curved (small green balls) regions of the bilayer. A visualisation of the Q_{II}^D phase is provided, (a)	97

5.11	2D GISANS pattern of monoolein spin coated with d-glycerol/h-glycerol in a D ₂ O environment. The glycerol ratio was chosen to contrast match D ₂ O. The lattice parameter is 94 Å and calculated from the middle of the second reflection rather than the split first reflection. .	99
5.12	d-Monoolein was successfully contrast matched to D ₂ O (bottom). To check that d-monoolein formed the right phase, the wafer was put in a H ₂ O atmosphere (top). When no longer contrast matched the Q _{II} ^D phase can be seen with a lattice parameter of 97 Å.	100
5.13	The 1D GISANS patterns of several spin coated thin films of lipid/glycerol mixtures. Despite the increase of signal to noise ratio from the orientated lipid film it is still hard to differentiate between the first and second reflections. Especially in the deuterated lipid sample where only one peak is visible. By contrast the peaks are quite distinguishable in the 2D patterns.	101
5.14	Monoolein(MO), Monopalmitin (MP), and cholesterol(chol) in a 80:10:10 molar ratio dissolved in 80 % (w/w) ethanol and mixed d-glycerol in 80 % (w/w) ethanol in a 60/40 (v/v) ratio. The d-MO and d-glycerol was contrasted matched to D ₂ O.	102
5.15	Azimuthal profile of the $\sqrt{3}$ reflection normalised to the $\sqrt{2}$ reflection. The difference in intensity between the deuterated and non-deuterated samples can be clearly seen in the on axis peaks.	103
5.16	d-MO/h-MP/h-chol in a 80:10:10 molar ratio dissolved in ethanol and mixed with 30% (v/v) glycerol in ethanol solution in a H ₂ O environment	104
5.17	Normalisation of the $\sqrt{3}$ reflections to the $\sqrt{2}$ reflections. The on axis peaks are separated from the other $\sqrt{3}$ reflections due to the 6 times greater intensity. The ratio of intensity is greater for the contrast matched system.	105
6.1	Photograph of the first iteration of humidity control used on the beam-line i22 at Diamond Light Source. Consisting of a modified plastic box, the air input was at the bottom and the humidity sensor was placed just above the sample wafer. All other holes or windows were covered in Kapton.	111
6.2	Thin film of Cithrol and glycerol mixture 80/20 (v/v) spin coated from 80 % (w/w) ethanol solution in which a phase change from Q _{II} ^G to Q _{II} ^D occurs with increasing humidity.	111
6.3	(above) Schematic of the Raspberry Pi set up. (below) Photograph of the Raspberry Pi set up. In this iteration to achieve the top range of higher humidities a second bubbler was added. The bright yellow cup contains desiccator beads and the dry pump. For scale a pound coin is next to the humidity sensor.	113

6.4	The design and set up of both the Raspberry Pi 3.0 and Arduino Uno. The pins used are coloured red (5V), grey (ground), purple for the fish tank pumps, and orange for the humidity sensors. The Raspberry Pi powers the Arduino Uno through a USB to USB-2 cable. The 5V and ground cables from the Arduino Uno are attached to the humidity sensor along with one cable into a digital pin.	115
6.5	Full circuit diagram of the humidity control system. The positive (5V) wires are labelled in red and the neutral (ground) wires are labelled in black. The pumps are purple while the wires going to them from the pins are green and blue. The humidity sensors are connected to the Arduino by an orange wire into the digital pins.	117
6.6	Schematic representation of the operations of the Raspberry Pi software written in Python.	118
6.7	The General User Interface (GUI) for the Raspberry Pi controlled humidity system. The target humidity or pump ratio can be imputed manually or through a preset conditions file, the settings can be controlled as can the recording of data through the GUI.	119
6.8	The relative humidity and expected relative humidity are plotted as a function of time with regards to changing pump ratio. The expected humidity is defined in Equation 6.4	119
6.9	Using the control loop, the target humidity and actual relative humidity are plotted as a function of time with regards to changing pump ratio.	121
6.10	3D printed box for the Raspberry Pi camera containing cross polarisers. The matt grey chamber was printed in black plastic to hold the camera at a distance to observe the phase changes of lipids under cross-polarised light. The camera and humidity sensors were both powered by the Raspberry Pi.	122
6.11	Phase changes of the two lipids monoolein and phytantriol, documented via changes in birefringence.	122
6.12	Phase change from L_{α} to micellar in oleic acid/sodium oleate mixture induced by elevated humidity levels (>90 %) in an levitated droplet. .	123
6.13	(a) Photograph of the Raspberry Pi system in use on ISIS Neutron and Muon Source's SANS2D beamline. Phase change from the Q_{II}^D (b) to the Q_{II}^G (c) phase due to reduction of humidity of a 20 % (w/w) Brij in phytantriol with 20 % (v/v) glycerol spin coated on a silicon substrate.	124
6.14	Humidity chamber concept and execution on the beamline. There are three gas flow input/outputs. One of which has been used to thread the humidity sensor cables through and then blocked off. For helium gas the input was placed at the bottom while for Nitrogen gas the input was at the top.	125

6.15	Comparison of different sample environments on i22 GISAXS data using a Q_{II}^D phase thin film uniaxially orientated in the [1,1,1] direction spin-coated from cithrol/glycerol 75/25 (v/v) in 80 % (w/w) ethanol. For (a) and (b) a large air gap between beam, sample, and detector was created by the hexapod. (a) The initial iteration of humidity control was used in air. For (b) the air gap scatter was aimed to be decreased by creating a helium 'balloon' between the beam and detector. Humidity control was poor due to such large volumes and small bubblers. (c) was collected on a vertical wafer (hence the rotation of spots) in the 1L sample box created where the air gap was minimised due to lack of hexapod.	126
6.16	Schematic representation of the set up of the mass flow controller system.	127
6.17	Change of humidity over time for changing flow rates of the 50 slm mass flow controllers	129
6.18	Manual calibration of the flow rate to humidity for the 50 slm mass flow controllers. The flow rates of each mass flow controller were changed sequentially and the box was left to equilibrate for 5 minutes before the humidity was read as were the actual flow rates. . . .	130
6.19	Automatic calibration of the flow rate to humidity for the 50 slm mass flow controllers capped at a 20 slm total volume through the box. The flow rates of each mass flow controller were changed sequentially in 0.1 increasing then decreasing steps. The box was left to equilibrate for 5 minutes (helium) or 3 minutes (nitrogen) before the humidity was read along with the actual flow rates for each mass flow controller. . .	131
6.20	Humidity control using the mass flow controllers using the loops in the schematic (a) . The data plotted in (b) was produced where the tolerance for the target humidity was 1 %. However less than 15 % humidity is currently unachievable due to the non-zero flow of the mass flow controllers.	133
6.21	The 1D diffraction data for a thin film of cithrol/glycerol of 80:20 (v/v) ratio. Humidity control using Nitrogen gas was used to induce phase changes by first increasing the humidity then decreasing it. A phase change from the Q_{II}^G phase to the Q_{II}^D phase takes place with increasing humidity. With decreasing humidity the film changes back to the Q_{II}^G phase and then to the micellar phase.	134
6.22	Phase change of a thin film of cithrol/glycerol of 75:25 (v/v) ratio from the Q_{II}^D phase to the micellar phase due to changes in humidity. . .	135

7.1	Schematic representations of properties of the neutral surface. (a) The molecular volume. (b) Distance from the center of the bilayer to the neutral surface. (c) Cross-sectional area per lipid at the neutral surface. (d) Volume per lipid underneath the neutral surface. By definition both the cross-sectional area and the volume underneath the neutral surface are invariant whilst the distance to the neutral surface will change.	141
7.2	Skeleton drawings of the lipids used to create inverse micelles. The carbon backbones are labelled in each.	143
7.3	Background subtracted 1D SAXS patterns for Cithrol micelles in hexadecane created with water and incubated and run at 30 °C	144
7.4	The 1D background subtracted scattering patterns for micelles of phytantriol of a concentration of 10mg/ml	145
7.5	Photograph of the change in colour due to potassium iodine in the different ester bond containing lipids used to form micelles. The organic layers containing micelles of monoolein (M), monolinolien (L) and Cithrol (C) turned a yellow/orange colour wehere the deepness of the colour depends on the unsaturation of the tail.	146
7.6	Core shell model of micelles of Cithrol 3 mg mL ⁻¹ with a water core at 30 °C. The χ^2 value was 1.36	148
7.7	Schematic drawing of a micelle with the radius of the water core r_w and the thickness of the shell or length of the lipid r_{lipid} marked. . . .	149
7.8	The lipid length calculated from Equation 7.2 for the Q _{II} phases and Equation 7.1 for the L _{α} phase plotted as a function of temperature (20 °C, 30 °C, 40 °C) against water volume fraction. Data obtained from Briggs et al. [?]	151
7.9	Schematic drawing of a micelle with the radius of the water core r_w and the thickness or the shell or length of the lipid r_{lipid} marked. . .	152
7.10	The ratio of the volume on the hydrophobic side of the neutral surface v_{ns} to the molecular volume v_l of the micelles plotted against temperature.	155
7.11	Cross-sectional area as a function of the distance from the tail terminal methyl group. There are 16 separate hydrations levels plotted in the Q _{II} ^G phase of which the driest and wettest are labelled on the graph as a weight ratio. The point at which the cross sectional area is the same for all the different hydration samples is where the neutral surface resides. The data was reproduced from values provided in Chung and Caffrey [?]	157
7.12	Cross-sectional area as a function of the distance from the tail terminal methyl group. There are 16 separate hydrations levels plotted of which the driest and wettest are labelled on the graph as a weight ratio. The data was reproduced from values provided in Chung and Caffrey [?] but with corrected lipid and water density values.	158

7.13	Values for distance on the hydrophobic side of the neutral surface d_{ns} , the volume on the hydrophobic side of the neutral surface v_{ns} , and the ratio of v_{ns} to the molecular volume v_l as a function of cross-sectional area A_{ns}	162
A.1	Phase diagram of Cithrol determined using Hot Stage Microscopy. The samples were heated and cooled at a rate of 2°C/min. The Q_{II} phase and fluid isotropic phase are isotropic and appear black under cross polarisers. The L_{α} and H_{II} phases are anisotropic and are birefringent. 166	

List of Tables

2.1	Characteristic [hkl] for the first 7 peaks of a lipid phase.	29
2.2	Characteristic peptide backbone vibrational modes. [?]	31
2.3	Characteristic lipid vibrational modes. [?]	32
2.4	Full list of micelles formed	35
2.5	Lipid phases of Cithrol at different glycerol concentrations at 30% RH. 37	
2.6	Scattering Length Density (SLD) and percentage weight to contrast match to D ₂ O of compounds used in GISANS experiments.	40
3.1	Lipid phases of Cithrol at different glycerol concentrations at low (< 25 % RH).	46
5.1	Wide Angle X-ray Scattering (WAXS) peaks for different structures.	86
6.1	List of components and their prices as of 2018	114
7.1	Calculated SLD for micelles	147
7.2	Lipid lengths r_{lipid} and the radius of the aqueous core r_w for inverse micelles created in hexadecane	149
7.3	Minimal surface characteristics	150
7.4	The molecular weight molecular weight M_W , density density of the lipid ρ_l , molecular volume molecular volume of a lipid molecule v_l , and cross-sectional area cross-sectional area per lipid molecule A_{cs} of each lipid.	153
7.5	The number of lipids in the inverse micelles created in hexadecane, the calculated distance on the hydrophobic side of the neutral surface d_{ns} and volume on the hydrophobic side of the neutral surface v_{ns} , and the ratio of the v_{ns} and the molecular volume v_l	154
7.6	Calculations for the neutral surface of monoolein.	159

7.7	Calculations for the neutral surface of phytantriol and phytantetrol at 20 °C.	161
7.8	The relaxed curvature of the micelles. The d_{ns} of Phytantetrol is calculated from a A_{ns} of phytantriol.	163

List of Equations

Symbols

H_{II} Lattice Parameter	53
H_{II} uniaxial [hk] values	53
Q_{II} Lattice Parameter	44

A

Area of a sphere	151
Azimuthal angle between two cubic vectors	44
Azimuthal angle between two hexagonal vectors	53
Azimuthal angle between two vectors	44

B

Bragg's Law	28
Bragg's Law, Derivation of	28

C

Condition for X-ray Diffraction	28
Critical Packing Parameter	3

D

Derivation of Lattice Parameter	26
---------------------------------------	----

F

Flow Rate Ratio	131
-----------------------	-----

G

Gaussian Curvature	4
GISANS: Normalisation of Q_{II} Reflections	102

H

Helfrich Equation: Curvature Elastic Energy	5
Hexagonal Lattice Parameter	52

L

L_{α} : Cross-sectional area	152
L_{α} : Lipid length	150

M

Mean Curvature	4
Micellar cubic Fd3m uniaxial [hkl] values	49
Micelle: Area of the neutral surface	152
Micelle: Number of lipids	151
Micelle: Radius to the neutral surface	152
Micelle: Volume under the neutral surface	153
Molecular volume	152

O

Orthogonal Axis	26
-----------------------	----

P

P63/mmc micellar uniaxial [hkl] values	55
Predicting diffraction peaks positions for uniaxial orientation	45
Principal Curvature of a Surface	4
Proportionality Gain	120

Q

Q_{II} : Lipid length	150
Q_{II}^P uniaxial [hkl] values	49

R

Raspberry Pi Expected Humidity	120
Raspberry Pi Pumps Percentage Run in Seconds	120
Real Space Vectors	25, 27
Reciprocal Space Vectors	27
Relationship between Real and Reciprocal Space	26
Relationship between SAXS detector to spot	45
Relative Humidity	110
Relaxed Curvature of a Micelle	162

S

SAXS Radial Geometry	45
----------------------------	----

V

Volume of a sphere	151
--------------------------	-----

W

Wave Vector Change	28
Wave Vector Change at Bragg Condition	28
Weighted Mean	102